USC
UNIVERSIDADE
DE SANTIAGO
DE COMPOSTELA

Departamento de Física de Partículas

HOLOGRAPHIC THERMALIZATION IN FINITE-SIZE SYSTEMS

Alexandre Serantes Rubianes
Santiago de Compostela, Febreiro de 2017


USC
UNIVERSIDADE
DE SANTIAGO
DE COMPOSTELA

UNIVERSIDADE DE SANTIAGO DE COMPOSTELA

Departamento de Física de Partículas

HOLOGRAPHIC THERMALIZATION IN FINITE-SIZE SYSTEMS

Alexandre Serantes Rubianes
Santiago de Compostela, Febreiro de 2017

UNIVERSIDADE DE SANTIAGO DE COMPOSTELA

Departamento de Física de Partículas

HOLOGRAPHIC THERMALIZATION IN FINITE-SIZE SYSTEMS

Tese presentada para optar ao grao
de Doutor en Física por:

Alexandre Serantes Rubianes

Febreiro, 2017


USC
UNIVERSIDADE
DE SANTIAGO
DE COMPOSTELA

UNIVERSIDADE DE SANTIAGO DE COMPOSTELA

Departamento de Física de Partículas

Javier Mas Solé, Profesor Titular de Física Teórica da Universidade de Santiago de Compostela,

CERTIFICO: que a memoria titulada *Holographic thermalization in finite-size systems* foi realizada, baixo a miña dirección, por Alexandre Serantes Rubianes, no departamento de Física de Partículas desta Universidade e constitúe o traballo de Tese que presenta para optar ao grao de Doutor en Física.

Asinado:

Javier Mas Solé
Santiago de Compostela, Febreiro de 2017


USC
UNIVERSIDADE
DE SANTIAGO
DE COMPOSTELA

A Suso, Narda, Mar e Andrea

Agradecementos

En primer lugar, no puedo más que expresar mi más profundo agradecimiento a mi director, Javier Mas. Por darme una oportunidad. Por guiarme con clarividencia y con una paciencia inagotable a través de las vicisitudes de nuestra investigación. La puerta de su despacho siempre permaneció abierta y, por muy atareado que se encontrase, siempre sacó ese tiempo, insustituible para mí, en el que su mente estaba totalmente focalizada en mis confusiones, corazonadas e ideas. Para mí, abordar un problema con Javier es una experiencia libre, creativa, enriquecedora y, por encima de todo lo demás, compartida. Interactuar con Javier en una base diaria ha sido una lección permanente para mí, de un valor que no me atrevo a calcular. Obviamente, a nivel intelectual, a Javier le debo quien soy a día de hoy como físico. Más allá de eso, permitidme la paráfrasis... ”La física es la cosa más importante de las cosas menos importantes”. Javier es una persona excelente, y soy sumamente afortunado de haberlo conocido. Me atrevería a decir que las mejores lecciones que me llevo de él tienen que ver con su inteligencia emocional y su saber hacer. Por todo esto, Javier, de corazón: muchísimas gracias!

También me gustaría expresar mi más sincera gratitud a las diferentes personas con las que he tenido el privilegio de colaborar. Ninguna parte de el trabajo presentado en esta tesis habría sido posible sin la insuperable capacidad, pasión y dedicación de Javier Abajo, Emilia da Silva, Esperanza López, Raúl Arias, Pablo Carracedo y Daniele Musso. Trabajar codo con codo junto a vosotros ha sido un placer que repetiría encantado una y otra vez. De cada uno, y especialmente de Esperanza, me llevo la emoción de haber comprendido algo que no entendía, de haber expandido mi mente con alguna idea que ni siquiera alcanzaba a atisbar. Gracias a todos por haberme enriquecido intelectual y personalmente.

I would also like to thank the other marvelous physicists I had the opportunity to meet during this years. Special thanks go to the Theory Group people at Santiago. They create such a great atmosphere out of their microscopic interactions. Apart from Javier himself, it is always a pleasure to assist to a talk with Prof. Edelstein and Prof. Ramallo. They give a student a real taste of what sharp thought and brilliance mean. I also had the opportunity to interact with outstanding postdoctoral researchers such as Niko Jokela, Georgios Itsios and Daniele himself. Javier and I started an unfinished project with Niko that lead to some of the results presented here. Georgios and I have never collaborated at the professional level, but our discussions (mostly not about physics, and usually accompanied by some lovely Italian food and some beers) have been one of the best times I had during these years. As for Daniele, I am looking forward to collaborating with you in the future! It is a fabulous experience! Out of the other stunning young researchers I have met, I hold the greatest memories of Xián O. Camanho and Ricardo Couso; even though our interactions were just occasional, they were enough for me to be impressed by their mastering of physics and their intelligence. Very special thanks go to Yago Bea and Aníbal Sierra. Being a doctorate student would have been even more baffling if it were not for the fact that I shared this experience with equally perplexed people. I count both of you as friends, with no more unnecessary adjectives. It was a pleasure sharing discussions, travels and English practicing with you. It has always been amazing to see our different ways of approaching the same problem interact with each another, and you have taught me lots of beautiful physics. I also want to say to J.M. Penín and Anxo F. Biasi that it has been a pleasure meeting them during the last year. I honestly think you have a bright future ahead, so don't give up the work! I don't want to miss this opportunity to thank all the other amazing people I have met at the different conferences, workshops, and schools I have attended. Thanks for making them a fabulous experience. Finally, last but not least, I want to thank Carlos Salgado for his invaluable support.

Que dicir da familia, tanto da primixenia como da gañada. Se comezo pola última, non podo máis que agradecerlle a Javi, Jesús, Adri, Turia, Chino, Dani e Sabela ter compartido estes anos en Compostela con eles. Proporcionaron un punto de referencia que me ancorou á vida real, liberáronme da matrix -e non é metáfora!- na que pasei tantas e tantas horas. Sostivéronme sen sabelo en momentos de bastante frustración, e sacáronme un sorriso sempre, tivese eu ganas del ou non. Sen eles, eu xamais tería podido contribuir ao traballo que se presenta nesta tese co mesmo entusiasmo. Grazas pola vosa alegría, pola voso bo humor, polo a veces incomprensible interese que amosábades no que estaba a facer! Aos de sempre, Adrián, Arantxa, Ramón, Borja, Javi, Jesús, Iago e Roi só podo dicirlles que non hai maior regalo nesta vida que o saber que, por moi lonxe que os nosos camiños nos leven neste planeta en crise perpetua, a seguinte vez que nos vexamos terá pasado só un instante. Nos momentos non tan bos, ter isto claro sempre me dou a forza necesaria. Grazas rapaces.

A miña irmá débolle, por riba de todo, ter sido sempre un oído paciente das miñas grandes penas, das de verdade. Grazas Mar por estar sempre ahí no momento necesario, por reconfortarme coa túa calma e co teu saber profundo. A meus pais, só lles digo que espero sinceramente, algún día, estar remotamente á súa altura. Son as mellores persoas que coñezo. O máis importante que apredín deles é que o amor, cando merece tal nome, é incondicional. De miña nai, do seu xeito humilde de afrontar a vida con xenerosidade, resolución e orgullo, da sua valentía inasequible a todo desalento, lévome as ansias cas que agora ollo ao futuro, as gañas de seguir adiante por este camiño con tantas luces como sombras. Sen meu pai, eu xamais tería sido físico. El, desde que teño uso de razón, sempre buscou a resposta ás grandes preguntas á súa maneira. Del aprendín a fascinación polo saber, por aprender, por comprender. E, tamén desde que recordo, sempre me apoiou, e non só regalándome un número verdadeiramente insano de libros de divulgación, senón ensinándome que o pracer da búsqueda sempre reside nun mesmo. Sei que esta tese é un paso máis ben infinitesimal nesa dirección papá pero, ao fin e ao cabo, sexamos optimistas. Confiemos en que outros, moito mellores, sempre terán tempo.

E xa por último, o primeiro. A Andrea, que está agora mesmo xunto a min mentres escribo estas liñas, só lle digo que sei que o camiño, a veces, foi moi duro, pero que non houbo un só día destes anos que non iluminase o seu sorriso. Como agora, ahí estiveches sempre, apoiándome, firme. Grazas.

This page is intentionally left blank


USC
UNIVERSIDADE
DE SANTIAGO
DE COMPOSTELA

Contents

Foreword

> The career of a young
> theoretical physicist consists of
> treating *black holes* in
> ever-increasing levels of
> abstraction.
>
> ---
>
> Sidney Coleman, updated by
> Andrew Strominger

With hindsight, the 20th century can be recalled as a critical time in Mankind's search for the underlying description of Nature. In this era, physicists discovered the *theory of (nearly) everything*: the combined framework provided by General Relativity and Quantum Field Theory. Each member of the theory of nearly-everything arises from the reconciliation of the Special Theory of Relativity and a different physical realm. In the case of General Relativity, this realm corresponds to nothing but Gravity herself. In the case of the Quantum Field Theory, it corresponds to Quantum Mechanics. Supplement with the proper experimental data, these two frameworks produce extremely powerful theories, and even in recent years we witnessed their respective triumphs in the description of real-world phenomena, with the discoverement of both the Higgs boson and gravitational waves.

However, and speaking *only* at the basic, theoretical level, their coexistence is far from peaceful. It turns out that there is a fundamental tension between their underlying physical principles, which is better appreciated when trying to understand quantum phenomena in a dynamical spacetime. Black holes have been instrumental in exposing this tension by their pivotal role in the formulation of the Holographic Principle and the discoverement of the Information Paradox. This last paradox, specially in its modern Firewall incarnation, points clearly to the fact that, in a curved spacetime, there might be a fundamental clash between the principles of locality and quantum-mechanical unitarity. As a consequence, we can rightfully ask ourselves if the framework of Quantum Field Theory breaks down at the basic level in the presence of gravity.

On the other hand, a candidate ultraviolet completion of both Quantum Field Theory and General Relativity has also been found: String Theory. First, as a perturbative framework allowing for a consistent quantum-mechanical description of the graviton. Second, as five different theories of supersymmetric strings that also contained the building blocks for assembling Particle Physics. And, finally, as different perturbative limits of the same underlying beast, whose fundamental nature still awaits to reveal herself in full splendor: M-theory.

It is in this context where the former status of Quantum Field Theory received a stunning twist. As discovered by Maldacena twenty years ago, Quantum Field Theory can serve as a nonperturbative definition of Quantum Gravity. This idea, that goes under the name of the holographic duality, gauge/gravity duality or the AdS/CFT correspondence, postulates that certain string theories in asymptotically anti-de Sitter spacetimes are secretly dual to Conformal Field Theories living in a fixed geometry of lower dimensionality.

The way in which this apparently impossible equivalence is implemented is by the weak/strong nature of the duality. The Conformal Field Theory standard perturbative regime corresponds to the highly-quantum, highly-stringy regime of the Quantum Gravity theory. Conversely, the classical and pointlike limit of the Quantum Gravity theory, which is nothing but Supergravity, corresponds to the large-N and strongly-coupled regime of the Conformal Field Theory.

It is by means of this last observation that String Theory has come closer to the everyday experimental world. In recent years, a plethora of strongly-coupled collective media have been discovered, ranging from Quantum Cromodynamics to Condensed Matter. These novel phases of matter defy a standard kinetic description based on weakly-coupled quasiparticles: even in the case where their underlying microscopic Lagrangian is known in closed form, as it happens for the Quark Gluon Plasma, their strongly-coupled nature rendes standard perturbative methods useless. In principle, if the microscopic description of the system is known, Lattice Field Theory allows a first-principles approach. However, the fact that lattice techniques suffer when dealing with highly-oscillatory, complex exponentials prevents a straightforward study of real-time processes, even though these are of the uttermost importance when characterizing these novel phases.

The hopeful expectation that arises is that, at strong coupling, Holographic Conformal Field Theories fall into the same broad universality class -*i*.e. they display the same kind of emergent behavior - as the underlying microscopic theories describing these systems. With this assumption, the AdS/CFT correspondence can deliver extremely valuable and general lessons about the physics of strongly-coupled quantum matter. Impressively, these developments take place through a geometrization of quantum-mechanical phenomena, which reduces answering standard field theory questions to the analysis of dual gravitational constructions. In this way, the AdS/CFT correspondence has emerged as the bedrock of an arena where black holes in particular, and gravity in general, talk to the rest of modern physics in unexpected and surprising ways.

About this thesis

In recent years, the problem of how macroscopic, isolated quantum systems driven out of equilibrium thermalize has been under intense survey. At the theoretical level, the hundreds of works done in this area employ tools that range from integrability to numerical simulations. Furthermore, it has also become possible to address this question directly in the laboratory: by manipulating cold atom systems with optical lattices, different kinds of perturbations can be introduced, and the system relaxation can be efficiently monitored. A major lesson that emerges from these studies is that the different routes to final equilibration the system has at its disposal build up a surprisingly rich landscape, that depends both on the microscopic interactions and the initial state. These include features like prethermalization stages, partial memory loss of the initial conditions or revivals, to mention a few of them.

Conversely, by studying gravitational collapse in asymptotically global AdS spacetimes, we have similarly found a surprisingly rich landscape of possible routes to final black hole formation, that depend crucially on the particular details of the action considered and the initial state in question. Given that a process of black hole formation corresponds to the thermalization of the dual field theory in the light of the AdS/CFT correspondence, it is natural to wonder if these two landscapes can be related.

The goal of this thesis is finding out which universal lessons the dynamics of gravity in asymptotically global AdS spacetimes entails about the thermalization of strongly-coupled, finite-sized systems in isolation.

The manuscript is based on our previous publications [1, 2, 3, 4, 5], and has the following structure:

- As a good friend once stated beautifully, “an exiting Ph.D. student feels the moral duty to be as useful as possible to the doctorate students following him”. In this spirit, in chapter 1 I provide a general introduction to the topics of quantum thermalization, the AdS/CFT correspondence (with a focus on real-time physics) and the dynamics of Einstein-Hilbert gravity in asymptotically global AdS spacetimes. The expert reader in these areas can of course skip this chapter. I also want to emphasize that the review only introduces the material needed to understand the work presented in the following chapters, and many important topics in the rich landscape of ”applied AdS/CFT” are left untouched.

- Chapter 2 focuses on the holographic interpretation of delayed gravitational collapse processes that take place in global AdS_4. We consider Einstein-Hilbert gravity with a real, massless scalar field. We discuss in detail the phenomenology displayed by this system, with emphasis on the dependence of the dynamical geometry on the initial state. Our major proposal is that these novel black hole formation processes correspond to quantum revivals on the dual CFT_3, *i*.e., unitary field theory evolutions where the initial state is reconstructed in a quasiperiodic way several times before an ergodic regime sets in. We back our proposal by a numerical computation of the propagation of entanglement. We find out that a simple model where this propagation is causal on average is sufficient to accomodate their phenomenology in certain cases, and discuss in detail the different regimes the entanglement entropy can fall in both before and after black hole formation takes place, commenting on their dependence on the initial state considered.

- Chapter 3 discusses the three-dimensional instance of the previous problem. We comment on the salient similarities and differences between quantum revivals in two- and three-dimensional holographic CFTs. We perform again a numerical entanglement entropy computation and illustrate how, as the energy density increases, its dynamics transitions progressively from causal propagation to a series of fast rephasing/dephasing phases separated by long plateaux of ergodic behavior. These two regimes are associated to two well-differentiated time scales, that display qualitatively similar properties to the ones observed experimentally in other systems.

- The experimental evidence available in the literature shows that the existence of exactly-periodic geometries in asymptotically global AdS spacetimes is ubiqutuous. This fact motivates the search of these solutions in simple, effective descriptions of the gravitational problem. With this goal in mind, in chapter 4 we demonstrate that, under mild dynamical assumptions, time-periodic geometries exist in an elementary thin-shell construction in any dimension.

- In chapter 5 we study holographic thermalization in finite-sized systems with the extra ingredients of electric charge and the possibility of obtaining spontaneous symmetry breaking. We unravel the phase diagram of our holographic CFT both in the microcanonical and the grand-canonical ensembles and discuss how the thermalization time depends not only on the conserved charges of the system but also on the properties of the initial state. We verify the previous hypothesis put forward in the literature regarding the gravitational dual of the mechanism behind thermalization or its absence. Finally, we discuss the late-time relaxation of one-point functions of non-conserved quantities in our model and comment on how our results relate to the planar case. We provide preliminary evidence of a new relaxation regime where the system supports long-lived oscillations.

- Chapter 6 is devoted to the first study of holographic, homogeneous quenches in the global context. We put our emphasis in the adiabatic limit. We identify a universal attractor that controls the late time dynamics of this kind of quench process. We uncover the existence of an intrinsic adiabaticity threshold in our system and undertake an analysis of the salient features of this attractor, focusing on the issue of its linear and nonlinear stability. Finally, we show that, in the three-dimensional case, the attractor at the adiabaticity threshold can be related to an extremal charged black hole through a chain of duality maps.

- Chapter 7 states briefly the conclusions about the work presented in this manuscript and dicusses future research directions this author finds worth pursuing.

- Finally, I provide a summary of the work contained in this thesis aimed at the curious but non-expert reader, written both in English (chapter 8) and Galician (chapter 9)

I would like to inform the reader that, in order to ease the task of going through the material contained in this work, at the beginning of chapters 2-6 I have included a brief summary of their content.

Chapter 1

Introduction

1.1 Thermalization

In this section, we are introducing several notions of entropy in classical and quantum physics, with the aim of presenting a quantity fundamental to this thesis: the *entanglement entropy*. Then, we move on to the study of a paradigmatic example of how to drive a quantum system out of equilibrium: a *quantum quench*. We will illustrate that, in this case, the entanglement entropy is an efficient tool to monitor the equilibration of the system. Finally, we discuss briefly the Eigenstate Thermalization Hypothesis, making several general remarks about the thermalization process itself.

1.1.1 Entropy in classical and quantum physics

At the classical level, entropy is defined as the Shannon entropy of the probability distribution $\rho(\mathbf{P}, \mathbf{Q}; t)$ in phase space

$$S(\rho) \equiv - \int\int \frac{d\mathbf{P} d\mathbf{Q}}{(2\pi\hbar)^D} \rho(\mathbf{P}, \mathbf{Q}; t) \log \rho(\mathbf{P}, \mathbf{Q}; t), \tag{1.1.1}$$

where $2D$ is the phase space dimension. The time evolution of ρ is determined by the Liouville theorem

$$\partial_t \rho = \{H, \rho\}, \tag{1.1.2}$$

which implies, in particular, that $S(\rho)$ is conserved, reflecting the microscopic reversibility of the dynamics. As we stressed before, any notion of irreversibility necessarily comes from a coarse-graining procedure. Imagine, for instance, that our system consists of N particles with positions $\mathbf{x}_1, ..., \mathbf{x}_N$ and momenta $\mathbf{p}_1, ..., \mathbf{p}_N$; assume that, as observers, we are solely interested in the dynamics of a subset of N_A particles. The reduced probability distribution that describes this subsystem is

$$\rho_A(\mathbf{x}_1, ..., \mathbf{x}_{N_A}, \mathbf{p}_1, ..., \mathbf{p}_{N_A}; t) \equiv \int\int d\mathbf{x}_{N_A+1} ... d\mathbf{x}_N d\mathbf{p}_{N_A+1} ... d\mathbf{p}_N \rho(\mathbf{x}_1, ..., \mathbf{x}_N, \mathbf{p}_1, ..., \mathbf{p}_N; t) \tag{1.1.3}$$

where we have averaged over the phase space coordinates of the remaining $N - N_A$ particles. Liouville theorem cannot be employed to constrain the time evolution of the entropy of ρ_A. In the thermodynamic limit $N_A, N \to \infty$, $0 < N_A/N \ll 1$, this entropy is expected to increase in time until saturating to the canonical ensemble value, provided that the system is ergodic [6].

In the quantum realm, the correspondence principle guarantees a similar development of events. The state of the system is now encoded by a density matrix ρ, whose time evolution is controlled by the quantum Liouville theorem[1]

$$\partial_t \rho = -i \left[H, \rho\right], \tag{1.1.4}$$

while the natural entropy to consider is the von Neumann entropy

$$S_{vN}(\rho) \equiv -\mathrm{Tr}(\rho \log \rho). \tag{1.1.5}$$

The von Neumann entropy can also be expressed as

$$S_{vN}(\rho) = -\sum p_i \log p_i, \tag{1.1.6}$$

where p_i is the i-th eigenvalue of the density matrix. This last expression shows that the von Neumann entropy is nothing but the Shannon entropy of the eigenvalue distribution $\{p_i\}$, in parallel with the classical case. Furthermore, (1.1.6) it is also usefu to prove several properties of von Neumann entropy.

First, when the system is in a pure state, there is a basis in which $\rho_{\text{pure}} = |\psi\rangle \langle\psi|$, so $S_{vN}(\rho_{\text{pure}}) = 0$; for a mixed state we always find that $S_{vN}(\rho_{\text{mixed}}) > 0$, since $p_i \in [0, 1)$. Therefore, S_{vN} can be though of as an order parameter distinguishing pure states from mixed ones. In particular, if the system is at thermal equilibrium within a given ensemble, its von Neumann entropy matches the expected thermodynamical entropy. Consider, for example, the microcanonical density matrix

$$\rho_{mc} = \sum_{n=1}^{D} \frac{1}{D} |n\rangle \langle n|, \tag{1.1.7}$$

where the states $|n\rangle$ in the microcanonical shell $\mathcal{H}_E$ are such that their energy $E_n \in [E - \Delta E, E + \Delta E]$, with $\Delta E \ll E$, and $D = \dim \mathcal{H}_E$. It is immediate to show that $S_{vN}(\rho_{mc}) = \log D$, as expected. Finally, from (1.1.6) we observe that any unitary transformation leaves $S_{vN}(\rho)$ invariant, since it does not change the eigenvalue distribution of ρ. Therefore, $S_{vN}(\rho)$ is conserved under time evolution, in parallel with its classical counterpart. Following a coarse-graining procedure analogous to the one employed in the classical case would allow us to introduce the notion of *entanglement entropy* (EE), which need not be conserved anymore.

Consider a quantum system with Hilbert space $\mathcal{H}$ and focus on a subsystem A. The full

---

[1] From now on we always work in $c = k_B = \hbar = 1$ units

Hilbert space is bipartitioned as $\mathcal{H} = \mathcal{H}_A \otimes \mathcal{H}_{\bar{A}}$. Observations restricted to A are now fully encoded in the reduced density matrix ρ_A,

$$\rho_A \equiv \mathrm{Tr}_{\bar{A}}(\rho), \tag{1.1.8}$$

where $\mathrm{Tr}_{\bar{A}}$ represents the partial trace over the complementary subsystem $\bar{A}$. The encoding is complete in the sense that, for any operator $\mathcal{O}_A \otimes \mathbb{I}$ restricted to A, we have that

$$\langle \mathcal{O}_A \rangle = \mathrm{Tr}(\rho(\mathcal{O}_A \otimes \mathbb{I})) = \mathrm{Tr}(\rho_A \mathcal{O}_A). \tag{1.1.9}$$

In fact, this identity alone fixes the reduced density matrix ρ_A to have the form (1.1.8) [7]. Let us assume that the system is in a pure state, so $\rho = |\Psi\rangle\langle\Psi|$, and introduce two complete orthonormal basis for the subsystems A, $\{|\phi_n\rangle\}$, and $\bar{A}$, $\{|\Phi_N\rangle\}$. In these basis, the total wavefunction can be factored as

$$|\Psi\rangle = \sum_{n,N} c_{n,N} |\phi_n\rangle |\Phi_N\rangle , \tag{1.1.10}$$

with $\sum_{n,N} |c_{n,N}|^2 = 1$. The partial trace operation corresponds to computing

$$\rho_A = \mathrm{Tr}_{\bar{A}}\rho = \sum_N \langle \Phi_N| \rho |\Phi_N\rangle , \tag{1.1.11}$$

which results in

$$\rho_A = \sum_{n,m} \left(\sum_N c_{n,N} c^*_{m,N} \right) |\phi_m\rangle \langle\phi_n| . \tag{1.1.12}$$

By Schmidt decomposition, we can always find new basis $\{|\sigma_n\rangle\}$ and $\{|\Sigma_N\rangle\}$ for A and $\bar{A}$ such that the original wavefunction reduces to

$$|\Psi\rangle = \sum_n \alpha_n |\sigma_n\rangle |\Sigma_n\rangle , \tag{1.1.13}$$

and ρ_A is diagonalized

$$\rho_A = \sum_n |\alpha_n|^2 |\sigma_n\rangle \langle\sigma_n| . \tag{1.1.14}$$

The entanglement entropy of A, S_A, is nothing but the von Neumann entropy of ρ_A,

$$S_A \equiv S_{vN}(\rho_A), \tag{1.1.15}$$

and can be expressed as $S_A = -\sum_n |\alpha_n|^2 \log |\alpha_n|^2$ if we choose to work on the Schmidt basis. A nonzero S_A measures the failure of subsystem A to be in a pure state. This failure is equivalent to the statement that, with respect to the Hilbert space bipartition, the complete system is not in a product state, but rather in an entangled one:

$$S_A \neq 0 \iff |\Psi\rangle \neq |\psi_A\rangle |\psi_{\bar{A}}\rangle . \tag{1.1.16}$$

Quantitatively, e^{S_A} represents the minimum number of auxiliary states we have to entangle A with in order to recover ρ_A from a pure state of the enlarged system [8]. For a spatially extended system, it is customary to take A as a compact spatial region and, sometimes, the term geometric entropy is employed to refer to this particular situation. Let us mention briefly some of the most relevant properties of the quantity we have just introduced.

First, looking at (1.1.13), one is easily convinced that the eigenvalues of ρ_A and $\rho_{\bar{A}}$ coincide if the system is in a pure state. Therefore, for pure states the identity

$$S_A = S_{\bar{A}} \tag{1.1.17}$$

is satisfied. The EE is also constrained to verify several other nontrivial relations when we consider more general partitions of the Hilbert space of the system. For instance, lets assume that $\mathcal{H} = \mathcal{H}_A \otimes \mathcal{H}_B \otimes \mathcal{H}_C$. It can be shown that the entanglement entropy is strongly subadditive [9, 10, 11],

$$S_{ABC} + S_B \leq S_{AB} + S_{BC}. \tag{1.1.18}$$

The strong subadditivity of the EE implies also its subadditivity,[2]

$$S_{AB} \leq S_A + S_B. \tag{1.1.19}$$

Furthermore, S_{AB} is also bounded from below by the Araki-Lieb inequality [12],

$$|S_A - S_B| \leq S_{AB}. \tag{1.1.20}$$

A rather obvious remark is that the EE departs from the classical thermodynamical entropy by being generically nonextensive, as shown by (1.1.17).

This lack of extensivity is manifest in the geometric entanglement entropy. In order to expose it, consider a QFT defined on a $(d+1)$-dimensional globally hyperbolic manifold of topology $\mathbb{R} \times \Sigma$ and choose, as subsystem, a region A belonging to the Cauchy surface Σ. Typically, the area law

$$S_A \sim \frac{\text{vol}(\partial A)}{\epsilon_{UV}^{d-1}} + ... \tag{1.1.21}$$

is satisfied.[3] The EE scales with the area of the entangling region, and not with its volume. The ultraviolet cutoff ϵ_{UV} is needed to obtain a finite answer since in any local QFT there are correlations of arbitrarily short wavelength across the dividing surface ∂A. If not regulated, these high-frequency correlations make a divergent contribution to the EE.[4] Obtaining more specific results about the ultraviolet behaviour of S_A requires one to make further assumptions. For example, from holographic and anomaly considerations, it is possible to argue [8] that for a CFT$_{d+1}$ in odd spatial dimensions,

$$S_A = a_{d-1}\left(\frac{L_A}{\epsilon_{UV}}\right)^{d-1} + ... + a_2\left(\frac{L_A}{\epsilon_{UV}}\right)^2 + (-1)^{\frac{d-1}{2}}\tilde{S}\log\frac{L_A}{\epsilon_{UV}} + a_0 + O(\epsilon_{UV}), \tag{1.1.22}$$

---

[2] Take B to be empty in (1.1.18).

[3] For fermionic QFTs there can be an additional logarithmic correction.

[4] Worse than that, they actually prevent the Hilbert space splitting, so generically we cannot assume that $\mathcal{H} = \mathcal{H}_A \otimes \mathcal{H}_{\bar{A}}$ unless the ultraviolet regulator is introduced.

while in even spatial dimensions

$$S_A = a_{d-1}\left(\frac{L_A}{\epsilon_{UV}}\right)^{d-1} + \ldots + a_1\frac{L_A}{\epsilon_{UV}} + (-1)^{\frac{d}{2}}\tilde{S} + O(\epsilon_{UV}). \tag{1.1.23}$$

In these expressions, L_A sets the size of the entangling region. The quantity $\tilde{S}$ is free of renormalization ambiguities[5] and depends on the CFT under consideration, the particular state we are in, and the choice of entangling region. Since it is determined by the infrared physics of the system, it allows to distinguish low-energy states from highly-excited ones, where it shows volume scaling, $\tilde{S} \sim \mathrm{vol}(A)$. In odd spatial dimensions, $\tilde{S}$ also carries non-trivial information about the conformal anomalies of the theory.

Finally, let us mention that exact results that surpass (1.1.22),(1.1.23) are scarce. Fortunately, it has been possible to take advantage of the infinite-dimensional symmetry algebra of two-dimensional CFTs to compute entanglement entropies in several situations [18, 19].[6] For instance, consider an interval of length l as entangling region. In the vacuum, the EE of this interval is given by

$$S(l) = \frac{c}{3}\log\frac{l}{\epsilon_{UV}}, \tag{1.1.24}$$

in accordance with (1.1.22). The parameter c is the central charge of the CFT. If we consider a thermal state instead, the entanglement entropy is given by

$$S(l,\beta) = \frac{c}{3}\log\left(\frac{\beta}{\pi\epsilon_{UV}}\sinh\left(\frac{\pi l}{\beta}\right)\right). \tag{1.1.25}$$

This expression reduces to the vacuum result in the $l \ll \beta$ limit, showing that the ultraviolet structures of the thermal and the vacuum states are identical,

$$S(l,\beta) = \frac{c}{3}\log\frac{l}{\epsilon_{UV}} + \frac{c\pi^2 l^2}{18\beta^2} + \ldots \tag{1.1.26}$$

In the opposite $l \gg \beta$ limit, the EE becomes extensive at leading order, as expected for a generic high-energy state,

$$S(l,\beta) = \frac{\pi c}{3\beta}l + \frac{c}{3}\log\frac{\beta}{2\pi\epsilon_{UV}} - \frac{c}{3}e^{-\frac{2\pi l}{\beta}} + \ldots \tag{1.1.27}$$

Furthermore, the leading order, extensive piece of the result above coincides with the thermal entropy,

$$S(l,\beta) = s_{th}(\beta)l, \tag{1.1.28}$$

in such a way that the thermodynamical entropy density and central charge are related as $s_{th}(\beta) = \frac{\pi c}{3\beta}$.

---

[5] This fact upholds even in odd spatial dimensions.

[6] These results are based on expressing the entanglement entropy in terms of analytically continued Rènyi entropies (the so-called replica trick).

There exist other relevant information-threoretical quantities that can be derived from the EE. A particularly important one is the *mutual information.* For two nonoverlapping subsystems A and B, the mutual information $I(A,B)$ is defined as

$$I(A,B) = S_A + S_B - S_{AB}. \tag{1.1.29}$$

Subadditivity of the EE implies that the mutual information is semipositive definite,

$$I(A,B) \geq 0. \tag{1.1.30}$$

Said otherwise, the mutual information measures the failure of the EE to be strictly additive. Unlike the EE, the mutual information is manifestly finite. Physically, it is interpreted as a measure of the degree of correlation between subsystems A and B, taking into account both classical and quantum contributions. In fact, it is possible to demonstrate that, for $d-$dimensional spin lattices, the connected correlation function $C(\mathcal{O}_A, \mathcal{O}_B) = \langle \mathcal{O}_A \otimes \mathcal{O}_B \rangle - \langle \mathcal{O}_A \rangle \langle \mathcal{O}_B \rangle$ between any two operators $\mathcal{O}_A, \mathcal{O}_B$ satisfies [20]

$$I(A,B) \geq \frac{C(\mathcal{O}_A, \mathcal{O}_B)^2}{2\|\mathcal{O}_A\|^2 \|\mathcal{O}_B\|^2}. \tag{1.1.31}$$

Note that a zero mutual information between A and B implies that the connected correlator of any two operators restricted to those subsystems vanishes. Unlike the EE, the mutual information between two regions in the vacuum state of a two-dimensional CFT is not universal. It contains exhaustive information about the dimensions of primary operators and the structure constants of the theory [21].

Another relevant information-threoretical quantity is the relative entropy. Consider two density matrices ρ and σ. Their relative entropy $S(\rho|\sigma)$ is defined as

$$S(\rho|\sigma) = \mathrm{tr}\left(\rho \log \rho\right) - \mathrm{tr}\left(\rho \log \sigma\right). \tag{1.1.32}$$

In terms of the spectral decompositions $\rho = \sum_n p_n \left|n\right\rangle \left\langle n\right|$, $\sigma = \sum_a q_a \left|a\right\rangle \left\langle a\right|$, (1.1.32) can be alternatively expressed as

$$S(\rho|\sigma) = \sum_n p_n \log(p_n) - \sum_{n,a} p_n \log q_a \left|\langle n|a\rangle\right|^2. \tag{1.1.33}$$

In particular, if both ρ and σ admit a spectral decomposition in the same basis, we recover

$$S(\rho|\sigma) = \sum_n p_n \log\left(\frac{p_n}{q_n}\right), \tag{1.1.34}$$

which is the standard definition of the relative entropy of the two classical probability distributions $\{p_n\}$ and $\{q_n\}$.

The relative entropy satisfies two crucial properties:

- Iff $\rho = \sigma$, $S(\rho|\sigma) = 0$. Iff $\rho \neq \sigma$, $S(\rho|\sigma) > 0$. The relative entropy between two density matrices is semipositive definite. Note that it cannot be employed directly to define a metric in the space of density matrices because it is not symmetric.

- Under any completely positive trace preserving (CPTP) operation $\mathcal{N}$ on both ρ and σ, the relative entropy is monotonous,
$$S(\mathcal{N}(\rho)|\mathcal{N}(\sigma)) \leq S(\rho|\sigma). \tag{1.1.35}$$
Let us bipartite our Hilbert space as $\mathcal{H} = \mathcal{H}_A \otimes \mathcal{H}_{\bar{A}}$, and define the partial trace operator as $\mathrm{Tr}_{\bar{A}} = \mathbb{I}_{\mathcal{H}_A} \otimes \mathrm{Tr}_{\mathcal{H}_{\bar{A}}}$. It follows that
$$S(\rho_A|\sigma_A) \leq S(\rho|\sigma). \tag{1.1.36}$$
In particular, imagine our quantum system is a QFT, with a Hilbert space bipartition specified by choosing a region A of a Cauchy surface Σ. Let ρ_A, σ_A be reduced density matrices associated to A. Consider now a subregion $B \subset A$. From the monotonicity of the relative entropy under the partial trace, we have that
$$S(\rho_B|\sigma_B) \leq S(\rho_A|\sigma_A). \tag{1.1.37}$$
When the volume of B tends to zero, the reduced density matrices ρ_B, σ_B should only be sensitive to the short-distance structure of the original quantum states in question, ρ and σ. In any local QFT, this ultraviolet structure coincides with the ultraviolet structure of the vacuum state. Therefore,
$$\lim_{|B|\to 0} S(\rho_B|\sigma_B) = 0, \tag{1.1.38}$$
where $|B|$ is the volume of B. The relative entropy is ultraviolet finite.

Employing these two properties we can prove several facts that shed light on the physical interpretation of relative entropy:

- For the bipartition $\mathcal{H} = \mathcal{H}_A \otimes \mathcal{H}_B$, let ρ be a joint state of the complete system, and ρ_A,ρ_B the reduced density matrices associated with $\mathcal{H}_A$, $\mathcal{H}_B$. We have that
$$S(\rho|\rho_A \otimes \rho_B) = S(\rho_A) + S(\rho_B) - S(\rho) = I(A, B). \tag{1.1.39}$$
In this case, the relative entropy measures the failure of the joint system to be in a product state. In particular, the fact that the relative entropy is semipositive definite implies that the mutual information is also semipositive semidefinite and, in consequence, that the entanglement entropy is subadditive.

- Imagine that our Hilbert space $\mathcal{H}$ has a finite dimension $D = \dim \mathcal{H}$. Take $\sigma = \mathbb{I}_{\mathcal{H}}/D$, and ρ a generic state. We have that
$$S(\rho|\sigma) = \log D - S(\rho). \tag{1.1.40}$$
The positivity of the relative entropy implies that σ is the maximally entangled state in $\mathcal{H}$. In this case, the relative entropy measures the failure of the state ρ to be maximally entangled. In particular, if our Hilbert space is the microcanonical shell $\mathcal{H}_E$ associated to some Hamiltonian H, the relative entropy measures the failure of the state ρ to be the thermal equilibrium one. Note that the time-dependence of the state ρ can be arbitrary.

- Take σ to be the density matrix associated to the equilibrium state in the canonical ensemble,

  $$\sigma = \frac{e^{-H/T}}{Z}, \qquad Z = \mathrm{tr}(e^{-H/T}) = e^{-F/T}. \tag{1.1.41}$$

  The relative entropy between σ and any other state ρ is given by

  $$S(\rho|\sigma) = \frac{1}{T}\left[\mathrm{tr}(\rho H) - TS(\rho)\right] - \frac{1}{T}F \equiv \frac{1}{T}(F(\rho) - F) = \frac{1}{T}\Delta\langle H\rangle - \Delta S, \tag{1.1.42}$$

  where the free energy $F(\rho)$ is defined in terms of the average energy $\langle H\rangle_\rho = \mathrm{tr}(\rho H)$ in the state ρ and its von Neumann entropy $S(\rho)$ by employing the standard thermodynamical relation $F = E - TS$. The positivity of the relative entropy implies that the thermal state minimizes this free energy with respect to any other quantum state. Again, this includes time-dependent states.

Let us consider the reference state specified by σ. Since σ is both hermitean and semipositive definite, it can be expressed as[7]

$$\sigma = e^{-H_\sigma}. \tag{1.1.43}$$

The hermitean operator H_σ is known as the *modular Hamiltonian.* We can picture (1.1.43) as the canonical density matrix associated to H_σ at temperature $T = 1$. Therefore, from (1.1.42) we have that, for any other density matrix ρ,

$$S(\rho|\sigma) = \Delta\langle H_\sigma\rangle - \Delta S. \tag{1.1.44}$$

The positivity of the relative entropy implies that the variation of the von Neumann entropy between the states σ and ρ is bounded by the variation of the expectation value of the modular Hamiltonian as

$$\Delta S \leq \Delta\langle H_\sigma\rangle. \tag{1.1.45}$$

For a generic state, the modular Hamiltonian is a nonlocal operator not known in closed form. This situation only changes in a handful of cases where H_σ is the integral of a local operator and generates a geometric flow. The trivial example involves the last item of our previous list, where the reference state was the canonical density matrix associated to the whole system, and $H_\sigma = \beta H$. In this case, the flow associated to the modular Hamiltonian is Euclidean time evolution.

1.1.2 Quantum quenches

A quantum quench is one paradigmatic example of how to drive a quantum system away from equilibrium. Let us consider that, initially, our system is prepared in an energy eigenstate $|\psi_0\rangle$ of some Hamiltonian H_0, that may depend on several external parameters $\{\lambda_i, i = 1, 2, 3...\}$. A sudden change $\lambda_j \to \lambda_j + \delta\lambda_j$, or *quench*, leads to a new Hamiltonian H, for which our original state $|\psi_0\rangle$ is, typically, a highly excited state. Therefore, the natural expectation is that the post-quench time evolution, implemented by the modified Hamiltonian H, leads to the thermalization of the system. We distinguish between global or local

---

[7] Any normalization factor that ensures $\mathrm{tr}(\sigma) = 1$ has been absorbed into H_σ.

quenches depending on whether the quench protocol is translational invariant or not; for example, a global quench could correspond to the sudden change of the external magnetic field in the one-dimensional transverse Ising Model.

In [22][23], Calabrese and Cardy showed that, under some technical assumptions, the high-degree of symmetry of $1+1$-dimensional CFTs allowed for an analytical understanding of the post-quench dynamics. These authors considered a global quench in which the initial state $|\psi_0\rangle$ was the vacuum of a gapped, local Hamiltonian H_{gapped}. After the sudden removal of the mass gap, $|\psi_0\rangle$ becomes a highly-excited state of the resulting gapless Hamiltonian, H_{CFT}. This excited then state evolves unitarily with H_{CFT}. Their major results, as summarized in [24], were:[8]

- One-point functions of non-conserved, local observables decayed exponentially to their values in the H_{CFT} groundstate.
- The horizon effect. *There exists a characteristic time scale after which nonlocal observables attain equilibrium.* For the EE of a length l interval at time t, $S(l,t)$, or two- or higher-point functions whose arguments are contained within a length l interval, equilibration is observed after a horizon time $t_{\text{hor}} = l/2$. The EE increases linearly with time up to this point, $S(l,t) = 2s_{th}(\beta)t$ for $t \leq t_{\text{hor}}$.
- After the horizon time t_{hor}, and up to exponentially-small corrections, the reduced density matrix of the interval agrees with the reduced canonical density matrix at a temperature fixed by the total energy.[9] In particular, the EE saturates to the thermodynamical entropy at the given temperature, $S(l,t) = s_{th}(\beta)l + ...$ for $t > t_{hor}$.

These results suggest an effective description of the post-quench dynamics based on quasiparticles [22]. Calabrese and Cardy imagined that the energy excess injected by the quench created a uniform distribution of pointlike pairs of entangled quasiparticles, each one consisting of a right- and a left-mover that traveled at unit speed.

Take an interval A of length l. To compute $S(l,t)$, we just have to count the number of unpaired quasiparticles within A at a given time. It is enough to consider the semi-infinite line to the right of A, $\bar{A}_+$, since $S(l,t)$ is twice the entanglement entropy of A with this region. At time t, a point $x' \in A = [0,l]$ is entangled with a point $x'' \in \bar{A}_+ = [l,\infty)$ iff a pair of entangled quasiparticles emitted from the point x at $t=0$ arrive simultaneously at x' and x''. Therefore, x' and x'' have to be related as $x'' = x' + 2t$ in order to contribute. In this way, the entanglement entropy is given by the following integral

$$S(l,t) = 2\rho_0 \int_0^l dx' \int_l^\infty dx'' \delta(x'' - (x' + 2t)), \tag{1.1.46}$$

where ρ_0 is the quasiparticle density created by the quench -the factor of two was explained before-. After performing the integral, we get: i) for $t < l/2$, $S(l,t) = 4\rho_0 t$, ii) for $t > l/2$,

---

[8] In the following, when referring to times t and lengths l, we assume that $t, l \gg 1/m$, where m is the mass gap of the original Hamiltonian. Said otherwise, we are quoting the results at leading order in $1/m$.

[9] The temperature is fixed through the relation $E = \langle\psi_0| H_{CFT} |\psi_0\rangle = \mathrm{Tr}(\rho_c H_{CFT})$. Here ρ_c is the canonical density matrix and E the total energy.

$S(l,t) = 2\rho_0 l$, which agree with the rigorous result if we identify $\rho_0 = s_{th}(\beta)/2$, in such a way that the initial quasiparticle density is set the energy injected by the quench.

While the Hamiltonian considered in [22] was integrable[10], the horizon effect is believed to hold generically for any quantum system with a local Hamiltonian. The Lieb-Robinson bound [25] shows that, even in non-relativistic quantum systems, locality constraints the maximum speed of information propagation. However, apart from $1+1$-dimensional CFTs, there are few field theory examples where explicit quench computations can be performed, higher dimensional free field and holographic theories standing as manageable cases. In particular, in the holography realm, it was shown in [26] that the horizon effect is present when computing entanglement entropies in a simple gravitational collapse background, demonstrating that this effect exists even in a strongly-coupled theory with no quasiparticles.

Incidentally, the Calabrese and Cardy computation illustrates what it is perhaps the most important property of the thermalization process. To wit, *the thermalization time is not a well-defined physical quantity.* Different observables can attain their final values at thermal equilibrium at different times. For instance, is we decided to monitor solely one-point functions, we would conclude that the system reaches a thermal state exponentially fast; however, this is not true, as nonlocal probes clearly show. At most, we can talk only about *the thermalization time for a given observable.*

A sufficient condition for a subsystem A to fully thermalize is that, at leading order in the subsystem size, its reduced density matrix ρ_A takes the canonical form. In turn, this is a sufficient condition for any observable $\mathcal{O}_A$ to take its expectation value at thermal equilibrium. Furthermore, it also implies that $S(\rho_A)$ must reduce to the thermodynamical entropy. Therefore, monitoring $S(\rho_A)$ is a useful way of determining when a subsystem attains thermal equilibrium. Because of this, in this thesis, we employ the EE as a proxy for thermalization.

1.1.3 The Eigenstate Thermalization Hypothesis

The above comment comes with one caveat. Since time evolution is unitary, ρ_A can never take *exactly* its canonical form. For instance, if the total system is in a pure state, the subleading corrections to ρ_A we mentioned must enforce the unitarity condition, $S_A = S_{\bar{A}}$. There must exist observables $\tilde{\mathcal{O}}_A$ able to probe this subleading corrections; these would allow to distinguish the effective thermal state from the actual one. Therefore, thermalization can only appear for a given subset of coarse-grained observables.

This last comment also applies when considering an isolated system as a whole. There must always exist probes that are able to distinguish the effective thermal state reached at $t \to \infty$ -this time, in the microcanonical ensemble- from the actual pure state of the system. The Eigenstate Thermalization Hypothesis (ETH) [27][28] provides an answer to the question of what specific properties these coarse-grained observables must satisfy. We expect that natural physical observables that can be measured in the laboratory belong to

---

[10] The extra conserved charges were zero due to the initial state chosen to simplify the computations.

this coarse-grained class.

For definiteness, let us consider an isolated quantum mechanical system with a gapped

$$E_0 > 0 \tag{1.1.47}$$

and nondegenerate

$$E_n - E_m = E_k - E_l \Rightarrow E_n = E_m, E_k = E_l \text{ or } E_n = E_k, E_m = E_l \tag{1.1.48}$$

energy spectrum, and focus on the microcanonical shell $\mathcal{H}_E$ of dimension D. Any pure state $|\psi\rangle \in \mathcal{H}_E$ at $t = 0$ can be expressed as

$$|\psi(0)\rangle = \sum_n c_n(0) \,|n\rangle \,, \tag{1.1.49}$$

with $\sum_n |c_n(0)|^2 = 1$. Hamiltonian evolution leads then to

$$|\psi(t)\rangle = \sum_n c_n(t) \,|n\rangle = \sum_n c_n(0) e^{-iE_n t} \,|n\rangle \,, \tag{1.1.50}$$

and implies that the expectation value of any observable $\mathcal{O}$ is given by

$$\langle \mathcal{O}(t) \rangle = \sum_{nm} c_m(0)^* c_n(0) e^{-i(E_n - E_m)t} \mathcal{O}_{mn}, \tag{1.1.51}$$

with

$$\mathcal{O}_{mn} = \langle m | \, \mathcal{O} \, | n \rangle \,. \tag{1.1.52}$$

For actual measurements with finite time-resolution we can trade $\langle \mathcal{O}(t) \rangle$ by its infinite time average

$$\overline{\langle \mathcal{O} \rangle} \equiv \lim_{t \to \infty} \langle \mathcal{O} \rangle_t \equiv \lim_{t \to \infty} \frac{1}{t} \int_0^t dt' \langle \mathcal{O}(t') \rangle = \sum_n |c_n(0)|^2 \, \mathcal{O}_{nn}, \tag{1.1.53}$$

where we appreciate that the cross-terms average-out. The result obtained is equivalent to putting the system in the *diagonal ensemble*

$$\rho_{\text{diag}} = \sum_n |c_n(0)|^2 \, |n\rangle \langle n| \,. \tag{1.1.54}$$

Note that ρ_{diag} depends *explicitly* on the intial state of the system. In contrast, we expect the system to thermalize as $t \to \infty$, in the sense that the final equilibrium state is solely determined by its conserved energy through the microcanonical density matrix (1.1.7). Therefore, as this simple example demonstrates, the Hamiltonian evolution of the system is apparently in conflict with the expectations drawn from statistical mechanics.

Here is where the ETH comes in. The ETH assumes that, for any coarse-grained operator, the identity

$$\mathcal{O}_{nn} = \langle n | \, \mathcal{O} \, | n \rangle = f_{\mathcal{O}}(E_n) = f_{\mathcal{O}}(E) + O(\Delta E), \tag{1.1.55}$$

holds in any energy eigenstate $|n\rangle \in \mathcal{H}_E$ [6]. Here, $f_{\mathcal{O}}(E)$ is a smooth function, effectively constant within the microcanonical shell. This seemingly trivial assumption implies right away that diagonal and microcanonical averages agree

$$\overline{\langle \mathcal{O} \rangle} = \mathrm{Tr}(\rho_{\mathrm{diag}} \mathcal{O}) = \sum_n |c_n(0)|^2 \, \mathcal{O}_{nn} \approx f_{\mathcal{O}}(E) \sum_n |c_n(0)|^2 = f_{\mathcal{O}}(E), \qquad (1.1.56)$$

$$\langle \mathcal{O} \rangle_{mc} = \mathrm{Tr}(\rho_{\mathrm{mc}} \mathcal{O}) = D^{-1} \sum_n \mathcal{O}_{nn} \approx f_{\mathcal{O}}(E) D^{-1} \sum_n 1 = f_{\mathcal{O}}(E), \qquad (1.1.57)$$

and, in consequence, ergodicity holds at the quantum level. The effective memory loss about the system's initial state is implement by a *dephasing* process, that disolves the off-diagonal correlations of the initial density matrix and reveals the thermal nature of each individiual energy eigenstate. At the conceptual level, this mechanism is fundamentally different from the chaos-based classical one.

The ETH also involves further assumptions about the off-diagonal $\mathcal{O}_{nm}$ matrix elements [6]. Specifically,

$$\mathcal{O}_{nm} = e^{-\frac{1}{2} S(\bar{E})} g_{\mathcal{O}}(\bar{E}, \omega) R_{nm}, \qquad (1.1.58)$$

where $\bar{E} = (E_n + E_m)/2$, $\omega = E_m - E_n$, and R_{nm} is a random real variable with zero mean and unit variance. $S(\bar{E})$ is the thermodynamical entropy at energy $\bar{E}$, ands $g_{\mathcal{O}}$ is also a smooth function of its arguments. With this information, it is possible to compute straightforwardly the variance of $\langle \mathcal{O}(t) \rangle$,

$$\sigma^2_{\langle \mathcal{O}(t) \rangle} = \lim_{t \to \infty} \frac{1}{t} \int_0^t dt' \left(\langle \mathcal{O}(t') \rangle^2 - \overline{\langle \mathcal{O} \rangle}^2 \right), \qquad (1.1.59)$$

with the result that

$$\sigma^2_{\langle \mathcal{O}(t) \rangle} \leq c e^{-S(\bar{E})}, \qquad (1.1.60)$$

where $c = O(1)$. Therefore, if the ETH holds, $\sigma^2_{\langle \mathcal{O}(t) \rangle}$ is suppressed in D^{-1}. Recalling that $D \gg 1$ for a macroscopic system, we find that, at almost any time, the expectation value of $\mathcal{O}$ takes the diagonal ensemble value, $\overline{\langle \mathcal{O} \rangle}$. As a consequence, the ETH provides a stronger statement that standard ergodicity, since it is $\langle \mathcal{O}(t) \rangle$, and not only its finite time average $\langle \mathcal{O} \rangle_t$, that equilibrates to $\overline{\langle \mathcal{O} \rangle}$ as $t \to \infty$.[11].

A natural question that arises is how long it takes for a given coarse-grained observable to attain the expectation value predicted by the diagonal ensemble. This time is to be identified with the thermalization time of the observable. This fundamental question is left unanswered by the ETH, since it depends on the particular observable, Hamiltonian and initial state under survey.

It must also be emphasized that the ETH is a *dynamical* statement: only for certain Hamiltonians the energy eigenstates in the microcanonical shell would have the right structure

---

[11] It must be emphasized that the actual fluctuations of $\mathcal{O}$ measured in an experiment are given by $\overline{\left\langle (\mathcal{O} - \overline{\langle \mathcal{O} \rangle})^2 \right\rangle}$ instead.

needed to satisfy (1.1.55),(1.1.58) for the experimentally relevant observables. In this regard, the ETH is fundamentally different than *typicality*.

Typicality applies to randomly chosen states within the microcanonical shell,[12] and is essentially a *kinematical* constraint, arising due to the large dimensionality of $\mathcal{H}_E$. Typicality-based results are blind to the particular Hamiltonian of the system. In constrat, the ETH depends essentially on the specific properties of the system Hamiltonian but, since it applies to individual energy eigenstates, it holds for arbitrary linear combinations of them, and not just for randomly chosen ones.[13]

A beautiful result introduced in [30] shows that, for a random state and *any* observable, the probability of finding an $\epsilon > 0$ deviation between $\overline{\langle \mathcal{O} \rangle}$ and $\langle \mathcal{O} \rangle_{\text{mc}}$ is controlled both by the dimension D of the microcanonical shell and the norm of $\mathcal{O}$, $\|\mathcal{O}\|$, as

$$\text{Prob}\left(\left| \overline{\langle \mathcal{O} \rangle} - \langle \mathcal{O} \rangle_{\text{mc}} \right| \geq \epsilon \right) \leq 2e^{-cD\frac{\epsilon^2}{\|\mathcal{O}\|^2}}, \tag{1.1.61}$$

where $c = O(1)$ and constant. Therefore, unless the largest eigenvalue of $\mathcal{O}$ scales as $\sqrt{D}$, this operator cannot distinguish the random state from the microcanonical one. Although illuminating, results of this kind cannot explain why an isolated quantum system driven out-of-equilibrium thermalizes, since the initial state prepared in any experiment is not typical by any means, and represents rather a fine-tuned starting point. The question of how, starting from this fine-tuned state, a typical state is reached would remain.

Nonetheless, typicality provides a necessary condition that any coarse-grained observable must satisfy. If $\|\mathcal{O}\| \sim \sqrt{D}$, the operator would be able to probe that we are not in the microcanonical equilibrium state. Therefore, coarse-grained operators always have $\|\mathcal{O}\| \ll \sqrt{D}$. For instance, in a chain of N spins, any coarse-grained operator must involve $k \ll N$ spins in its construction. This is the reason why *few-body* operators are usually considered in the condensed matter literature as coarse-grained observables.

1.2 Holography: the AdS/CFT correspondence

1.2.1 Motivating the correspondence

As we have said, the AdS/CFT correspondence is, fundamentally, the statement that certain non gravitational quantum mechanical systems, defined on a fixed $d-$dimensional spacetime $\mathcal{B}$, are equivalent to quantum gravity theories defined on a higher-dimensional spacetime $\mathcal{M}_{\mathcal{B}}$ [7]. This higher-dimensional spacetime is a manifold with a boundary $\partial\mathcal{M}_{\mathcal{B}}$ that can be identified with the original non-dynamical spacetime where the dual quantum mechanical system lives, $\partial\mathcal{M}_{\mathcal{B}} = \mathcal{B}$. Conventionally, $\mathcal{B}$ is referred to as *the boundary*, while $\mathcal{M}_{\mathcal{B}}$ is referred to as *the bulk*. In the examples we are considering, the non-gravitational system is going to be a quantum field theory with conformal symmetry, or conformal field theory for

---

[12] For instance, with respect to the Haar measure.

[13] Although we can reframe the ETH as stating that, for the Hamiltonians where it holds, energy eigenstates are "random enough to be typical" [29].

short (CFT), living on d-dimensional Minkowski space, $\mathbb{R}^{1,d-1}$, or on a $d-1$-dimensional sphere cross time, $\mathbb{R} \times S^{d-1}$. On the other hand, the dual spacetime $\mathcal{M}_{\mathcal{B}}$ is going to be asymptotically anti-deSitter (AdS). This is the reason why the correspondence goes usually under the name AdS/CFT. Let us analyse what this acronyms represent in more detail. We shall center on the symmetries of the objects they refer to.

By CFT, we mean a QFT whose spacetime symmetry group is the group formed by the conformal transformations of $\mathcal{B}$, $Conf(\mathcal{B})$ [31]. A conformal transformation is an invertible mapping $x \to x' = f(x)$ that leaves the metric tensor g_{ab} invariant up to a Weyl transformation

$$g'_{ab}(x') = \Omega(x) g_{ab}(x). \tag{1.2.62}$$

For definiteness, lets analyse the the case $\mathcal{B} = \mathbb{R}^{1,d-1}$, with $d > 2$. It can be shown [31] that the conformal group $Conf(1, d-1) \equiv Conf(\mathbb{R}^{1,d-1})$ is formed by:

- Translations, $x'^a = x^a + v^a$.
- Lorentz transformations, $x'^a = \Lambda^a_b x^b$.
- Dilatations, $x'^a = \lambda x^a$.
- Special conformal transformations (SCT), $x'^a = (1 - 2vx + v^2x^2)^{-1}(x^a - v^a x^2)$.

  They are a composition of an inversion, $x^a \to x^a/x^2$, a translation, $x^a \to x^a - v^a$, and another inversion.

These results follow from considering the infinitesimal transformation $x^a \to x^a + \epsilon v^a(x)$, under which (1.2.62) reduces to the conformal Killing vector equation in Minkowski space, $\mathcal{L}_v \eta_{ab} = \omega(x)\eta_{ab}$, and then exponentiating the result. Unsurprisingly, $Conf(1, d-1)$ contains the Poincaré group as a subgroup. Its Lie algebra, $conf(1, d-1)$, admits a basis formed by $1/2d(d-1)$ generators of Lorentz transformations M_{ab}, d traslation generators P_a, another d SCT generators K_a, and an additional dilatation generator D. They add up to a total of $1/2(d+1)(d+2)$ elements. Apart from the standard Poincaré algebra, and the statement that D and K^a transform respectively as a scalar and a vector under Lorentz transformations, the nonzero commutation relations of the conformal algebra are [32]

$$[D, P_a] = -iP_a, \qquad [D, K_a] = iK_a, \qquad [K_a, P_b] = 2i(\eta_{ab}D + M_{ab}). \tag{1.2.63}$$

Let us introduce the new antisymmetric generators J_{AB}

$$J_{ab} = M_{ab}, \qquad J_{a,d} = \frac{1}{2}(K_a - P_a), \qquad J_{a,d+1} = \frac{1}{2}(P_a + K_a), \qquad J_{d+1,d} = D. \tag{1.2.64}$$

with $A, B = 0...d+1$. The new generators J_{AB} satisfy

$$[J_{AB}, J_{BC}] = -i\left(\eta_{AC}J_{BD} + \eta_{BD}J_{AC} - \eta_{BC}J_{AD} - \eta_{AD}J_{BC}\right). \tag{1.2.65}$$

These are nothing but the commutation relations of the Lie algebra $so(2, d)$ in a spacetime $\mathbb{R}^{2,d}$ with metric $\eta_{AB} = \mathrm{diag}(-1, 1, \ldots, 1, -1)$. From this observation, we obtain that

$$conf(1, d-1) \cong so(2, d). \tag{1.2.66}$$

Note that the dimensions of both algebras match because dim $so(d,2) = \frac{1}{2}(d+1)(d+2)$ due to the antisymmetry of J_{AB}.

The special orthogonal group $SO(2,d)$ is the group formed by the linear transformations $\Lambda : \mathbb{R}^{2,d} \to \mathbb{R}^{2,d}$ that leave the quadratic form

$$\eta_{AB}X^AX^B = -(X^0)^2 + (X^1)^2 + ... + (X^d - 1)^2 + (X^d)^2 - (X^{d+1})^2 \tag{1.2.67}$$

invariant. Therefore, $SO(2,d)$ can be thought of as the isometry group of the hyperboloid defined by $\eta_{AB}X^AX^B = -L^2$, with $L \in \mathbb{R}^+$. By introducing coordinates[14]

$$\begin{aligned} X^0 &= L\sec(x)\sin t, \\ X^{d+1} &= L\sec(x)\cos t, \\ X^i &= L\tan(x)\Omega_i,\ \ i = 1\dots d \end{aligned} \tag{1.2.68}$$

we find that the induced metric on this hyperboloid reads

$$ds^2_{\mathrm{AdS}} = \frac{L^2}{\cos(x)^2}(-dt^2 + dx^2 + \sin(x)^2 d\Omega^2_{d-1}) \tag{1.2.69}$$

with $t \in [0, 2\pi]$, $x \in [0, \pi/2]$ and $\vec{\Omega}^2 = 1$. Avoiding closed timelike curves requires decompactifying the temporal direction and going to the universal cover, where $t \in \mathbb{R}$. The coordinate chart (1.2.68) covers the resulting manifold entirely. This manifold is anti-deSitter space. Topologically, it corresponds to a solid cylinder with boundary $\mathbb{R} \times S^{d-1}$. Our construction shows that its isometry algebra is isomorphic to the conformal algebra in d dimensions. Alternatively, AdS$_{d+1}$ can be characterized as the maximally symmetric[15] solution of $d+1-$dimensional Einstein gravity with negative cosmological constant $\Lambda = -d(d-1)/(2L^2)$.

The coordinate system (1.2.68) and the metric (1.2.69) are useful to establish a handul of properties of AdS. First, a comment is in order: AdS is homogeneous by being maximally symmetric, so the special status attributed to the line $x = 0$ in this coordinate system is an artifact. A crucial fact about the metric (1.2.69) is its behavour in the opposite $\pi/2 - x \to 0$ limit

$$ds^2_{\mathrm{AdS}} = \frac{L^2}{(\pi/2 - x)^2}(-dt^2 + dx^2 + d\Omega^2_{d-1}) + O(\pi/2 - x) \tag{1.2.70}$$

This double pole divergence of ds^2 implies that the proper distance between the hypersurfaces $x = \pi/2 - \epsilon$ and $x = \pi/2$ diverges logarithmically when $\epsilon \to 0$: AdS$_{d+1}$ is not compact. The hypersurface $x = \pi/2$ can be rigorously defined as a boundary, however, if we consider the conformal compactification of AdS$_{d+1}$. A suitable compactification is provided by the $d+1$-dimensional Einstein Static Universe (ESU$_{d+1}$), a product spacetime with topology $\mathbb{R} \times S^d$ and metric

$$ds^2_{ESU} = -dt^2 + d\Omega^2_d = -dt^2 + dx^2 + \sin(x)^2 d\Omega^2_{d-1}, \tag{1.2.71}$$

---

[14] Ω_i parameterize an unit d-sphere.

[15] That AdS$_{d+1}$ is maximally symmetric can be easily seen from the fact that the maximum number of independent Killing vector fields in a $d+1$-dimensional manifold, $1/2(d+1)(d+2)$, matches the dimensionality the AdS$_{d+1}$ isometry algebra.

as long as we restrict the range of the angular coordinate x to the interval $[0, \pi/2]$. In this way, we can define the AdS_{d+1} boundary as the inverse image of the ESU$_{d+1}$ $x = \pi/2$ timelike hypersurface under the conformal compactification map. More generally, any metric $\Omega(x)^2 ds^2_{AdS}$ such that $\Omega(x)$ has a simple zero at $x = \pi/2$ leads to an equivalent construction. The induced metric at the boundary is thus defined up to Weyl rescaling: the AdS boundary cannot be associated a metric in an univocal way. Instead, it is endowed with a well-defined causal structure, defined by an equivalence class of metrics related to each other by conformal transformations. In this way, if we are going to picture that a QFT is living on this boundary, it must be a CFT so as to be compatible with this fact. Notice also that since the AdS boundary has a timelike direction this is a Lorentzian CFT.

Null geodesics can overcome the infinite spatial distance to the boundary in *finite* time. In particular, a radial null geodesic departing from $x = \epsilon$ would reach $x = \pi/2$ after a coordinate time $\Delta t = \pi/2 - \epsilon$. In consequence, AdS$_{d+1}$ is not globally hyperbolic, since it does not admit a Cauchy surface: there is no spacelike codimension-one hypersurface able to intersect every radial null geodesic departing from $x = \pi/2$. For instance, imagine specifying initial data for a hyperbolic PDE on the slice $t = t_0$. With no further imput, the null hypersurfaces $\Sigma_{\pm} = \{(t, x, \vec{\Omega}) \in AdS_{d+1} : t = t_0 \pm \pi/2 + x\}$ form a Cauchy horizon, and bound the spacetime region where the solution to the PDE can be determined univocally in terms of these initial data. Evolution outside this domain is ill-posed unless extra boundary conditions are provided at $x = \pi/2$. This need of extra boundary conditions is of the uttermost importance for the implementation of the AdS/CFT correspondence, as we are going to review in the next subsection.

The coordinate change $x \to \arctan(r/L), t \to Lt$ puts the AdS metric (1.2.69) in the more familiar form

$$ds^2 = -\left(1 + \left(\frac{r}{L}\right)^2\right) dt^2 + \frac{dr^2}{1 + \left(\frac{r}{L}\right)^2} + r^2 d\Omega^2_{d-2} \tag{1.2.72}$$

with r being a standard Schwarzschild coordinate. This coordinate system is particularly useful, since it allows us to redefine

$$t \to t/\lambda, \qquad r \to \lambda r, \qquad \theta_1 \to \theta_1/\lambda, \qquad \theta_i \to \theta_i \ (i = 1, \ldots, d-2) \tag{1.2.73}$$

and then take the singular $\lambda \to \infty$ limit. In this limit, the metric becomes

$$ds^2 = -\frac{r^2}{L^2} dt^2 + \frac{L^2}{r^2} dr^2 + r^2 d\mathbf{x}^2. \tag{1.2.74}$$

The boundary S^{d-1} has been flattened to a $(d-1)$-dimensional plane. This geometry is known as the Poincarè patch, or *planar* AdS. It should be noted that the Poincarè patch does not cover the whole original hyperboloid (1.2.67), nor its universal cover. The null hypersurface $r = 0$ is a Killing horizon, commonly known as the Poincarè horizon, while the boundary at $r \to \infty$ is conformally equivalent to d-dimensional Minkowski space, a fact that makes planar AdS the standard case of study in practical applications of AdS/CFT. The $r = 0$ horizon has zero temperature and a vanishing entropy density, since the determinant of the induced metric on a constant time slice is vanishing there. Importantly, the metric (1.2.74) is manifestly invariant under the action of the scaling transformations $t \to t/\lambda$, $\mathbf{x} \to \mathbf{x}/\lambda$ on the boundary coordinates iff $r \to \lambda r$. Under this scaling symmetry, the energy of a boundary excitation should scale as $E \to \lambda E$: zooming into short-distance, high-energy processes on the boundary theory is equivalent to going to large radial distance in the bulk. The bulk geometry is organized in such a way that its properties in the IR encode the UV of the dual CFT. In this way, the extra radial holographic direction can be thought of as the energy scale of the dual CFT. This fact is known as the UV/IR connection. Discussing a covariant UV/IR map would have to wait until we introduce the EE in the context of holography.

Symmetries apart, extra motivation for the existence of AdS/CFT comes from two important physical insights that took place years before Maldacena discovered the correspondence in 1997 [33]. Let us review them. First, from the QFT perspective, AdS/CFT gave, for the first time, a specific example of an idea that 't Hooft introduced in the seventies [34]: the $N \to \infty$ limit of a $SU(N)$ gauge theory is an effective string theory.[16] In this limit, any amplitude A admits the expansion

$$A = \sum_{h=0}^{\infty} N^{2-2h} \sum_{k=0}^{\infty} c_{h,k} \lambda^k = \sum_{h=0}^{\infty} N^{\chi(h)} f_h(\lambda), \tag{1.2.75}$$

where $\lambda = g_{YM}^2 N$ is known as the 't Hooft coupling. Each Feynman diagram contributing to A can be pictured as a specific triangulation of a genus h closed two-dimensional manifold. This expansion is topological, with $\chi(h)$ being the Euler characteristic of the manifold. In the large N, fixed λ limit this topological expansion is dominated by planar diagrams, *i*.e., diagrams that can be drawn on a sphere without self-intersecting. This structure parallels the one present in perturbative closed string theory, provided we identify the string coupling constant g_s and the rank of the gauge group as $g_s \propto N^{-1}$.

Let us carry on this analogy further, and assume that there exists a string theory dual to our original gauge theory. We observe that taking the large N limit in the gauge theory is equivalent to suppressing loop corrections in the putative string theory dual, reducing it to tree level. Note that besides the massless modes, this classical string theory would contain an infinite tower of massive states. Although suggestive, this construction has several apparent drawbacks. First, it is unable to inform us about the precise stringy parameter that relates to the 't Hooft coupling λ. Secondly, and most importantly, it is useless from a practical point of view, since it would be necessary to resum the infinite $\{c_{0,k}\}$ series of planar diagrams to reconstruct the theory at tree level.

The other insight explicitly materialized by AdS/CFT was the holographic principle. The holographic principle is based on the Bekenstein bound [35], and was introduced in the early nineties by 't Hooft [36] and Susskind [37], soon before the original Maldacena construction appeared. Essentially, the holographic principle postulates that given some space region M, in a theory of QG the total number of degrees of freedom associated with M does not scale

---

[16] A closed string theory when considering pure glue only.

as its volume V, but as the area A of its boundary ∂M. This observation implies that, in the quantum regime, gravity cannot be described by a local QFT -since then necessarily volume scaling hols-, but rather by a holographic quantum-mechanical theory that encodes the actual degrees of freedom living on ∂M.

Motivating the holographic principle involves an easy gedankenexperiment. Consider that there exists some matter distribution in M with higher entropy but lower energy than the smallest black hole able to contain the region. If some extra energy is injected, this black hole will form, and the Second Law would be violated. In particular, since the final black hole entropy scales as A, if the initial entropy scaled as V the Second Law would be *massively* violated. A contradiction is reached, implying that our original assumption, volume scaling, fails.

Of course, the holographic principle is at most an elementary kinematical constraint on any consistent theory of QG. Neither it informs us about the precise nature of the fundamental degrees of freedom that live on ∂M, nor about the the quantum theory that describes them.

When pondered together, the large N limit and the holographic principle suggest that the putative string theory dual to the gauge theory must live in a higher-dimensional spacetime. What Maldacena found originally was a pair of theories that are related exactly in the way we have outlined [33].

On the field theory side, we have four-dimensional $\mathcal{N}=4$ supersymmetric $SU(N)$ Yang-Mills theory. This is the maximally supersymmetric Yang-Mills theory in $d=4$, and can be regarded as the simplest interacting QFT in four dimensions. Its matter content consists of one gauge field, six scalars and four Weyl fermions. Both the scalar and the fermionic sectors are invariant under a global internal $SO(6)\cong SU(4)$ R-symmetry. The matter contect of the theory dictates that the β-function is zero and, as a consequence, $\mathcal{N}=4$ SUSY YM is conformal invariant at the quantum level.

Maldacena conjectured that this CFT is dual to type IIB string theory on $AdS_5\times S^5$, with N units of five-form flux through the S^5, and a curvature radius L equal in both the AdS_5 and the S^5 factors. The CFT can be pictured as living on the boundary of AdS_5. As expected from our discussion so far, the conformal symmetry group of the field theory maps to the AdS_5 isometry group. A novel ingredient now is that its $SU(4)\cong SO(6)$ symmetry group is also identified with the five-sphere isometry group.

Maldacena construction is, succinctly, an open/closed string duality. It just assumes that the interpolation between D-branes and p-branes upon increasing the coupling commutes with restricting to the low energy description of the system [38]. This construction also provides the specific relation between gauge/string theory parameters that more generic arguments miss. We have that

$$\frac{L^4}{\alpha'^2}=\lambda, \qquad \frac{\lambda}{4\pi N}=g_s \tag{1.2.76}$$

where α' sets the string length l_s as $l_s=\sqrt{\alpha'}$. In the large N limit at fixed λ, g_s vanishes. As expected from our previous discussion, quantum gravity effects, associated to string loops, are suppressed: the type IIB string theory becomes classical. Let us take now the large λ

limit. The planar gauge theory becomes strongly-coupled. On the other hand, the string length vanishes with respect to the AdS_5, S^5 curvature radius, L. The geometry becomes weakly-curved, and it is unable to resolve the extended nature of the string, *i.*e., strings behave as pointlike particles. Since the energy of an excited string state is $\propto l_s^{-1}$, the infinite tower of massive string states decouples from the massless modes, which are now the only excitations allowed. These modes are described by a classical gravitational field theory, type IIB supergravity on $AdS_5 \times S^5$, which encodes completely the dynamics of $\mathcal{N} = 4$ SUSY YM in the planar and strongly-coupled regime.

From the point of view of the holographic principle, the remarkable feature about the Maldacena construction is that the quantum theory describing the elementary degrees of freedom living on $\partial\mathrm{AdS}_5$ is a *local* QFT. Along this line, weakly-coupled gravity in AdS can be understood as an emergent phenomenon, arising from an infinite number of strongly-interacting fields in a gauge theory. Let us close this section by making two comments on this point of view.

First, it must be emphasized that the weak/strong nature of the AdS/CFT duality is its most compelling aspect, both from a practical and from a theoretical perspective. We already commented on the former one in our Foreword. Regarding the latter, it should be noted that the failure of perturbative QFT at strong coupling also signals a more serious conceptual breakdown [39], as our physical intuition cannot rely on the familiar weak-coupling picture based on quasiparticles interacting through Feynman diagrams. Even though the field theory Lagrangian is formulated in terms of some degrees of freedom, we don't know how these degrees of freedom reorganize themselves at strong coupling.[17] What AdS/CFT offers, at least for certain gauge theories, is a new perturbative framework and, as a consequence, a new way of thinking. It identifies the right degrees of freedom at infinite N, infinite λ, and then provides a systematic way of computing corrections to the leading order results in a $1/N, 1/\sqrt{\lambda}$ expansion. The incredible feature of this expansion is that these new degrees of freedom are weakly-gravitating objects in a higher-dimensional spacetime, so it allows employing gravitational intuition to think about otherwise unaddressable field theory problems.

The second and final comment is that, even if the original Maldacena duality has been tested successfully in numerous examples -including finite N and λ corrections-, understanding *how* it works at the fundamental level is an issue far from settled, at least to this author's knowledge.[18] This understanding would involve finding all the entries in the *holographic dictionary* relating field-theoretical and gravitational entities. In the remaining part of this section, we review several well-established entries of this dictionary. It should be noted, however, that its construction is not yet finished.

---

[17] QCD is one paradigmatic example. While being a theory of quarks and gluons microscopically, at finite coupling, the right degrees of freedom are colorless hadrons.

[18] For instance, understanding how bulk locality emerges from the underlying microscopical CFT degrees of freedom is extremely challenging. Since the gravitational theory is diffeomophic invariant, every spatial direction in the bulk is on an equal footing. However, the CFT origin of the spatial AdS_5 directions couldn't be more different from the the five-sphere ones [40].

1.2.2 The holographic dictionary

The precise map between gravitational and field theory entities implemented by the duality is known as the holographic dictionary. As in any other duality, both the partition functions as well as the Hilbert spaces of the bulk QG theory and the boundary CFT are identified

$$Z_{QG} = Z_{CFT}, \qquad \mathcal{H}_{QG} = \mathcal{H}_{CFT}, \tag{1.2.77}$$

while there is also a way of associating gauge-invariant observables in both theories, which we will review next. Let us just note first that when classical supergravity is applicable, we expect that at least *some* states in $\mathcal{H}_{QG}$ reduce to classical geometries. At least some, because not every state on the field theory admits a dual geometrical description. To see this, consider two states, $|\psi_1\rangle$ and $|\psi_2\rangle$, with dual spacetime geometries G_1 and G_2, and take their linear superposition, $\alpha\,|\psi_1\rangle + \beta\,|\psi_2\rangle$. It is by no means guaranteed that this superposition can also be described as some geometry G_{1+2}, *i*.e., quantum-mechanical linearity has no generic counterpart when considering solutions of the supergravity equations. Such a linear superposition should rather be thought of as providing a classical probability distribution over an ensemble of classical spacetimes [41], if we assume that different geometrical states are orthogonal at leading order in N. In the supergravity regime, there are also proposals that relate QFT information-theoretical quantities, such as entanglement entropies and complexities, to bulk geometrical constructs. We discuss the holographic prescription for computing the entanglement entropy in subsection 1.2.4.

Energies are straightforwardly related by the dictionary. The energy density of the CFT state corresponds directly to the ADM energy density of the dual geometry.[19] Therefore, the geometry corresponding to the CFT ground state is the minimal energy solution of the supergravity equations of motion, which is nothing but empty AdS itself. Consistently, the fact that the CFT vacuum is invariant under $SO(2, d)$ has a direct counterpart in the fact that empty AdS is invariant under the action of this group. An excited state is characterized by some bulk excitations placed above empty AdS.

Any excited state must reduce to the vacuum state when probed at infinitesimally short distances. Under the UV/IR connection, the geometry dual to this excited state must reduce to empty AdS in the infrared: it must be *asymptotically AdS*. As shown by Fefferman and Graham [42], any asymptotically AdS$_{d+1}$ metric admits a near-boundary expansion of the form

$$ds^2 = \frac{dz^2}{z^2} + \frac{h_{\mu\nu}(z,x)}{z^2} dx^\mu dx^\nu, \qquad h_{\mu\nu} = \eta_{\mu\nu}(x) + \ldots + t_{\mu\nu}(x) z^d + \ldots, \tag{1.2.78}$$

where $\eta_{\mu\nu}$ is the boundary metric and x^μ, $\mu = 0 \ldots d-1$, are boundary coordinates. *Planar asymptotics* correspond to selecting $\mathbb{R}^{1,d-1}$ as the boundary manifold, while *global asymptotics* correspond to selecting $\mathbb{R} \times S^{d-1}$.[20] It must be emphasized that any sufficiently well-behaved

---

[19] The asymptotic timelike Killing vector field of the bulk geometry, which we employ to define its associated ADM energy density, also determines the temporal direction of the boundary theory, which in turn fixes the CFT Hamiltonian.

[20] With their standard Minskowkean metrics.

$d-$dimensional manifold can be chosen as a boundary: the CFT can be placed on a black hole spacetime, or even on a cosmological solution. In this way, AdS/CFT provides a window into the large N, strongly-coupled dynamics of CFTs in general curved spacetimes of physical relevance [43].

As another important comment, note that in the original Maldacena construction we have that the ten-dimensional Newton's constant scales as $G \sim L^8 N^{-2}$. Therefore, for a field theory state to have a finite backreaction, its energy density E must scale as $E \sim N^2$. Generically, deformed geometries represent CFT states in which every elementary degree of freedom if excited. States with energy densities parametrically smaller than N^2 are represented by nonbackreacting excitations in the bulk.

Having made this clarifications, let us introduce now the most fundamental piece of the holographic dictionary. This is nothing but the celebrated Gubser-Klebanov-Polyakov-Witten (GKPW) relation [44, 45] between the CFT and QG vacuum generating functionals[21] $W = -i \ln Z$

$$W_{QG}[\phi \to \phi_0] = W_{CFT}[\phi_0] = -i \ln \left\langle e^{i \int d^d x \phi_0(x) \mathcal{O}(x)} \right\rangle_{CFT} \tag{1.2.79}$$

Here the CFT Lagrangian density $\mathcal{L}_{CFT}$ is deformed as

$$\mathcal{L}_{CFT} \to \mathcal{L}_{CFT} + \phi_0(x) \mathcal{O}(x), \tag{1.2.80}$$

where $x-$coordinates label boundary directions and $\mathcal{O}$ is a single-trace, primary operator sourced by ϕ_0. Through the source ϕ_0, a bulk field ϕ is associated to the operator $\mathcal{O}$. Both ϕ and $\mathcal{O}$ have to belong to the same representation of the conformal group, so they share the same quantum numbers. The precise way in which the source ϕ_0 relates to this bulk field ϕ is by specifying the contour conditions the latter should satisfy when approaching the AdS boundary. We are suppressing any possible index structure in (1.2.80), so it is understood that the Lagrangian deformation is invariant under the appropriate spacetime and internal symmetries.

While the rhs of the GKPW relation is perfectly defined, we have to remain agnostic about the precise nature of the lhs: the explicit form of the QG partition function is unknown in general. However, in the large N, large λ limit it can be evaluated in a saddle-point approximation

$$W_{QG}[\phi \to \phi_0] \approx W_{SUGRA}[\phi \to \phi_0] \equiv I_{SUGRA}[\phi \to \phi_0], \tag{1.2.81}$$

since the bulk string theory reduces to classical supergravity. In the expression above, $I_{SUGRA}[\phi \to \phi_0]$ is the on-shell supergravity action, *i.e.*, the action evaluated on a field configuration ϕ that solves the supergravity equations of motion with the asymptotic boundary conditions prescribed by ϕ_0. Once that $W_{SUGRA}[\phi_0]$ is known, QFT connected correlation functions for the operator $\mathcal{O}$ can be computed by standard functional differentiation with respect to the source $\phi_0(x)$

$$\langle O(x_1)...O(x_n)\rangle_c = \frac{\delta}{\delta\phi_0(x_1)} \cdots \frac{\delta}{\delta\phi_0(x_n)} W_{SUGRA}[\phi_0]. \tag{1.2.82}$$

---

[21] For definiteness, we consider the Euclidean version of the theories.

A caveat is in order. Due to the non-compact nature of any asymptotically AdS geometry, I_{SUGRA} is infrared divergent. Through the AdS/CFT dictionary, this divergence is directly related to the ultraviolet divergences of the CFT side, and provides one further example of the UV/IR connection. Obtaining finite physical answers requires, first, to choose a bulk infrared cutoff in the form of a timelike codimension-one hypersurface and, second, to regularize I_{SUGRA}, in such a way that the total action remains finite once the cutoff is removed. The actual form of the supergravity action one deals with is

$$I_{SUGRA} = I_{bulk} + I_{GH} + I_{ct}. \tag{1.2.83}$$

I_{bulk} is the original supergravity action, I_{GH} a standard Gibbons-Hawking term, and I_{ct} a counterterm action. I_{ct} is build from diffeomorphic invariant quantities that depend solely on the intrinsic geometry of the cutoff hypersurface. This procedure is known as *holographic renormalization* [46], and has been extensively studied [47].

For definiteness, let us introduce a free massive scalar field ϕ into the bulk gravitational theory, with planar asymptotics. Its action is given by

$$S_\phi = -\frac{1}{2}\int d^{d+1}x\sqrt{-g}\,\big((\partial\phi)^2 + m^2\phi^2\big). \tag{1.2.84}$$

The scalar field satisfies the Klein-Gordon equation,

$$\left(\Box - m^2\right)\phi = 0, \qquad \Box \equiv \frac{1}{\sqrt{-g}}\partial_\mu\left(\sqrt{-g}g^{\mu\nu}\partial_\nu\right). \tag{1.2.85}$$

The Klein-Gordon equation defines naturally a scalar product over solutions,

$$(\phi_1, \phi_2) = -i\int_\Sigma \sqrt{-\gamma}n^\mu\left(\phi_1^*\partial_\mu\phi_2 - \phi_2\partial_\mu\phi_1^*\right), \tag{1.2.86}$$

where Σ is codimension-one spacelike hypersurface with induced metric $\gamma_{\mu\nu}$ and normal n^μ. A solution ϕ to the Klein-Gordon equation is said to be normalizable if $(\phi,\phi) < \infty$, and non-normalizable otherwise. Since the Klein-Gordon equation is a second-order differential equation, there exist two linearly independent fundamental solutions, ϕ_- and ϕ_+. In Fefferman-Graham coordinates, they behave as

$$\phi_-(x,z) = A(x)z^{d-\Delta} + \ldots, \qquad \phi_+(x,z) = A(x)z^{\Delta} + \ldots \tag{1.2.87}$$

where $x^\mu = (t, \mathbf{x})$. The exponent Δ satisfies

$$\Delta = \frac{d}{2} + \nu = \frac{d}{2} + \sqrt{\frac{d^2}{4} + m^2L^2}. \tag{1.2.88}$$

The normalizability properties of the fundamental solutions are the following

- The ϕ_+ solution is normalizable for $\nu \geq 0$.
- The ϕ_- solution is non-normalizable for $\nu \geq 1$, and normalizable for $0 \leq \nu < 1$.

Note that tachyonic scalar fields are allowed if they respect the Breitenlohner-Freedman bound [48, 49]

$$m^2 \geq m_{BF}^2 = -\frac{d^2}{4L^2} \tag{1.2.89}$$

and that, in the mass window

$$m_{BF}^2 \leq m^2 < m_{BF}^2 + 1, \tag{1.2.90}$$

both ϕ_+ and ϕ_- are normalizable. Let us comment on the $\nu \geq 1$ case. We can promote the classical scalar field to a quantum operator $\hat{\phi}(z,x)$ by introducing a basis of orthonormal solutions $\{f_I\}$ to the Klein-Gordon equation and defining

$$\hat{\phi}(z,x) = \sum_I \left(f_I a_I + f_I^* a_I^\dagger \right), \tag{1.2.91}$$

where a_I, $a_I^\dagger$ are annihilation and creation operators. The vacuum state $|0\rangle_{\text{bulk}}$ is identified with global AdS$_{d+1}$ in the absence of ϕ-quanta and it is annihilated by a_I, $a_I\,|0\rangle_{\text{bulk}} = 0$. Since we are considering a free scalar field, our Hilbert space is the Fock space built out of $|0\rangle_{\text{bulk}}$ by the action of the creation operators $a_I^\dagger$. The identification of the bulk and boundary Hilbert spaces leads naturally to the requirement that $|0\rangle_{\text{bulk}} = |0\rangle_{\text{CFT}}$. This entails that we can construct a CFT operator $\mathcal{O}(x)$ out of $\hat{\phi}(z,x)$ by defining

$$\mathcal{O}(x) = \lim_{z\to 0} z^{-\Delta}\hat{\phi}(z,x). \tag{1.2.92}$$

Since the background spacetime is asymptotically AdS, we can employ the Fefferman-Graham construction to show that, in the $z \to 0$ limit, the transformation $x \to \lambda x$,$z \to \lambda z$ results in $\hat{\phi}(\lambda z, \lambda x) = \hat{\phi}(z,x)$. As a consequence, from (1.2.92) we obtain

$$\mathcal{O}(\lambda x) = \lambda^{-\Delta}\mathcal{O}(x). \tag{1.2.93}$$

This identity implies that $\mathcal{O}$ transforms as a primary operator under scale transformations, with Δ being its conformal weight. Since the Lagrangian deformation (1.2.80) must have scaling dimension d, the scaling dimension of the source $\phi_0(x)$ is $d - \Delta$,

$$\phi_0(\lambda x) = \lambda^{-(d-\Delta)}\phi_0(x). \tag{1.2.94}$$

Therefore, the source must be identified with

$$\phi_0(x) = \lim_{z\to 0} z^{\Delta - d}\phi(z,x) \tag{1.2.95}$$

and corresponds to the non-normalizable mode in the bulk.[22] Therefore, a generic solution of the Klein-Gordon equation has the asymptotic behavior

$$\phi(z,x) = \phi_0(x) z^{d-\Delta} + B(x) z^{\Delta} + \ldots \tag{1.2.96}$$

---

[22] This is natural, since ϕ_0 is a classical background field on the dual CFT that does not belong to the CFT Hilbert space. Through the AdS/CFT dictionary, the dual to ϕ_0 cannot belong to the bulk Hilbert space. As the bulk Hilbert space is build out of the normalizable modes, the dual to the source must be a non-normalizable mode. This author first learned this argument in [50].

By applying standard holographic renormalization techniques to the scalar field action (1.2.84), and the relation (1.2.82) when $n = 1$, the vacuum expectation value (vev) of $\mathcal{O}$ is

$$\langle \mathcal{O}(x) \rangle = 2\nu B(x). \tag{1.2.97}$$

In this way, the vev of $\mathcal{O}$ is fixed by the leading order term of the normalizable part of ϕ.[23] Let us note that the scalar field ϕ must also be restricted to satisfy suitable boundary conditions in the interior of the geometry; for instance, ϕ needs to be regular at the origin for global asymptotics. For a given source ϕ_0, this condition can only be met for a specific $\langle \mathcal{O} \rangle$. As a consequence, the vev is a functional of the source, $\langle \mathcal{O} \rangle = \langle \mathcal{O} \rangle [\phi_0]$. This is crucial for the implementation of linear response theory in holography, as we discuss in subsection 1.2.6.

The identification of the conformal weight of $\mathcal{O}$ with Δ, together with the relation (1.2.88) between Δ and m^2, implies that [44, 45]

- If $m^2 > 0$, $\Delta > d$ and $\mathcal{O}$ is an irrelevant operator.
- If $m^2 = 0$, $\Delta = d$, and $\mathcal{O}$ is a marginal operator.
- If $m^2_{BF} \geq m^2 < 0$, $d/2 < \Delta < d$ and $\mathcal{O}$ is a relevant operator.

The relation above implies that the lowest conformal weight of a scalar operator is $d/2$. In any unitary CFT, there exist a bound on this quantity. However, this unitarity bound can be shown to be

$$\Delta \geq \frac{d}{2} - 1. \tag{1.2.98}$$

A puzzle arises. Our construction is apparently unable of representing the dual fields of CFT scalar operators with $\Delta \in [d/2 - 1, d/2)$. To solve this conundrum, we must analyze the situation when $0 \leq \nu < 1$.

In this case, the scalar field mass lies in the window (1.2.90). The crucial point is that now both ϕ_+ and ϕ_- are normalizable solutions and there exist two possible ways of quantizing ϕ. Our previous one, which corresponds to considering a basis of orthonormal eigenfunctions with $A(x) = 0$, goes under the name of *standard quantization*. As we have seen, in the standard quantization we obtain a scalar operator $\mathcal{O}_s$ whose conformal weight satisfies

$$\frac{d}{2} \leq \Delta_s. \tag{1.2.99}$$

The novel choice that arises corresponds to considering a basis of orthonormal eigenfunctions with $B(x) = 0$, and goes under the name of *alternative quantization*. In this case, from our novel $\hat{\phi}_a$ we obtain a scalar operator $\mathcal{O}_a$ with scaling dimension

$$\frac{d}{2} - 1 \leq \Delta_a \leq \frac{d}{2} \tag{1.2.100}$$

---

[23] We have skipped an important subtlety: in evev d, there are extra logarithmic terms in the near-boundary expansion, and the vev can depend on the coefficient of the leading order logarithm. In each case, the relation between $\langle \mathcal{O} \rangle$ and the coefficients of the near-boundary expansion must be established in terms of the proper holographic renormalization of the system. In this sectio, for illustrative purposes only, we obviate this fact.

The names of standard and alternative quantization are obvious if we realize that each choice of boundary conditions defines an inequivalent Fock space in the bulk. When renormalizing holographically the bulk theory, the alternative quantization can be implemeted by adding a suitable boundary term to the scalar action [51].

What about other operators that are not scalars? In the case of conserved currents, a background gauge field can be introduced by covariantizing the CFT action. The natural linearized couplings for a conserved current J^μ, associated to a global internal symmetry, or the conserved energy-momentum tensor $T^{\mu\nu}$, associated to Poincarè invariance, are

$$S_{CFT} \to S_{CFT} + \int d^d x \, (a_\mu J^\mu + h_{\mu\nu} T^{\mu\nu}) \, . \tag{1.2.101}$$

Note that a_μ, $h_{\mu\nu}$ must correspond to a gauge field and a metric perturbation because conservation of J_μ, $T_{\mu\nu}$ implies that, for any α, χ_μ falling fast enough at infinity, the redefinitions

$$a_\mu \to a_\mu + \partial_\mu \alpha, \qquad h_{\mu\nu} \to h_{\mu\nu} + \partial_\mu \chi_\nu + \partial_\nu \chi_\mu, \tag{1.2.102}$$

correspond to gauge transformations that leave S_{CFT} invariant.

Through the GKPW relation (1.2.79), these CFT background fields must source bulk fields A_μ, $g_{\mu\nu}$, in such a way that a_μ, $\eta_{\mu\nu} + h_{\mu\nu}$ can be read-off from their leading asymptotic behavior. The boundary gauge symmetry (1.2.102) must descend consistently to the bulk gauge symmetry of A_μ, $g_{\mu\nu}$. Therefore, a conserved current is dualized into a bulk gauge field, while the energy-momentor tensor is dualized into the bulk metric. This discussion exemplifies a trademark of AdS/CFT: global symmetries in the boundary correspond to local symmetries in the bulk, as we already saw in the relation between the CFT and AdS symmetry groups.

At the CFT level, any operator with spin s must have a conformal weight that respects the unitarity bound

$$\Delta \geq d - 2 + s. \tag{1.2.103}$$

If the operator saturates this bound, it obeys free field equations of motion. Said otherwise, it corresponds to a conserved spin-s current. Therefore, we must have that $\Delta_{J_\mu} = d - 1$ and $\Delta_{T_{\mu\nu}} = d$. In the latter case, $\langle T_{\mu\nu} \rangle$ is recovered from $h_{\mu\nu}(z, x)$ in (1.2.78) as

$$\langle T_{\mu\nu} \rangle = \frac{d L^{d-1}}{16 \pi G} t_{\mu\nu} \tag{1.2.104}$$

by standard holoraphic renormalization. Owing to the Fefferman-Graham asymptotic expansion (1.2.78), in principle one could thick that any choice for $t_{\mu\nu}$ defines a geometrical state of the dual CFT. However, this is not true. There are additional physical requirements that any geometry must satisfy in order to allow for such interpretation. For instance, a generic choice for $t_{\mu\nu}$ would lead to the apperance of naked singularities in the bulk.

1.2.3 Equilibrium physics in holography

As mentioned after equation (1.2.78), the manifold where the CFT is defined can be specified at will. In particular, imagine we want to analyse a CFT in the canonical ensemble. The CFT partition function at finite temperature is given by

$$Z_{CFT}(\beta) = \mathrm{Tr} \exp\left(-\beta H_{CFT}\right) \tag{1.2.105}$$

where $\beta = T^{-1}$. This expression admits the functional representation

$$Z_{CFT}(\beta) = \int_{PBC} [d\Phi] \left\langle \Phi \left| e^{-\beta H_{CFT}[\Phi]} \right| \Phi \right\rangle = \int_{PBC} [d\Phi]\, e^{-\int_0^\beta d\tau \int d^{d-1}x \mathcal{L}_{CFT}[\Phi]}, \tag{1.2.106}$$

where Φ denotes the collection of CFT fields and PBC refers to the boundary conditions that must be imposed to enforce the trace operation (specifically, bosons are periodic and fermions antiperiodic, both with periodicity β). From this last identity, it is immediately seen that $Z_{CFT}(\beta)$ can be computed from the CFT generating functional on an Euclidean geometry where the Lorentzian time coordinate has been analytically continued, $t \to i\tau$, and identified, $\tau \sim \tau + \beta$. Through the GKPW relation, in the large N, large λ limit the partition function (1.2.105) is going to be dominated by a Euclidean supergravity solution with a compact direction whose periodicity at the boundary coincides with β. Defining the CFT free energy $F_{CFT}(\beta)$ through the relation $Z_{CFT} \equiv \exp\left(-\beta F_{CFT}(\beta)\right)$, we find that the GKPW prescription implies that

$$F_{CFT}(\beta) \simeq \beta^{-1} I_{SUGRA}[\beta] \equiv F_{SUGRA}[\beta]. \tag{1.2.107}$$

Therefore, for asymptotically AdS geometries, old-fashioned Euclidean QG is encoding the thermodynamics of a large N, strongly-coupled CFT in the most straightforward way imaginable; for thermodynamical quantities, the holographic dictionary reduces to the identity.[24] By employing the definition (1.2.107), standard thermodynamical relations can be applied to compute the energy

$$\langle E \rangle = \beta \frac{\partial F}{\partial \beta} + F, \tag{1.2.108}$$

and entropy,

$$S = \beta(\langle E \rangle - F). \tag{1.2.109}$$

Note in particular that when the thermal cycle is non-contractible, there is no need to impose any regularity condition in the IR of the geometry. Therefore, no metric parameter is functionally dependent on the temperature, the bulk action is linear in β, $\langle E \rangle = F$ and $S = 0$.

There can exist several saddle-points contributing to $Z_{CFT}(\beta)$ for a given temperature

$$Z_{CFT}(\beta) \simeq e^{-\beta F_1(\beta)} + e^{-\beta F_2(\beta)} + ... \tag{1.2.110}$$

The saddle-point with the lowest free energy is going to dominate. As the temperature changes, this dominant saddle-point can switch from one supergravity solution to another.

---

[24] When referring to these quantities, we shall omit the subscripts indexing bulk and boundary in the following.

Therefore, saddle-point competition models classical phase transitions in the dual CFT.

The most well-known example of this behavior is the Hawking-Page transition in global AdS_{d+1} [52]. This is a first-order phase transition that takes place at a temperature

$$T_c = \frac{(d-1)}{2\pi L}, \tag{1.2.111}$$

where the Euclidean AdS spacetime (EAdS) dominating the canonical ensemble for $T < T_c$ switches places with a Euclidean Schwarzschild black hole solution (ESBH) with horizon radius $r_+ = L$. The discontinuous jump on the entropy from $S_{EAdS} = O(G^0)$ to $S_{ESBH} = O(1/G) = O(N^2)$ is interpreted, from the dual field theory point of view, as the result of a deconfinement transition, where the dominant phase changes from a gas of colorless glueballs to a gluon plasma [45, 53].[25]

It is important to realize that we have a nontrivial phase transition because the CFT is placed on $\mathbb{R} \times S^{d-1}$. Due to conformal invariance, there are only two energy scales into the game: the inverse sphere radius $1/L$ and the temperature T. They can be combined in the dimensionless ratio $\eta = TL$. Dimensional analysis implies then that the free energy density is given by $f(T, 1/L) = T^d \hat{f}(\eta)$. When taking the flat space $L \to \infty$ limit at fixed temperature, $\eta \to \infty$ and the free energy density becomes $f(T, 0) = T^d \hat{f}(\infty)$: no phase transition is possible since the T dependence is trivial. At finite temperature, the theory is always in the deconfined phase in the infinite volume/planar AdS limit.

Phase transitions in planar AdS require the introduction of another energy scale the temperate can be measured against. Let us start by considering the dual CFT at finite charge density. The introduction of a bulk abelian gauge field A_μ couples the CFT to a conserved global current J_μ, as discussed after equation (1.2.101). For a translationally-invariant CFT state, only the t-components A_t, J_t are relevant after gauge fixing. The near-boundary $r \to \infty$ expansion

$$A_t(t, r) = \mu + ... - \frac{\rho}{r^{d-2}} + ... \tag{1.2.112}$$

fixes the leading order term μ to be the CFT chemical potential, which coupled to the current, leads to the finite charge density $\langle J_t \rangle \propto \rho$. The gravitational solution dual to a state with $\langle J_t \rangle \neq 0$ at thermal equilibrium is the AdS-Reissner-Nordstrom (AdSRN) black hole, which is endowed with a nontrivial gauge field profile.

Furthermore, the presence of additional bulk fields can lead to new phases. This enrichment takes place because, for asymptotically AdS geometries, a black hole solution is not univocally determined by its conserved charges. For example, including additional charged scalar fields can lead to the appearance of hairy black hole solutions in the corresponding Einstein-Maxwell-scalar theory [54][55][56]. These are solutions that, at fixed T/μ, display a nontrivial scalar field profile outside the black hole horizon. On the CFT side, the dual scalar

---

[25] In QCD at small baryon density the phase transition smoothes out into a crossover; the large-N limit is to be held responsible for the sharpness of the transition here. We also employ the terms glueball and gluon plasma in a broad sense, to highlight that the dual CFT does not contain fundamental matter.

operator $\mathcal{O}$ gets a nonzero expectation value, $\langle \mathcal{O} \rangle \neq 0$. Therefore, hairy black holes correspond to superfluid states, since an operator with nonzero global charge condenses at thermal equilibrium.[26] The first normal-superfluid transition found in the holographic context involved a massless scalar that condensed below a critical T_c at fixed μ, where a condensate built up in a mean-field-like fashion, $\langle O \rangle \propto (T_c - T)^{1/2}$. AdSRN solutions of course still exist below the critical point but they are subdominant saddles, $F_{hairy}(\mu, T) - F_{AdSRN}(T, \mu) \leq 0$ for $T \leq T_c$. Since then, more exotic phases have been modeled, like p-wave superfluids [57][58] where a vector condenses. Dropping the requirement of spatial homogeneity enriches the situation even further, in a way that allows describing momentum relaxation at strong-coupling or stripped phases. For reviews of AdS/CFT applications to the Condensed Matter realm see [59, 60].

In chapter 5, we will discuss normal-superfluid phase transitions in the global AdS$_4$ context. It must be emphasized that in global AdS finite charge states display a nontrivial phenomenology even in the absence of additional operators, since now the partition function can depend on two dimensionless quantities, TL and μL. There is no need of considering hairy black holes to find generalizations of the Hawking-Page transition [61] [62].

Two last conceptual remarks are in order. The first one is that finite temperature phase transitions are determined by the non-analyticities of the free energy. Therefore, they are strictly forbidden in systems with a finite number of degrees of freedom N at finite volume, since the total partition function is a sum of analytic terms, $Z = \sum_n g_n e^{-\beta E_n}$. For them to be allowed, it is necessary to go to the thermodynamic limit: $N, V \to \infty$ with fixed N/V. In AdS/CFT, going to the large N regime can be pictured as taking a non-standard thermodynamic limit at finite volume. This, in particular, implies directly that finite N corrections are going to smooth any global AdS phase transition, like the Hawking-Page transition, to a crossover.

The second one is that, for global asymptotics, the thermodynamical stability/dominance of a given static black hole solution can change depending on the ensemble considered. We discuss this issue in section 2.3. It is also clearly illustrated by the results we present in section 5.4.

1.2.4 Entanglement entropy in holography

In 2006, Ryu and Takayanagi (RT) introduced one of the most beautiful entries in the holographic dictionary [63][64]. They put forward a proposal that reduced the entanglement entropy computation in the CFT to a simple variational problem in the bulk geometry. Initially, only time-independent states were considered. The construction was further extended to time-dependent situations by Hubeny, Rangamani and Takayanagi (HRT) [65]. Recently, the original RT prescription has been proven correct by Lewkowycz and Maldacena [66], while demonstrating the HRT prescription is underway [67]. Having clarified this, let us refer to the HRT recipe as the holographic entanglement entropy (HEE) prescription or for-

---

[26] Actually, these hairy solutions usually go under the name of holographic superconductors. In this thesis, we refer to them as superfluids to emphasize that, in principle, the field theory broken symmetry is global, not gauged. Going from one description to the other involves neglecting the effect of virtual photons.

mula.

The HEE prescription states the following [7]. Let $A \subset \mathcal{B} = \partial AdS_{d+1}$ be our entangling region. The entanglement entropy of A, S_A, is then given by

$$S_A = \frac{1}{4G}\text{Area}(\sigma_A) \tag{1.2.113}$$

where σ_A is a bulk codimension-2 surface such that:

- The boundary of σ_A coincides with the boundary of A, $\partial A = \partial\sigma_A$.
- σ_A is homologous to A, in the sense that it exists a closed codimension-1 bulk region R_A such that $\partial R_A = A \cup \sigma_A$. This condition is referred to as the *homology constraint*.
- σ_A extremizes the area functional. If several saddles exist, the one with the minimal area is to be chosen.

For a static background geometry, extremization reduces to minimization, and the HEE prescription reduces to the original RT proposal.

Some remarks are in order. First, the HEE prescription only encodes the dominant $O(1/G) = O(N^2)$ contribution to the actual EE for geometrical states [68]. It is possible to compute subleading corrections in a $1/N$ expansion that involves considering bulk quantum effects; for example, determining the $O(1)$ correction requires to take into account the quantum fluctuations of bulk fields across the entangling surface σ_A [69].

Second, the HEE prescription is completely consistent with the properties of EE we introduced in section 1.1. First, it is obvious that $S_A > 0$. In the time-independent case, simple geometric reasoning is sufficient to prove that it satisfies the strong subadditivity inequalities [70].[27] This was one of the first consistency checks the prescription passed.

There are also nontrivial entropy inequalities implied by the RT formula that are not generically true for a quantum mechanical system. The most well-known example is the monogamy of mutual information [71],

$$I_3(A:B:C) = I(A,B) + I(A,C) - I(A,BC) \leq 0, \tag{1.2.114}$$

where A, B, C are three nonoverlapping boundary regions. I_3 is the tripartite information, which can be thought of as a measure of the extensivity of mutual information. The fact that $I_3 < 0$ implies the mutual information is never subextensive, since the degree of correlation between A and the combined system BC is never smaller than the degree of correlation between A and the individual subsystems B and C. An immediate consequence of (1.2.114) is that any state for which mutual information is subextensive cannot be described by a geometric dual. Both strong subadditivity and monogamy can also be proven to hold in time-dependent geometries, provided that the null energy condition is satisfied in the bulk.

---

[27] The beautiful simplicity of the holographic proof of strong subadditivity should be contrasted with the particularly unenlightening algebraic quantum mechanical original derivation.

Having analyzed the status of the EE inequalities in holography, let us go back and discuss how other slightly simpler properties that geometric EE should satisfy are realized in AdS/CFT. First, the noncompact nature of AdS implies that the area law is automatically respected: the logarithmic divergence of the radial proper distance when approaching the boundary is responsible for this. The area law has been explicitly demonstrated for free bosonic QFTs, and the HEE formula implies that it also holds in holographic QFTs.

For definiteness, let us work out a specific example. Consider a planar $d+1$-dimensional AdS-Schwarzschild black hole as our background geometry, and take a ball of radius R as entangling region

$$\bar{A} = \{(t, \mathbf{x}) \in \mathbb{R}^{1,d-1} : t = 0, \mathbf{x}^2 \leq R^2\}. \tag{1.2.115}$$

By symmetry, the entangling surface σ_A must be parameterized as[28]

$$\sigma_A = \{(t, z, r, \Omega_i) \in SAdS_{d+1} : t = 0, z = z(r)\}. \tag{1.2.116}$$

The function $z(r)$ must satisfy the boundary conditions $z(R) = 0$ by the first requirement of the HEE prescription, while regularity at the entangling surface tip, $z^* \equiv z(0)$, implies that $z'(0) = 0$. We work in units such that $L = 1$. The black hole metric is

$$ds^2 = \frac{1}{z^2}\left(-f(z)dt^2 + \frac{dz^2}{f(z)} + d\mathbf{x}^2\right), \qquad f(z) = 1 - mz^d. \tag{1.2.117}$$

Computing the EE associated to A implies finding the bulk surface that minimizes the area functional

$$S_A = \frac{1}{4G}\mathrm{Vol}(S^{d-2})\int_0^R dr\mathcal{L} \equiv \frac{1}{4G}\mathrm{Vol}(S^{d-2})\int_0^R dr r^{d-2}\frac{1}{z(r)^{d-1}}\sqrt{\frac{z'(r)^2}{f(z(r))} + 1}. \tag{1.2.118}$$

In the near-boundary limit $z \ll 1$, $R - r \ll 1$, we can employ the Euler-Lagrange equations derived from (1.2.118) to show that $z(r) \sim (R-r)^{1/2}$ at leading order, as long as $d > 2$. Expanding (1.2.118) and performing the integral, we get

$$S_A \sim \frac{\mathrm{Vol}(S^{d-2})R^{d-2}}{\epsilon^{d-2}}, \tag{1.2.119}$$

where we cut-off the integral at the ultraviolet scale $z = \epsilon$. The area law is satisfied as expected. Subleading corrections result in an expansion of the form (1.1.22),(1.1.23).

For $d = 2$, it is possible to find σ_A analytically in a straightforward way. Note that, in this case, $\mathcal{L}$ does not depend explicitly on the radial coordinate, so the Hamiltonian $\mathcal{H} = z'\partial\mathcal{L}/\partial z' - \mathcal{L} = -z_*^{-1}$ is conserved, and sets the turning point of σ_A in the bulk. From $\mathcal{H}$ conservation, we obtain the equation

$$z'(r) + \frac{\sqrt{1 - mz(r)^2}\sqrt{z_*^2 - z(r)^2}}{z(r)} = 0, \tag{1.2.120}$$

---

[28] We have described a constant time slice of the boundary in terms of spherical coordinates (r, Ω_i).

which is solved by

$$z(r) = \frac{\sqrt{1 - \cosh(\sqrt{m}r)^2 \operatorname{sech}(\sqrt{m}R)^2}}{\sqrt{m}}, \tag{1.2.121}$$

an expression that reduces to the vacuum result, $z(r) = \sqrt{R^2 - r^2}$, when $m = 0$. Regularity at the entangling surface tip relates the geodesic turning point z_* with the entangling interval size R as

$$z_* = \frac{\beta \tanh(\frac{2\pi}{\beta}R)}{2\pi}, \tag{1.2.122}$$

where we have employed the relation between the black hole mass and its thermal wavelength, $\beta = 2\pi/\sqrt{m}$. As promised, equation (1.2.122) provides a diffeomorphism invariant and quantitative UV/IR map. At finite temperature, we must distinguish two different regimes. When $R \ll \beta$, we recover the scaling-based result for the vacuum state, $z_* = R$. This result is consistent with the fact that every CFT state looks like the vacuum when probed at sufficiently short distances; under the AdS/CFT duality, this is guaranteed by the asymptotically AdS boundary conditions satisfied by any admissible geometry. In the opposite $R \gg \beta$ limit, (1.2.122) shows that the energy scale associated to the boundary region reduces to the temperature, $z_*^{-1} = 2\pi T$. Again, this is consistent with the fact that thermal fluctuations erase any lower energy excitations of the system, providing a mass gap that results in an effective infrared cutoff.

This way of employing the HEE prescription to associate bulk and boundary regions is an example of the so-called *subregion-subregion* duality [72][73]. To introduce this idea, let us note that ρ_A determines completely the CFT state in the causal development of A. We denote this spacetime region by $D(A)$. Subregion-subregion duality identifies the holographic dual of ρ_A with the reduced density matrix of the bulk state on R_A. In this way, the bulk dual of $D(A)$ is the *entanglement wedge*, *i.e.*, the bulk domain of dependence of R_A, $D(R_A)$ [74]. The full development of this set of ideas promises a coordinate invariant formulation of the UV/IR map.

Inserting (1.2.121) into (1.2.118), we get the result

$$S_A = \frac{1}{2G} \log\left(\frac{\beta}{\pi\epsilon} \sinh\frac{2\pi R}{\beta}\right), \tag{1.2.123}$$

where we have introduced the ultraviolet cutoff $z = \epsilon$ and substituted $Vol(S^0) = 2$. This matches the CFT computation (1.1.25), based on the replica trick, iff we identify

$$G = \frac{3L}{2c}, \tag{1.2.124}$$

where we have reintroduced the curvature radius. This is a well-known relation first uncovered by Brown and Henneaux [75]. In 1986, these authors proved that the asymptotic symmetry algebra of AdS_3 is isomorphic to two copies of the Virasoro algebra with the central charge (1.2.124). This asymototic symmetry algebra is also to the conformal symmetry algebra of a $1+1$-dimensional CFT.

Knowing the explicit form of the entangling surface, we can obtain a geometrical understanding of the asymptotic behavior of the EE of the thermal state in the limits $R/\beta \to 0, \infty$ (recall the discussion after equation (1.1.25)). In particular, when $R/\beta \to \infty$, the infrared piece of the entangling surface licks the black hole event horizon, in such a way that the area of this infrared piece is determined by the event horizon area. The saturation of the EE to its thermal value follows straightforwardly.

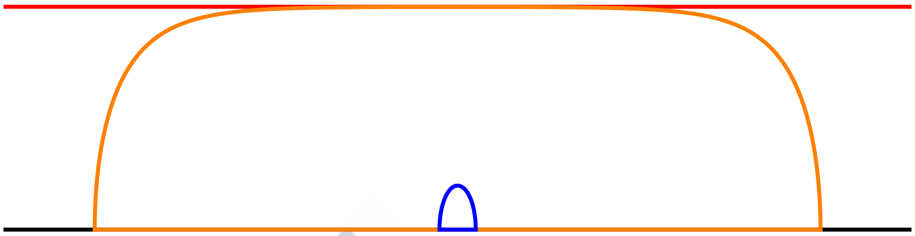

Figure 1.1: Schematic representation of the fact that the thermalization of EE is controlled by the infrared behavior of the entangling surface. The asymptotic boundary is depicted in black, the horizon in red.

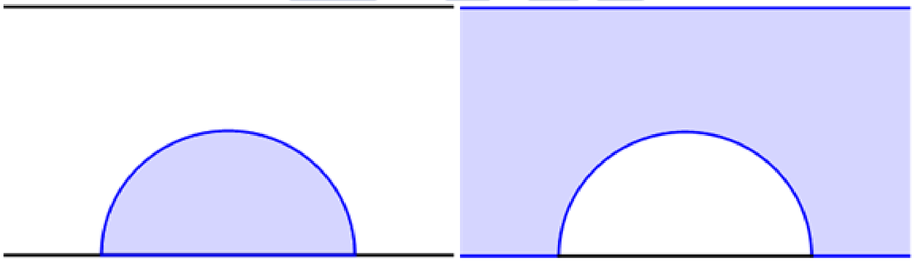

Figure 1.2: Schematic representation of the entangling surfaces computing S_A (left) and $S_{\bar{A}}$ (right) for the vacuum/thermal state of the CFT_{1+1}. The lower black segment corresponds to the asymptotic boundary, the upper black one to the Poincaré/black hole horizon.

The HEE prescription also allows for a geometrical diagnose of a state's purity, due to the homology constraint. Let us illustrate this with another two-dimensional example. We place ourselves in the vacuum state of the CFT_{1+1}, which corresponds to a planar AdS_3 geometry. In this case, the entangling surface $\sigma_{\bar{A}}$, which is associated to the complementary region

$$A = \{(t, z, x) \in AdS_3 : t = 0, x \notin [-R, R]\} \tag{1.2.125}$$

corresponds to σ_A plus a piece that runs along the Poincaré horizon. This piece is needed in order to satisfy the homology constraint. Therefore,

$$S_{\bar{A}} = S_A + S_{hor}, \tag{1.2.126}$$

where S_{hor} represents the entropy of the Poincaré horizon, which is zero. As a consequence, $S_{\bar{A}} = S_A$ and the state is pure, as expected. Figure 1.2 represents schematically this geometrical construction.

On the other hand, for a planar black hole geometry, the horizon is located at $z = z_h < \infty$, and a constant time slice of it has a finite area density. When computing $S_{\bar{A}}$, the contribution from the disconnected piece of $\sigma_{\bar{A}}$ that runs along the horizon results in an infrared divergent answer. As a consequence, $S_{\bar{A}} \neq S_A$. The black hole geometry corresponds to a mixed state, as expected. In particular, note that if we choose a whole constant time slice of the boundary as our entangling region, *i.*e., $A = \mathbb{R}$, we obtain that our entangling surface corresponds just to the black hole horizon. Therefore, the EE density on the boundary matches trivially the thermodynamical entropy density.

1.2.5 Bottom-up versus top-down constructions

The original Madacena duality between $\mathcal{N} = 4$ SU(N) SUSY YM and type IIB string theory on AdS$_5\times$ S^5 is a particular example of a *top-down* construction. Top-down constructions are pairs of dual QFTs and gravitational theories identified by taking a suitable decoupling limit of a full-fledged brane system embedded in String Theory. Since the initial Maldacena breakthrough, dozens of other examples have been found, and conformal invariance or supersymmetry are not essential for their existence [76][77][78][79].

In this thesis, we follow a complementary, *bottom-up* approach. Let us explain the phlilosophy behind it. We consider general actions of the form,

$$I_{bulk} = \frac{1}{16\pi G}\int d^{d+1}x(R-2\Lambda) + I_{matter} \tag{1.2.127}$$

which corresponds to $d+1$-dimensional Einstein-Hilbert gravity with negative cosmological constant plus matter, and interpret them as the generating functional of some *unkown* CFTs through the GKPW relation (1.2.79). Note that the different entries of the holographic dictionary we have discussed so far apply naturally to a bottom-up construction. The groundstate of our putative CFT still corresponds to vacuum AdS$_{d+1}$, and a thermal equilibrium state still corresponds to a static black hole geometry, as our discussion in subsection (1.2.3) illustrates. The relations between boundary operators and bulk fields we have introduced also uphold, in particular at the level of their quantum numbers, scaling dimensions and masses, or identification of the source and the expectation value in terms of non-normalizable and normalizable modes. In the same vein, as shown in [66][67], the HEE prescription can also be employed, as it follows from a bulk geometrization of the replica trick at the boundary that relies on the GKPW relation.[29]

In bottom-up constructions, we assume that the *effective number of elementary degrees of freedom* of the dual CFT, c_{eff}, scales as $c_{eff} \sim G^{-1}$ with respect to the bulk Newton's constant. Therefore, geometries deformed with respecto to the AdS vacuum, and in particular black hole spacetimes, are endowed with an energy density $\sim c_{eff}$. The strongly-coupled nature of the putative dual CFT is made manifest by realizing that, since we are restricting ourselves to a few number of bulk fields, there must exist a large gap on the spectrum of conformal dimensions of the primary operators (see [8] for a detailed explanation of these

---

[29] We refer the reader to [80] for a very nice discussion about how perturbative QFT in asymptotically AdS spacetimes can be employed to build a CFT in the large N regime.

two statements).

The obvious drawback of a bottom-up construction is that we don't have access to the microscopic nature of the dual CFT, if any. For instance, we don't know how the operators the bulk fields correspond to are constructed out of the elementary fields of the CFT. At most, a bottom-up construction should provide an effective field theory description of a strongly-coupled QFT at a large number of elementary degrees of freedom. The underlying expectation of a bottom-up based research is that the new phenomena that might be uncovered by it are independent of the specific details of the underlying CFT, at least to a reasonable extent. Said otherwise, the usefulness of this approach is based on the assumption that it can capture universal properties of a CFT at a large number of elementary fields and/or strong-coupling. This is particularly true for applications to condensed matter, where the equivalent of the gauge theory large N regime is not easy to identify, and we are mostly interested in how the strong coupling regime and the associated absence of a quasiparticle-like description manifest themselves in different physical properties of the macroscopic system.

1.2.6 Holography near equilibrium

As subsection 1.2.3 shows, there is a vast landscape of equilibrium states with a dual geometrical description. In this thesis, we are interested in how perturbations around these equilibrium states evolve and possibly relax, even in the sense of how large perturbations can connect different equilibrium points in the landscape. Before we start to discuss this fully out-of-equilibrium regime, let us briefly review how weak perturbations around equilibrium are treated in AdS/CFT. Following [81], we distinguish two different regimes. The first one contains small-amplitude and arbitrary-frequency perturbations, which are the subject of linear response theory; the second one encompasses arbitrary-amplitude and small-frequency perturbations, which are the subject of hydrodynamics.

Linear response theory in holography

Lets place ourselves in a translationally-invariant equilibrium state, and perturb the CFT by introducing a coupling ϕ_j^0 to the operator $\mathcal{O}_j$,

$$S_{CFT} \to S_{CFT} + \int d^d x \phi_j^0 \mathcal{O}_j. \tag{1.2.128}$$

We assume that $\|\phi_j^0\| \ll 1$. The basic identity of linear response theory is

$$\delta_{\phi_0} \langle \mathcal{O}_i(\omega, \mathbf{k}) \rangle = -G_{ij}^R(\omega, \mathbf{k}) \phi_j^0(\omega, \mathbf{k}) \tag{1.2.129}$$

which defines the retarded correlator G_{ij}^R. This quantity encodes the response of the vacuum expectation value of the operator $\mathcal{O}_i$ to the deformation (1.2.128) introduced by ϕ_j^0. In position space, we have

$$\delta_{\phi_0} \langle \mathcal{O}_i(x) \rangle = -\int d^d y G_{ij}^R(x-y) \phi_j^0(y) \tag{1.2.130}$$

with $G^R_{ij}(x-y) = -i\Theta(x^0-y^0)\left\langle[\mathcal{O}_i(x),\mathcal{O}_j(y)]\right\rangle$. The Heaviside Θ-function enforces the causal response of the system to the applied external source. From (1.2.129), it is immediate to compute the retarded correlator in any equilibrium CFT state with a gravity dual: it suffices to solve the linearized bulk equations of motion for the dual field ϕ_i, subjected to the asymptotic boundary conditions determined by ϕ^0_j, and with the appropriate regularity conditions at the IR of the geometry.

For instance, in case we were computing G^R_{ii} on a thermal state for a scalar operator $\mathcal{O}_i$,[30], dual to a bulk scalar field ϕ, we would need to solve the linearized ϕ equation of motion on the associate black hole background, with infalling boundary conditions imposed at the horizon:[31]

$$\phi(\omega,\mathbf{k},r) = A(\omega,\mathbf{k})r^{d-\Delta} + ... + B(\omega,\mathbf{k})r^{-\Delta} + ... \tag{1.2.131}$$

$$G^R(\omega,\mathbf{k}) \propto -\frac{B(\omega,\mathbf{k})}{A(\omega,\mathbf{k})} \tag{1.2.132}$$

Sourceless solutions with $A(\omega,\mathbf{k}) = 0$ correspond to poles on the retarded correlator and represent physical excitations of the system. It is expected that, for the given IR boundary conditions, the requirement that $A(\omega,\mathbf{k}) = 0$ can only be met by a discrete set of eigenfrequencies $\{\omega_n(\mathbf{k}), n \in \mathbb{N}\}$, at fixed $\mathbf{k}$. Imposing the boundary condition that scalar waves are absorbed at the horizon leads to a non-hermitean problem and, in consequence, to a complex eigenfrequency spectrum. In this case, the eigenfunctions are the so-called *quasinormal modes* of the black hole. In the absence of a horizon, there is no source of dissipative behavior,[32] and we obtain a hermitean problem with a real eigenfrequency spectrum. The eigenmodes are known as *normal modes* in this case.

Causality implies that the quasinormal modes imaginary part is negative, *i*.e., $\omega_n(\mathbf{k}) = \Omega_n(\mathbf{k}) + i\Gamma_n(\mathbf{k})$ with $\Gamma_n(\mathbf{k}) < 0$. In this way, any perturbation of a black hole background dies-off exponentially, with a relaxation time equal to $\Gamma_0(\mathbf{k})^{-1}$ at leading order.[33] This is to be contrasted with asymptotically flat black holes where, in addition to exponential relaxation, late-time polynomial tails may also appear.

For a planar AdS-Schwarzschild black hole, conformality and dimensional analysis imply that $\Gamma_n(0) = f(0)T$, so any perturbation of the thermal state is effectively suppressed at $t = O(1/T)$ [82]. This behavior is not restricted to this simple example, however. The relaxation time is generically set by T in a strongly-coupled, large N gauge theory. For example, on supersymmetric mass deformations of $N = 2^*$ gauge theories, scalar operators also display relaxation times $O(1/T)$, with a proportionality factor with just mild T-dependence [83].

Global AdS-Schwarzschild black holes are endowed with a quasinormal frequency spectrum that shows more intrincate behavior than their planar counterparts [82][84]. For a horizon radius r_h such that $r_h \gg L$, it is also found that $\Gamma_n(0) \propto T$ by consistency with the planar case. However, for $r_h \ll L$, we have that $\Gamma_n(0) \propto r_h^2$: the absorption rate is

---

[30] We forget the indices from now on.

[31] Outgoing boundary conditions compute the advanced propagator.

[32] For instance, in global AdS only origin regularity is to be imposed on the solution.

[33] We assume that the fundamental quasinormal mode has the smallest imaginary part.

proportional to the black hole area, *i.e.*, to its scattering cross section. This is expected. In the $r_h \to 0$ limit, we must recover the global AdS result, where the quasinormal frequencies reduce to normal frequencies, with zero imaginary part. Therefore, $\Gamma(0)$ cannot be proportional to T, since the temperature of a small black hole is divergent in that limit. Also note that while, naively, one could expect to recover the asymptotically flat behavior in this $L \to \infty$ limit, this does not happen because the quasinormal mode spectrum depends crucially on the boundary conditions imposed at infinity.

Quasinormal modes associated to conserved currents are exceptions to the fast relaxation behavior. In this case, retarded correlators display *hydrodynamic poles*, *i.e.*, poles with a dispersion relation such that $\omega(\mathbf{k}) \to 0$ as $\|\mathbf{k}\| \to 0$. Consider such a conserved current and take a space-independent source $\phi_0(t)$, that we assume to be slowly-varying [50]. It is satisfied that

$$\delta_{\phi_0}\langle\mathcal{O}(t)\rangle = -\chi\partial_t\phi_0(t), \qquad (1.2.133)$$

where χ defines the transport coefficient associated to $\mathcal{O}$. Fourier transforming (1.2.133) we get

$$\delta_{\phi_0}\langle\mathcal{O}(\omega,0)\rangle = i\omega\chi\phi_0(\omega). \qquad (1.2.134)$$

This expression should be compared with the $\mathbf{k}=0$ version of (1.2.129). We observe that the low-frequency, zero-momentum behaviour of the retarded correlator determines the transport coefficient through the Kubo formula

$$\chi = -\lim_{\omega\to 0}\lim_{\|\mathbf{k}\|\to 0}\frac{\text{Im }G_R(\omega,\mathbf{k})}{\omega}. \qquad (1.2.135)$$

It possible to show [85] that, in a non-extremal black hole geometry with metric

$$ds^2 = g_{tt}dt^2 + g_{zz}dz^2 + g_{xx}\delta_{ij}dx^i dx^j, \qquad (1.2.136)$$

an operator $\mathcal{O}$ dual to a massless scalar bulk field φ with action

$$S[\varphi] = -\frac{1}{2}\int d^{d+1}x\sqrt{-g}\frac{\partial_\mu\varphi\partial^\mu\varphi}{q(z)} \qquad (1.2.137)$$

has an associated transport coefficient given by

$$\frac{\chi}{s} = \frac{4G}{q(z_0)}, \qquad (1.2.138)$$

where z_0 is the radius of the black hole and s its entropy density. In particular, by considering the transverse-transverse energy-momentum tensor correlator $G^R_{T_{xy}T_{xy}}$ in the state dual to the geometry (1.2.136), we get that the ratio of shear viscosity η and entropy density s of the dual field theory plasma is given by

$$\frac{\eta}{s} = \frac{1}{4\pi}, \qquad (1.2.139)$$

since in this case $q(z_0) = 16\pi G$.[34] This is the celebrated Policastro, Son and Starinets (PSS) result [86][87]. It indicates that, in a QFT whose dual description is provided by

---

[34] See the next item for a definition of the shear viscosity.

Einstein gravity,[35] in the large N, strong coupling regime an equilibrated plasma behaves almost as an ideal fluid. It does not matter that the holographic QFT in question is or is not conformal, confining, supersymmetric, or has additional chemical potentials. Above/but close to the QCD deconfinement transition, experimental results on the QGP shear viscosity show a value compatible with the PSS result, suggesting that the QGP formed is indeed a strongly-coupled, almost ideal fluid. This piece of experimental evidence is clear regarding the strongly-coupled nature of the QGP because, at weak-coupling, η/s would behave like [39]

$$\frac{\eta}{s} = \frac{A}{\lambda^2 \log \frac{B}{\sqrt{\lambda}}}, \tag{1.2.140}$$

and diverges as $\lambda \to 0$.[36]

Hydrodynamics in AdS/CFT: the fluid/gravity correspondence

Fluctuations that fall into the hydrodynamic regime can be described in terms of a nonlinear effective field theory (EFT): fluid dynamics. This description applies to any QFT state that achieves local thermal equilibrium, in the sense that, around each spacetime point x, there exist a mesoscopic region where the energy-momentum tensor T_{ab} agrees with the ideal fluid one, T_{ab}^{ideal}, up to derivative corrections. Therefore, fluid dynamics starts from the assumption that, at each x, we have that

$$T_{ab}(x) = \epsilon(x)u_a(x)u_b(x) + P(x)(g_{ab}(x) + u_a(x)u_b(x)) + \Pi_{ab}(x), \tag{1.2.141}$$

where $\epsilon(x)$ is the local energy density, $P(x)$ is the local pressure, and $u(x)$ is the local fluid velocity, which we assume to be normalized, $u(x)^2 = -1$. The fluid equation of state relates $P(x)$ and $\epsilon(x)$, $P(x) = P(\epsilon(x))$. As a consequence, the fluid energy-momentum tensor (1.2.141) depends on d independent quantities. The viscosity tensor Π_{ab} encodes the deviation from ideality and can be organized as a gradient expansion in terms of the local thermodynamical variables

$$\Pi_{ab} = \sum_k \Pi_{ab}^{(k)}(\epsilon(x), \nabla\epsilon(x), \ldots, u(x), \nabla u(x), \ldots), \tag{1.2.142}$$

where the k-th order viscuous correction, $\Pi_{ab}^{(k)}$, involves term with k derivatives. In the standard philosophy of EFT, $\Pi_{ab}^{(k)}$ has the form

$$\Pi_{ab}^{(k)} = \sum_j c_j \Pi_{ab}^{(k,j)}, \tag{1.2.143}$$

where, in principle, the only restriction to be imposed on $\Pi_{ab}^{(k,j)}$ is to be compatible with the underlying symmetries of the physical setup. The coefficient c_j is a transport coefficient. In

---

[35] In Einstein-Gauss-Bonnet gravity the bound depends on the Gauss-Bonnet coupling and can in fact be lower.

[36] At weak coupling, η/s is proportional to the ratio of the plasma quasiparticles mean free path and their average separation. At $\lambda = 0$, the mean free path diverges, so momentum can flow without being dissipated.

EFT, the precise value of the transport coefficients is left for experimental determination, since a first-principles computation of these quantities demands access to the underlying microscopical description of the system. However, as any other EFT, hydrodynamics must satisfy several consistency requirements. Imposing these allows restricting the form of the allowed transport coefficients. For instance, there must exist an entropy current J_s with semi-positive divergence

$$\nabla_a J_s^a \geq 0, \tag{1.2.144}$$

in agreement with the Second Law.

The dynamical constraint that the hydrodynamic expansion must satisfy is just energy-momentum conservation,

$$\nabla_a T^{ab} = 0, \tag{1.2.145}$$

which provides d equations that determine the d unkown variables in (1.2.141).

For a conformal fluid, the energy-momentum tensor is traceless, and the condition $T_a^a = 0$ provides the necessary equation of state. The first-order viscous correction is

$$\Pi_{ab}^{(1)} = \eta \sigma_{ab}, \tag{1.2.146}$$

where σ is the transverse, symmetric, traceless part of the velocity gradient ∇u. A suitable first-order entropy current can be constructed, in such a way that

$$\nabla_a J_s^a = \frac{\eta}{2T} \sigma_{ab} \sigma^{ab}, \tag{1.2.147}$$

which is positive definite iff $\eta \geq 0$. It is in this precise sense that the viscosity quantifies the deviation of a fluid from ideality, which corresponds to adiabatic flow.

It is natural to conjecture that, through the holographic dictionary, the counterpart of the CFT hydrodynamical regime are the of out-of-equilibrium, long wavelength fluctuations of the black holes representing the thermal equilibrium state. A fluid flow in a CFT can be described in terms of the local temperature, $T(x)$, and the local velocity, $u(x)$. When the flow reaches thermal equilibrium, these quantities become spacetime independent, and the fluid is ideal. The geometry corresponding to these situation is the boosted black brane metric [88]

$$ds^2 = -2u_a dx^a dr + r^2 (\eta_{ab} + (1 - f(r/\pi T))\, u_a u_b) dx^a dx^b. \tag{1.2.148}$$

A straghtforward computation of the energy-momentum tensor associated to this geometry indeed reveals that it has the ideal fluid form. In order to address the hydrodynamical regime, both T and u in (1.2.148) must be promoted to collective fields of the boundary coordinates, $T(x)$ and $u(x)$. The resulting metric would not be a solution of the Einstein equation. However, if $T(x)$ and $u(x)$ are slowly-varying,

$$T(x)^{-1} \partial_a \log T(x) = O(\epsilon), \qquad T(x)^{-1} \partial_a u_b(x) = O(\epsilon), \qquad \epsilon \ll 1 \tag{1.2.149}$$

we can introduce the ϵ-expansion

$$g_{AB} = \sum \epsilon^k g_{AB}^{(k)}(r, \epsilon x), \qquad T = \sum_k \epsilon^k T^{(k)}(\epsilon x), \qquad u_a = \sum_k \epsilon^k u_a^{(k)}(\epsilon x), \tag{1.2.150}$$

into the Einstein equation, and them solve it recursively order-by-order in ϵ.[37] Note that the construction assumes nothing about the amplitude of the original black hole perturbation: the effective linearization comes from the slow variance of the fields. Once the expansion (1.2.150) is solved to the desired order, the energy-momentum tensor, T_{ab}, can be computed by employing standard holographic renormalization techniques. The result is that T_{ab} has the fluid form (1.2.141)-(1.2.142) and can be expressed solely in terms of the original collective fields, $T(x)$ and $u(x)$. The conservation of T_{ab} is guaranteed by the nondynamical components of the Einstein equation, and provides a set of constraint equations that $u(x), T(x)$ must satisfy. These are the equations of fluid dynamics. As a final benefit, the transport coefficients c_j are automatically determined by this procedure. At first order, it is found again that $\eta/s = 1/(4\pi)$.

As we mention briefly at the end of subsection 1.2.2, the bulk geometry defined by a generic boundary energy-momentum tensor does not correspond automatically to an allowed state of the CFT. However, it is possible to show that if $T(x)$ and $u(x)$ have the form determined by the ϵ-expansion (1.2.150), singularities are shielded by event horizons, so cosmic censorship upholds. Remarkably, and despite their teleological character, the location of these event horizons can also be found locally in an ϵ-expansion. More importantly, pulling back the event horizon area density $d-1$-form to the boundary along infalling null geodesics results in an entropy current J_s^a with the right properties [89].

The construction we just described is known as the fluid/gravity correspondence. For reviews, see [90][91]. As it is clear from our previous discussion, this correspondence establishes a one-to-one map between admissible fluid flows and deformed planar black holes. At the theoretical level, it show that, for holographic CFTs, Einstein gravity can be thought of as the ultraviolet completion of hydrodynamics. This is an important observation, since it allows to establish the limits of validity of the hydrodynamic expansion. Rather than being controlled by *how large* the deviation from local thermal equilibrium is, the holographic perspective indicates that the approach to the hydrodynamic regime depends on *how fast* the dual black hole eats the massive, non-hydrodynamic quasinormal modes [92]. That this way of thinking describes well the underlying physics has been observed in numerical experiments of black hole formation, where low-order hydrodynamics becomes applicable even when the difference between longitudinal and transverse pressures is order one (*i*.e., in the presence of large gradients [93]) and has lead to a clear conceptual distinction between the *hydronamization* time and the thermalization time.[38]

A natural question is whether this picture is valid outside AdS/CFT or not. Is it a universal property of low-order hydrodynamics to be applicable in the presence of large gradients? Recent numerical simulations of weakly-coupled $SU(N)$ gauge theory on a dynamical geometry[39] show that, after a transient period, kinetic theory is well approached by low-order

---

[37] This quantity is a bookkeeping parameter that counts the number of spacetime derivatives and can be set to unity at the end of the computation.

[38] By low-order hydrodynamics, we refer to keeping only the first or second gradient correction in the viscosity tensor (1.2.142).

[39] The initial state of the system is chosen to be a thermal state; the dynamical geometry interpolates

hydrodynamics, even while gradients remain large [94].

In AdS/CFT, the transient modes that determine the onset for the validity of the hydrodynamic gradient expansion are well identified: they correspond to the dual black hole massive quasinormal modes. Quite remarkably, the existence of these modes can be inferred from the hydrodynamic gradient expansion herself, as originally shown in [95] for conformal, boost-invariant holographic fluid flows. Just as it happens in perturbative QFT, this expansion is an asymptotic series with zero radius of convergence. It is possible to prove that the large-k divergence of the series coefficients is controlled by the first non-hydrodynamic quasinormal mode: its frequency can even be computed from these coefficients by using resurgence and transseries techniques. Applying a similar analysis to weakly-coupled hydrodynamics leads to the same structure [96]: the hydrodynamic series is still asymptotic, and its divergence still indicates the presence of extra, exponentially-damped modes. The decay of these transient modes is to be held responsible for reaching the hydrodynamic regime; the size of the gradients plays no role in the discussion again. In this way, the validity of the low-order hydrodynamic expansion outside its naive domain of application matches a similar phenomenon familiar from the work with asymptotic series in quantum theory.

This digression is a wonderful example of how AdS/CFT can be a fruitful source of physical insight about open problems in other disciplines. At a more practical level, it is worth mentioning that the fluid/gravity construction can be employed to build the hydrodynamics of charged fluids, or even superfluids. The starting point is replacing the boosted black brane (1.2.148) by the corresponding AdS-Reissner-Nordstrom or hairy solution. This procedure has allowed obtaining, even in first-order hydrodynamics, new terms that were missed in standard pre-fluid/gravity studies.

Having discussed briefly what holography has to teach us about near-equilibrium physics at strong coupling, let's move on to the analysis of the fully out-of-equilibrium regime.

1.2.7 Far-from-equilibrium physics in holography: the flat case

Studying how generic perturbations of a given equilibrium state in a holographic CFT evolve requires mastering Einstein gravity in its fully nonlinear regime. Analytical tools are doomed: our understanding can only be upheld by new approximation schemes. Two major approaches can be distinguished:

- Thin shell spacetimes
- Numerical holography

The specific kind of problems that have been undertaken by employing these techniques includes, but is not restricted to:

---

between Minkowski space at $t = 0$, and a spacetime with an expanding x^i direction ($g_{ii}(t) \sim t^2$) at late times.

- **Holographic quenches**

  In a holographic CFT, a quantum quench admits a relatively simple bulk description. A fast variation in the field theory Hamiltonian can be traded for a Lagrangian deformation of the form (1.2.80), which we recall now

  $$\mathcal{L}_{CFT} \to \mathcal{L}_{CFT} + \phi_0 \mathcal{O}.$$

  A local quench is implemented by a boundary source ϕ_0 sharply located in space and time, $\lim_{|x^a|\to\infty} \phi_0(x) = 0$, $\lim_{|t|\to\infty} \phi_0(x) = 0$, while a global quench corresponds to a translationally-invariant ϕ_0 profile sharply located in time. Typically,[40] ϕ_0 sources an infalling pulse of its corresponding bulk field, which propagates inward from the boundary, until it crosses its Schwarzschild radius and a black hole forms. This highly excited black hole then relaxes, in such a way that its equilibration process models the field theory entering into the hydrodynamic, linear response and static regimes. The whole thermalization process can be monitored with the help of the AdS/CFT dictionary, which prescribes how different observables such as one-point functions or entanglement entropies are to be computed.

  Different quenching processes of physical interest can be assembled by choosing both the initial CFT state and the deformation (1.2.80) judiciously. Over the vacuum, couplings to various operators have been considered: the energy-momentum tensor [97] and marginal or relevant scalar operators [98][99]. Scalar quenches over a thermal state have been addressed in [100][101][102] at the perturbative level. Quenches across finite-temperature critical points have also been extensively studied [103].

- **Holographic boost-invariant flow and shockwave collisions**

  The quick approach to the hydrodynamic regime observed experimentally in the QGP calls for a holographic understanding. The gravitational quench studied in the pioneering work of Chesler and Yaffe [97] paved the way for more involved models of far-from-equilibrium plasma formation and relaxation. These include studies of boost-invariant plasma flows [93, 104] or shockwave collisions [105, 106], and have been historically focused on the question of how fast the hydrodynamization process at strong-coupling is. These studies have already inspired highly nontrivial results in formal hydrodynamics, as we commented in the previous item of this section.

- **Holographic turbulence**

  The existence of the fluid/gravity correspondence suggests that the turbulence phenomenon, familiar from standard fluid dynamics, should have a counterpart in the holographic context. It has indeed been found [107], and brings surprising features such as fractal-like horizons.

---

[40] For instance, in planar holographic CFTs.

In this subsection, we focus on the results that have been obtained regarding HEE propagation in holographic quenches with planar asymptotics. Gravitational collapse in global AdS, being the main subject of this thesis, would be separately introduced in the next section.

Time-dependent horizons and thermodynamical entropy

As a previous overall comment, it is worth noting that there exist several horizon notions in black hole physics which, despite agreeing at thermal equilibrium, need not do so generically. The event horizon, defined in our case as the boundary of the causal past of future timelike infinity, cannot be determined locally in a generic time-dependent metric by any means. Diagnosing black hole formation in a numerical experiment requires considering the apparent horizon instead. The apparent horizon, on a given spacelike slice, is the outermost trapped surface present in the spacetime, and it is defined as the codimension-two hypersurface for which the expansion of an orthogonal, outgoing and future-directed congruence of null geodesics vanishes. Given a congruence $l(x)$, finding the apparent horizon amounts to determining which x solve the equation $\nabla_\mu l^\mu(x) = 0$, which is a local statement. Once this hypersurface is found, a classic theorem in black hole mechanics guarantees that it is inside the true event horizon, as long as suitable energy conditions hold [108].

Before the discovery of the HEE formula, there could be some room for doubting which is the correct notion of entropy that applies in a far-from-equilibrium holographic CFT. It is worth remembering now that the laws of black hole thermodynamics are meant to work solely in near-equilibrium situations and that while, by the Area Theorem, the event horizon cross-sectional area density is non-decreasing along its null generators, identifying it directly with the actual CFT entropy density through the Bekenstein-Hawking formula is problematic. Consider a translationally invariant state. First, at a given boundary time t, and within the Wheeler-DeWitt patch associated with this boundary slice, different bulk spacelike slices would have different entropy densities at the event horizon, so there is no univocally defined way of selecting the correct one. Even if we made the natural choice of picking up the maximum one, there is also no univocally defined way of pullbacking it to the boundary. Moreover, even if we also made the natural choice of pullbacking it along the associated infalling null geodesic, we still face two problems. First, as the conformal soliton example shows [109], the entropy density defined in this way can even be diverging. Second, and at a conceptual level, due to the nonlocal nature of the event horizon, the CFT entropy density as we have defined it does not only depend on the CFT state at time t but also on its entire future evolution. As a slogan, we can say that the entropy density of our system *today* would depend on whether, for instance, we decide to quench the system *tomorrow*.

This situation is completely changed with the advent of the HEE formula, since it provides a coordinate independent way of computing a particular notion of entropy in quantum physics that is well defined in time-dependent situations and, more importantly, just depends on the Wheeler-DeWitt patch associated with the boundary slice at time t.

Holographic propagation of entanglement entropy from thin shell spacetimes

In order to study HEE in time dependent situations, thin shell spacetimes have been widely employed as simplified models of gravitational collapse. This is because they provide semi-analytically known backgrounds that alleviate the task of computing nonlocal observables. Although useful, thin shell spacetimes rely on drastic simplifications of the physical setup. Results obtained within this framework must be compared with the ones coming from realistic constructions.

The simplest known model of a spacetime undergoing gravitational collapse is the Vaidya metric[41]

$$ds^2 = -f(v,r)dv^2 + 2dvdr + r^2 d\vec{x}^2, \qquad f(v,r) = \left(r^2 - \frac{m(v)}{r^{d-2}}\right) \tag{1.2.151}$$

that describes an infalling pulse of pressureless radiation -null dust-, with energy-momentum tensor

$$T_{ab} = 2(d-1)\frac{\dot{m}(v)}{r^{d-1}}\delta_{av}\delta_{bv}. \tag{1.2.152}$$

The null energy condition demands that $\dot{m}(v) \geq 0$, otherwise, this function is completely free. For instance, by taking

$$m(v) = m\Theta(v), \tag{1.2.153}$$

we are modelling an instantaneous energy injection on the AdS vacuum at $v = 0$, that results in an infalling shockwave in the bulk. Inside the shockwave, spacetime is still planar AdS; outside, it reduces to the AdS-Schwarzshild solution, due to Birkhoff's theorem. Eventually, the shockwave crosses its Schwarzschild radius and a black hole forms.

This collapsing background is dual to an instantaneous global quench over the CFT vacuum. In particular, the CFT energy-momentum tensor reaches its final equilibrium value just after the quench, so the fact that the post-quench state is still not thermal can only be distinguished by nonlocal probes.

The study of these nonlocal probes was started in [26][111][112]. Remarkably, in the three-dimensional case, it was shown that the HEE evolution reproduces the post-quench EE evolution originally computed by Calabrese and Cardy for a single interval. The horizon effect they observe is still present, and in this example entanglement propagates as if it were carried by free-streaming quasiparticle pairs, even if we are in a strongly-coupled field theory.[42]. It has also been possible to employ the three-dimensional Vaidya model to analyse the propagation of the mutual and tripartite information [113][114]. While the mutual information displays a characteristic peak expected from the quasiparticle picture, the holographic tripartite information results do not agree with this free-streaming model. This is because

---

[41] For scalar field collapse in planar AdS, the Vaidya metric is the leading order contribution to the total spacetime metric in a low-energy expansion [110].

[42] Note that the Vaidya model represents a global quench over the vacuum state of a CFT which, contrary to the Calabrese and Cardy initial state, has long-range entanglement. The quasiparticle model of [22] can be modified to take this fact into account [26]

it is imposible to entangle three regions with only EPR pairs.

Higher-dimensional thin shell Vaidya models were also considered in [115][116], where the different regimes of entanglement propagation were thoroughly discussed in any dimension. Take our entangling surface A to be of arbitrary shape -unless said otherwise-, define R to be the height of its future domain of dependence, and focus on the EE difference between the quenched state and the initial state at time t, $\Delta S_A(t) = S_A(t) - S_A(t=0)$. The system also has an intrinsic local equlibration scale l_{eq}, after which the production of thermodynamical entropy is stopped, $l_{eq} \sim s_{th}^{1/(d-1)} \sim \beta$. For entangling regions such that $R \gg l_{eq}$, the different regimes found are the following:

- Pre-local-equilibration growth. For $t \ll l_{eq}$,

$$\Delta S_A(t) = \frac{\pi}{d-1} \epsilon \mathrm{Vol}(\partial A) t^2 + ..., \tag{1.2.154}$$

  where ϵ is the local energy density.

- Post-local-equilibration linear growth. For $R \gg t \gg l_{eq}$,

$$\Delta S_A(t) = v_E s_{th} \mathrm{Vol}(\partial A) t + ..., \tag{1.2.155}$$

  where v_E is a dimensionless constant independent on the shape of A, but dependent on the final equilibrium state,

$$v_E = \frac{(\eta-1)^{\frac{1}{2}(\eta-1)}}{\eta^{\frac{1}{2}\eta}}, \qquad \eta = \frac{2(d-1)}{d}. \tag{1.2.156}$$

  In particular, $v_E = 1$ for $d = 2$, as expected.

- Saturation. Eventually, $\Delta S_A(t)$ saturates to its value at thermal equilibrium,

$$\Delta S_A(t > t_s) = s_{th} \mathrm{Vol}(A). \tag{1.2.157}$$

  For a strip, linear growth persists up to the saturation time $t_s = R/v_E + O(R^0)$, where $\Delta S_A(t)$ has a discontinuous first derivative. For a sphere, the saturation time is $t_s = R/c_E - (d-2)/4\pi\beta \log R + O(R^0)$, with $c_E = \eta^{-\frac{1}{2}}$. At times $t_s - t \ll l_{eq}$, $\Delta S_A(t)$ approaches its thermal value like in a continuous phase transition, with a characteristic exponent $\gamma = (d+1)/2$, $\Delta S_A(t) - s_{th}\mathrm{Vol}(A) \propto -(t_s - t)^{\gamma}$. The only exception happens in $d = 3$, where an additional $\log(t_s - t)$ modulation appears.

- Late-time memory loss. For a sphere, between post-local equilibration growth and saturation, and additional regime appears for times $t_s \gg t_s - t \gg l_{eq}$. In this regime, $\Delta S_A(t) - s_{th}\mathrm{Vol}(A) = -s_{th}\lambda(t_s - t)$ for some function λ that depends both on l_{eq} and on the difference $R - t$, but not on t and R separately.

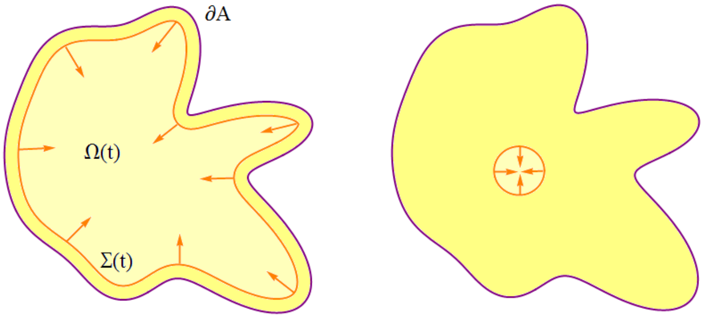

Figure 1.3: Cartoon of the entanglement tsunami for an entangling region of arbitrary shape. Left: post-equilibraton linear growth. Right: late time saturation.

As a physical interpretation of these results, the authors of [115][116] proposed the so-called *tsunami picture*. The crucial observation is that, after local equilibration, the three regimes of entanglement propagation just described can be subsumed into the expression

$$\Delta S_A(t) = s_{th}(\mathrm{Vol}(A) - \mathrm{Vol}(\Omega(t))). \qquad (1.2.158)$$

Therefore, we can imagine that entanglement propagates inwards from ∂A as a sharp wavefront $\Sigma(t)$, in such a way that the region already covered by this wavefront, $A - \Omega(t)$, is entangled with $\bar{A}$, while the region to-be-covered, $\Omega(t)$, is yet to-be-entangled. Just after the quench, the tsunami builds up, until the moment when local equilibration is attained; afterwards, it propagates freely with speed v_E. For a strip, this continues to be the case up to saturation. For a sphere, note that the tsunami speed cannot be equal to v_E up to saturation, since that would imply that $t_s = R/v_E$, which is greater than the actual saturation time $t_s = R/c_E + ...$, as $c_E \geq v_E$. This difference can be understood as an effect of the nontrivial selfinteraction of the entanglement wavefront, that now propagates non-freely. The late-time memory loss expression reduces to a particular case of (1.2.158) if we identify $\lambda(t_s - t)$ with the volume of $\Omega(t)$. In particular, the fact that this volume does not depend explicitly on R suggests that, given an arbitrary entangling surface, the information about its size and shape is going to be forgotten at sufficiently late times, but well before saturation.[43] Finally, sufficiently close to saturation we must have that $\lambda(t_s - t) \sim (t_s - t)^\gamma (d \neq 3)$, $(t_s - t)^2 \log(t_s - t)(d = 3)$. A natural question to ask is if an effective model of how the tsunami propagates can be devised.

The tsunami speed v_E was also computed in more general Vaidya-like geometries; for example, with finite charge.[44] After the local equilibration time, it was always found that the entanglement propagation rate, which can be quantified by the dimensionless ratio

$$\mathcal{R}_A(t) = \frac{1}{s_{th}\mathrm{Area}(\partial A)} \frac{dS_A(t)}{dt}, \qquad (1.2.159)$$

---

[43] Geometrical data defining ∂A of course determine t_s; the point is that, in the late-time memory loss regime, we cannot distinguish the tsunamis associated with two surfaces with different shapes but the same t_s.

[44] We discuss the four-dimensional charged Vaidya geometry in chapter 5.

was less or equal than (1.2.156), which is the value in a final Schwarzschild black hole geometry,

$$\mathcal{R}_A(t) \leq v_E^{(S)} \equiv \frac{(\eta-1)^{\frac{1}{2}(\eta-1)}}{\eta^{\frac{1}{2}\eta}}. \tag{1.2.160}$$

This observation lead the authors of [115][116] to speculate that perhaps (1.2.160) is an upper bound for $\mathcal{R}_A(t)$ in QFT, at least for entangling regions such that $R/l_{eq} \gg 1$.

Within the thin shell approximation, the bound (1.2.160) was shown to be robust in [117][118] for $d = 4$. In these works, homogeneous planar shells with timelike trajectories were considered. These shells were made of a perfect fluid with a linear equation of state, $p = c\sigma$ -p and σ are the shell's pressure and energy density, respectively-. As we are going to review in chapter 4, the shell trajectory, $r = r_s(v)$, is obtained from the Israel junction conditions, which guarantee that Einstein's equations are well defined in a distributional sense. Birkhoff's theorem demands then just to perform the change $\Theta(v) \to \Theta(r - r_s(v))$ in (1.2.153) to obtain a solution to Einstein's equations. The shell must be released from an initial radial position $r_s(0)$, and the authors of [117][118] choose to do it with zero initial speed. Therefore, at early times and in terms of the shell comoving time τ, the shell trajectory is $r_s(\tau) = r_s(0) - 1/2a\tau^2 + ...$ Its acceleration a determines the pre-local-equilibration growth of the EE through a relation of the form

$$\Delta S_A(t) = F(r_s(0), f(r_s(0)), a)\epsilon \text{Vol}(\partial A)t^2 + ..., \tag{1.2.161}$$

so the Vaidya result gets modified in a complicated way, but the pre-local equilibration quadratic growth stands. For a strip, and in the $r_s(0) \to \infty$ limit, it is found that $F = 3\pi(1 + c) + ...$, so there is a well-defined way in which the shell equation of state is dual to the initial acceleration of the entanglement wavefront. At sufficiently late times, the shell trajectory, independently of its equation of state and initial position, approaches a null geodesic. In consequence, the Vaidya result $\mathcal{R}_A(t) = v_E^{(S)}$ is reproduced.

Further evidence in favor of the tsunami picture can be found in [119]. For the three-dimensional Vaidya metric, and in the case where the entangling interval is disconnected, the actual holographic computations of entanglement propagation are in conflict with the predictions of free-streaming quasiparticle models but, however, agree with the tsunami picture.

The bound (1.2.160) has not yet been proven from first principles in the context of QFT. At most, it has been possible to show that, after local equilibration, the tsunami speed v_E is constrained by causality

$$v_E \leq 1. \tag{1.2.162}$$

This has been achieved by employing information-theoretical arguments based on the positivity of mutual information [120] or the monotonicity of relative entropy [121].[45] Notice that the result is remarkable, in the sense that, in principle, v_E does not correspond to a *physical* speed, so there is no apparent reason for it to satisfy the bound (1.2.162), other

---

[45] We discussed the definition and physical meaning of these quantities in section 1.1.

than that entanglement should be carryed around by physical excitations. More robustly, it has been proven that, in $d > 2$ dimensions, the bound (1.2.160) cannot be accounted for quasiparticle-based models à la Calabrese and Cardy [120]. Assuming that the quench at $t = 0$ generates a sea of entangled quasiparticle pairs, which then propagate freely with unit speed, the velocity of the entanglement wavefront is bounded by

$$\mathcal{R}_A(t) \leq v_E^{\text{free}} = \frac{\Gamma(\frac{d-1}{2})}{\sqrt{\pi}\Gamma(\frac{d}{2})}, \tag{1.2.163}$$

so for $d > 2$, $v_E^{\text{free}} < v_E^{(S)}$. At $d = 2$, both speeds coincide and saturate the bound provided by causality, $v_E^{\text{free}} = v_E^{(S)} = 1$. Including quasiparticle interactions in these free-streaming models is mandatory in order to see how $\mathcal{R}_A(t)$ changes with respect to the conjectured holographic bound.

Holographic propagation of entanglement entropy from realistic quenches

The results obtained from thin shell descriptions of gravitational collapse must be checked against less restricted models of black hole formation. In contrast to the Vaidya case, realistic holographic quenches correspond to the injection of some bulk matter distribution with nontrivial selfinteraction. Pressure is now naturally incorporated into the problem and the quench, although fast, is not instantaneous. The question of how entanglement propagates in these novel backgrounds must be addressed, so as to determine in which degree the description provided by the tsunami picture is universal.

We are discussing two selected examples in detail. They correspond to two different quench processes, originally analyzed in [103] and [97]. The HEE propagation in these dynamical backgrounds was studied in [122] and [123] respectively. The motivation behind discussing in depth ref. [103] stems from the fact that we are making contact with it in chapter 5. On the other hand, the motivation behind discussing ref. [97] is the historical importance of this work, as it can be regarded as one of the founding papers of Numerical Holography.

Our first example is the thermal quench studied in [103]. Here, a four-dimensional planar hairy black hole was perturbed by the action of a Gaussian boundary source, ϕ_0, conjugate to a condensed tachyonic scalar, ϕ. At fixed quench duration τ, and depending on the source amplitude δ, three different regimes were found in the late-time dynamics of the scalar vev $|\langle\mathcal{O}\rangle|$:

- For $\delta_c < \delta$, the system underwent overdamped relaxation to the normal phase, *i*.e. the final equilibrium state was a Reissner-Nordstrom black hole (regime a).

- For $\delta_* < \delta \leq \delta_c$, the system underwent overdamped relaxation to a new superfluid phase,*i*.e. the final equilibrium state was a hairy black hole (regime b).

- For $\delta \leq \delta_*$, the system underwent underdamped relaxation to a new superfluid phase (regime c).

The scale δ_c corresponds to final states such that their temperature is above the critical temperature for the normal-superfluid transition, $T > T_c$. The new scale δ_* is related to a new temperature scale T_*, that would provide a finite-temperature and collision-dominated analog of the collisionless Landau damping transition observed in BCS superconductors. Note that the three relaxation regimes can be subsumed into a relation of the form

$$\|\langle \mathcal{O}(t)\rangle\| \sim \|\langle \mathcal{O}\rangle_f + Ae^{-i\omega_0 t}\|, \tag{1.2.164}$$

where $\|\langle \mathcal{O}\rangle_f\|$ is the vev in the final equilibrum state reached, and ω_0 the lowest quasinormal mode frequency, which should be the only surviving contribution at sufficiently late time.

By virtue of the relation above, the existence of the new scale T_* can be inferred by analyzing the final black hole quasinormal modes. Time-reversal invariance implies that quasinormal frequencies appear in pairs, symmetric with respect to the imaginary axis

$$\omega \leftrightarrow -\omega^*. \tag{1.2.165}$$

As we mentioned in the previous section, the system's response being causal implies that $\mathrm{Im}(\omega) \leq 0$. Thus, the late-time dynamics is governed by the quasinormal frequency pair with the smallest imaginary part. What happens to this pair?

Since at $T = T_c$ the global $U(1)$ symmetry of the dual field theory is spontaneously broken, this pair coalesces at $\omega = 0$, signaling the appearance of a Goldstone mode associated to this breaking.

Into the superfluid phase, one member of the pair must stay at $\omega = 0$. This is the so-called phase mode, associated to the spontaneous breaking of the U(1) symmetry. It corresponds to a hydrodynamic mode. As this new superfluid phase is a stable quantum state, the only possibility compatible with causality and the symmetry (1.2.165) is that the other member of the pair becomes purely imaginary. This is the so-called amplitude mode. It turns out that, upon progressively lowering the temperature below T_c, this quasinormal frequency travels down the imaginary axis. Eventually, this purely imaginary quasinormal frequency has the same imaginary part as the next excited quasinormal mode pair, signaling the transition in $\|\langle \mathcal{O}\rangle\|$ from overdamped to underdamped relaxation. This sets the new scale T^*.

The existence of the new scale T_* is thus universal, since it could appear in any translationally invariant system with a spontaneously broken continuous symmetry. In chapter 5, we will provide evidence in favor of the existence of this universal phenomenon in holographic superfluids at finite volume.

The behavior of the EE in the system just described was considered in [122], where the entangling region A was taken to be a strip of lenght $2L$. The major results were:

- In the pre-local equilibration regime, and independently of the quench amplitude δ and the strip width, $\Delta S_A(t)$ was found to violate the quadratic growth observed in the Vaidya case. Instead, a dip appeared. $\Delta S_A(t)$ first decreased until it reached a negative minimum, after which quadratic growth followed. Therefore, at sufficiently short times, and rather counterintuitively, entanglement seemed to be expelled from A.

- The post-local equilibration regime still exists. For sufficiently large strips, and as δ augmented, the tsunami speed raised from zero, at $\delta = 0$, and increased monotonically up to a L-dependent saturation value $v_E^{\rm s}(L)$, reached in the $\delta \to \infty$ limit. This bound on the tsunami speed decreases with L and always respects the relation $v_E^{\rm s}(L) < v_E^{(S)}$.

- The linear growth regime is abandoned at a time t_p at which $\Delta S_A(t)$ is continuous but non-differentiable in the relaxation regimes a and b we discussed before, *i.*e., if $\delta > \delta*$. After this time, $\Delta S_A(t)$ increases monotonically to its final thermal equilibrium value for $\delta \geq \delta_*$, while for $\delta < \delta_*$ this approach is non-monotonic and displays weak oscillations. This behavior is not surprising if we take into account that the late-time dynamics of the system, and in particular of its metric tensor, is controlled by the fundamental quasinormal frequency of the final state. Therefore, the EE should behave in the same way as the scalar vev.

Taken together, these results validate both the tsunami picture, at least in the post-local equilibration linear growth regime, as well as the bound (1.2.160). The subsequent evolution of $\Delta S_A(t)$ is indeed more involved than its simple Vaidya counterpart. For example, and within the tsunami picture, any damped oscillation of $\Delta S_A(t)$ before reaching its final equilibrium value must be originated by a $\Omega(t)$ that pulsates as it shrinks exponentially: due to its selfinteraction, the entanglement wavefront must show some resistance to contracting.

A drawback of this holographic quench is that it relies on the existence of a specific scalar sector in the bulk theory. Universal results pertaining any holographic CFT can be obtained, however, by restricting ourselves to the gravitational sector alone.

Gravitational quenches were first addressed by Chesler and Yaffe in their seminal work [97]. These authors considered that the background metric h_{ab} where the CFT is placed undergoes a time-dependent shear deformation

$$dh^2 = -dt^2 + e^{B_0(t)}(dx^2 + dy^2) + e^{-2B_0(t)}dz^2, \tag{1.2.166}$$

$$B_0(t) = \frac{1}{2}c\left(1 - \tanh(t/\tau)\right), \tag{1.2.167}$$

while keeping translational invariance and rotational symmetry in the transverse (x, y) plane. These symmetries imply that the bulk metric can be written as

$$ds^2 = -A(v,r)dv^2 + \Sigma(v,r)\left(e^{B(v,r)}(dx^2 + dy^2) + e^{-2B(v,r)}dz^2\right) + 2drdv, \tag{1.2.168}$$

and is subjected to the boundary condition $r^{-2}g_{AB}\delta^A_a\delta^B_b \to h_{ab}$ as $r \to \infty$. In the Eddington-Finklestein coordinate system chosen, the Einstein equation decomposes into a nested system of nonlinear ODEs.[46] The initial state at $t \to -\infty$ is taken to be the Poincarè patch and, as usual, the final state at $t \to \infty$ corresponds to a Schwarzschild black brane of temperature T, formed by the collapse of the gravitational wave sourced by the time-dependent boundary metric. The original focus of [97] was to determine how fast the pressure gradient

---

[46] Solving numerically the Einstein equation in this way has become the standard method to study gravitational collapse in planar AdS [124] and was, in particular, how the thermal quench we previously discussed was addressed.

$P_x(t) = P_y(t) \neq P_z(t)$ induced by the quench isotropized. The answer was that fast relaxation upholds, in the sense that the isotropization time is of the form $t_{\text{iso}} = O(1)/T$. This fast relaxation is consistent with the behavior found experimentally for the QGP.

The behavior of the HEE in this quench was addressed in [123], for strips as entangling surfaces. Due to the symmetries of the geometry, there exist two different cases: i) strips where the finite interval of length $2L$ lies along the transverse (x,y) plane and ii) strips where the finite interval of length $2L$ lies along the longitudinal z direction. Technical reasons limit computing HEE in this gravitational collapse background: the interior of the apparent horizon must be excised from the numerical solution, and entangling surfaces tend to penetrate it. Therefore, the $L \gg l_{eq}$ limit where the tsunami picture should uphold could not be directly accessed. Nevertheless, for sufficiently large strips, evidence of both a linear growth regime and a saturation time increasing with L was found. In every case analyzed in [123], it was observed that the HEE approached non-monotonically its thermal equilibrium value, with damped oscillations set by the lowest quasinormal mode of the final black hole. The main difference between longitudinal and transverse strips is that their HEE is in phase-opposition in this ringdown regime.

A question that remains is if the quasinormal ringdown of the HEE would persist in the $L \gg l_{eq}$ limit or, on the other hand, is a genuine finite size effect. This observation is a particular instance of a drawback common to the two examples we have analyzed: at present, we don't know if the deviations from the tsunami picture discovered in these examples are genuine, or rather correspond to finite size effects. Further numerical experiments are called for, so as to disentangle the finite size effects associated to strips with $L \gtrsim l_{eq}$ and potential deviations from the tsunami picture when $L \gg l_{eq}$.

1.3 Gravitational collapse in global AdS

Studying gravitational collapse in asymptotically global AdS_{d+1} spacetimes is the major subject of this thesis. Before reviewing the state-of-the-art of this corner of the AdS/CFT landscape, let us remark some facts briefly.

Firstly, as the existence of the Hawking-Page transition vividly exemplifies, new physical phenomena may arise when considering a CFT_d at finite volume. As we are discussing in this section, this is a general fact not restricted to the equilibrium regime.

Secondly, to draw universal lessons about the dynamics of an out-of-equilibrium CFT_d at finite volume, we must restrict ourselves to the study of gravitational perturbations of global AdS_{d+1}. In the nonlinear regime, addressing this problem in full generality requires mastering pure Einstein gravity in a highly non-symmetric situation, that is currently beyond computational reach. Simplifying assumptions are called for; commonly, we are considering only rotationally-invariant states. As gravitational waves carry no monopolar mode, assuming rotational invariance erases any nontrivial bulk dynamics unless a consistent supergravity truncation that carries additional scalar fields is considered. Universality is lost. In principle, the results obtained within this approach pertain exclusively to a *particular* CFT_d.

Thirdly, and as a consequence of the second point, if we are interested in obtaining general results, any new phenomenon we might identify must be critically examined. It must be checked whether the physical mechanism responsible for it is also present in the gravitational sector or, at least, does not depend on the particular form of the scalar action. In particular, any physical process that depends fundamentally on the assumed spherical symmetry of the problem would hold only in a zero-measure set of the gravitational theory phase space. The slightest deviation from spatial homogeneity would eliminate it.

A fact related to this last observation makes up the final point we should emphasize. In top-down AdS/CFT constructions, the bulk spacetime takes the form $\mathrm{AdS}_{d+1} \times X$, where X is an internal compact manifold, such that its isometry group encodes a global symmetry group of the dual CFT_d. We have already encountered an example of this: in the original Maldacena duality, $X = S^5$ encodes the $SU(4)$ R-symmetry group of the $\mathcal{N} = 4$ SUSY YM theory. In the planar constructions we reviewed in the previous section, we were secretly considering states with zero R-charge and, as a consequence, gravitational backgrounds homogeneous in X. This assumption, although harmless in the planar case, is non-trivial in the global one.

In global $\mathrm{AdS}_{d+1} \times X$, assuming homogeneity in X could imply that, at a given energy, the black hole state reached after a process of gravitational collapse might not be the preferred state in the corresponding microcanonical ensemble. Take the $AdS_5 \times S^5$ case as an example. It is possible to show that, below a horizon radius $r_{+,c} = 0.4402L$, five-dimensional Schwarzschild black holes, smeared over the S^5, are unstable to localizing on the S^5, forming eventually a ten-dimensional Schwarzschild black holes [125][126]. This linear instability, known as the Gregory-Laflamme instability [127], is present for $r \leq r_{+,c}$: the five-dimensional smeared black hole background has an unstable gravitational mode on the S^5, with positive imaginary part.[47] The caveats we expressed regarding our previous assumption of spherical symmetry apply in this case even in a more painful way. Even if we were able to master the nonlinear evolution of gravitational waves in global AdS_{d+1}, overlooking the slightest perturbation of the internal manifold might render the whole process we are interested in (and have struggled to simulate) irrealistic. Perhaps, when departing from the particular submanifold of the phase space we are artificially putting ourselves in, the evolution of the system proceeds in an entirely different fashion.

As in any unstable system, the relevance of the Gregory-Laflamme instability is a matter of the time scales involved in the gravitational collapse process. Let M_c be the mass below which the five-dimensional Schwarzschild black hole becomes Gregory-Laflamme unstable. Take initial data with $M \leq M_c$, homogeneous in X, and add a nontrivial perturbation of X of norm $O(\epsilon)$, with $\epsilon \ll 1$. Now, let t_c be the time needed to form a five-dimensional Schwarzschild black hole when $\epsilon = 0$ and t_{GL} the time necessary for the Gregory-Laflamme

---

[47] The particular value of $r_{+,c}$ implies that large, five-dimensional, Schwarzschild black holes are immune to this instability, a conclusion that extrapolates directly to planar black holes upon scaling.

instability to fully develop (in the sense that the X perturbation grows from being $O(\epsilon)$ to being $O(1)$). There are two limiting situations:

- $t_{GL} \ll t_c$. The collapse process would produce a ten-dimensional Schwarzschild black hole on the time-scale t_{GL}; the breaking of the CFT$_d$ internal symmetry group happens right away.

- $t_c \ll t_{GL}$. The collapse process would result in an intermediate metastable state, which barely breaks the CFT$_d$ internal symmetry group. Full breaking and final thermalization of the theory happen on the longer time-scale t_{GL}. In this regime, the formation of a five-dimensional smeared Schwarzschild black hole corresponds to a pre-thermalization of the theory.

With these four caveats in mind, let us address now the current state of gravitational collapse in global AdS$_{d+1}$. The vast majority of the recent research on the subject focuses on spherically symmetric spacetimes and employs scalar fields as sources for the dynamics. We shall review non-exhaustively notable works in this area, commenting finally on what is known about the purely gravitational case.

1.3.1 The AdS instability problem

Among the three different maximally symmetric spacetimes, both Minkowski and de Sitter were shown to be nonlinearly stable in the past decades [128][129]. Nonlinear stability here means that small perturbations -again, in some appropriate norm, with a certain degree of analicity- remain forever small under time evolution. The issue of the nonlinear stability of global AdS remained open until the year 2011, when it was first addressed by Bizon and Rostworowski in their seminal work [130].

These authors considered a masless scalar field ϕ in an asymptotically AdS$_4$ geometry. For future reference, let us quote the action, ansatz and equations of motion for any d. The Einstein-scalar action is[48]

$$S = \frac{1}{2}\int d^{d+1}x\sqrt{-g}\left(R + d(d-1) - (\partial\phi)^2\right). \tag{1.3.169}$$

The scalar field energy-momentum tensor is given by

$$T^{\phi}_{\mu\nu} = \partial_\mu\phi\partial_\nu\phi - \frac{1}{2}g_{\mu\nu}(\partial\phi)^2, \tag{1.3.170}$$

and the equations of motion the system must satisfy are

$$G_{\mu\nu} - \frac{d(d-1)}{2}g_{\mu\nu} = (d-1)T^{\phi}_{\mu\nu}, \tag{1.3.171}$$
$$\Box\phi = 0. \tag{1.3.172}$$

---

[48] Unless stated otherwise, in this section we work with units such that $L = 1$, $8\pi G = d - 1$.

When restricting to spherically symmetric spacetimes, a suitable metric ansatz is provided by

$$ds^2 = \frac{1}{\cos^2(x)}\left(-f(t,x)e^{-2\delta(t,x)}dt^2 + f(t,x)^{-1}dx^2 + d\Omega^2_{d+1}\right), \tag{1.3.173}$$

in such a way that global AdS_{d+1} corresponds to $f(t,x) = 1, \delta(t,x) = 0$, while an AdS_{d+1} Schwarzschild black hole to $f(t,x) = 1 - M\cos(x)^d \sin(x)^{2-d}, \delta(t,x) = 0$. The ansatz (1.3.173) does not fix completely the gauge freedom of the system: there exists a residual one-parameter family of diffeomorphisms that leave the ansatz (1.3.173) invariant, but change the physical meaning of the coordinate t. This residual freedom is fixed by specifying at which spatial point $\delta(t,x)$ vanishes. The two common choices are the *origin time gauge*, where $\delta(t,0) = 0$, and the *boundary time gauge*, where $\delta(t,\pi/2) = 0$. In the former case, t corresponds to the proper time of a static observer placed at the origin. In the latter, t is the proper time of a static observer placed at the conformal boundary (if we identify this boundary with the $x = \pi/2$ hypersurface in ESU_{d+1}).

The existence of an apparent horizon in the system corresponds to a zero of the blackening factor, $f(t,x) = 0$. It is convenient to define the new fields

$$\Phi(t,x) = \partial_x\phi(t,x), \qquad \Pi(t,x) = \frac{e^{\delta(t,x)}}{f(t,x)}\partial_t\phi(t,x), \tag{1.3.174}$$

in such a way that the scalar equation of motion $\Box\phi = 0$ can be casted in first-order form as

$$\partial_t\Phi(t,x) = \partial_x(f(t,x)e^{-\delta(t,x)}\Pi(t,x)), \tag{1.3.175}$$

$$\partial_t\Pi(t,x) = \cot^{d-1}(x)\partial_x(\tan^{d-1}(x)f(t,x)e^{-\delta(t,x)}\Phi(t,x)). \tag{1.3.176}$$

Due to our symmetry assumptions, the Einstein equation for the background spacetime reduces to two nonlinear, elliptic ODEs, that determine the metric tensor in terms of the scalar degrees of freedom,

$$\partial_x f(t,x) = \frac{d-2+2\sin^2(x)}{\sin(x)\cos(x)}(1-f(t,x)) + f(t,x)\partial_x\delta(t,x), \tag{1.3.177}$$

$$\partial_x\delta(t,x) = -\sin(x)\cos(x)(\Phi(t,x)^2 + \Pi(t,x)^2). \tag{1.3.178}$$

There is also an additional equation, which corresponds to the momentum constraint, and that is automatically satisfied if the background solves the remaining equations,

$$\partial_t f(t,x) + 2\sin(x)\cos(x)f(t,x)^2 e^{-\delta(t,x)}\Phi(t,x)\Pi(t,x) = 0. \tag{1.3.179}$$

Let us come back now to the four-dimensional problem discussed in [130]. Rather than quenching the system by turning on a particular boundary source $\phi_0(t)$ for the scalar field, Bizon and Rostworowski considered Gaussian initial data on the $t = 0$ hypersurface,

$$\Pi(0,x) \equiv \Pi_0(x) = \frac{2}{\pi}\epsilon e^{-\frac{4}{\pi^2\sigma^2}\tan(x)^2}, \qquad \Phi(0,x) \equiv \Phi_0(x) = 0, \tag{1.3.180}$$

with $\sigma = 1/16$, and analyzed their subsequent time evolution. Remarkably, they found that there exists a sequence of critical amplitudes $\{\epsilon_n, n = 1,2,3...\}$, with $\epsilon_{n+1} < \epsilon_n$, such that, if the amplitude ϵ of the initial data (1.3.180) satisfies $\epsilon_{n+1} < \epsilon < \epsilon_n$, a black hole is formed after n AdS ligth-crossing times, $t_{\text{lc}} = \pi$.[49] Let $t_c(\epsilon)$ be the collapse time, *i*.e., the time needed for form an apparent horizon. This quantity, when plotted against the amplitude, has two salient features: i) a series of plateaux with $t_c \approx n\pi$, corresponding to $\epsilon \in [\epsilon_{n+1}, \epsilon_n]$ and ii) an ϵ^2-scaling, $t_c(\epsilon^2) \sim \epsilon^{-2}$, when $\epsilon \ll 1$.

Due to the finite resolution unavoidable in any numerical experiment, the critical sequence could not be continued past some finite $\epsilon_N > 0$. A question that arises naturally at this point is if the critical sequence is actually infinite and accumulates at $\epsilon = 0$. A positive answer would imply that AdS$_4$ is nonlinearly unstable with respect to scalar perturbations of the form (1.3.180).

In [130], both numerical and analytical evidence was provided in favor of the existence of this instability. Firstly, it was shown that, as $\epsilon \to 0$, the rescaled function $\epsilon^{-2}\Pi(\epsilon^2 t, 0)^2$ approached an universal form in the slow-time $\tau = \epsilon^2 t$

$$\epsilon^{-2}\Pi(\epsilon^2 t, 0)^2 \to \pi(\tau)^2. \tag{1.3.181}$$

There exists a critical τ_c such that, for $\tau = \tau_c$, an apparent horizon forms. This is signaled by a seeminly divergent $\pi(\tau)^2$ as $\tau \to \tau_c^-$, which implies a divergent Ricci scalar curvature at $x = 0$, since

$$R(t, 0) = -12 - 2\Pi(t, 0)^2. \tag{1.3.182}$$

If the scaling symmetry (1.3.181) actually holds in the $\epsilon \to 0$ limit, any initial data of the form (1.3.180) would form a black hole in a time $t_c = \tau_c \epsilon^{-2}$, as it happens for the numerical simulations with $\epsilon > 0$.

Secondly, a perturbative expansion in ϵ was constructed, in order to address the nonlinear evolution of the scalar field analytically. The ansatz

$$\phi = \sum_{n=0}^{\infty} \phi_{2n+1}\epsilon^{2n+1}, \qquad f = 1 + \sum_{n=1}^{\infty} f_{2n}\epsilon^{2n}, \qquad \delta = \sum_{n=1}^{\infty} \delta_{2n}\epsilon^{2n} \tag{1.3.183}$$

was employed. At $O(\epsilon)$, this ansatz reduces to the scalar equation of motion on a fixed AdS$_4$ background

$$\partial_t^2\phi(t,x) - \cot(x)^2\partial_x(\tan^2(x)\partial_x\phi(t,x)) = 0, \tag{1.3.184}$$

which can be explicitly solved by separation of variables, $\phi(t,x) = e^{i\omega_n t}e_n(x)$, with the boundary conditions provided by origin regularity and normalizability. The resulting normal modes, $\{e_n(x), n \in \mathbb{N}\}$, are

$$e_n(x) = \sqrt{\frac{16(n+1)(n+2)}{\pi}}\cos^3(x)\,{}_2F_1\left(-n, 3+n, \frac{3}{2}, \sin^2(x)\right), \tag{1.3.185}$$

and form an orthonormal basis for any square-integrable function in $L^2([0,\pi/2], \tan(x)^2)$,

$$(e_n, e_m) = \int_0^{\frac{\pi}{2}} \tan(x)^2 e_n(x)e_m(x) = \delta_{n,m}. \tag{1.3.186}$$

---

[49] The light-crossing time t_{lc} is defined as the time needed for a radial null geodesic to travel between two antipodal points on the boundary sphere.

In consequence, a generic solution of (1.3.184) has the form

$$\phi(t,x)=\sum_{n=0}^{\infty}a_n\cos(\omega_n t+b_n)e_n(x), \tag{1.3.187}$$

with $\{(a_n,b_n),n\in\mathbb{N}\}$ set by the initial data. The eigenfrequency spectrum, $\{\omega_n,n\in\mathbb{N}\}$, is given by

$$\omega_n=3+2n, \tag{1.3.188}$$

and is *resonant*, or *non-dispersive*, since the group velocity $v_g=\partial_n\omega_n=2$ is independent of n. Note that (1.3.187) together with (1.3.188) imply that, in the absence of backreaction, any scalar perturbation of global AdS$_4$ is exactly periodic, with period 2π: AdS$_4$ is linearly stable. The apparent AdS$_4$ instability observed numerically must be necessarily of nonlinear nature.

In [130], one-mode $\phi_1(0,x)=e_0(x)$, $\partial_t\phi_1(0,x)=0$ and two-mode $\phi_1(0,x)=e_0(x)+e_1(x)$, $\partial_t\phi_1(0,x)=0$ initial data were fed into the ansatz (1.3.183). After solving explicitly δ_2,f_2 by direct integration, at $O(\epsilon^3)$ it is found that

$$\phi_3=\sum_{n=0}^{\infty}c_n(t)e_n(x) \tag{1.3.189}$$

satisfies and equation of the form

$$\ddot{c}_n+\omega_n^2c_n=S_n\equiv(S_3,e_n)\,, \tag{1.3.190}$$

where S_3 is a functional of ϕ_1,δ_2,f_2. Let $I=\{n:a_n\neq 0\}$ be the set of indices of the non-zero eigemodes of the linearized solution ϕ_1. It can be shown that, for each resonant triplet $(n_1,n_2,n_3)\in I^3$ such that $\omega_n=\omega_{n_1}+\omega_{n_2}-\omega_{n_3}$, a secular term proportional to $t\cos(\omega_n t)$ or $t\sin(\omega_n t)$ appears in S_n. Certain secular terms can be reabsorbed into a frequency redefinition à la Poincarè-Lindstedt; however, avoiding completely the appearance of secular terms in ϕ_3 is not generically possible. For instance, while the ϵ-expansion seeded by one-mode initial data can be continued to arbitrary high order, for two-mode initial data non-removable secular terms appear at $O(\epsilon^3)$. These secular terms are $O(\epsilon^3 t)$ and, in consequence, become $O(\epsilon)$ at time $t_{\text{breakdown}}=O(\epsilon^{-2})$, rendering the ϵ-expansion invalid.

Taken alone, the existence of the new time scale t_{beakdown} does not imply that the scalar field must undergo gravitational collapse.: a failure of the perturbative expansion can be a mathematical artifact with no physical relevance. Nonetheless, the fact that $t_c=O(t_{\text{breakdown}})=O(\epsilon^{-2})$ suggests that the non-removable secular terms that appear in the ϵ-expansion are the precursors of the nonlinear instability that is observed numerically. From this perspective, the nonlinear instability seems to be directly tied to the resonant character of the eigenfrequency spectrum (1.3.188), since the resonant triplets only exist because the eigenfrequencies are equally spaced.

In [131], further steps were taken in order to characterize the AdS instability in frequency space. The ADM energy of our system

$$M = \frac{1}{2}\mathrm{Vol}(S^2)\int_0^{\frac{\pi}{2}} \tan(x)^2 f(t,x)\left(\Phi(t,x)^2 + \Pi(t,x)^2\right) \tag{1.3.191}$$

can be decomposed as

$$M = \sum_{n=0}^{\infty} E_n = \sum_{n=0}^{\infty} \Pi_n^2 + \omega_n^{-2}\Phi_n^2 \tag{1.3.192}$$

by defining the projections $\Phi_n = \left(f^{1/2}\Phi, e'_n\right)$, $\Pi_n = \left(f^{1/2}\Pi, e_n\right)$ onto the eigenmode basis. By examining the time evolution of the energy spectrum $\{E_n, n \in \mathbb{N}\}$, it was found that the progressive sharpening of the scalar pulse in position space has a direct counterpart in an energy cascade from low-n to high-n eigenmodes. In this way, an energy spectrum exponentially suppressed at high-n at $t = 0$, such as the one corresponding to initial data of the form (1.3.180), becomes polynomial right before a black hole is formed at $t = t_c$,

$$E_n \sim n^{-\alpha}, \qquad n \gg 1 \tag{1.3.193}$$

where $\alpha \simeq 1.2$ is an universal exponent independent of the particular family of initial data considered. This energy cascade is refered to as *turbulent*, in analogy with the Kolmogorov energy cascade familiar from fluid mechanics.

To sum up, the initial studies provided evidence that arbitrarily small scalar perturbations of global AdS$_4$ are nonlinear unstable to black hole formation. The instability manifests herself as a turbulent energy cascade, that is apparently seeded by the growth of the non-removable secular terms that appear in perturbation theory due to the resonant eigenfrequency spectrum. Based on these observations, the authors of [130] proposed that global AdS is nonlinearly unstable under arbitrarily weak, generic scalar perturbations. Let us explain this statement in more detail [132].

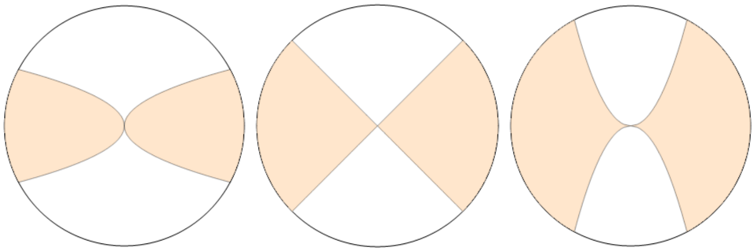

Figure 1.4: Cartoon of the three different possibilities for $r(0)$. The orange shaded region represents V_c, while the white region corresponds to V_{nc}. The radial direction can be thought of as the total energy, and the angular one as the energy radial distribution. The origin is global AdS. Left: $r(0) = \infty$. Middle: $r(0)$ finite. Right: $r(0) = 0$.

Consider initial data $(\Phi_0(x), \Pi_0(x))$, with norms $\|\Phi_0(x)\|, \|\Pi_0(x)\| \leq \epsilon$. Let $V_c(\epsilon)$ be volume of the phase space region occupied by initial data that lead to collapse at times

$t \lesssim \epsilon^{-2}$, and $V_{nc}(\epsilon)$ the volume of the phase space region occupied by initial data that never result in black hole formation during this time scale.[50] Bizon and Rostworowski conjectured that the ratio

$$r(\epsilon) = \frac{V_c(\epsilon)}{V_{nc}(\epsilon)} \tag{1.3.194}$$

diverges when $\epsilon \to 0$. The *AdS instablity problem* consists in finding out which one of the three options

$$\lim_{\epsilon\to 0} r(\epsilon) = \infty, \qquad 0 < \lim_{\epsilon\to 0} r(\epsilon) < \infty, \qquad \lim_{\epsilon\to 0} r(\epsilon) = 0 \tag{1.3.195}$$

is actually realized. A schematic representation of the three possibilities can be found in figure 1.4.

Note that the proposed physical mechanism behind the turbulent instability observed in [130] holds for any scalar field with any m^2 and in any dimension since, in these cases, the eigenfrequency spectrum is given by $\omega_n = \Delta + 2n$ and thus the criterium $\partial_n \omega_n = 2$ is still satisfied. Furthermore, $O(\phi^3)$ corrections to the scalar potential are not generically expected to remove every secular term present at $O(\epsilon^3)$ in perturbation theory and, in consequence, AdS should also be nonlinearly unstable in arbitrary supergravity truncations involving scalar fields.

When an $O(\epsilon)$ scalar perturbation has a nontrivial angular dependence, the spherical symmetry of the metric is ony broken at $O(\epsilon^2)$. As a consequence, any infinitesimal scalar field fluctuation can be decomposed into normal modes of the form

$$e_{n,l,m}(t,x,\theta,\phi) = \exp(i\omega_{n,l}t)e_{n,l}(x)Y_{l,m}(\theta,\phi), \tag{1.3.196}$$

where $Y_{l,m}(\theta,\phi)$ is a spherical harmonic on the two-sphere, and l and m are the standard angular momentum quantum numbers. The radial part and the eigenfrequency are independent of m, while l only enters the eigenfrequency spectrum through the combination $2n+l$,

$$\omega_{n,l} = \Delta + 2n + l. \tag{1.3.197}$$

Since the spectrum is still resonant, the arguments put forward in [130] also apply. We expect the turbulent instability to be present even for non spherically symmetric scalar fields. In subsection 1.3.6 we discuss the status of the turbulent instability in the purely gravitational case.

Let us close this subsection by noticing that, from the AdS/CFT viewpoint, the existence of the turbulent instability looks natural. Naively, one would made the educated guess that any excited state in the dual CFT$_d$ with macroscopic energy density must eventually thermalize. Let us reintroduce the radius of curvature L, and recall that the radius R of the boundary sphere is given by $R = L$. We note that the collapse time t_c satisfies

$$t_c(MR) \sim MR, \;\; MR \gg 1 \tag{1.3.198}$$

$$t_c(MR) \sim (MR)^{-1}, \;\; MR \ll 1 \tag{1.3.199}$$

---

[50] We assume that there exist some regularization that allows one to define these quantities.

As in the Hawking-Page transition, t_c is nontrivial due to the fact that R provides a length scale against which the energy can be measured. In the planar $R \to \infty$ limit, the fine subbranch structure present at $\epsilon \leq \epsilon_1$ is erased, and only prompt collapse is observed [98].

1.3.2 Kinematics versus dynamics in the AdS instability problem

The turbulent instability found in [130] is essentially dynamical since it depends on the resonant character of the normal mode eigenfrequency spectrum. As we are considering a classical system, we might expect that AdS is unstable due to more general reasons. If the dynamics were sufficiently ergodic, and since the background spacetime where the scalar field propagates is effectively compact, the gravitational system would explore randomly its microcanonical shell $\Omega(E)$, until the scalar field configuration finds itself trapped behind an apparent horizon. Collapse follows. If this line of reasoning were correct, also four-dimensional Minkowski spacetime enclosed in a cavity would be nonlinearly unstable.

This last setup is particularly handy because, in this case, the normal mode eigenfrequency spectrum varies depending on the boundary conditions chosen. Let the cavity be a two-sphere of radius R. There are two possibilities:

- Dirichlet boundary conditions, $\phi(t,R) = 0$, $\omega_n = \frac{\pi}{R} n$.
- Neumann boundary conditions, $\partial_r \phi(t,R) = 0$, $\omega_n = \frac{\pi}{R}\left(n + \frac{1}{2}\right) + O(n^{-1})$.

Therefore, while for Dirichlet boundary conditions the spectrum is still resonant, for Neumann boundary conditions it is only *asymptotically resonant*. The numerical experiments performed in [133][134] indicate that, in the latter case, sufficiently small scalar perturbations do not collapse, at least for initial data of the form (1.3.180). In particular, the scaling (1.3.181) is absent. However, for Dirichlet boundary conditions, the Ricci scalar at $x = 0$ shows the correct ϵ-scaling again. Furthermore, when considering the energy spectrum, a turbulent cascade is also found; in particular, the exponent α takes the AdS$_4$ value.

Another confirmation that kinematical confinement is not enough to trigger a nonlinear turbulent instability was provided in [135]. These authors considered a complex massless scalar field in AdS$_4$ with an artificial, reflecting wall placed at $x_{max} < \pi/2$, where Dirichlet boundary conditions were imposed. Again, this renders the spectrum of scalar fluctuations on the restricted geometry dispersive. Consistently, when evaluating the collapse time $t_c(\epsilon)$ for Gaussian initial data of amplitude ϵ at $\sigma = 1/16$, an apparent divergence appears at $\epsilon = \epsilon_c(x_{max}) > 0$, signalling the stability of small-amplitude initial data.

It is important to acknowledge that this research was highly motivated by [136], where the authors put forward formal perturbation theory arguments in favor of the necessity of having an exactly resonant spectrum for a turbulent cascade to be present. The two works we have discussed in this subsection indeed provide solid evidence in favor of a dynamical turbulent instability linked to the resonant character of the eigenfrequency spectrum. It remains to be seen if this resonant character is a sufficient condition for the instability and not just a necessary one. For instance, [137] summarized the results pertaining several $1+1$-dimensional nonlinear PDEs that, although being defined on a compact domain and having a resonant spectrum, are immune to the turbulent instability. Other toy models, such as a scalar field with a $\lambda\phi^4$ potential over a fixed AdS$_4$ background, also share this phenomenology [138].

It should be emphasized that the absence of a turbulent instability does not necessarily imply the nonlinear stability of the system. An ergodic instability could still be present, but be only relevant at a time scale t_{ergodic} parametrically larger than ϵ^{-2}, making it inaccessible by the currently doable numerical experiments. From now on, we will forget the possible existence of an ergodic instability and focus solely on time scales $O(\epsilon^{-2})$. A process of gravitational collapse that takes place during this time scale is thus associated to *fast thermalization*, in the sense that the system attains thermal equilibrium in the shortest timescale allowed by the dynamics [132][139].

1.3.3 Stability islands

In [135], it was noticed that the turbulent instability disappeared for Gaussian initial data of the form (1.3.180) when $\sigma > \sigma_c$.[51] As ϵ decreases, the function $t_c(\epsilon)$ departs from its behavior at $\sigma < \sigma_c$. Monotonicity is lost, and a critical ϵ_c emerges: for $\epsilon < \epsilon_c$, no black hole is found within the times computationally accessible. As $\epsilon \to \epsilon_c^+$, $t_c(\epsilon)$ looks divergent.[52] The nonlinear stability of these one-parameter families of initial data when $\epsilon < \epsilon_c$ implies the existence of highly excited states in the dual CFT$_d$ that avoid fast thermalization.

The picture that has gradually emerged is that there exist *stability islands* in the phase space of the system: within these regions, the turbulent instability is absent. What is the reason behind their existance? As we already mentioned, one-mode initial data are nonlinearly stable at level of the ϵ-expansion. At finite amplitude, these initial data branch off to *exactly periodic* solutions that never undergo gravitational collapse [140]. We will refer to these time-periodic solutions as *oscillons*. It is natural to postulate that each oscillon creates a stability island: initial data sufficiently close to it could be regarded as a *perturbed oscillon* and would avoid the turbulent instability if the eigenfrequency spectrum of scalar fluctuations around this oscillon is nonresonant. As argued in [141], this line of reasoning can explain the nonlinear stability of wide Gaussian initial data that we discussed in the previous paragraph.

The relation between nonlinear stability and a nonresonant spectrum of scalar fluctuations has been explicitly confirmed for a complex scalar field in [134]. Due to the particular form of its energy-momentum tensor, a complex scalar field admits *boson star* solutions [135][142]. These are exactly periodic solutions with a time-independent metric and a harmonic scalar

---

[51] For a scalar field with zero mass in AdS$_4$, $\sigma_c \approx 0.3$.

[52] Of course, it is impossible to determine whether a function is divergent or not in a numerical experiment. Notice that even a simple streched exponential like $\exp(1/\epsilon)$ can look divergent when probed with finite resolution.

field profile,

$$\phi(t,x) = e^{i\omega t}\varphi(x), \tag{1.3.200}$$

endoved with finite energy and charge. In [134], a perturbative computation demonstrated that linearized scalar fluctuations over the boson star have an asymptotically resonant eigenfrequency spectrum. Consistently, when perturbed with Gaussian initial data of the form (1.3.180) with $\sigma = 1/16$, numerical simulations show nonlinear stability below a critical ϵ. While a scalar pulse can propagate coherently through AdS$_4$, over a boson star the pulse eventually disperses. The energy spectrum is found to stabilize around an exponential distribution,

$$E_n \sim e^{-\rho(t)n}, \qquad n \gg 1 \tag{1.3.201}$$

with $\rho(t)$ oscillating around a positive mean.

Let us close this subsection with a last remark. The numerical experiments we have described so far clearly establish that, at *finite* amplitude, there exist both nonlinearly unstable and stable families of initial data. The latter ones lie in the stability islands and are stabilized by the time-periodic solutions sitting at their center. The natural question to wonder about these stability islands is *how* their measure shrinks as the amplitude of the time-periodic solution sourcing them vanishes. As shown in [143], the improved perturbative framework we describe in the next subsection allows answering this question.

1.3.4 The resonant approximation

Imagine we had no access to the evidence provided by numerical experiments. How would we interpret the time scale $t_{\text{breakdown}}$ that signals the limit of applicability of the ϵ-expansion? Rather than adscribing any physical meaning to it, we would blame ourselves for our inhability to devise a better perturbative framework to address the problem.

It turns out that several such improved perturbative frameworks have been already found. They can be pictured as resummed ϵ-expansions, free of secular terms and, in consequence, uniformly valid up to times scales $O(1/\epsilon^2)$. The different methods that have been proposed include multiscale (the so called *Two Time Formalism* [144]), renormalization group [145] and Hamiltonian averging [146] techniques, and are equivalent up to $O(\epsilon^5)$ corrections [146]. Thus, at $O(\epsilon^3)$, we would refer to them as the *resonant approximation*, with no loss of generality [147].

The physical reason behind the existence of the resonant approximation is that the AdS instability problem is naturally endowed with a hierarchy of time scales in the $\epsilon \to 0$ limit. Imagine we decompose our scalar field as

$$\phi(t,x) = \sum_{n=0}^{\infty} c_n(t) e_n(x). \tag{1.3.202}$$

When considering the evolution of the $c_n(t)$ coefficients, phase oscillations take place at a time scale $O(1)$; during each oscillation, the energy-per-mode, $E_n(t)$, is effectively constant.

Energy transfer between different eigenmodes takes place on a parametrically longer time scale $O(1/\epsilon^2)$. As a consequence, an effective description of the system that focuses on this energy transfer can be obtained by integrating out the fast oscillations in $c_n(t)$.

In order to perform this integration, we assume that $c_n(t) = O(\epsilon)$ and introduce the eigenmode decomposition (1.3.202) into the Einstein-scalar equations of motion, keeping only terms up to $O(\epsilon^3)$. This result in a time evolution equation for $c_n(t)$ of the form

$$\ddot{c}_n + \omega_n^2 c_n = \sum_{ijk} \Omega_{ijkn} c_i c_j c_k. \tag{1.3.203}$$

Going to the interaction picture varables

$$c_n = \left(\beta_n e^{i\omega_n t} + \beta_n^* e^{-i\omega_n t}\right), \tag{1.3.204}$$

$$\dot{c}_n = i\omega_n \left(\beta_n e^{i\omega_n t} - \beta_n^* e^{-i\omega_n t}\right). \tag{1.3.205}$$

equation (1.3.203) becomes

$$2i\omega_n \dot{\beta}_n = \sum_{ijk} \Omega_{ijkn} c_i c_j c_k e^{-i\omega_n t}. \tag{1.3.206}$$

Each c_i coefficient in the sum of the *rhs* of the equation above has the form (1.3.204). Therefore, each coefficient of the sum is weighted by a $e^{-i\Lambda t}$ phase factor, with $\Lambda = \omega_n \pm \omega_i \pm \omega_j \pm \omega_k$. Performing a change of variables to the slow-time $\tau = \epsilon^2 t$ and rescaling $\beta_n(t) = \epsilon \alpha_n(\tau)$, this phase factor becomes a highly-oscillatory exponential, $e^{-i\Lambda\tau/\epsilon^2}$, that can be neglected unless the (i, j, k, n) quartet is resonant and $\Lambda = 0$. Finally, after neglecting the non-resonant terms, the effective equations governing the remaining resonant interactions of the system are given by

$$2i\omega_n \frac{d\alpha_n}{d\tau} = \sum_{ijk} \Omega_{ijkn} \alpha_i \alpha_j \alpha_k^*. \tag{1.3.207}$$

where the sum runs over the resonant quartets the n-th eigenmode belongs to. Out of the different resonant channels in principle possible, the only one that appears is

$$\omega_n = \omega_i + \omega_j - \omega_k. \tag{1.3.208}$$

We shall refer to these equations as the *flow equations.* A crucial property of the flow equations is the existence of a new scaling symmetry,

$$\alpha_n(\tau) \longrightarrow \epsilon^{-1} \alpha_n(\tau/\epsilon^2). \tag{1.3.209}$$

Another important observation is that the flow equations can be derived from a Lagrangian [146]

$$L = \sum_n i\omega_n \left(\alpha_n^* \frac{d\alpha_n}{d\tau} - \alpha_n \frac{d\alpha_n^*}{d\tau}\right) + 2W, \tag{1.3.210}$$

which has new continuous symmetries. These symmetries give rise to extra conservation laws valid on the time scale $O(1/\epsilon^2)$ [146][148]. To wit,

- Global phase shifts, $\alpha_n \to e^{i\theta}\alpha_n$, lead to conservation of the free motion energy $E = \sum_n \omega_n^2 |\alpha_n|^2$.
- Mode-dependent phase shifts, $\alpha_n \to e^{i\omega_n \theta}\alpha_n$, lead to conservation of the particle number $N = \sum_n \omega_n |\alpha_n|^2$.
- Time translations, $\tau \to \tau + \tau_0$, lead to conservation of the interaction energy W.

E is not the total energy of the system, since it neglects the interaction energy. Interestingly, N conservation is related to the fact that, as we have mentioned, $\omega_k = \omega_l + \omega_m - \omega_n$ is the only resonant channel that appears. The resonant channels

$$\omega_k = \omega_l - \omega_m - \omega_n, \tag{1.3.211}$$

$$\omega_k = \omega_l + \omega_m + \omega_n, \tag{1.3.212}$$

are not present beacuse their associated Ω-coefficients vanish, even if in principle they are kinematically allowed. This phenomenon was first uncovered in [146] by an explicit computation; more recently, it has been linked to hidden symmetries of the flow equations, that give rise to selection rules enforcing this vanishing [149][150].

The existence of additional conservation laws, appart from energy conservation, has nontrivial consequences regarding collapse. This fact is familiar from two-dimensional incomprensible fluid mechanics with zero viscosity, where the conservation of the enstrophy gives rise to *dual cascades*: when one conserved quantity flows to high wavenumbers, the other must flow in the opposite direction. In the resonant approximation, we face a similar situation. Since high eigenmodes have more energy per particle that lower eigenmodes, a fixed amount of energy cannot flow directly to high eigenmodes by a turbulent cascade, since that would reduce the particle number, violating N conservation. The must exists a simulataneous inverse cascade to low eigenmodes.

One major outcome of the resonant approximation has been the discoverement of new quasiperiodic solutions that avoid collapse [144]. By taking the ansatz

$$\alpha_n(t) = A_n e^{-iB_n t}, \tag{1.3.213}$$

and imposing the coherent phase condition

$$B_n = B_0 + n(B_1 - B_0), \tag{1.3.214}$$

(1.3.207) reduces to an infinite-dimensional system of algebraic equations. Truncating to $n = n_{\max}$, we obtain a finite-dimensional system of $n_{\max} + 1$ equations for the $n_{\max} + 3$ unknowns $\{B_0, B_1, A_n, n = 0, ..., n_{\max}\}$, where we assume, with no loss of generality, that $A_n \in \mathbb{R}$. Two free parameters remain, and they can be identified with the conserved free-motion-energy E and particle number N of the quasiperiodic solution.

The stability of these novel quasiperiodic solutions was addressed in [151], both at the linear and at the nonlinear level. It was shown that, at fixed E and N, the quasiperiodic solutions minimize the interaction energy W. This minimization property is correlated with the linear stability of these solutions. It turns out that the spectrum of scalar fluctuations associated to the quasiperiodic solutions is asymptotically resonant and, furthermore, that from the leading order term of its dispersion relation, $\partial_n \omega_n = c + ...$, it is possible to predict the recurrence times observed numerically in several examples, that involve initial data characterized by the same E and N as the quasiperiodic solution. These include perturbed quasiperiodic solutions, but also two-mode initial data with equal energy-per-mode and $\sigma = 4/10$ gaussian initial data of the form (1.3.180). Within the resonant approximation, these results validade the picture that non-collapsing configurations should be interpreted as perturbed quasiperiodic equilibria: each quasiperidic solutions seeds a new stability island.

The resonant approximation is not only helpful to study noncollapsing solutions: it can also be employed to analyse the turbulent instability herself. In [147], the authors considered two-mode initial data of the form

$$\phi(0,x) = \epsilon\left(\frac{1}{4}e_0(x) + \frac{1}{6}e_1(x)\right), \qquad \Pi(0,x) = 0, \tag{1.3.215}$$

placed over AdS$_5$, and followed their time evolution in the resonant approximation and at the fully nonlinear level. In the latter regime, black hole formation was observed at times $t_c = \tau_c/\epsilon^2$. In the former, the flow equations were truncated at a finite N and solved numerically. It was found that the time derivatives of the phases B_n diverged at a finite $\tau = \tau^*$, signaling the appearance of a oscillatory singularity. Apart from this observation, a fit of the eigenmode spectrum around τ^* to the ansatz

$$A_n(\tau) = C(\tau) n^{-\gamma(\tau)} e^{-\rho(\tau) n} \qquad (n \gg 1) \tag{1.3.216}$$

showed $\rho(\tau)$ hit zero at τ^*. Therefore, at $\tau = \tau^*$, the amplitude spectrum becomes purely polynomial, with a characteristic exponent $\gamma(\tau^*) = 2$. This is also the exponent that appears in the fully nonlinear numerical simulations.

Once this value is known, the ansatz (1.3.216) can be employed to determine how B_n must behave asymptotically in n when the system is about to hit the oscillatory singularity. The result obtained relies crucially on the asymptotic behavior of the Ω-coefficients. The phases were predicted to be *coherent* for every resonant quartet

$$B_n = B_i + B_j - B_k, \tag{1.3.217}$$

and logarithmically divergent individually,

$$B_n = a_n \log(\tau^* - \tau) + b_n. \tag{1.3.218}$$

An explicit fit of the numerical results shows indeed that, in the asymptotic regime, a_n, b_n are linear in n, while τ^* is n-independent and agrees nicely with the time τ_c found in the fully nonlinear evolution: $\tau^* \approx 0.509$ while $\tau_c \approx 0.514$. These results, when pondered together with the ϵ-scaling symmetry of the flow equations, imply that, for the initial data

(1.3.215), the turbulent instability is present in the $\epsilon \to 0$ limit, and constitutes the first semianalytical confirmation of this fact.[53] As further evidence in favor of this conclusion, the authors of [147] compared the rescaled Ricci scalar at the origin (cf. equation (1.3.181)) for fully nonlinear simulations of progressively lower energy with simulations of the resonant system at progressively higher truncation order N. This quantity, in both schemes, seemed to approach the same limiting curve either when $E \to 0$ or $N \to \infty$.

A similar method was employed in [153] to show that, in four dimensions, Gaussian initial data of the form (1.3.180) collapse in finite slow-time. Therefore, the initial data originally studied by Bizon and Rostworowski in [130] display an infinite critical sequence that accumulates at $\epsilon = 0$. Interestingly, at the collapse time τ^*, the critical exponent $\gamma(\tau^*)$ was shown to be compatible with $3/2$, rather than the $8/5$ value originally reported in [130]. Two-mode, equal energy initial data of the form (1.3.215) were also considered in [153]. In striking contrast with the five-dimensional case, these initial data collapse in infinite slow time: the function $\rho(t)$ decreases exponentially to zero and never vanishes.

The phase coherent ansatz (1.3.217) was brought to the center of the stage in [154], where it was proposed that phase coherence is a necessary ingredient to have an ultraviolet cascade leading to collapse: a power-law amplitude spectrum must necessary be accompanied by a coherent phase spectrum.[54] In particular, since both conditions are only satisfied simultaneously due to the particular asymptotic form of the Ω-coefficients, it might be that not only a resonant spectrum, but also a specific asymptotic behavior of Ω_{ijkl}, is needed in order to have a turbulent instability.

In this regard, the absence of the turbulent instability reported in [138][155] is particularly intriguing. There, a nonbackreacting massless scalar field with a $\lambda\phi^4$ potential was placed over a *fixed* AdS$_4$ background. The eigenfrequency spectrum is resonant. However, in contrast to the fully backreacting case, the absence of scalar selfinteraction mediated by metric implies that spacetime derivatives do not appear in the $O(\epsilon^3)$ correction to the free Lagrangian. This fact modifies the asymptotic behavior of Ω_{ijkl} completely. For instance, while in the backreacting case we find that, for $\gamma \gg 1$,

$$\Omega_{\gamma i,\gamma j,\gamma k,\gamma l} \sim \gamma^d \Omega_{i,j,k,l}, \tag{1.3.219}$$

in the $\lambda\phi^4$ scalar theory the result is

$$\Omega_{\gamma i,\gamma j,\gamma k,\gamma l} \sim \gamma^{-1} \Omega_{i,j,k,l}, \tag{1.3.220}$$

making the phase coherent ansatz, and the power law amplitude spectrum, impossible to be obtained.

---

[53] While there could be some room for doubting whether the oscillatory singularity reported in [147] is just implying the breakdown of the resonant approximation, [152] showed that this oscillatory singularity is associated to a divergent redshift emerging between $x = 0$ and $x = \pi/2$. Therefore, at present, there is strong evidence that, rather than being an artifact of the resonant approximation, the oscillatory singularity represents a genuine physical effect associated with black hole formation.

[54] This statement refers to the $n \gg 1$ regime.

Note that the results discussed on the preceding paragraphs only identify sufficient conditions for the existence of the turbulent instability, or vindicate its persistence in the zero amplitude limit. They do not address the question of how the measure of the phase space region V_c shrinks in this limit. Can the resonant approximation, and in particular the scaling symmetry (1.3.209), be employed to determine what the value of $r(0)$ is? As demonstrated in [143], it turns out that a careful analysis of how perturbative and fully nonlinear results relate to each other, when combined with the scaling symmetry (1.3.209), allows discarding the option $r(0) = \infty$.

Recall that, at finite energy, there is solid numerical evidence favoring the existence of stability islands of finite measure. The authors of [143] were able to demonstrate rigorously that this measure does not vanish faster than the energy when the energy of the quasiperiodic solution sourcing the stability island goes to zero. Therefore, *global AdS is not nonlinearly unstable under generic perturbations*, and the original conjecture put forward in [130] can be discarded. The possible resolutions of the AdS instability problem, as currently understood, correspond to a finite $r(0)$ or to $r(0) = 0$.[55] These options are represented schematically in the middle and right plots of figure 1.4.

1.3.5 The AdS$_3$ case

Our discussion up to this point applies iff $d > 2$. As we are going to exemplify in detail in chapter 3, three-dimensional AdS spacetime is fundamentally different from its higher-dimensional counterparts. Already at the kinematical level, there is *mass gap* on the spectrum of static black hole solutions. The lightest black hole has energy[56] $M = 1$ [156][157]. Static solutions with $0 < M < 1$ correspond to naked singularities placed at $x = 0$. They posses a conical deficit angle of $2\pi M$ and can be regarded as point particles. Therefore, by energy conservation alone, initial data with $M < 1$ cannot form a black hole. At most, they can form a naked singularity, if they are going to equilibrate in finite time to a static configuration.

However, the eigenfrequency spectrum of a massless scalar field is still resonant and, in consequence, the turbulent instability must still be present. A natural question arises: can the turbulent instability lead to the formation of a naked singularity in *finite* time? If so, this would represent a strong violation of cosmic censorship. Unlike the case for the Choptuik critical solution [158], this time the region of the phase space of the gravitational theory leading to a naked singularity would not be of zero measure.

In [159], this problem was addressed by fully nonlinear numerical simulations. Starting from Gaussian initial data

$$\phi(0,x) = \epsilon e^{-\tan(x)^2/\sigma^2}, \qquad \dot{\phi}(0,x) = 0, \tag{1.3.221}$$

---

[55] The arguments put forward in [143] only uphold if the maximum local energy density of the solution remains bounded by ϵ for times $\lesssim \epsilon^{-2}$ and, as a consequence, cannot be directly applied to collapsing families of initial data.

[56] In appropriate units, of course.

with $\sigma = 1/32$, a turbulent cascade was found. By fitting the asymptotic form of the energy spectrum to the ansatz

$$E_n(t) = C(t)n^{-\gamma(t)}e^{-\rho(t)n}, \tag{1.3.222}$$

it is found that, after a transient period,

$$\rho(t) = \rho_0 e^{-t/T}, \tag{1.3.223}$$

with the relaxation time scaling as $T = T_c/\epsilon^2$. Therefore, since $\rho(t)$ only vanishes in the $t \to \infty$ limit, at any finite time the scalar field configuration remains smooth, and no naked singularity forms. Cosmic censorship upholds. The presence of the turbulent cascade can be faithfully demonstrated by the exponential growth of higher Sobolev norms. For instance,

$$\dot{H}_2 \equiv \|\phi''(t,x)\|_2 \propto e^{t/T}. \tag{1.3.224}$$

A natural question that emerges is what happens at the other end of the naked singularity spectrum. According to [159], smoothness is conserved for any initial data with $M < 1$. Black hole formation, *i.e.*, the evolution of initial data with $M \geq 1$, was addressed in the pioneering[57] work of Pretorius and Choptuik [160], albeit in a different coordinate system. For thin scalar pulses, centered around $x = 0$, only prompt black hole formation was considered, with the aim of uncovering any critical behavior present in the collapse process. Time evolutions longer than one light-crossing time were only studied for widely distributed initial data. The collapse time t_c was found to scale nonmonotonically with M as $M \to 1$; more remarkably, no collapse whatsoever could be found below a critical mass $M_c > 1$, within the simulation times computationally accessible. Therefore, [160] was the first paper pointing to the existence of a *stability band* above the mass gap, where the kinematically allowed collapse is dynamically forbidden.

The existence of a stability band has also been identified in planar geometries with a gapped black hole spectrum, such as the hard wall model [161] of the AdS soliton [162]. To date, it is unclear what is the precise physical mechanism behind the existence of the stability band. Perturbative methods are of no help since the scalar field distributions massive enough to result in black hole formation cannot be regarded as *small* by any means.

Nevertheless, the numerical experiments performed so far support the following heuristic picture. Consider a scalar pulse with mass $M > 1, M - 1 \ll 1$ located in the asymptotic region. When the pulse infalls, its gravitational selfinteraction leads to its breaking into one or more subpulses that, individually, do not have enough energy to collapse and form a black hole. The appearance of an apparent horizon requires a sizable energy transfer between subpulses and is disfavored. In this way, the existence of the stability band is sort of a diffractive effect. We are going to analyze in detail one example of such behavior in chapter 3.

1.3.6 The AdS instability problem in the purely gravitational case

In contrast to the Einstein-scalar case, the study of the stability of global AdS to purely gravitational perturbations is in a very preliminary stage. So far, only one example of numerical

---

[57] To this author's knowledge, this is the first paper that studies numerically gravitational collapse in AdS.

evolution of gravitational waves in global AdS has ever been performed [163], and relied on restrictive symmetry assumptions. Addressing this problem in full generality remains a pending task of the community. Fortunately, it had been possible to translate the perturbative ϵ-expansion of [130] directly to the gravitational sector [164][165] in AdS$_4$, gaining some enlightenment about what to expect in future numerical experiments. Spoiler: nonremovable secular terms appear again, suggesting that the turbulent instability is still present.

The spacetime metric is assumed to acquire the form

$$g = \bar{g} + \sum_n \epsilon^n h^{(n)}, \tag{1.3.225}$$

with $\bar{g}$ being the global AdS$_4$ metric. At each order in perturbation theory, Einstein's equations result in

$$\Delta_L h^{(n)}_{\mu\nu} = T^{(n)}_{\mu\nu}, \tag{1.3.226}$$

where Δ_L depends solely on the background metric $\bar{g}$, and $T^{(n)}$ is a functional of $\{h^{(j)}, j = 1...n-1\}$, and their derivatives. The rotational invariance of $\bar{g}$ can be taken advantage of to decompose both $h^{(n)}, T^{(n)}$ into scalar and vector type modes. These are symmetric two-tensors build from scalar and vector real spherical harmonics on S^2, respectively. For a given tensor, say A, we have

$$A = \sum_{l_s,m_s} A^{(s)}_{l_s,m_s} + \sum_{l_v,m_v} A^{(v)}_{l_v,m_v} + \cos\varphi \leftrightarrow \sin\varphi. \tag{1.3.227}$$

It turns out that any solution to (1.3.226) separates into two decoupled PDEs at the given l and m, one associated with the scalar modes, and another with the vector ones. At $O(\epsilon)$, since the background is time independent, both equations can be Fourier transformed in time. Regularity at $x = 0$ and the demand that the metric is asymptotically AdS$_4$ fix the eigenfrequency spectra to be:

$$\omega_{l_s,m_s} = 1 + l_s + 2n_s, \;\; n_s \in \mathbb{N} \quad \text{(scalar)} \tag{1.3.228}$$

$$\omega_{l_v,m_v} = 2 + l_v + 2n_v, \;\; n_v \in \mathbb{N} \quad \text{(vector)} \tag{1.3.229}$$

In contrast to the scalar field case, now we have two different normal mode sectors. Each normal mode, being it scalar or vector, is completely characterized by its $\{l, m, n\}$ triplet, with $l \geq 2$, $l \geq |m|$; n is still an overtone number. Since (1.3.228),(1.3.229) are still resonant, it is expected that higher orders in the ϵ-expansion are populated by nonremovable secular terms. It turns out that, while $h^{(2)}$ is always bounded in time, nonremovable secular terms appear in $h^{(3)}$, like in the scalar field case. Importantly, now the ϵ-expansion mixes the two different normal mode sectors: an initial $h^{(1)}$ seed with only scalar eigenmodes can source vector eigenmodes at higher orders, and vice versa.

In contrast with the scalar field case, not every seed that consists of one-mode initial data can be backreacted up to $O(\epsilon^3)$ to yield a time-periodic solution.[58] The only cases where

---

[58] But note that, as found out latter in axis-symmetry, each linearized eigenfrequecy can indeed be backreacted [166].

this is possible, as identified in [165], are: i) for scalar modes, $\{l_s, \pm l_s, 0\}$, $\{2, 0, 0\}$, $\{2, 1, 0\}$ and ii) for vector modes, $\{2, 0, 0\}$. Even though nonremovable secular terms do appear in the other cases, their frequency always coincides with the frequency of the seed, so no turbulent energy cascade is generated in perturbation theory. Creating new secular resonances demands to consider two-mode initial data.

For two-mode initial data, if both modes admit a time-periodic extension, only two nonremovable secular terms are generated at third-order, as in the scalar field case. However, if one mode does not admit this extension, additional nonremovable secular terms are created. They come not only from the original eigenmode with no nonlinear extension but also from the interaction between the two.

Thus, the final lesson coming out of the analysis of [164][165] is that, within pertubartion theory, the turbulent cascade is present also in the gravitational sector and, furthermore and more impressively, is harder than her scalar field counterpart.

As a final comment, it must be mentioned that the nonlinear gravitational solutions that branch of the scalar $\{l_s, \pm l_s, 0\}$ mode have been explicitly constructed numerically [167]. Following Wheeler, they were named *geons*. Geons are time-periodic, smooth horizonless geometries with a helical Killing vector field, that at asymptotic infinity reduces to $K = \partial_t + \Omega \partial_\varphi$. Ω is identified with the geon angular velocity. It appears in the First Law for the geon as $dE = \Omega dJ$.

The fully nonlinear regime of the AdS gravitational turbulent instability awaits the improvements in our numerical computation abilities. As a first step ahead, we could try to check if an improved perturbative expansion still exists in this setup, even though we have two different normal mode sectors that mix. If we are fortunate enough, this resummed expansion, if available, might be addressable with current simulation techniques.

Chapter 2

Holographic quantum revivals in AdS$_4$

2.1 Summary

Despite its fundamental importance, the relaxation of isolated quantum systems is still a subject of debate both from the theoretical and the experimental perspective. The recent availability of highly controllable quantum simulators, together with the awareness of their conceptual importance, has stimulated the interest on quantum thermalization (for reviews see [6] [168]).

To place this subject in a historical perspective, already in the classical realm interest in a similar question was behind the seminal work of Fermi, Pasta, Ulam and Tsingou (FPUT) on the dynamics of a one-dimensional discrete, nonlinear string [169]. Contrary to Fermi's expectation, the presence of nonlinearities was not enough to trigger the ergodicity required for energy equipartition. Fermi suspected this was something deep and new and, indeed, this problem marks the starting point for two branches of classical dynamics that developed rapidly: integrability and chaos.

For quantum systems, the situation is much less clear even at the theoretical level. From the experimental data, mounting evidence points towards a rich variety of possible evolutions, depending both on the microscopic dynamics and the initial conditions. In some cases, like for hard-core atomic interactions, integrability inhibits thermalization by freezing the momentum distribution, in such a way that memory of the initial state is not lost [170]. In others, the system thermalizes after passing through a quasi-stationary plateau at intermediate times, which has received the name of prethermalization [171][172]. Theoretical efforts have been put into trying to derive a statistical description for these quasi-stationary states by means of a Generalised Gibbs Ensemble [173][174][175][176][177]. Further work is still necessary to clarify the different routes from integrability to quantum chaos and quantum ergodicity.

On the other hand, the study of how quantum entanglement is generated, propagates and relaxes in out-of-equilibrium processes is a topic receiving increasing attention. In chapter 1, we already discussed the pioneering Calabrese and Cardy computation in $1+1$-dimensional gapped-to-critical global quenches (section 1.1) and the recent work in the AdS/CFT context that resorts to the HEE prescription (section 1.2.4) to address this question, both by simplified setups like the Vaidya model or full-fledged numerical computations (section 1.2.7).

These different examples involved field theories living on non-compact spacetimes. As a consequence, the entanglement entropy evolves right away towards saturating at its value at thermal equilibrium. The overall lesson of these studies is that this saturation is always attained after a horizon time depending on the size of the entangling region.

In this chapter, we want to push this venue further, and construct holographic models whose out-of-equilibrium dynamics departs from a fast approach to ergodic behavior. We will focus on isolated quantum systems of finite size.

A simple example where neither equilibration nor thermalization take place involves free fields with a linear dispersion relation on a circle. For such system, any initial state will reconstruct periodically in time, and the entanglement entropy would likewise oscillate. In [178], a dual counterpart of this behavior was proposed to be the periodic formation and evaporation of a quantum black hole in an asymptotically global AdS$_3$ spacetime. Finding a similar phenomenon in a strongly-coupled, holographic CFT just ammounts to finding out if bouncing geometries exist in classical General Relativity with global asymptotics.

However, owing to our discussion about the AdS instability problem in chapter 1 (section 1.3), we know that this is indeed the case. With global asymptotics, there exists the possibility of obtaining geometries in which black hole formation does not happen promptly, as in the Vaidya model, but rather after a time long enough for the turbulent instability to act efficiently on the scalar pulse. In this chapter, we are relating these gravitational collapse processes to delayed thermalization patterns, in which the holographic CFT exhibits a series of quantum revivals, *i.*e., partial reconstructions of the initial state, before an ergodic regime sets in. We back our proposal with a numerical entanglement entropy computation, performed by means of the HEE prescription.

This chapter is structured as follows. In section 2.2 we review our gravitational theory. To be concrete, we are employing the same Einstein-scalar theory as Bizon in Rostworowski in [130]. Since its action, ansatz, equations of motion and boundary conditions have been throughly discussed in section 1.3, we urge the reader familiar with that part of this manuscript to skip it. In section 2.3, we discuss how the phenomenology of gravitational collapse in our model depends on the initial data considered, focusing on a position-space analysis. We also comment both on the pre- and the post-collapse dynamics of the scalar field, *i.*e., its evolution before and after an apparent horizon first forms.[1] Then, in section 2.4 we discuss the dual interpreation of the bounces. We illustrate how, for narrow scalar field profiles, a simple model of causal propagation of entanglement based on previous field-theoretic and holographic studies suffices to predict their main features, owing to the compact nature of the boundary sphere. Based on this, we put forward a *heuristic* interpretation that relates the position of the scalar field to the typical separation of entangled excitations, and its amplitude to their density. We illustrate how this heuristic model allows for an understanding of characteristic features of the gravitational collapse process in terms of general field theory expectations.

Finally, in section 2.5 we introduce the major results of this chapter: the entanglement

---

[1] Actually, in the coordinate system we are employing, apparent horizon formation cannot be detected in *finite* time. We discuss this fact in this section, and refer the reader to chapter 5 (section 5.7) for an explicit illustration of this fact in the Vaidya model.

entropy computation in the bouncing background in terms of the HEE prescription. Our entangling regions consist of spherical caps. We find out that the entanglement entropy evolution is sensitive to the structure of the initial state, as it displays very different features depending on whether the bouncing geometry is sourced by a narrow or a broad scalar pulse. These differences are manifest both in the characteristic periodicity of its oscillations and the temporal evolution of their amplitude.

2.2 The model

We are considering Einstein-Hilbert gravity with negative cosmological constant and a massless real scalar field, *i.e.*, the same setup analyzed by Bizon and Rostworowski in [130]. Our Einstein-scalar action is[2]

$$S = \frac{1}{2}\int d^{d+1}x\sqrt{-g}\left(R + d(d-1) - (\partial\phi)^2\right).$$

We restrict ourselves to spherically symmetric geometries and employ the metric ansatz

$$ds^2 = \frac{1}{\cos^2(x)}\left(-f(t,x)e^{-2\delta(t,x)}dt^2 + f(t,x)^{-1}dx^2 + d\Omega^2_{d+1}\right).$$

In it convenient to define the following quantities in terms of the scalar field ϕ,

$$\Phi(t,x) = \partial_x\phi(t,x), \qquad \Pi(t,x) = \frac{e^{\delta(t,x)}}{f(t,x)}\partial_t\phi(t,x),$$

since in this way the scalar field equation of motion can be casted in a first-order form suitable for numerical integration

$$\begin{aligned}\partial_t\Phi(t,x) &= \partial_x(f(t,x)e^{-\delta(t,x)}\Pi(t,x)),\\ \partial_t\Pi(t,x) &= \cot^{d-1}(x)\partial_x(\tan^{d-1}(x)f(t,x)e^{-\delta(t,x)}\Phi(t,x)).\end{aligned}$$

A virtue of our metric ansatz is that the equations of motion for f and δ take also a first-order, elliptic form

$$\begin{aligned}\partial_x f(t,x) &= \frac{d-2+2\sin^2(x)}{\sin(x)\cos(x)}(1-f(t,x)) + f(t,x)\partial_x\delta(t,x),\\ \partial_x\delta(t,x) &= -\sin(x)\cos(x)(\Phi(t,x)^2 + \Pi(t,x)^2),\end{aligned}$$

and can be integrated straighforwardly. The system closes with the momentum constraint

$$\partial_t f(t,x) + 2\sin(x)\cos(x)f(t,x)^2e^{-\delta(t,x)}\Phi(t,x)\Pi(t,x) = 0,$$

which is not an independent equation, since it is satisfied if the remaining ones hold. The momentum constraint guarantees that the energy density, to be introduced in the following, is a conserved quantity.

---

[2] Even though we discuss the action, ansatz and equations of motion of this system in chapter 1 (section 1.3) we decide to reproduce them here again for the convenience of the reader.

We have set $l = 1$ and normalized the scalar field as

$$\phi = \sqrt{\frac{8\pi G}{d-1}}. \tag{2.2.1}$$

As initial data on the $t = 0$ hypersurface, we will either employ origin-centered

$$\Phi(0,x) = 0\,, \qquad \Pi(0,x) = \Pi_o(x) = \epsilon \exp\left(-\frac{4\tan^2 x}{\pi^2\sigma^2}\right)\,. \tag{2.2.2}$$

or boundary-centered Gaussian profiles

$$\Phi(0,x) = 0\,, \qquad \Pi(0,x) = \Pi_b(x) = \epsilon \exp\left(-\frac{4\tan^2(\pi/2 - x)}{\pi^2\sigma^2}\right)\cos^{d-1} x\,. \tag{2.2.3}$$

The choice of boundary-centered Gaussian profiles is inspired by the physics of a holographic quench.[3] Our initial-value problem is supplemented with the boundary conditions we describe next.

First, we work in the boundary time gauge, $\delta(t, \pi/2) = 0$. With this choice, our time coordinate t corresponds to the proper time of a boundary observer. Regarding the other boundary conditions at $x = \pi/2$, we demand a normalizable scalar field profile: the source $\phi_0(t)$ vanishes and the CFT Hamiltonian is time-independent. Since here is no energy exchange between the CFT and its environment, we are considering an isolated system. Standard holographic renormalization [46] leads to the following formula for the conserved energy M of the dual CFT

$$M = \frac{(d-1)}{16\pi G}\,\mathrm{vol}(S^{d-1})\,\mathcal{M}\,, \tag{2.2.4}$$

where $\mathrm{vol}(S^{d-1})$ is the volume of a unit $(d-1)$-sphere and

$$\mathcal{M} = \int_0^{\pi/2} dx \tan^{d-1} x f(\Phi^2 + \Pi^2)\,. \tag{2.2.5}$$

the energy density per species of the dual CFT, since the effective number of elementary degrees of freedom, c_{eff}, and Newton's constant, G, are related as $c_{eff} \sim 1/G$. As usual, obtaining a finite backreaction in the $c_{eff} \to \infty, G \to 0$ limit implies that the CFT energy density is macroscopic, $\langle T_{tt}\rangle \sim 1/G$. We define the mass density function ρ of our system by the relation

$$\rho(t,x) \equiv \tan^{d-1} x f(\Phi^2 + \Pi^2), \tag{2.2.6}$$

in such a way that

$$\mathcal{M} = \int_0^{\pi/2} \rho(t,x). \tag{2.2.7}$$

Focusing now on the $x = 0$ boundary conditions, we observe that regularity enforces that $f(t,0) = 1$ and $\Phi(t,0) = 0$. This conditions imply that δ, f, Π are even functions of x, while

---

[3] We discuss full-fledged holographic quenches in this system in chapter 6.

Φ is odd. It must be emphasized that the absence of a naked singularity at $x = 0$ implies that the dynamical geometries we are considering correpond to CFT pure states evolving unitarily, even if at $t \to \infty$ the system relaxes to a black hole [178].

In the remaning part of this chapter, we will discuss solely the $d = 3$ case, leaving the analysis of the $d = 2$ one for the next. As the simulation code we have employed both in this chapter, chapter 3 and chapter 5 uses *the same* algorithms, we refer the reader to appendix 5.A.2 for explanations and checks.

2.3 Bouncing geometries: phenomenology

After the discussion presented in section 1.3 of chapter 1, we know that the gravitational dynamics of asymptotically global AdS geometries is fundamentally different from its planar counterpart. While in the latter case any scalar field pulse located in the near-boundary region at $t = 0$ collapses gravitationally to a Schwarzschild black hole during its first infall [98][110], with asymptotically global boundary conditions, there is the possibility of obtaining *bouncing geometries*.

At the thermodynamical level, the black hole reached by a bouncing geometry after it undergoes gravitational collapse always corresponds to a small AdS$_4$-Schwarzschild black hole with negative specific heat. It is worth emphasizing that this fact is non-problematic. Since we are considering a CFT$_3$ at fixed energy, the thermodynamical stability of the final equilibrium state reached by our CFT$_3$ has to be analyzed within the microcanonical ensemble, ant not the canonical one. In this setup, the relevant thermodynamical potential to be minimized corresponds to the entropy, and not the free energy. It can be shown that small black holes are thermodynamically dominant over a thermal gas if their horizon radius is parametrically larger than the Planck scale [179]. For future reference, we mention that, with our conventions, the threshold mass $\mathcal{M}_{th}$ separating small and large AdS$_4$-Schwarzschild black holes is

$$\mathcal{M}_{th} = \frac{2}{3\sqrt{3}} = 0.385\ldots \tag{2.3.8}$$

Regardless of the specific form of initial data under consideration, for $\mathcal{M} \geq \mathcal{M}_{th}$ prompt black hole formation is observed. The time t_h at which an apparent horizon forms satisfies $t_h < t_{lc} = \pi$, and the scalar pulse is completely trapped behind the apparent horizon location, x_h. In our coordinate system, x_h is defined by the condition $f(t, x_h) = 0$. At the physical level, $f(t, x)$ never actually vanishes at any finite value of t: the sudden decrease of $f(t, x)$ at $x = x_h$ is accompained by a diverging origin-boundary redshift, signaled by a divergent $\delta(t, 0)$, in such a way that the gravitational dynamics at $x \leq x_h$ frozens. Therefore, at the practical level, t_h must be defined as the time where the minimum value of $f(t, x)$, $f_m(t)$, drops below an observer-defined cutoff.

Progressinly decreasing the energy density below $\mathcal{M}_{th}$, the initial apparent horizon is generated only by a fraction of the scalar pulse, while the remaining part scatters towards the asymptotic boundary. Eventually, a critical energy density $\mathcal{M}_{c,1}$ is reached, where the apparent horizon forms at $x_h = 0$, and a naked singularity is created. This naked singularity corresponds to the Choptuik critical solution [158] in the region $x \ll 1$ [130].

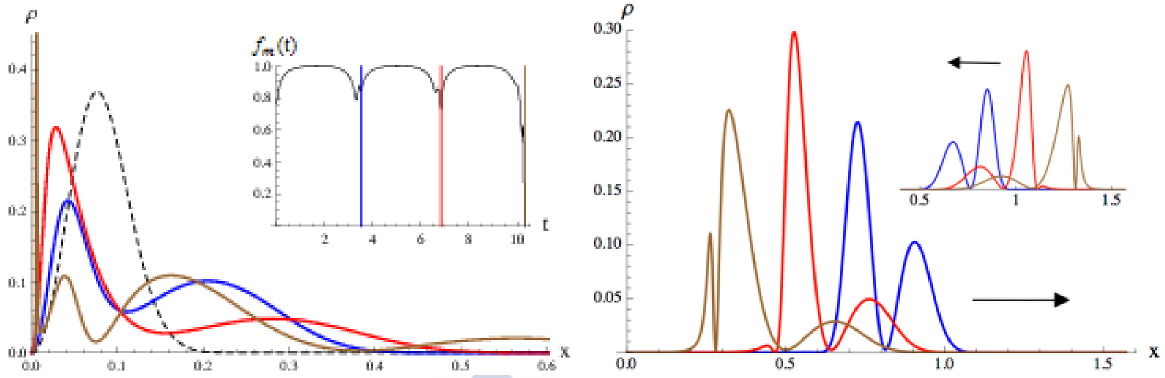

Figure 2.1: Evolution of a narrow pulse (2.2.2) with $\sigma = 1/16$ and $\mathcal{M} = 0.015$. Left: the dashed line shows the initial mass distribution function. The colored curves denote the mass density profile at the times when the pulse bounces against the origin producing a minimum of $f(t,x)$ (see inset). Right: scalar profiles from the first (blue), second (red) and third (brown) bouncing cycles; the arrows indicate the direction of movement.

As discussed in chapter 1 (section 1.3), for $\mathcal{M} < \mathcal{M}_{c,1}$ the gravitational dynamics of asymptotically global AdS spacetimes departs from the asymptotically flat case. In the latter, the scalar pulse is reflected at $x = 0$, and then disperses towards future null infinity while, in the former, the presence of the asymptotic boundary leads to a futher reflection at $x = \pi/2$ and a subsequent infall. An apparent horizon forms afterwards. The AdS turbulent instability implies that, for sufficiently narrow pulses, progressively decreasing the initial energy density leads to the appearance of a critical sequence $\mathcal{M}_{c,2}, \mathcal{M}_{c,3}, \ldots$ such that, for $\mathcal{M}_{c,n+1} < \mathcal{M} < \mathcal{M}_{c,n}$, an apparent horizon forms after n reflections at the asymptotic boundary [130]. In real space, the turbulent instability manifests herself in the progressive sharpening of at least one scalar field subpulse after each bounce against the origin, where the effect of nonlinear selfinteraction is stronger due to the energy density concentration. Eventually, this sharp subpulse triggers a sudden decrease of $f_m(t)$, which freezes out the gravitational dynamics for $x \leq x_h$. A generic example can be observed in the inset of figure 2.1a.

We would like to point out a generic effect accompanying the turbulent cascade: each time the scalar pulse scatters at $x = 0$ and part of it sharpens, the rest tends to increase is radial dispersion. This behavior, which will prove to bear important consequences for the dual CFT$_3$, is illustrated in figure 2.1a by employing a narrow initial profile which requires three bounces for collapse. We have plotted $\rho(t,x)$ at the times of closest approach to the origin. Figure 2.1b is meant to illustrate the fact that, while $\rho(t,x)$ gets modified after scattering at $x = 0$, it remains unaffected after reflecting at $x = \pi/2$ (see inset). The blue, red and brown profiles correspond respectively to configurations after the first, second and third bouncing cycles. The apparent horizon is generated from the spiky front in the brown profile.

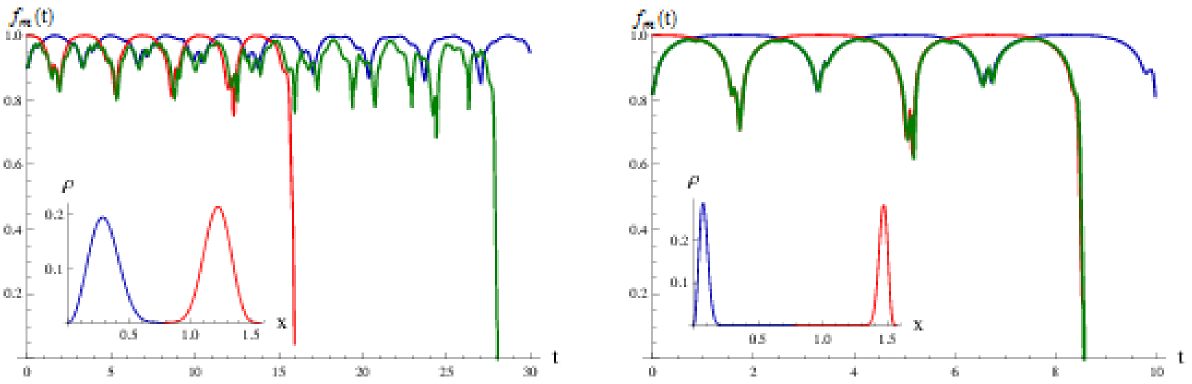

Figure 2.2: Evolution of the initial data (2.2.2) (blue), (2.2.3) (red) and the combined profile (2.3.9) (green) for the following subpulse data. Left: $\sigma = 1/4$ and $\mathcal{M} = 0.012$. Right: $\sigma = 1/16$ and $\mathcal{M} = 0.029$. In the inset, the initial mass density function. The left initial data have a larger overlap than the right ones. The horizon formation time for the fast collapsing pulse (red curve) gets affected and delayed (green curve), whereas it remains unaltered in the nonoverlapping case on the right.

Besides the energy density, the scalar pulse broadness (set by σ in (2.2.2)-(2.2.3)) has a strong influence on the gravitational dynamics [135]. Sufficiently broad pulses quickly develop a subpulse structure with infalling and outgoing components that scatter among themselves. In order to understand better the interaction between subpulses, let us consider a different initial profile, formed by a linear combination of (2.2.2) and (2.2.3)

$$\Phi(0, x) = 0\,, \qquad \Pi(0, x) = \Pi_o(x) + \Pi_b(x)\,. \tag{2.3.9}$$

We choose them to have the same $\mathcal{M}$ -when considered individually- and equal σ. As we can observe in figure 2.2a, for a nonzero overlap the formation of an apparent horizon is delayed with respect to the independent evolution of the subpulse that would collapse first.[4] Hence, subpulse scattering tends to work against the turbulent instability, which is however not evaded in this example. Interestingly, subpulses with negligible initial overlap are practically transparent to each other, as illustrated in figure 2.2b. We inform the reader that the relation between collapse time and subpulse scattering has also been discussed in [180].

Collapse processes induced by broad initial profiles present distinguished characteristics. They are radially delocalized for the major part of their time evolution. The oscillation periodicities of these solutions are determined, besides radial displacement, by their internal subpulse structure. As a result, the bouncing cycles are not neatly defined (see figure 2.3a). Furthermore, the horizon emerges supported by a finite fraction of the pulse energy, in contrast to the case of narrow pulses, where this fraction can be vanishingly small. Delocalized pulses require $\mathcal{M} \approx 0.4\mathcal{M}_{th}$ to generate an apparent horizon. When the total mass is decreased, a point is reached where the time elapsed until horizon formation abruptly increases [135][141]. For masses below this threshold our results join previous analysis supporting the

---

[4] For the initial data considered in 2.2a, this subpulse corresponds to Π_b

establishment of a regular quasi-standing wave [141].

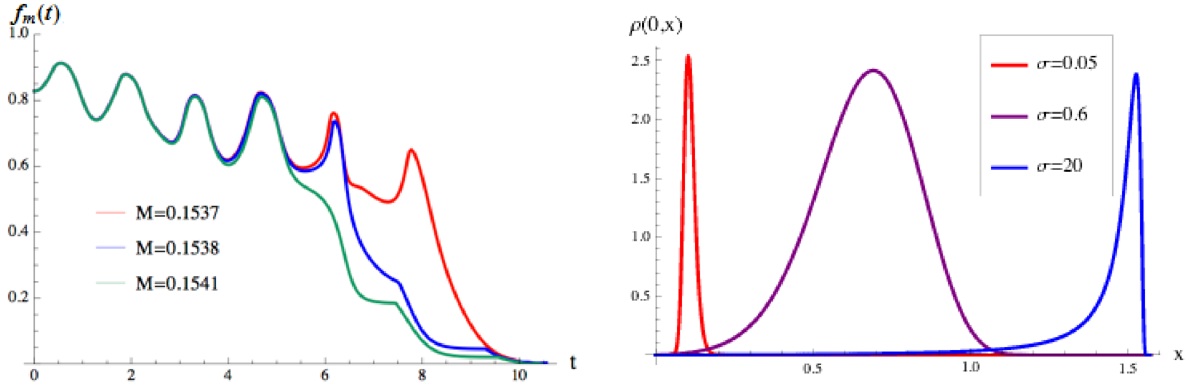

Figure 2.3: Left: Broad initial profiles of the form (2.2.2) with $\sigma = 0.6$. Right: Influence of σ on the initial mass density function $\rho(0, x)$.

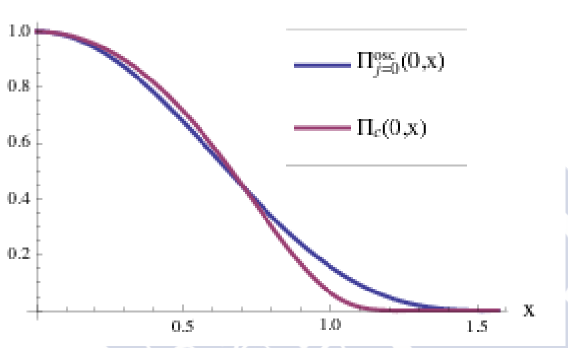

Figure 2.4: Initial data $\Pi_c(x)$ with $\sigma = 0.6$ and $\Pi_{j=0}(0, x)$ as given in (2.3.10), chosen to have the same height. The overlap is substantial, supporting the argument that their time developments, for small amplitude, are in the same island of stability around the time-periodic nonlinear solution constructed in [140].

For initial data of the form (2.2.2), the threshold broadness for the existence of regular solutions, σ_c, appears to be $\sigma_c \approx 0.35$ [135]. In [141], the numerical analysis at $\sigma = 0.6$ confirmed the regularity of the evolution. However, for large values of σ, gravitational collapse is observed again. The interpretation thereafter is that, for intermediate values of σ, the evolution lies within the domain of attraction of the exactly periodic solution that bifurcates from the fundamental mode of the linearized scalar wave equation in AdS$_4$.[5] This mode is given by

$$\phi_{j=0}(t, x) = \epsilon \cos(3t + \alpha) \cos^3 x \,, \tag{2.3.10}$$

with $\epsilon, \alpha \in \mathbb{R}$. For $\alpha = \pi/2$, the initial conditions

$$\Pi_{j=0}(0, x) = 3\epsilon \cos^3 x \,, \qquad \Phi_{j=0} = 0 \,, \tag{2.3.11}$$

---

[5] For extra information, we invite the reader to the discussion in section 1.3 about stability islands.

are actually very similar to those coming from (2.2.2) with $\sigma = 0.6$, as illustrated in figure 2.4.

On the other hand, the sharpness of the initial scalar field profile should be established based on the energy density function, $\rho(0, x)$, rather than on the profile itself. We observe from figure 2.3b that, indeed, sharply localized profiles exist both at $\sigma \ll 1$ and $\sigma \gg 1$. Similar reasoning can be applied to initial conditions of the form (2.2.3). When $\sigma \gtrsim 2$, the exponential factor in the profile can be neglected, and $\Pi_b(0, x) \approx \Pi_{j=0}(0, x)$. We have checked that for sufficiently low amplitudes the evolution of these initial data is regular up to the reach of our computational capabilities.

2.3.1 Post-collapse evolution

It is standard to stop numerical simulations at $t = t_h$. However, to provide a dual interpretation for the gravitational collapse processes we are considering, we need to pursue the time evolution as closest to the final thermal state as possible. Even though the dynamics for $x \leq x_h$ gets frozen for $t \geq t_h$, the remaining scalar field profile at $x > x_h$ continues travelling back and forth between the apparent horizon location and the asymptotic boundary. Its post-collapse evolution can be accessed in our original coordinate system, provided we increase sufficiently the discretization grid resolution.[6]

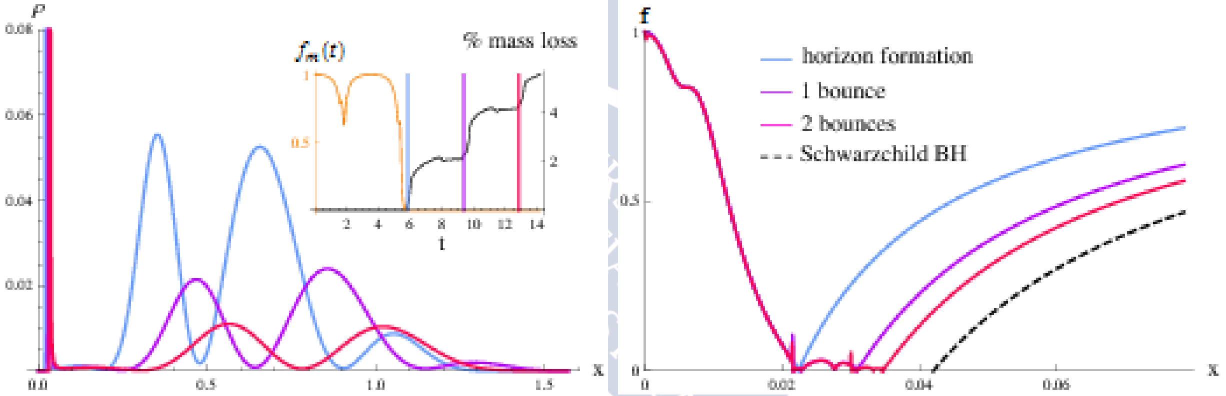

Figure 2.5: Evolution of a narrow pulse (2.2.3) with $\sigma = 0.1$ and $\mathcal{M} = 0.021$. Left: leftover scalar pulse after horizon formation and two post-collapse bounces. Right: horizon growth.

In figure 2.5 we plot the post-horizon evolution of a narrow profile for which $f(t, x)$ abruptly drops after one bounce (see inset). The horizon radius at that moment is approximately half the one of a Schwarzschild black hole of the total mass. When the apparent horizon emerges, the leftover scalar profile has already started its way to the AdS boundary. The mass distribution function at this moment is shown in figure 2.5a (light blue). Subsequently, this outgoing fraction of the pulse bounces at the boundary and falls in again, being partially

---

[6] Commonly, this procedure demands grids of $N = 2^{16} - 2^{17}$ points. We have checked that the momentum constraint remains under control, the relative mass loss of the simulated solution does not exceed the percent level, and that the results converge smoothly upon resolution variation.

absorbed and partially reflected. As a result, a new minimum of $f(t,x)$ drops to zero at a larger value of x, in accordance with the expected growth of the horizon. This is shown in figure 2.5b. We managed to follow this process past the completion of a second bounce with an acceptable precision.[7]

The horizon radius after two bounces is still far from that of a Schwarzschild black hole of the total mass (dashed black line in figure 2.5b). Several further bouncing cycles appear to be necessary to complete the collapse process. This is likely a generic feature. As discussed in chapter 1, at a linearized level one can calculate the absorption of scalar field to be consistent with an outside amplitude that decreases exponentially with time, $|\phi|_{out} \sim \exp(-\omega_l t)$ with $\omega_l \sim r_h^2$, [82].

As for pre-collapse dynamics, the post-collapse evolution is also σ-dependent. Scalar pulses of intermediate broadness show some degree of radial localization along the pre-collapse evolution. However, once an apparent horizon first emerges, the fraction of the scalar pulse left outside loses radial localization and a quasi-standing wave sets in. This fact is indeed consistent with a result presented in the previous subsection: the turbulent instability implies, together with the progressive sharpening of a subpulse, the radial dispersion of the rest.

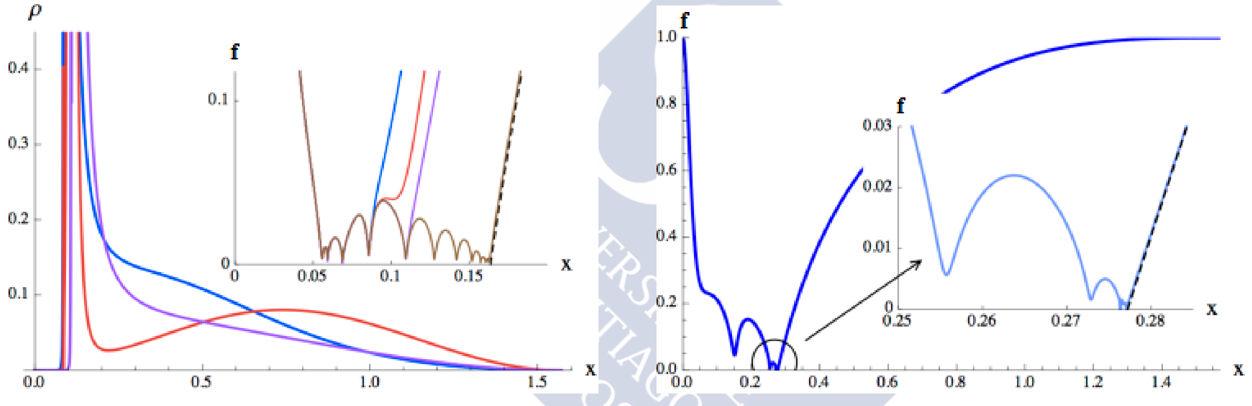

Figure 2.6: Left: cycle of the post-collapse damped standing wave for a profile (2.2.2) with $\sigma = 1/4$ and $\mathcal{M} = 0.085$. In the inset we have plotted $f(t,x)$ when the collapse process is nearly completed. The dashed black line shows $f(x)$ for a Schwarzschild black hole of the total mass. Right: Same plot as in the inset for a profile (2.2.2) with $\sigma = 3/5$ and $\mathcal{M} = 0.1538$.

This behavior is illustrated in figure 2.6a for initial data (2.2.2) with $\sigma = 0.25$. After two well defined bouncing cycles, $f_m(t)$ suddenly drops. As the evolution continues new minima of f appear at growing values of the radial coordinate, until the final value given by the radius of a Schwarzschild black hole of the total mass is reached. We have plotted a complete cycle of the left-out quasi-standing wave (blue, red and magenta curves), which perfectly matches the generation of a new f minimum.[8]

---

[7] The total mass of the scalar pulse, obtained by integrating $\rho(t,x)$, should keep constant along the evolution. In this example, it suffers a 2% loss in each post-collapse cycle for a grid of $N = 5 \times 10^4$ points (see inset). The numerical noise around the minima of f in figure 2.5b is linked to this fact.

[8] At the numerical level, following the post-collapse evolution for broad initial data is less demanding than

In the case of radially delocalized pulses, the function $f(t,x)$ does not drop abruptly to zero. This can be observed in figure 2.3b for several pulses with $\sigma = 0.6$. Similar dynamics to the quasi-standing wave of figure 2.6a, but with stronger damping, is established when the minimal radial value of f stops oscillating and starts decreasing. However, the minimum of f only becomes vanishingly small at a radial position very close to the final event horizon radius. This can be appreciated in figure 2.6b for the scalar pulse with $\mathcal{M} = 0.1538$ from figure 2.3a.

The periodicity of the bouncing cycles provides valuable information for the dual interpretation of the collapse processes. The bouncing period of narrow pulses always satisfies $T \gtrsim \pi$, increasing with the energy density and broadness of the scalar field profile.[9] Instead, for broad pulses with radially delocalized dynamics, a shorter periodicity emerges, $T \gtrsim \pi/3$. This periodicity governs the metric oscillations of the broad initial profiles shown in figure 2.3a, as well as the damped quasi-standing wave of figure 2.6. The presence of a faster oscillation should be traced back to the internal dynamics of the delocalized scalar pulse, rather than to radial propagation. The fact that $T \gtrsim \pi/3$ suggests that the origin of this faster oscillation is related to the substantial overlap between broad initial data and the exactly time-periodic oscillons found in [140].[10]

2.4 Dual interpretation of the bounces

In order to propose a field theory interpretation for the bouncing geometries treated in the previous section, let us first recall the holographic model of thermalization based on a Vaidya metric. Vaidya metrics describe the collapse of a shell composed of null dust. We consider now Poincaré instead of global coordinates, such that the dual field theory lives on Minkowski space. For simplicity, we focus on the $\mathrm{AdS}_3/\mathrm{CFT}_2$ instance of the duality, and the limit in which the infalling shell is infinitely thin. The resulting geometry is that of a BTZ black hole outside the shell and empty AdS_3 inside. This model describes a sudden action on the dual CFT vacuum which creates a homogeneous plasma with non-trivial quantum correlations and its subsequent unitary evolution [26].[11] It has been used as a holographic analog of a quantum quench.

In 2005 Calabrese & Cardy studied quantum quenches from gapped to critical systems in 1+1 dimensions [22].[12] They showed that the entanglement entropy of a single interval of length l increases with time until it saturates around

$$t = l/2\,. \tag{2.4.12}$$

---

for narrow pulses. In our example, we are able to reach a horizon radius up to within 3% of the final value, while keeping the relative mass loss $\leq 0.1\%$ by employing a $N = 2 \times 10^4$ resolution.

[9] It is satisfied that T is practically π when measured with respect to the origin proper time[130]. However, for a boundary observer higher mass pulses take a longer time to climb their own gravitational potential.

[10] The oscillon periodicity is actually $T = 2\pi/3$. This results in a periodicity $T = \pi/3$ for the metric oscillations, since they are sourced by the squares of scalar field derivatives.

[11] See section 1.2.7 for a discussion of entanglement entropy propagation in planar AdS/CFT.

[12] See section 1.1.2 for an extended discussion of their results.

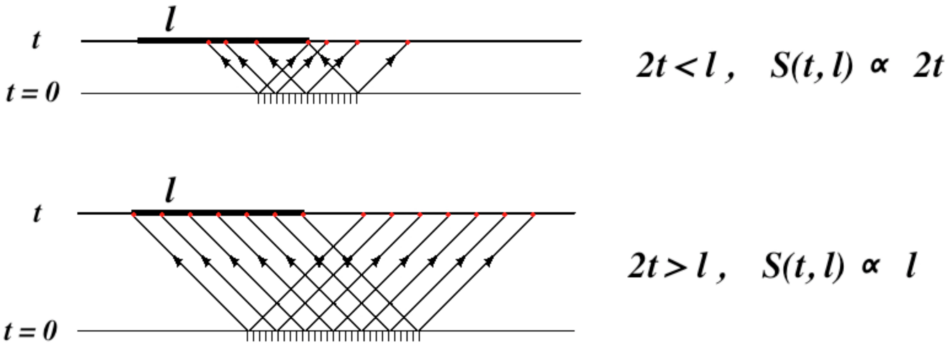

Figure 2.7: Assuming that the excitations behave as free quasiparticles, the entanglement entropy of an interval, $S(t, l)$, is proportional to the number of entangled pairs (shaded region) such that one component lies on the chosen interval and the other on its complementary [22]. For simplicity it is considered that only excitations created at the same point are entangled.

The limiting value attained at later times scales extensively precisely as it would do if the system inside the interval were in contact with a thermal bath given by the complementary system outside. Remarkably, this behavior can be explained kinematically, as a mere result of entangled excitations flying apart at unit speed (see figure 2.7). Consistently, the holographic model based on the collapse of a null dust shell leads to the same saturation time (2.4.12) for the entanglement entropy as found in the CFT computation. According to the HEE prescription (1.2.113), the entanglement entropy of an interval is given by the length of the bulk geodesic that anchors at the AdS boundary on the interval endpoints. For sufficiently small intervals or sufficiently late times, geodesics will lie outside the infalling shell. Since this part of the geometry is that of a BTZ black hole, the entanglement entropy for such intervals will be the same as that of a thermal state. The bound (2.4.12) corresponds to geodesics whose central point just reaches the infalling shell (either because l is large enough, or because t is small enough) [26][111]. Similar results apply to the extremal surfaces computing the entanglement entropy of spherical regions in 2+1 and 3+1 dimensions. They reach the infalling shell at

$$t = R, \tag{2.4.13}$$

where R is the radius of the sphere [111][112][181]. We are thus led to propose a meaning for the position of the pulse in the radial direction as capturing the typical separation of entangled components of the QFT wavefunction. When the pulse is close to the boundary, entanglement is to be stronger between nearest neighbors, whereas the pulse falling towards the origin of AdS should represent entangled excitations flying apart. Analogous arguments were used in [182] to construct a holographic model for a local quench.

There is an important difference between the gapped-to-critical quenches studied in [22] and the holographic Vaidya model. In the former case, quantum correlations in the initial out-of-equilibrium state are short-ranged, of the order of the inverse mass gap before the quench. The Vaidya model represents a homogeneous action on the CFT vacuum which creates a plasma with long-ranged correlations. Actually, the entanglement entropy and two-point functions just after a sudden perturbation practically coincide with those of the CFT vacuum [26][111]. This fact implies that correlations are strongest among excitations sourced at neighboring points and decay with their distance as a power law. Hence, the minimum separation of entangled components coincides with the distance across which quantum correlations are stronger. It is this distance that we relate to the radial position of the shell. The long-ranged correlations are instead encoded in the AdS geometry interior to the shell.

2.4.1 Dephasing and self-reconstruction

An important notion in out-of-equilibrium physics is that of dephasing time. This quantity is the time that a system takes to lose quantum coherence. Since we are dealing with isolated systems, this notion will refer to the moment at which microscopic entanglement becomes inaccessible to macroscopic observables. After dephasing, the system is expected to relax to a stationary state, generically a thermal one.

The horizon effect (2.4.12) implies that, independently on how long we wait after a global quench in an infinite system, there will always exist sufficiently large regions where quantum-coherent correlations can be detected [22][26]. Namely, dephasing is never achieved at the global level. With the aim of providing a dual interpretation for the bouncing geometries studied in the previous section, we review now the different scenarios that can arise on a compact space. We assume that the initial state that triggers the field theory evolution presents stronger entanglement among neighboring degrees of freedom. The typical separation of entangled components will start growing as it does in the non-compact case. However, what happens after the maximal separation is achieved depends, crucially, on interactions.

The simplest case to consider is that of a noninteracting theory with linear dispersion relation living on a circle. Any initial state reconstructs itself periodically, preventing the system to equilibrate. When this state is homogeneous, this periodicity is

$$t_0 = \frac{L}{2v} \tag{2.4.14}$$

with L the length of the circle and v the propagation velocity of the excitations [178] [183]. We will refer to t_0 as propagation time, since it is the time that two particles moving apart with speed v on the circle take to meet again.

The pattern in an interacting field theory is expected to differ substantially. Let us consider a global quench of a field theory placed on a circle. Generically, as entangled excitations created at nearby points reach maximal separation on the circle and start approaching again, interactions will have randomized their relative phases preventing the initial state from reconstructing [178]. A strongly-interacting holographic version of this behavior is provided by the three-dimensional Vaidya model with global asymptotics. The absence of pressure induces the formation of a black hole by direct collapse, and the entanglement entropy of the semicircle achieves its final value at

$$t = \frac{L}{4}. \tag{2.4.15}$$

This time consistently equals the one needed by two particles that separate at the speed of light to reach opposite points on the circle.

The evolution of dephasing not only hinges upon the microscopic dynamics but also depends upon the structure of the initial state. Let us illustrate this statement with an easy example, by looking at the behavior of free systems with a nonlinear dispersion relation. Consider a periodic chain of coupled harmonic oscillators

$$H = \frac{1}{2} \sum_{i=1}^{N} \left[\pi_i^2 + \nu^2 (\phi_{i+1} - \phi_i)^2 \right] . \tag{2.4.16}$$

Its spectrum is given by non-interacting modes of momentum $p = 2\pi n/N$ with $n = 0, \ldots, N-1$ and frequency

$$\omega_p = 2\nu \sin \frac{p}{2} . \tag{2.4.17}$$

For $p \ll \pi$ the dispersion relation becomes linear, $\omega_p \simeq \nu p$. An initial wave packet constructed out of low momenta will reconstruct itself with period $t_0 = N/2\nu$, as in (2.4.14). No sign of relaxation will appear until enough time has passed to render important the nonlinearity of the dispersion relation. If the wave packet is centered around frequency $\bar{\omega}$, this time is [168]

$$t \simeq \frac{N^2}{\bar{\omega}} . \tag{2.4.18}$$

Afterward, the system dephases and tends to a stationary state.[13] The dephasing time can be much larger than the propagation time t_0 if $\bar{\omega}$ is chosen sufficiently small. It is important to emphasize here that this dependence of the relaxation process on the initial state is indeed seen in experimental setups [170] [171][172][175].

We can now put forward our major proposal: *collapses which require bouncing on the AdS boundary before forming a horizon are holographically dual to field theory evolutions where the initial state is partially reconstructed several times before achieving equilibration.*

In other words, their dephasing time is larger than the typical propagation time, in analogy with the case of the harmonic chain above. The periodic nature of the bouncing geometry is tantamount to the reconstruction, or revival, of the initial dual quantum state. Evidence for revivals has been observed experimentally in cold atoms systems [184]. At a theoretical level, it has been seen in quantum spin chains [185][186] and also in 1+1-dimensional CFTs [187]. We have argued that in an interacting field theory the presence of revivals should not be generic.However, that reasoning can fail for states with sufficiently small energy density. The finite size of the system introduces an intrinsic scale and, hence, the dynamical process can also depend on the energy density of the initial state. This is precisely what is found in the holographic models based on the collapse of a massless scalar profile [130]. When the mass of the scalar shell is above the threshold (2.3.8) for the formation of a large black hole, the shell is completely trapped behind a horizon by direct collapse. Bouncing with the AdS

---

[13] The stationary state generically differs from the canonical thermal equilibrium one since the occupation numbers of noninteracting modes are conserved along the evolution, and should rather be described by a Generalized Gibbs Ensemble that takes this new infinite set of conserved charges constraining the dynamics of the system into account.

boundary is only required when the final black hole to be formed is small.

In the same way that an infalling scalar pulse is to be holographically interpreted as a growing separation between entangled excitations, the stages of the evolution when it moves towards the AdS boundary should represent entangled excitations joining again. This can be neatly seen using a thin shell of null dust that travels outwards and reaches the boundary at $t=0$. The same reasoning that for an infalling shell sets the bound $t_{th} = l/2$ leads now to

$$0 \leq l \leq -2t \,, \tag{2.4.19}$$

for the size of intervals producing a thermal result for the entanglement entropy. Hence their size decreases as the system evolves towards $t=0$, as can be predicted from the qualitative quasiparticle picture of Calabrese & Cardy.

A very nontrivial support for this picture comes from the periodicity of the scalar pulse in the bulk. From the numerical simulations, one can see that its evolution from the boundary to the center and back completes a full roundtrip with a period of approximately π (see for example the inset in figure 2.1a). Now, recalling that in the gravitational system we have fixed the radius of the boundary sphere to unity, the expected reconstruction time (2.4.14) is

$$t_0 = \frac{L}{2} = \pi \tag{2.4.20}$$

where $L = 2\pi$ is the length of an equator. As we have mentioned in section 2.3, the exact periodicity is slightly bigger than π and this delay increases with the amplitude of the pulse. We will relate this fact to the presence of interactions in section 2.5.1.

2.4.2 Broadness versus time span

In our setup, no reference is made as to how the initial state that triggers the evolution is generated. In order to understand the implications of broad scalar profiles, it is however useful to discuss several characteristics of field theory perturbations that can holographically relate to them.

To gain insight, we can resort again to the familiar case of the Vaidya metric

$$ds^2 = \frac{1}{\cos^2 x}\left[-\left(1 - m(v)\frac{\cos^3 x}{\sin x}\right) d^2v + 2dvdx + \sin^2 x \, d\Omega_2^2\right] \tag{2.4.21}$$

with v an Eddington-Finkelstein infalling coordinate. We choose a mass function satisfying

$$m(v) = \begin{cases} 0 & v < -\Delta t \,, \\ M & v > 0 \,. \end{cases} \tag{2.4.22}$$

It represents the build up of an energy density M in a finite time span Δt starting from the CFT vacuum. The null dust shell sourcing the metric (2.4.21) has support in the region $v \in [-\Delta t, 0]$. Upon transforming to the Schwarzschild coordinates (t, x), the shell exhibits a finite broadness in the radial direction.[14] This is shown in figure 2.8a, where the intersection of a succession of constant t slices with the location of the shell, highlighted in yellow, determines its radial localization. Its profile at several t slices is plotted in figure 2.8b.

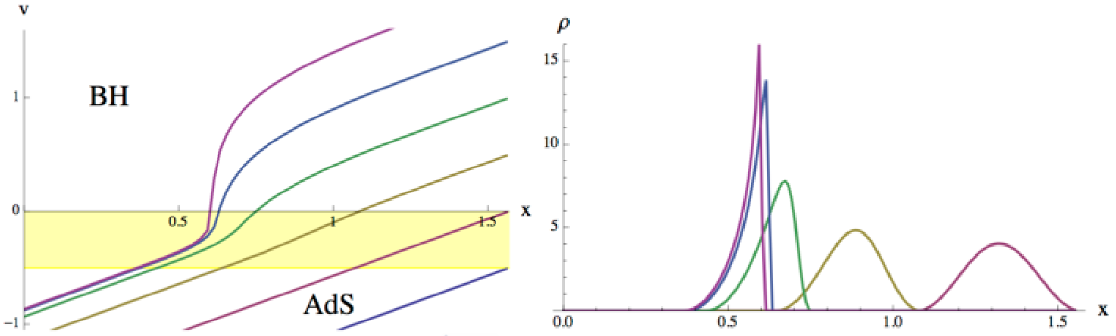

Figure 2.8: Left: intersection a null dust shell with $\Delta = 1/2$, signaled in yellow, with the lines of constant $t = -0.5, 0, \ldots, 2$ in the (v, x) plane. Right: mass distribution function at the same t slices.

The mass distribution function in figure 2.8b corresponding to $t = 0$ provides the analogue of the initial data we are dealing with in this chapter. Its value at a given x reflects the density of excitations created at a prior time

$$t \approx x - \pi/2 \leq 0\,. \tag{2.4.23}$$

The earlier some excitations have been created, the further entangled components are able to fly apart and the deeper their holographic representation reaches in the x direction. We will adopt this point of view in order to interpret the scalar profiles, as sketched in figure 2.9. Hence, the dual field theory state associated to a broad pulse should describe a configuration with entanglement over many length scales.

The field theory dual to the collapse processes we are considering is in a pure state along the complete evolution (see below) [26][178]. One pertinent question is: how much correlation exists between the components x_1 and x_2 that build up the profile in figure 2.9a? Let us recall the evolution of the initial profile (2.3.9), which is composed of two sharply localized subpulses. When the overlap between subpulses is negligible, the gravitational dynamics renders them transparent to each other (see figure 2.2b). This is however not the case for the profile in figure 2.2a, where the pulses have a small overlap. Both effects point to the existence of entanglement among the adjacent components of the profile in a way that grows with their proximity.

On general grounds, the time that a quantum system takes to dephase should depend on the amount of strongly correlated components it contains, rather than on the total energy density. According to our interpretation, the height in $\rho(0, x)$ provides a qualitative measure of the number of initially strongly correlated excitations. Hence the time for horizon formation, to be related with the dephasing time in the dual field theory, must be influenced by

---

[14] We refer the reader to section 5.7 for a throughout discussion of this coordinate change in the case of the four-dimensional charged Vaidya metric.

this value. This is indeed what we find in figure 2.9b, where we plot the evolution of three different pulses whose initial mass distributions can be seen in the inset. The blue one has half the broadness of the other two. It coincides with the black one in the value of the initial amplitude and with the red one in the total mass. The time of horizon formation is very similar for the pulses with the same amplitude (blue and black). However, when we compare pulses of the same mass, it is much longer for the broader one (red).

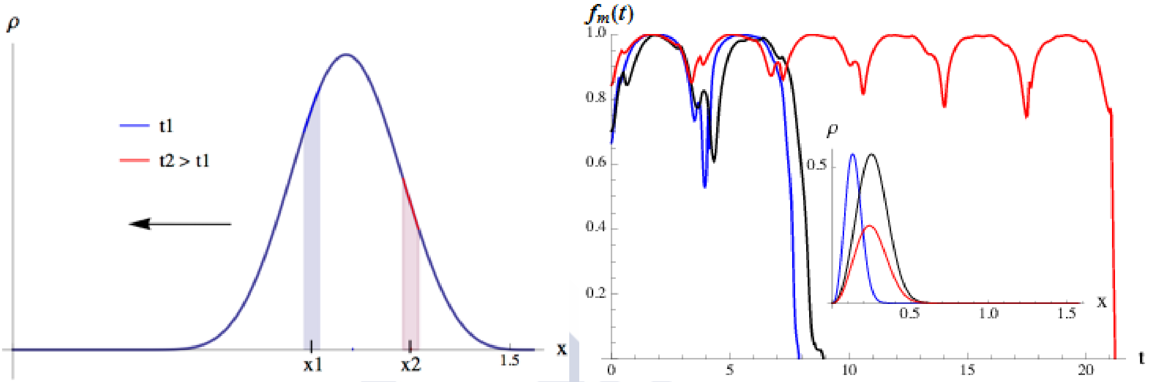

Figure 2.9: Left: Excitations sourced during small time intervals around $t_1 \sim x_1 - \pi/2$ and $t_2 \sim x_2 - \pi/2$. Right: Evolution of $f_m(t,x)$ for several pulses: $\sigma = 0.1$ and $\mathcal{M} = 0.035$ (blue), $\sigma = 0.2$ and $\mathcal{M} = 0.066$ (black) and $\sigma = 0.2$ and $\mathcal{M} = 0.035$ (red). In the inset we plot the initial mass density distribution for each pulse.

2.5 Entanglement entropy

Saturation of a subsystem's entanglement entropy to its thermal equilibrium value provides a necessary condition for the subsystem to have thermalized.[15] With this motivation, we will employ the HEE prescription to characterize the CFT$_3$ state dual to the bouncing geometry.[16] As entangling region, we will choose a two-dimensional spherical *cap*

$$C = \{x \in \mathbb{R} \times S^2 : t = t_0, \theta \leq \theta_0, \varphi \in [0, 2\pi]\}, \tag{2.5.24}$$

where θ_0 denotes the cap opening angle. The spherical symmetry of the gravitational background dictates that the entangling surface σ_C is parametrized as

$$\sigma_C = \{(t(\theta), x(\theta), \theta, \varphi) \in AdS_4 : \theta \in [0, \theta_0], \varphi \in [0, 2\pi]\} \tag{2.5.25}$$

where we have allowed for a nontrivial embedding of σ_C in the timelike direction, being the geometry time-dependent. The embedding functions $t(\theta), x(\theta)$ will be subjected to the boundary conditions

$$x'(0) = 0, x(\theta_0) = \pi/2 \tag{2.5.26}$$

$$t'(0) = 0, t(\pi/2) = t_0, \tag{2.5.27}$$

---

[15] See section 1.1.

[16] See section 1.1 for and introduction to entanglement entropy and section 1.2.4 for an introduction to entanglement entropy in holography.

where , with no loss of generality, we assume $\theta = 0$ to correspond to the entangling surface tip. Since the entanglement entropy is ultraviolet divergent, we must choose a suitable regularization. The entanglement entropy of a cap in the AdS$_4$ vacuum has been computed in [188], with the result

$$\text{Area}(\sigma_C) = 4GS_C = 2\pi\left(\frac{\sin\theta_0}{\epsilon} - 1\right)\,, \tag{2.5.28}$$

where the ultraviolet cutoff $x \leq x_m$, $\epsilon = \cot x_m$ has been introduced. Threfore, a suitably regularized entanglement entropy in a generic time-dependent setup is provided by

$$S(t,\theta_0) = \frac{2\pi}{4G}\left(\frac{\text{Area}(\sigma_A)}{2\pi} - \frac{\sin\theta_0}{\epsilon}\right). \tag{2.5.29}$$

Smoothness of the gravitational background at $x = 0$ implies that σ_C is both homologous to C and $\bar{C}$. As a consequence, $S_C = S_{\bar{C}}$, and we are modelling holographically the unitary evolution of a pure state, even if at $t \to \infty$ the geometry relaxes to a static Schwarzschild black hole [26][178]. Furthermore, this equality also implies that it suffices to consider caps with $\theta_0 \leq \pi/2$ as entangling regions.

An important remark is in order. The spacetime region covered by the (t, x) coordinate system does not reach behind the apparent horizon. However, it has been shown that the extremal surfaces computing entanglement entropy in Vaidya models can cross both the event *and* the apparent horizons [26]. They do so for boundary times and entangling regions with sizes larger than the scale set by the collapsing shell, which is proportional to $\mathcal{M}^{-\frac{1}{3}}$. Since we are focusing on scalar field configurations for which this scale is larger than the size of the boundary sphere -as these are the only ones giving rise to a bouncing geometry-, we find natural to assume that our extremal surfaces will not reach the apparent horizon and, as a consequence, that our coordinate system suffices to describe them.[17]

Having clarified our strategy, let us show some results. In figure 2.10 we plot the entanglement entropy evolution for a bouncing geometry that avoids gravitational collapse. The scalar field dynamics have both a pulsating and a radially localized component. Consistently, two distinct periodicities, $\pi/3$ and π, are clearly distinguished in the entanglement entropy oscillation.

In the next subsections, we will analyze the most relevant features of the holographic entanglement entropy evolution. Our aim is twofold: we want to learn about the non-equilibrium dynamics of finite-sized isolated systems at strong coupling and, at the same time, explore the holographic dictionary in dynamical situations.

2.5.1 Early time dynamics

We shall start our analysis by focusing on the growth of the entanglement entropy as the scalar pulse first falls towards the interior. To that purpose we consider narrow initial profiles localized close to the boundary, as described by (2.2.3).

---

[17] While the existence of entangling surfaces probing inside the apparent horizon is a common feature of Vaidya models, there exist realistic collapse scenarios where this property seems to be absent [189].

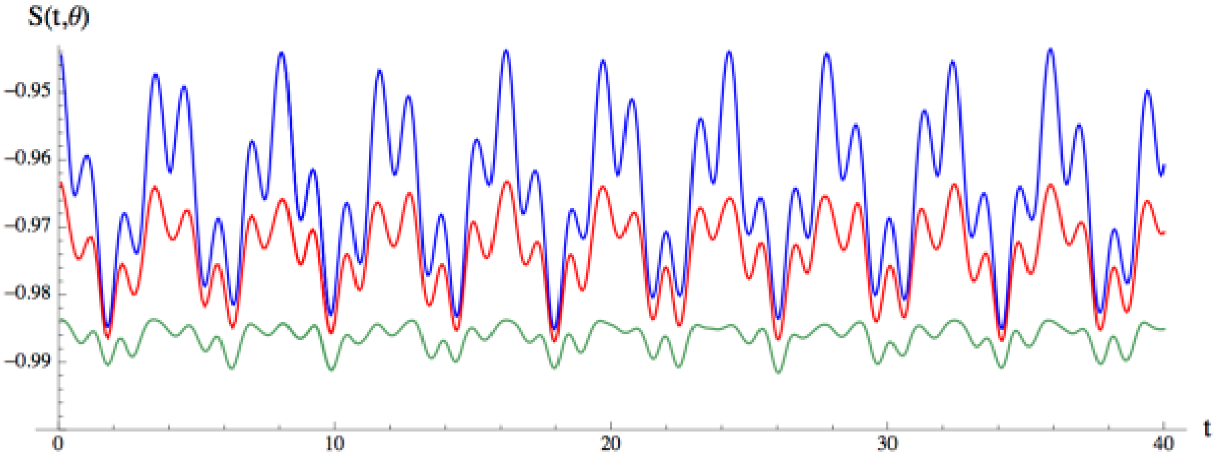

Figure 2.10: Entanglement entropy oscillation for an initial profile (2.2.2) with $\sigma = 0.4$ and $\mathcal{M}=0.09$. Different colors correspond to caps with opening angle $\theta_0=0.9, 1.2, 1.5$.

In figure 2.11a we compare two well-localized pulses of the same broadness but different amplitudes. One of them gives rise to a black hole of the total mass by direct collapse ($\mathcal{M}=0.3$), while the other requires three bounces for the emergence of an apparent horizon ($\mathcal{M}=0.012$). For the sake of comparison, we have rescaled the entanglement entropies of the latter case such that they coincide with the former ones at their maxima. We find no significant difference between the entanglement entropy growth to its first maxima for the small mass pulse and to its final values for the direct collapse one. Pursuing this line, in figure 2.11b we compare a one-bounce ($\mathcal{M}=0.014$) with a many-bounce pulse ($\mathcal{M}=0.008$) using the same rescaling of entropies as before. In this case, there is a perfect match in the growth of the entanglement entropy for both pulses. The decrease to the subsequent minimum also agrees. The only significant difference is the time that $S(t,\theta)$ spends at its maximum, which grows with the mass.[18]

These results allow us to sharpen the dual interpretation. The early time dynamics proceeds as in non-compact space. Namely, the evolution of the entanglement entropy is quantitatively well described by the free-streaming model, where the entangled components of the dual state separate at the speed of light. The red curve in figure 2.11a illustrates this. This curve gives the value of the entanglement entropy at $t=\theta_0$, and very approximately signals the moment at which $S(t,\theta_0)$ saturates to its maximum. Moreover, we have compared the entanglement entropy growth for narrow shells which form a black hole by direct collapse and Vaidya configurations of approximately the same broadness and mass, observing no important difference again.

The effective propagation of entanglement at the speed of light implies that the pairs of entangled excitations have reached their maximal separation on the two-sphere at $t\approx\pi/2$.

---

[18] A detailed analysis of the dependence of this delay time with the energy density can be found in section 3.2.

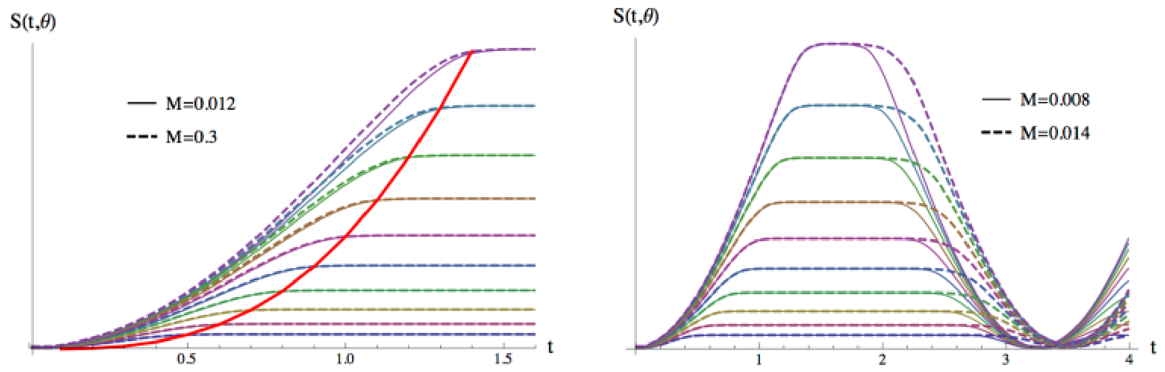

Figure 2.11: Entanglement entropy evolution for several pulses with $\sigma = 1/16$. Different colors correspond to caps with $\theta_0 = 0.5, 0.6, .., 1.4$. In each graph, the entanglement entropy values for the lower mass pulse have been rescaled to coincide with those of the larger mass one at their maxima for the sake of comparison. The red line on the left figure gives, for the pulse with larger mass, the entanglement entropy at $t = \theta_0$.

However, the period needed by the scalar shell to complete a bouncing cycle is always above, although close to π. It is practically π for pulses of small mass and increases for more massive ones, as can be seen in figure 2.11b.

A dual heuristic picture for this effect could be as follows. Strong interactions might have generated a phase shift on the field theory wavefunction that effectively induces a larger radius for the two-sphere. Since the entanglement entropy depends on the actual size of the region considered, the only natural imprint of the phase shift on the entanglement entropy would be to prolong the time interval that it keeps at its maximum values. Being an effect due to interaction, it should increase with the energy density of the state. This precise pattern is what we observe in figure 2.11b.

2.5.2 Holographic evolution

In this subsection, we study the evolution of the entanglement entropy based on radially localized pulses. The collapse of narrow pulses is led by an energy transfer towards high momentum modes, such that a fraction of the pulse develops a peak sharp enough to become trapped by an emerging horizon. The remaining pulse is swallowed in a stepwise fashion by the growing horizon until a final black hole of the total scalar shell mass sets in.

Let us analyze first the evolution of the entanglement entropy before a horizon emerges. Remarkably, we find that the entanglement entropy of large regions not only oscillates but its maxima in each bouncing cycle slightly decrease. We illustrate this effect in figure 2.12a with a narrow pulse which starts close to the origin and requires three bounces to generate a horizon. We showed in section 2.3 that when the pulse reaches the origin, two opposite effects take place. Namely, together with the sharpening of a fraction of the pulse, the rest tends to increase its radial dispersion (see figure 2.1a). As a result, the extremal surfaces associated to the entanglement entropy maxima of large boundary regions intersect, at each successive bounce, a growing and more spread fraction of the scalar pulse. This fact causes the decrease in area and, hence, on $S(t,\theta)$, as it is visible in figure 2.12a.

Although this is a small effect, we find it relevant. It has been suggested that the entanglement entropy of half the space could provide a definition of coarse-grained entropy [178]. Despite the oscillations, we might have expected that the maxima of the entanglement entropy monotonically increase along the evolution, and their value still serves as a notion of coarse-grained entropy. We have seen that not even this is true in general.

The radial minimum of the metric function $f(t,x)$ is a useful indicator of how far from horizon formation the gravitational system is at a given time slice. The example plotted in figure 2.12a suggests that the maxima of the entanglement entropy do not necessarily relate to the minima of $f(t,x)$. Since extremal surfaces do not lie in a constant t slice in our dynamical geometries, we have to analyze what region they explore deep in the bulk before reaching the previous conclusion. Figure 2.12b shows a projection on the (t,x) plane of the surfaces whose areas give the entanglement entropy maxima of large caps in the last pre-horizon cycle. They stay indeed well before the time slice where the minimum value of f drops to zero. The area of an extremal surface seems to be maximized by a competition between reaching deep in the bulk and keeping outside the traveling shell. After the turbulent mechanism has acted on the scalar pulse, the area maximizing configuration arises slightly before $f_m(t)$ drops to its local minimum. Indeed, the minima along the time evolution of $f_m(t)$ describe a different situation: the moments at which a well-localized peak of the scalar profile is at its closest approach to the origin. Hence the entanglement entropy turns out not to be precisely correlated with the moment at which a horizon emerges. In particular, it decreases the instants before an apparent horizon first forms.

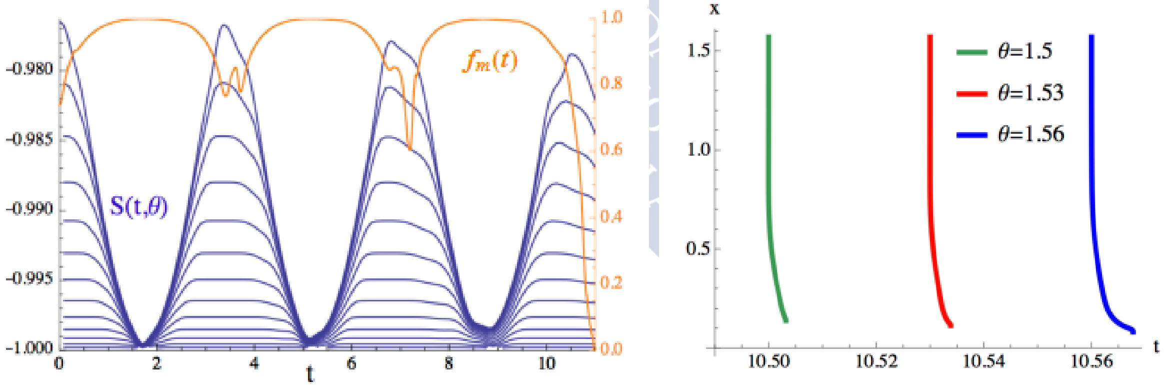

Figure 2.12: Scalar profile (2.2.2) with $\sigma = 0.1$ and $\mathcal{M} = 0.012$. Left: Evolution of the entanglement for caps with $\theta = 0.5, \ldots, 1.5$. We have superposed $f_m(t)$ in orange. Right: Projection on the (t,x) plane of the entangling surfaces responsible for the entanglement entropy maxima of large caps in the last bouncing cycle before the horizon forms.

It is interesting to describe the behavior of the extremal surfaces with respect to the t slicing. As long as they do not reach the scalar shell, they live on slices of constant t. If an extremal surface intersects a fraction of the falling pulse, the involved part deviates from constant t

towards smaller values of the time coordinate. On the contrary, it deviates towards bigger values when it intersects a fraction of the pulse traveling towards the AdS boundary. This is the case in figure 2.12b, where the projections in the (t, x) plane show that the extremal surfaces tilt towards larger values of t at their inner portion. Indeed, they reach the part of the scalar profile not trapped by the emerging horizon, and which has started to move away from the origin before the horizon neatly forms.

In figure 2.13, we have plotted the post-collapse evolution of the entanglement entropy. Using a grid of $N = 7 \times 10^4$ points we could complete five oscillations beyond horizon formation with a relative mass loss below 3%. The oscillations of entanglement entropy neatly reflect the impact of the horizon, decreasing their amplitude at a pace correlated with the approach of the horizon to its final location. The maxima of $S(t, \theta)$, whose value dropped along the pre-collapse phase, should rise to the result prescribed by a black hole of the total mass. Indeed, we observe that the maxima slowly but monotonically increase along the post-collapse cycles. The green dashed line in figure 2.13 signals the value that the entanglement entropy of a $\theta = 1.5$ cap should reach. Its slight decrease just reflects that we did have into account the effective mass loss of the numerically simulated solution.

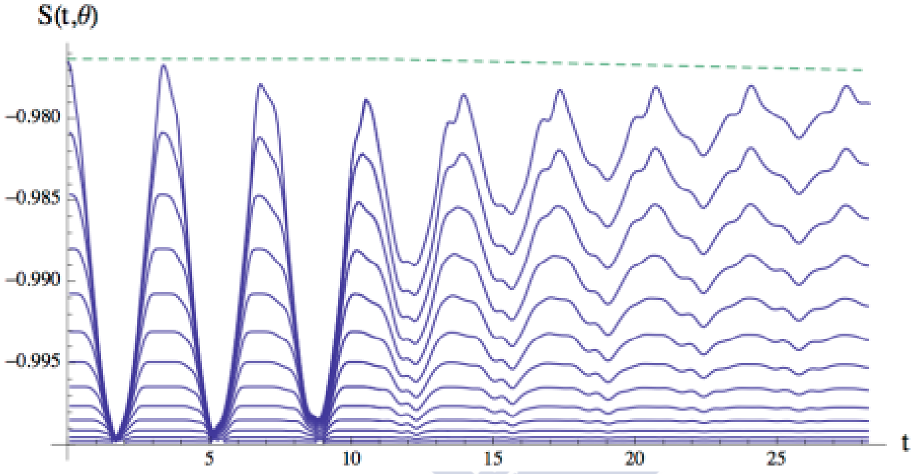

Figure 2.13: Post-collapse evolution of the entanglement entropy for the same case plotted in figure 2.12. The time for the first collapse is $t_h \approx 11$, and at around $t = 28$ the horizon radius is 83% of its final value. The green line gives $S(\theta = 1.5)$ for a static black hole of the total mass, where we did have into account the numerical mass loss along the evolution.

The traveling pulse keeps radial localization along the first five post-collapse cycles. Radial localization is manifest in the time span of the oscillations, which is close to π before and after a horizon first forms. Despite this, the radial spread of the profile progressively increases (see figure 2.5a for a similar example). This spread can be detected in the emergence of an additional modulation in $S(t, \theta)$ with a shorter period, consistent with $\pi/3$. Following the argumentation in section 2.4, this suggests that while part of the system dephases in correspondence with the appearance of an apparent horizon, part of it still retains quantum coherence. Moreover, a typical separation linked to the radial position of the pulse can be associated with the remaining entangled degrees of freedom. The pattern that emerges is that the system undergoes a stepwise loss of quantum coherence, triggered by the dephasing of a subset of the degrees of freedom.

Before closing this section, we would like to draw attention to the striking similarity between the entanglement entropy oscillations shown in figure 2.13, and those of a different, albeit also nonlocal, operator of the XY quantum spin chain studied in [185] (see figure 1).

2.5.3 Behavior across critical points

A very relevant characteristic in the collapse of narrow pulses is that the fraction of energy in the sharp front which generates the horizon can become arbitrarily small. The transition between processes with n and n+1 bounces happens indeed as the energy of the trapped front vanishes. Therefore, it becomes relevant to investigate the behavior of the entanglement entropy across these critical collapses. The question we want to answer is whether the appearance of a horizon, no matter how small, leaves an imprint in the subsequent evolution of the entanglement entropy. On line with the results in the previous subsection, the answer we find is negative.

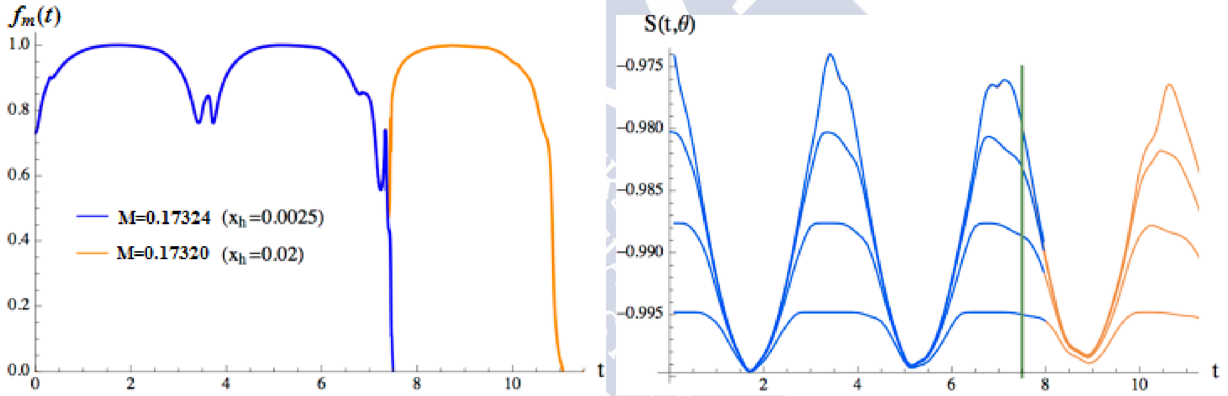

Figure 2.14: Two pulses with $\sigma = 0.1$ and masses slightly above (blue) and below (orange) critical collapse. Left: minimal radial value of $f(t, x)$. Right: Entanglement entropy evolution for caps with $\theta = 0.9, 1.2, 1.4, 1.56$. The green line marks horizon formation time for the above-critical pulse.

In figure 2.14a we plot the evolution of $f_m(t)$ for two initial profiles (2.2.2) with $\sigma = 0.1$ and masses $\mathcal{M} = 0.17324$, $\mathcal{M} = 0.1732$. The first one generates a horizon after two bounces with radius $x_h = 0.0025$, which is 4.4% of the Schwarzschild radius associated with its total mass. A trapped horizon emerges for the latter after three bounces with a radius one order of magnitude larger, $x_h = 0.02$, which is 35% of its corresponding Schwarzschild radius. Hence the masses of the two profiles are close to the critical value for the transition between two and three bouncing pre-horizon cycles, being the former slightly above and the latter slightly below. Pursuing the evolution of the profile above critical past the time when $f_m(t)$

abruptly drops, at $t_h \approx 7.5$, is numerically very demanding.[19] As seen in figure 2.14b, there is no difference between the oscillations of the entanglement entropy in the two cases, both before t_h and shortly afterward, even for spherical caps very close to a hemisphere.

2.5.4 Dependence on the initial state

We analyze now how the evolution of the entanglement entropy is influenced by the shape of the scalar profile, which according to our arguments mainly relates to the entanglement configuration of the initial state. We have focussed above on sharply localized pulses. We will consider now the effect of an increasing broadness by taking as example the two $\sigma = 0.25$, $\sigma = 0.6$ pulses studied in figure.2.6.

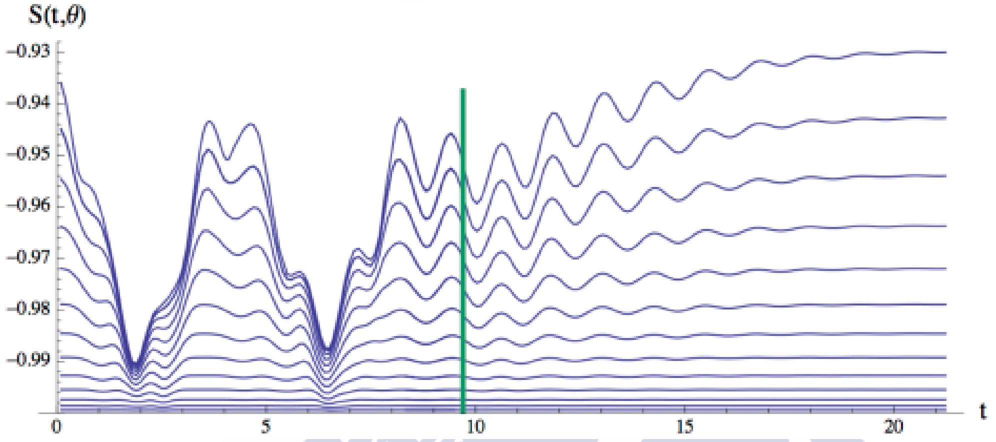

Figure 2.15: Entanglement entropy equilibration for caps $\theta = 0.5, .., 1.5$ derived from an initial scalar profile (2.2.2) with $\sigma = 0.25$ and $\mathcal{M} = 0.036$. The time at which $f_m(t) < 6 \times 10^{-3}$ has been signaled in green.

The $\sigma = 0.25$ pulse exhibits some degree of radial localization prior to the emergence of an apparent horizon, while its post-collapse dynamics is that of a quasi-standing wave (see figure.2.6a). These two regimes are clearly distinguished by the entanglement entropy, which we show in figure 2.15. For $t < t_h$ (signalled in green), $S(t, \theta)$ oscillates with a period $T > \pi$ and, furthermore, its value at the local maxima does not increase with time. A faster modulation is clearly appreaciated on top of these characteristic features of narrow pulses. For $t \geq t_h$, only oscillations with periodicity $T \approx \pi/3$, characteristic of radially delocalized dynamics, are present. They are in one-to-one correspondence with the minima of f shown in the inset of figure 2.6a. The damped nature of the post-collapse evolution is reflected in the decrease of the entanglement entropy oscillation amplitude. Its maxima monotonically approach the equilibrium value corresponding to a Schwarzschild black hole of the total mass. The approach is more efficient in this case than in the narrow pulse of figure 2.13, which retains some radial localization along the post-collapse evolution.

---

[19] With a grid of $N = 10^5$ points we could only prolong one further time unit while keeping an acceptable precision.

The $\sigma = 0.6$ scalar pulse in figure 2.6b is radially delocalized along its complete evolution. Its mass is $\mathcal{M} = 0.4\mathcal{M}_{\text{th}}$. Hence it develops quite massive subpulses that experience a significant time-delay in climbing their own gravitational potential. This favors the recombination of subpulses into a single very broad peak, as can be observed in the first two snapshots of figure 2.16a. At some point, this dynamics gives way to the establishment of a strongly damped oscillation (this time corresponds to the orange vertical line in figure 2.16b). The third snapshot of the mass distribution profile corresponds to this regime. At $t = t_h \approx 11$,[20] (signalled in green in figure 2.16b) the whole scalar pulse has been almost completely trapped by the emergent apparent horizon.

The evolution of the entanglement entropy for this initial data is shown in figure 2.16b. In striking contrast with the examples we analyzed before, the $S(t,\theta)$ maxima do not decrease with time. The amplitude of the entanglement entropy oscillations starts decreasing once the damped quasi-stationary regime sets in. At t_h, the entanglement entropy has practically reached its final equilibrium value. Throughout the entire evolution, the oscillations have a period $T \gtrsim \pi/3$.

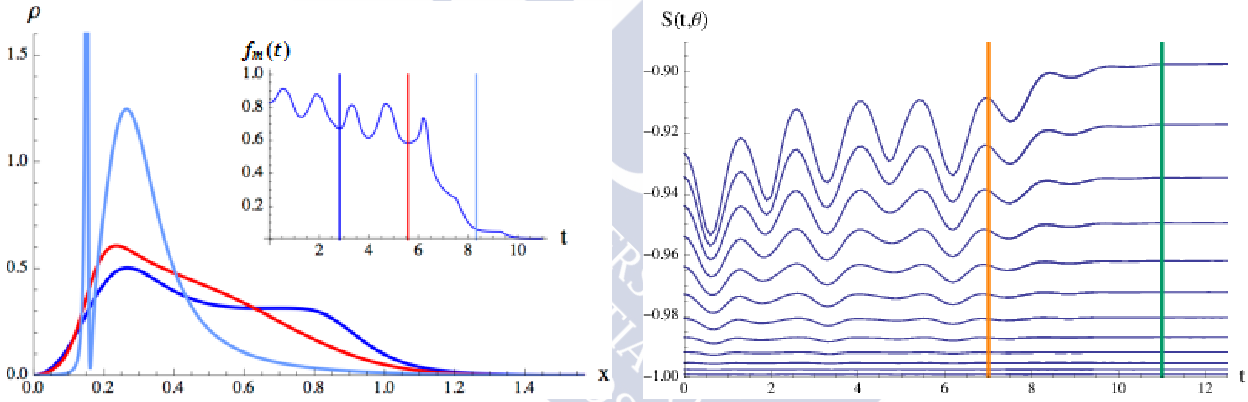

Figure 2.16: Initial profile (2.2.2) with $\sigma = 0.6$ and $M = 0.1538$. Left: three snapshots in the evolution of the scalar pulse. Right: entanglement entropy for caps $\theta = 0.5, .., 1.5$. The time at which the quasi-stationary regime sets in has been signaled in orange and t_h in green.

Finding a qualitative field theory explanation for this period seems difficult. Its gravitational origin is in the internal dynamics of the scalar profile rather than on the radial propagation. From the field theory point of view, this hints towards having its root in the strong coupling dynamics of the out-of-equilibrium state.

We have argued that the collapse of narrow pulses describes a stepwise relaxation process, triggered by the dephasing of a subsystem. The evolution of broad pulses suggests a quite different mechanism. The dynamics leading to the strongly damped oscillations involves, in this case, the whole system. We proposed in section 2.4 that broad pulses correspond

---

[20] We define t_h as the time such that $f_m(t \geq t_h) \leq 6 \times 10^{-3}$.

configurations with entangled excitations over many length scales. Hence we conclude that, in such situation, dephasing triggered by a subsystem is disfavored. Moreover, when the mass of a broad pulse drops below a certain threshold, no horizon appears to be formed [135]. This fact would indicate that reaching a stationary state is harder for states of small energy when this involves the complete system, than when it affects only a subsystem. For the former case, and under the assumption of a spherically symmetric collapse, the dual field theory seems never to lose quantum coherence below a certain energy density.

Chapter 3

Holographic quantum revivals in AdS$_3$

3.1 Summary

In this chapter, we undertake the analysis of three-dimensional bouncing geometries, which we put into correspondence with quantum revivals in two-dimensional CFTs. We perform a detailed analysis of the salient similarities and differences between the asymptotically global AdS$_3$ and AdS$_4$ bouncing geometries that were discussed in chapter 2. See section 2.2 for a discussion of the Einstein-scalar model we are using.

In section 3.2, we comment on the dependence of the revival time t_r on the spacetime dimension, the energy density of the initial state and the scalar pulse shape. As discussed in chapter 1 (section 1.3), AdS$_3$ Einstein-Hilbert has stricking differences with respect to its higher-dimensional counterparts, and this bears crucial consequences for the dynamics of the bouncing geometries. We illustrate how in the three-dimensional instance it is perhaps even possible to obtain revival processes with an arbitrary t_r. We comment on the phenomenology of initial states with energies above-but-close to the mass gap, explaining that they show a non-monotonic thermalization time that displays a possibly chaotic structure. We comment on the existence of the stability band: a region above the mass gap where thermalization is halted, up to our accessible simulation times. We illustrate the gravitational mechanism behind this phenomenon by discussing in detail one example.

In section 3.3, we compute the entanglement entropy in the CFT$_2$ states dual to these new bouncing geometries, discussing the interpretation in of our results 3.4. We illustrate that, unlike the three-dimensional delayed thermalization processes analyzed in chapter 2, in the two-dimensional case the revival time t_r and the dephasing time t_c emerge as two well-distinguished time scales as the initial energy density is increased. Therefore, while at low energy density the entanglement entropy evolution is well described in terms of the free streaming of entangled excitations [22], as the energy density increases interaction effects change the pattern into a series of collapses and revivals with similar properties to those observed experimentally in a variety of systems [190, 191, 184, 192].

We demonstrate that, for narrow Gaussian initial data, the precise value of t_c always follows from assuming that entanglement propagates causally, and also address the dependence of the dephasing time t_c with the scalar field shell thickness, showing that broad Gaussian initial data provide a faithfull representantion of field theory actions with a finite time span. On the other hand, we establish clearly that the elongated revival time t_r we found is related to the strong gravitational redshift that sufficiently massive shells experience at the point of maximal implosion.

Finally, in section 3.5 we introduce two simple quantum-mechanical systems supporting coherent states that, just like the holographic CFTs under consideration, display a revival time that increases with the energy density.

3.2 Revival time

As in chapter 2, we are interested in gravitational collapse processes where a mater shell does not generate a trapped surface by direct collapse, but needs at least one bounce off the AdS boundary to do so. We will focus here on how the time invested on the first bounce depends on the mass and thickness of the initial shell, interpreting this time as that at which the initial out-of-equilibrium state of the dual CFT undergoes the first revival. We will consider either origin-centered (2.2.2) or boundary-centered (2.2.3) Gaussians as initial data.

An interesting question is how symmetry constraints influence the evolution of a system towards relaxation. With this motivation in mind, we will compare the phenomenology of scalar collapse in AdS$_3$ and AdS$_4$, dual respectively to a CFT on a circle and a sphere.

There exist important differences between three- and four-dimensional gravity with asymptotically global AdS boundary conditions, already at the level of static solutions: in AdS$_3$ there is a mass threshold for the existence of black holes [156]. For a unit length boundary S^1, curvature singularities are hidden behind a horizon only for masses above

$$\mathcal{M} = 1\,. \tag{3.2.1}$$

Static geometries with mass below threshold contain an unshielded conical singularity at their center. On the contrary, AdS$_4$ admits black holes of any positive mass.

This has important consequences for scalar collapse. In AdS$_4$ any thin shell appears to induce the formation of a black hole after a sufficient number of bounces off the boundary [130]. The number of bounces required for the emergence of trapped surfaces decreases with increasing mass[1] until, above some threshold value, this happens at the first implosion. The limiting line among these two situations is depicted in figure 3.1a. We observe that bouncing geometries are only obtained for quite small $\mathcal{M}$ [130, 135, 1]. Correspondingly, revivals in the dual CFT$_3$ happen for initial out-of-equilibrium states with an energy density per species clearly small compared to the system size.

---

[1] When a trapped surface emerges, it generically does not capture the complete shell. A fraction of it can yet escape to the boundary and require several further bouncing cycles to be completely absorbed.

In contrast to AdS$_4$, the eventual collapse of shells below the threshold (3.2.1) in AdS$_3$ could only end up forming a naked singularity. As far as we could push our numerical simulations, we have not found this to be the case. For low masses, the analysis of [159] points towards excluding the formation of such singularity in finite time. In these cases equilibration is never achieved and instead the dual field theory undergoes an infinite series of revivals. Even above the threshold (3.2.1), there is a small window where at least one bounce off the AdS$_3$ boundary is required before collapse [160]. Figure 3.2a shows the curve separating bouncing geometries in AdS$_3$ from trapped surface formation at the first implosion. Hence, holographic models of CFT$_2$ dynamics admit revivals for ratios of the energy density to the system size substantially larger than in higher dimensions.

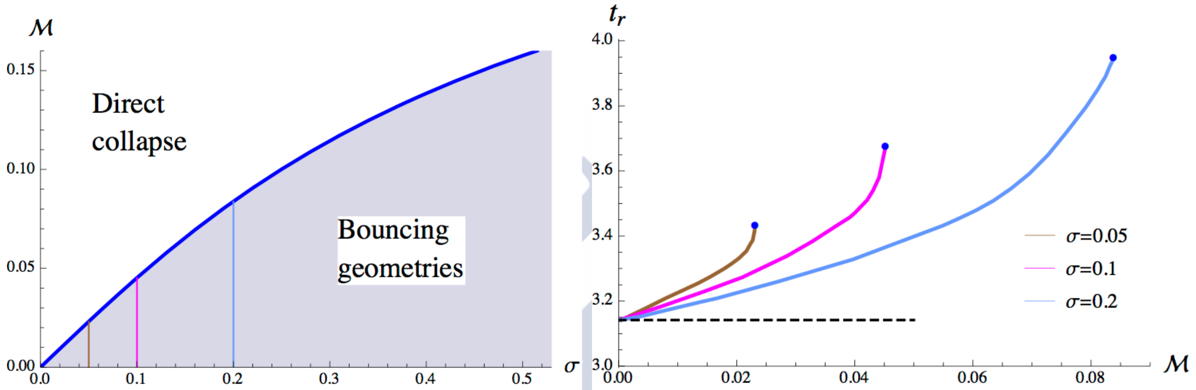

Figure 3.1: Left: Phase diagram for scalar collapse with initial data (2.2.3) in AdS$_4$. The shaded region signals processes requiring at least one bounce for collapse. Right: Dependence of the bouncing period with the mass for fixed $\sigma = 0.05, 0.1, 0.2$. The blue dots signal the threshold value for direct collapse. The dashed line is $\tau = \pi$.

For concreteness, we characterize the revival time as the time invested in completing the corresponding oscillation cycle of the function $f_m(t) = \min_x f(t,x)$. Generically, the shell motion is quasiperiodic and the revival time stays almost constant along the evolution. However, for AdS$_3$ shells close or above the black hole threshold, $\mathcal{M} \gtrsim 1$, the time span of successive bounces might vary. Therefore, to avoid ambiguities, we will denote with t_r the time elapsed in the first revival. Both in AdS$_3$ and AdS$_4$, the value of t_r tends to π for scalar pulses of low mass, $\mathcal{M} \to 0$. This is expected since a null ray originating at the boundary and traversing diametrically AdS returns to the boundary after a time $t = \pi$. The value of t_r monotonically increases with the shell mass, see figures 3.1b and 3.2b.

The mass window for the existence of bouncing geometries in AdS$_4$ closes down to zero as $\sigma \to 0$, see figure 3.1a. For this reason the revival time associated to thin pulses in AdS$_4$ is always approximately π. Pulses of intermediate broadness need small but finite masses for direct collapse. They can reach revival times that, although close, are appreciably larger than π. This phenomenology is illustrated in figure 3.1b.

The comparatively higher masses compatible with revivals in AdS$_3$ have a drastic impact on the allowed values of t_r. The revival time strongly increases for shells whose mass approaches $\mathcal{M} = 1$, see figure 3.2b. The increase is entirely due to the shell being kept by its own gravitational potential at the point of maximal implosion for a long time before expanding again. Pulses leading to revivals with $\mathcal{M}$ higher than one take extremely long to complete the first bounce. Our results suggest that t_r possibly diverges at the upper end of the mass window compatible with bounces. This is shown in the inset of figure 3.2b. The relevance of the mass window above the black hole threshold relies on providing transition processes between infinite revivals and fast thermalization in holographic CFT_2 models. Consistently with the AdS_4 results, it closes down in the $\sigma \to 0$ limit (see figure 3.2a).

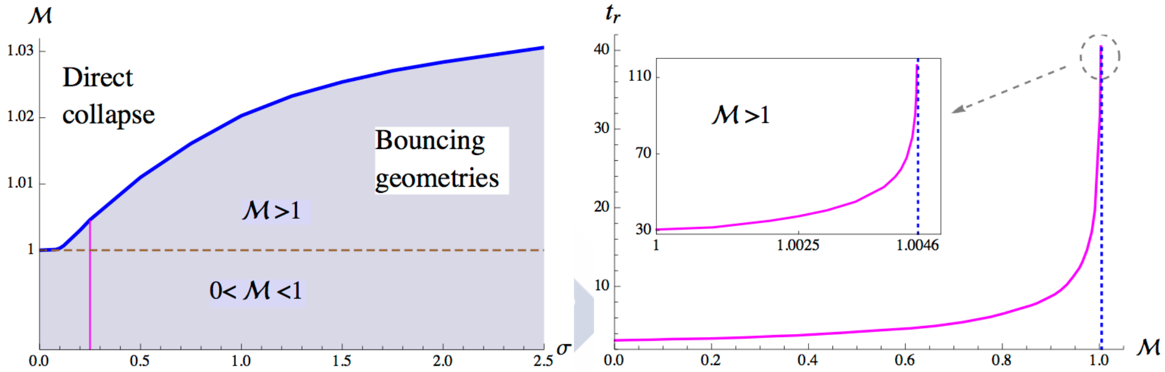

Figure 3.2: Left: Phase diagram for scalar collapse with initial data (2.2.3) in AdS_3. Right: Mass dependence of t_r for initial pulses (2.2.3) with $\sigma = 0.25$ in AdS_3. In the inset, detail of the plot in the small window above threshold compatible with bounces. The apparent change of slope is due to the rescaling of the vertical axes.

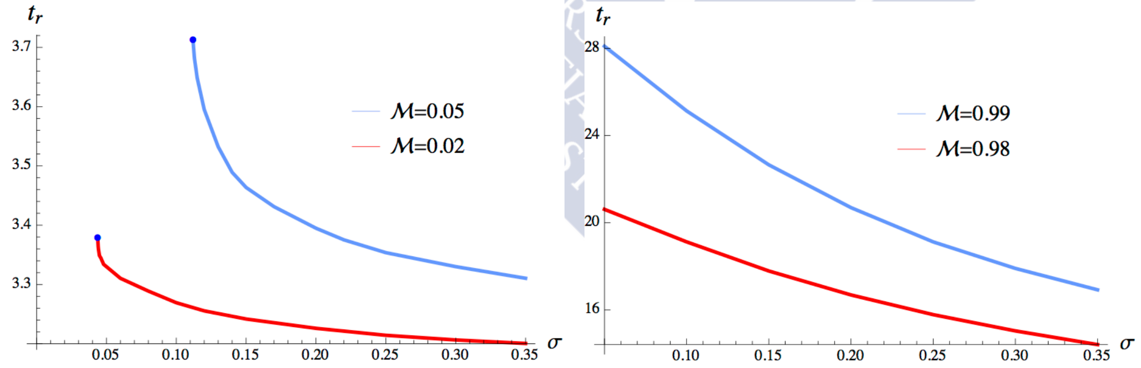

Figure 3.3: Left: Variation of t_r with σ for AdS_4 pulses of fixed mass $\mathcal{M} = 0.02, 0.05$. The blue dots signal the threshold value for direct collapse. Right: Variation of t_r with σ for AdS_3 pulses of fixed mass $\mathcal{M} = 0.98, 0.99$.

When AdS_3 pulses with $\mathcal{M} > 1$ implode without collapsing, they develop several extremely narrow spikes. Small differences in the initial pulse get amplified in this process and have an strong influence in the subsequent evolution. As a result, the periodicity of successive bounces shows a random behavior, a feature not observed in low mass pulses. While the time required to complete the first bounce exhibits a regular monotonic growth with $\mathcal{M}$, that of subsequent bounces can both increase or decrease with the shell mass. Also the number of bounces for collapse does not decrease smoothly with the mass: for the $\sigma = 0.25$ profiles reported in figure 3.2a, $\mathcal{M} = 1.004$ appears to need only one bounce for collapse, while $\mathcal{M} = 1.0045$ requires several. The described features point towards a role of chaos in the evolution of these AdS$_3$ pulses, a fact that was already noticed in [160].

Finally, it is interesting to notice that the time span of the first revival not only behaves smoothly as a function of the shell mass, but also of its thickness. Indeed, t_r decreases monotonically with σ, as shown in figure 3.3a and figure 3.3b for AdS$_4$ and AdS$_3$ pulses respectively.

3.2.1 Zooming into the $0 < \mathcal{M} - 1 \ll 1$ region

In this subsection, we want to elaborate further on the long-time dynamics of scalar pulses with masses right above the gap. With this aim in mind, we consider origin-centered Gaussian initial data (2.2.2) with $\sigma = 1/16$ and $\mathcal{M} = 1.00825$. Although being sharply located in position space, these initial data result in a bouncing geometry that do not collapse gravitationally during our simulation times. We employed a discretization grid with an initial resolution of $N = 2^{14} + 1$ points.

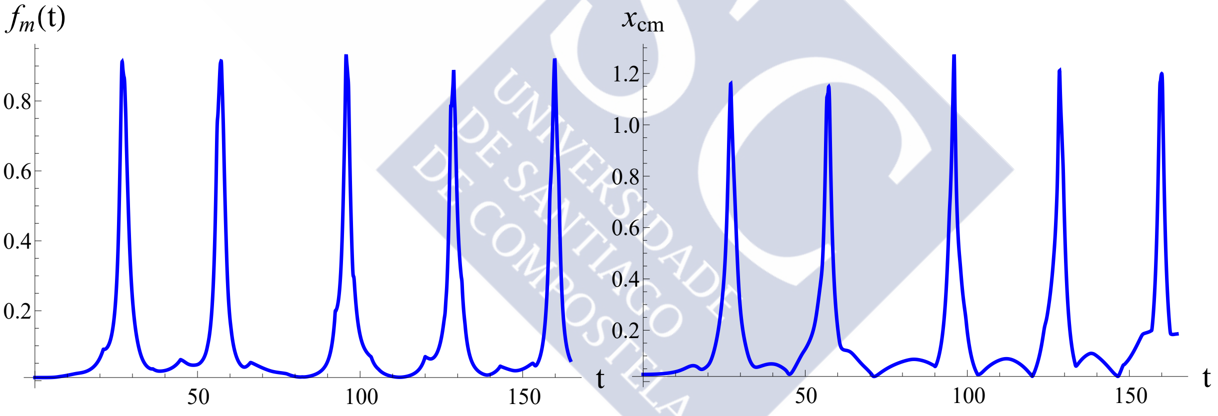

Figure 3.4: $f_m(t)$ (right) and $x_{cm}(t)$ (left) for the initial data described in the main text.

Since $\int_0^{\frac{\pi}{2}} dx\rho(t,x) = \mathcal{M}$, we can take the relation

$$\int_0^{\frac{\pi}{2}} dy\rho(t,y)y = x_{cm}(t)\mathcal{M} \tag{3.2.2}$$

as the definition of the center-of-mass of the energy distribution at time t [193]. We plot this quantity, together with f_m, in figure 3.4. Then, we sample the energy distribtution function $\rho(t,x)$ at times t such that $x_{cm}(t) = \pi/4$ and $\dot{x}_{cm}(t) > 0$, *i.e.*, the center-of-mass of the energy distribution is located at the midpoint between the origin and the asymptotic boundary, and its travelling from the former to the latter. The resulting $\rho(t,x)$ profiles are depicted in figure 3.5.

Several comments are in order. First, the initial scalar pulse takes a substantial time in climbing its own gravitational potential. In doing so, its shape is modified: note that, at $t = 26.0752$, the original Gaussian pulse has developed a fine substructure, and if fact looks like the superposition of two sharp Gaussian pulses with displaced centers. After the subsequent bouncing cycle, these two subpulses separate from each other and become clearly distinguishable, as the $t = 56.0774$ plot illustrates. Afterward, the sharpest pulse undergoes a process of energy focusing, becoming more localized in position space. At the same time, the other subpulse starts bouncing in opposition with respect to the sharp subpulse. This is clearly seen in the plot corresponding to $t = 94.8761$ in figure 3.5. Finally, at $t = 158.808$, we observe that a process of energy transfer has taken place between both subpulses, sharpening the former more dispersed subpulse. At this later time, the total mass of each subpulse is $\mathcal{M}_1 = 0.546375$ for the left one, and $\mathcal{M}_2 = 0.461875$ for the right one.[2] Individually, they don't have enough mass to collapse gravitationally. To form a black hole, a substantial energy transfer between both pulses would be needed. This energy transfer process seems to be disfavored by the dynamics in our example. In fact, the opposite scenario takes place: the more massive subpulse is losing energy as time passes. In this regard, we roughly have that $\mathcal{M}_1 \approx 0.87$ at $t = 94.8761$ and $\mathcal{M}_1 \approx 0.77$ at $t = 127.863$.

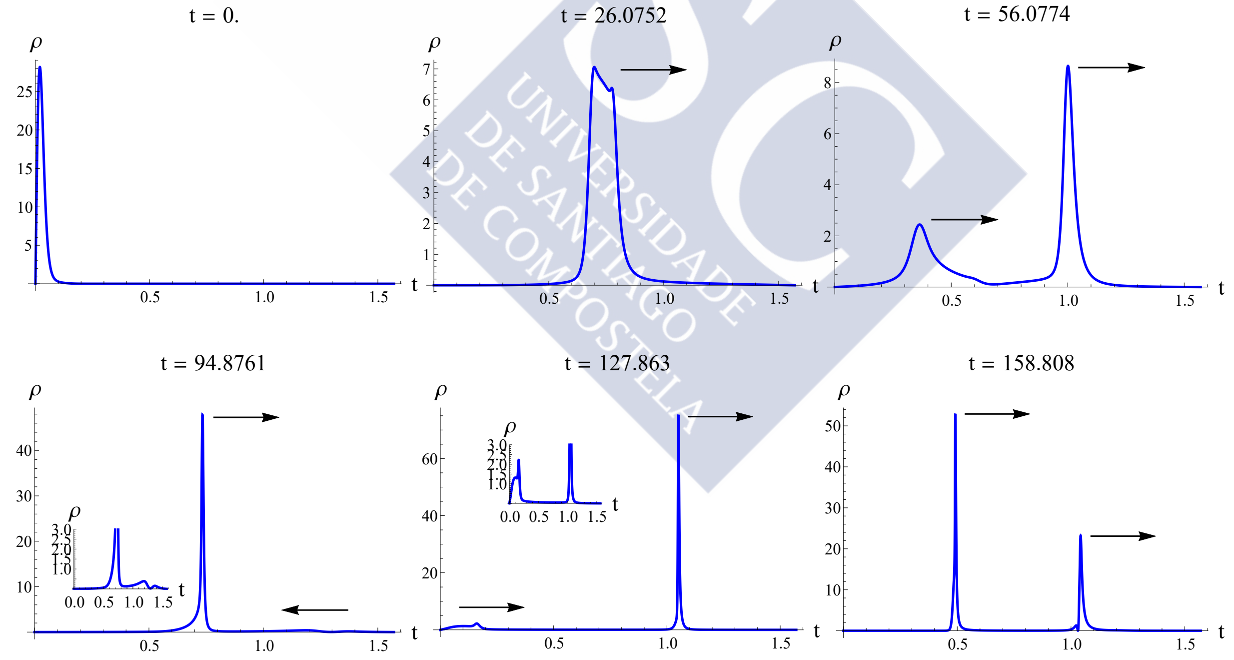

Figure 3.5: $\rho(t, x)$ at different snapshots of time for the initial data described in the main text. The propagation direction of each supulse has been signalled with a black arrow.

As we discussed in section 1.3, the effect of a sharp pulse breaking into two subpulses due

---

[2] We habe defined $\mathcal{M}_1 = \mathcal{M}(t, x = \pi/4)$, and $\mathcal{M}_2 = M - \mathcal{M}_1$. Here, $\mathcal{M}(t, x)$ is the mass aspect function.

to its gravitational self-interaction has also been observed in other theories with a mass gap in their black hole spectrum; in particular, in has been discussed to some extend in five-dimensional Einstein-Gauss-Bonnet gravity [229, 194]. The evidence available so far points to the fact that this effect is responsible for the existence of the stability band above the mass gap. Furthermore, as we have metioned, the non-monotonic nature of the collapse time upon lowering the mass for initial data above the gap must come from the fact the dynamics of this energy transfer shows some chaotic-like features.

3.3 Entanglement entropy

The construction of a detailed holographic dictionary between the gravitational dynamics and the field theory evolution is far from straightforward. In the collapse backgrounds there is no timelike Killing vector that could extend field theory constant time slices into the higher-dimensional dual geometry. The description of the field theory time evolution should be based on the evaluation of holographic observables. To this aim we choose the entanglement entropy.

As in chapter 2, our choice of boundary entangling regions consists of caps, both for the three- and the four-dimensonal case. Since our geometries are asymptotically AdS, the entanglement entropy is ultraviolet divergent, and must be regularized. Let Area(γ_C) be the area of the bulk entangling surface γ_C associated with a given cap. We introduce the *regularized area*

$$L_C = \mathrm{Area}(\gamma_C) - \mathrm{Area}(\gamma_C^{AdS})\,, \tag{3.3.3}$$

where γ_A^{AdS} is the extremal surface in pure AdS ending on the same cap C. This is equivalent to eliminating the intrinsic cutoff dependence of the entanglement entropy by defining it with respect to a reference value, which we take as that in the CFT vacuum. According to the HEE prescription, the regularized entanglement entropy of region C is given by $S_C = L_C/(4G)$.

Processes in the CFT$_3$ dual to AdS$_4$ evolve on the unit two-sphere. Thin shells located initially close to the AdS boundary gave rise to the following evolution pattern in entanglement entropy of spherical caps. The backreaction on the geometry of a shell placed closed to the boundary is small, and the resulting geometry is approximately pure AdS$_4$. With our regularization, the value of the entanglement entropy at $t=0$ is almost vanishing. As the shell falls, the entanglement entropy grows. It achieves a maximum at $t\approx\theta/2$, after which the extremal surface γ_C keeps outside the imploding shell. The value at the maximum coincides with that of the entanglement entropy of a cap in a AdS$_4$ black hole of the same total mass. If the shell does not form a trapped surface by direct collapse, it will start expanding. At $t\approx t_r-\theta/2$ it intersects the entangling surface again. From then on, the entanglement entropy decreases until it approximately vanishes at $t=t_r$. This behavior repeats in subsequent bounces. An example of the behavior we just described is provided in figure 3.6a. We have marked with dotted lines $t=\theta/2$ and $t=t_r-\theta/2$ in the first bounce, and $t=t_r+\theta/2$ and $t=2t_r-\theta/2$ in the second, showing the accuracy of the described pattern.

In AdS$_4$ only thin shells of low mass avoid direct collapse, and for them $t_r \approx \pi$. In order to have processes with t_r appreciably larger than π, it is necessary to consider broader shells. But for them the simple oscillation pattern of the entanglement entropy described above does not hold. The transition at $t \approx \theta/2$ and $t \approx t_r - \theta/2$ is not sharp, neither the value of the entanglement entropy exhibits a well defined plateau at its maximum (see figure 3.6b). As we argued in chapter 2, broad shells are holographically related to excited states created by a field theory action with a finite time span, rendering natural a more involved evolution of entanglement.

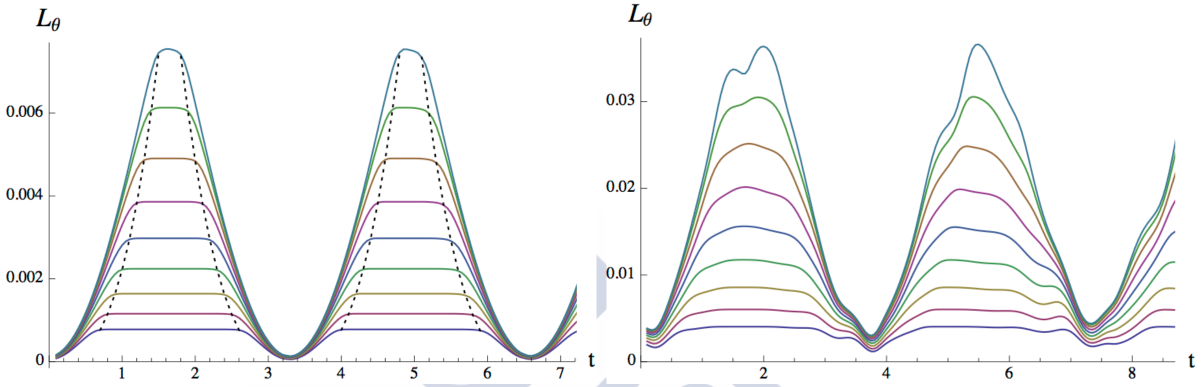

Figure 3.6: Entanglement entropy evolution of spherical caps with $\theta = 1.4, .., 3$ in two AdS$_4$ processes which bounce twice before collapse. Left: Scalar profile with $\sigma = 0.05$ and $\mathcal{M} = 0.017$. The dotted lines signal $t = \theta/2, t_r - \theta/2, t_r + \theta/2, 2t_r - \theta/2$. Rigth: $\sigma = 0.3$ and $\mathcal{M} = 0.09$.

AdS$_3$ offers the possibility to explore processes generated by thin shells covering a wide range of values for t_r. We have analyzed the entanglement entropy of an interval on the unit circle where the dual CFT$_2$ lives. The length of the interval is $\theta \in [0, \pi]$, with $\theta = \pi$ corresponding to the semicircle. The holographic dictionary reduces this problem to evaluating the length of certain bulk geodesics. The results are plotted in figure 3.7a. We observe the same pattern as in figure 3.6a, but now sustained over long cycles. Processes with masses close or above the black hole threshold (3.2.1) lead to very large t_r and still analogous results, see figure3.7b. This has the important consequence that even the entanglement entropy of the semicircle remains a long time at its maximum. Contrary to AdS$_4$ processes, two independent time scales emerge. The first one corresponds to the revival time t_r, which increases monotonically with the energy density of the initial state until the threshold for fast thermalization is reached. The second one is the time at which the entanglement entropy of the semicircle reaches its maximum, which turns out to be independent of the initial conditions to a very good approximation,

$$t_c \approx \frac{\pi}{2} \,. \tag{3.3.4}$$

This is the time after which some coarse-grained observables, such as the entanglement entropy, achieve values characteristic of an ergodic state. In this sense, the subscript in the previous definition stands for collapse. The pattern just described persists along successive revival cycles, in spite that their duration might vary, as shown in figure 3.8.

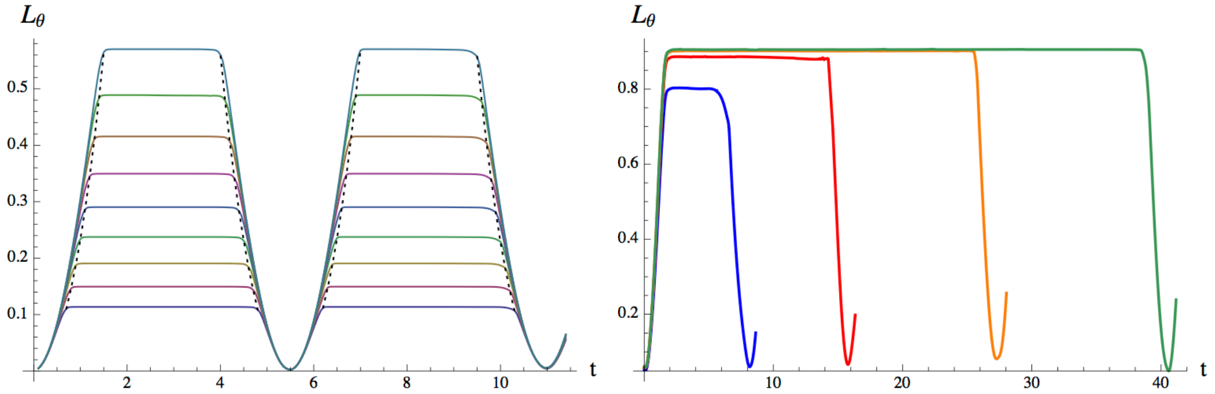

Figure 3.7: Left: Same as in figure 3.6a,b for an AdS$_3$ shell with $\sigma = 0.05$ and $\mathcal{M} = 0.68$. Right: Entanglement entropy of an interval with $\theta = 3.14$ along the first bouncing cycle of AdS$_3$ shells with $\sigma = 0.25$ and $\mathcal{M} = 0.88, 0.98, 1, 1.003$.

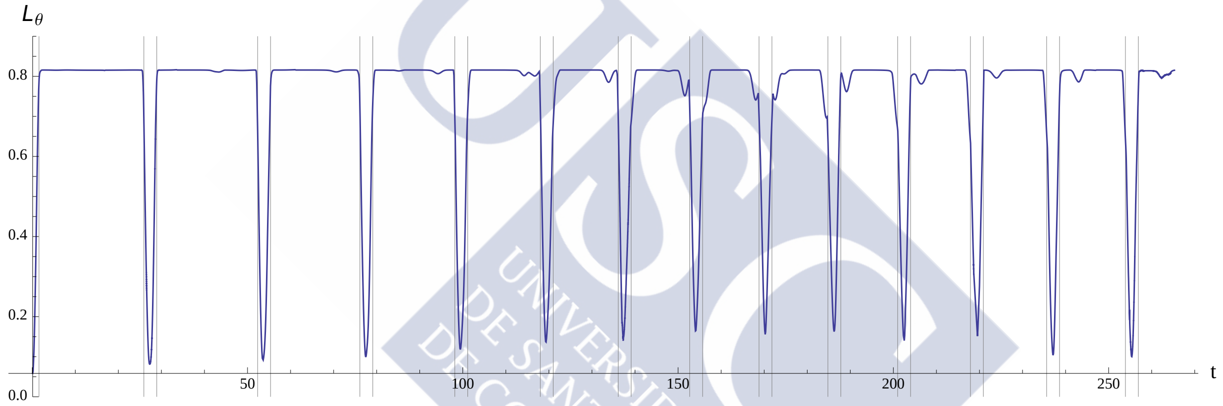

Figure 3.8: Entanglement entropy evolution for $\theta = 3$, in a AdS$_3$ process with $\sigma = 0.25$ and $\mathcal{M} = 1$. The vertical lines mark equal intervals whose extent is $\Delta t = \theta$, except for the first line that is located at $t = \theta/2$.

3.4 Field theory interpretation

In the bouncing geometries we have analyzed in the previous section, the early time evolution of the entanglement entropy follows the free-streaming model introduced by Cardy and Calabrese in [22]. Let us asume that the narrow boundary-centered Gaussian initial data (2.2.3) we are considering provide an accurate representation of the initial state the dual CFT reaches after a sufficiently fast global quench. In this vein, imagine that this state contains a homogeneous distribution of entangled quasiparticle excitations that have been produced at coincident points and travel at unit speed in opposite directions. At $t = \theta/2$, excitations inside a spherical cap of size θ could only be entangled with those outside, leading to a maximal value for the entanglement entropy of this region and a shrap horizon effect. This behavior is holographically reproduced by the implosion of the scalar field shell, as the dotted lines in figure 3.6a and figure 3.7a clearly show.

It is important to recall that the free-streeming model of [22] was originally ment to provide a physical picture of the horizon effect present in the time-evolution of the entanglement entropy of $1+1$-dimensional CFTs on a line after a global quench. *A priori*, in a compact system this picture should apply only to the early time evolution, when the additional length scale introduced by the finite size of the system should not play a role. Therefore, its usefulness to address finite size effects must be analysed on a case-by-case basis.

The entanglement entropy evolution after a global quench of a rational CFT on a circle was studied in [187]. Partial revivals of the initial state were found at integer multiples of

$$t_r = \pi \, , \tag{3.4.5}$$

for a circle of unit radius. This coincides with the time needed for free quasiparticles emitted together in opposite directions and moving at unit speed to rejoin again, in agreement with the free-streaming model of [22]. However, AdS$_3$ bouncing geometries are only associated with quantum revivals satisfying (3.4.5) for sufficiently low energy densities. Notice that this fact does not need to contradict [187]: a CFT$_2$ only allows for a classical gravitational description in the strict $c=\infty$ limit. Hence, a holographic CFT$_2$ is *not* rational by any means.[3] Revivals, however, are not only expected in integrable models or rational CFTs, since they might be a feature tight to the finite size of the system. A consistent picture for the departure of the holographic revival times from (3.4.5) calls for an interpretation as an effect of interactions in the field theory. We will give support for it in the following paragraphs.

On generic interacting systems, it is natural to expect that as the energy density created by a global quench increases, a fast evolution towards equilibration sets in frustrating the possibility of revivals. The holographic representation of a fast approach to ergodic behavior is the formation of a black hole trapping the complete shell by direct collapse. The AdS$_4$/CFT$_3$ models clearly follow this expectation. The number of bounces necessary for gravitational collapse decreases with increasing mass of the scalar profile. Moreover thin AdS$_4$ shells only require bounces before collapse for quite small values of $\mathcal{M}$, a quantity holographically related to the field theory energy density per species, and for them $t_r \approx \pi$. This implies that only field theory processes reasonably described by the simple propagation model exhibit revivals. Soon after the effect of interactions starts to play a significant role, a fast approach to ergodicity sets in.

This is not the case in AdS$_3$/CFT$_2$ models, a fact which from the dual point of view should be related to the strong symmetry properties of two-dimensional CFTs. For them, considerably larger ratios of energy density per species to system size are compatible with revivals. As result, values of $t_r \gg \pi$ can be obtained. The evolution of entanglement entropy in figure 3.7 leads to the following interpretation. At $t_c \approx \pi/2$ after the quench the isolated system

---

[3] It is reasonable to assume that at large-but-finite central charge the previous conclusion also applies, since otherwise *a priori* subleading bulk quantum effects would radically change the classical picture of gravitational collapse.

appears, at the macroscopic level, to have dephased and thermalized. Then, the microscopic dynamics leads to a rephasing that starts at a later time

$$t \approx t_r - \frac{\pi}{2}\,. \tag{3.4.6}$$

Finally, the initial state undergoes a revival at t_r, at least in the sense that entanglement returns to be peaked on neighboring degrees of freedom. The evolution during the dephasing and rephasing phases appears to be well described by the free-streaming model of [22]. The fact that t_r increases with the energy density of the initial state supports linking its value with interaction effects (recall figures 3.2b and 3.7b).

Regarding the holographic dictionary, we obtain the following consistent pattern. The free propagation model provides a good account of the evolution at times corresponding to the implosion and expansion of the matter shell. The interaction effects map to the strong gravitational dynamics generated when the shell reaches minimum size, and scatters against itself before starting to expand again. It is then that the profile of the shell changes, tending to radially focus a fraction of the pulse. This facilitates the formation of a horizon at a subsequent implosion, representing irreversible dephasing on the dual field theory. The large values of t_r for AdS_3 shells close or above threshold are explained by the difficulty that these shells find in climbing their own gravitational potential, which retains them for a long time at the point of maximal implosion. Hence, we are relating the dynamics which determines the formation or not of a horizon with the dynamics of dephasing-rephasing which leads in the field theory to revivals or to equilibration.

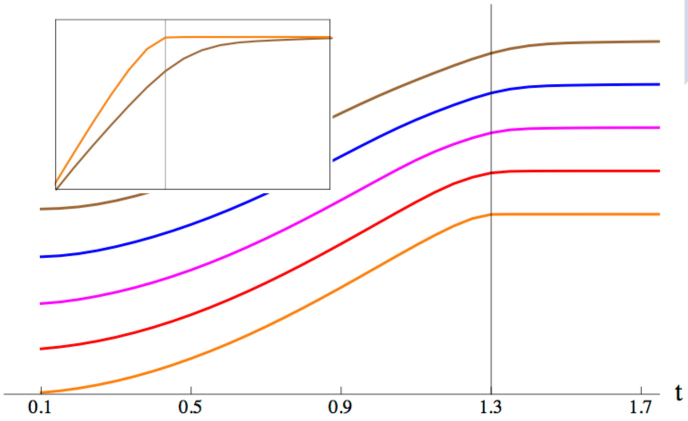

Figure 3.9: Entanglement entropy growth for $\theta = 2.6$ along the implosion of AdS_3 shells with $\mathcal{M} = 0.68$ and $\sigma = 0.01, 0.05, 0.1, 0.15, 0.2$ from bottom up. We have displaced vertically the lines for the sake of comparison. In the inset, $\sigma = 0.01, 0.2$ lines without displacement.

In order to close this section, we will address an issue left open above. Namely, the relation of the shell thickness with the time span of the field theory perturbation generating the initial out-of-equilibrium state. Let us start by noticing that, when the perturbation that brings a system out-of-equilibrium has a finite time span, there will be entangled excitations produced at different instants of time. This will cause the entanglement entropy not to reach its maximum until those entangled components emitted last have reached a separation larger that the region considered. If the shell thickness relates to the time span of the perturbation, the mentioned effect should explain the difference between the entanglement entropy plots in figure 3.6, holographically derived from AdS$_4$ collapses. Indeed it roughly does. While the entanglement entropy associated to the thin shell clearly saturates at $t \approx \theta/2$, that derived from the broad shell does not and instead keeps on growing with a smaller slope to its maximum. A cleaner effect can be observed in figure 3.9a, where we plot the entanglement entropy evolution along the first implosion of several AdS$_3$ shells of the same mass and different thickness σ. The approach of the entanglement entropy to its maximum is sharper for the thinner shell, while it smoothness out and requires a longer time for the broader ones.

If the radial thickness of the initial pulse indicates the time span of the perturbation bringing the field theory out-of-equilibrium, its mass distribution profile $\rho(0, x)$ should qualitatively measure the density of entangled excitations generated at each instant of time, as we argued in chapter 2. Hence, according to this qualitative interpretation, the mass window for bouncing geometries closes down when $\sigma \to 0$ because narrow shells require a smaller mass for reaching the same maximal value of $\rho(0, x)$. Namely, the larger $\bar{\rho} \equiv \max_x \rho(0, x)$, the bigger the initial density of entangled excitations, and the less stable the system becomes against dephasing. The analysis in AdS$_3$ is less straightforward that its four-dimensional counterpart because the threshold mass (3.2.1) dominates over any other criterium for collapse. In any case, the fact that the mass window above threshold before direct collapse closes down for thin shells remains (see figure 3.2a).

3.5 Collapse time

Remarkably holography allows to model a system which, depending on the initial conditions, exhibits revivals of a quite different nature. For small energy density they are well described by the free streaming of entangled quasiparticle pairs which rejoin again on a finite space. For larger energy density, the evolution turns out to bear a stronger resemblance with a series of collapses and revivals of the system wavefunction. We will compare the phenomenology we have found in the latter case with that of well-known quantum systems which undergo collapse and revivals in their evolution. Namely, a Bose-Einstein condensate of atoms in an optical trap and a two-level atom coupled to quantized radiation in a cavity.

The behavior of a condensate of atoms with repulsive interactions trapped in a three-dimensional confining potential has been studied both theoretically [191] and experimentally [184]. The repulsive interactions in the setup of [184] were reasonably described by the simple hamiltonian $H = \frac{1}{2} U \hat{n}(\hat{n} - 1)$, where $\hat{n}$ is the operator counting the number of atoms. When the system is prepared in a coherent superposition of states with different particle number, it undergoes perfect revivals at integer multiples of $t_r = 2\pi/U$. Indeed

$$|\alpha(t)\rangle = e^{-\frac{|\alpha|^2}{2}} \sum_n \frac{\alpha^n}{\sqrt{n!}} e^{-\frac{1}{2} U n(n-1) t} |n\rangle \,, \tag{3.5.7}$$

with α a complex number characterizing the coherent state.

An important observable is the matter wavefield of the condensate, defined by $\Psi(t) \equiv \langle\alpha(t)|a|\alpha(t)\rangle$, which represents the fraction of individual atoms that are coherent over the total number of atoms in the trap. Collapse/revival of this wavefield signals decoherence/recoherence of these atoms, again in a coarse-grained sense. The evolution of this observable is straightforwardly obtained in the simple case above

$$\Psi(t) = \alpha\, e^{-|\alpha|^2(1-\cos Ut)}\, e^{i|\alpha|^2 \sin Ut}\,. \tag{3.5.8}$$

The matter wavefield becomes exponentially suppressed at $t_c \approx \pi/U|\alpha|$ due to the different phases in (3.5.7)(see figure 3.10a). Since $|\alpha|$ determines the average particle number, $\bar{n} = |\alpha|^2$, the quotient between the revival and the collapse time grows with $\bar{n}$,

$$\frac{t_r}{t_c} = 2\sqrt{\bar{n}}\,. \tag{3.5.9}$$

As we have demonstrated, a qualitatively analogous relation holds in the holographic models.

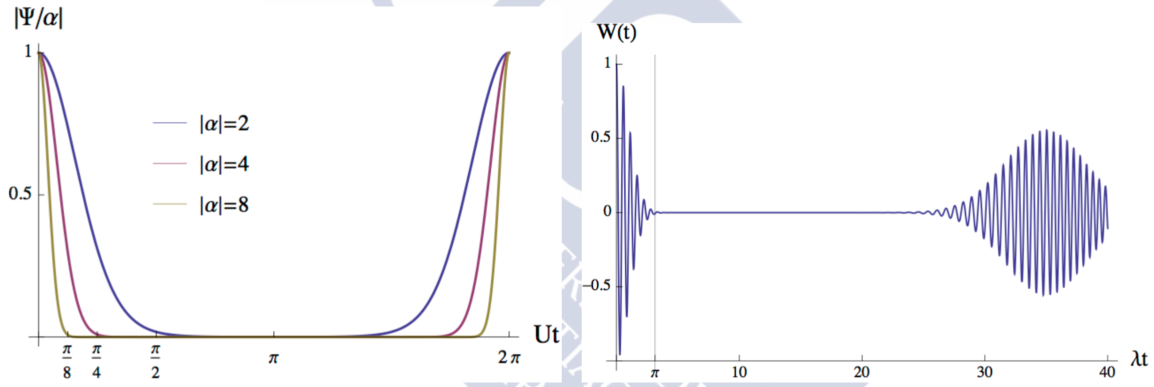

Figure 3.10: Left: Evolution of the matter wavefield along a revival cycle for several values of α. Right: Evolution of $W(t)$ for $\alpha = 30$. The vertical line signals the collapse time $\lambda t_c = \pi$.

Let us review now the behavior of a two-level atom in a cavity coupled to quantized radiation. This system is described by the Jaynes-Cummings model [190]. Its Hamiltonian is $H = \omega(\sigma_3/2 + a^\dagger a) + \lambda(\sigma_+ a + a^\dagger \sigma_-)$, where $a^\dagger, a$ are the photon creation and annihilation operators and $\sigma_{3,\pm}$ the Pauli matrices referring to the two-level atom. The previous hamiltonian refers to the resonant case, where the photon frequency coincides with the energy splitting among the atomic levels. When the radiation field starts in a coherent superposition of states of different photon number and the atom in the excited state $|+\rangle$, we have

$$|\Psi(t)\rangle = e^{-\frac{|\alpha|^2}{2}} \sum_n \frac{\alpha^n}{\sqrt{n!}} \left[\cos(\lambda\sqrt{n+1}\,t)\,|+\rangle\,|n\rangle - i\sin(\lambda\sqrt{n+1}\,t)\,|-\rangle\,|n+1\rangle\right]. \tag{3.5.10}$$

The probability to find the atom in the excited state minus that of finding it in the ground level, $W(t) = |\langle+|\Psi(t)\rangle|^2 - |\langle-|\Psi(t)\rangle|^2$, shows a series of collapses and revivals along its evolution. It starts being one but becomes exponentially suppressed at $t_c \approx \frac{\pi}{\lambda}$, as can be observed in figure 3.10b, loosing the imprint of the initial state. At $t_r \approx \frac{2\pi|\alpha|}{\lambda}$ the function $W(t)$ returns to have finite values, and the initial dominance of the excited state is partially reconstructed. Since the average photon number is again $\bar{n} = |\alpha|^2$, collapse and revival times also satisfy (3.5.9) in this case. However, now t_c is determined by the intrinsic properties of the system Hamiltonian, while t_r grows with the total energy of the coherent state, in closer analogy with the holographic models.

The qualitative agreement between such different systems can be understood as follows. It is natural that an increase in the quasiparticle pair density created by a global quench, or the average occupation numbers in the initial coherent states considered above, results in strengthening the tendency of a system to dephase. This is so even if, after dephasing, the system rephases and undergoes a revival. When the dynamics is so constrained that some observables exhibit a series of collapses and revivals with separate time scales, the previous expectation can be fulfilled both by shorter collapse times or longer revival ones. Unless energy levels have a commensurate splitting the stretching of the revival time can be expected to be generic. The holographic counterpart of this fact is found in the gravitational redshift generated by the shell at the point of maximal implosion, where the curvature builds up very sharply.

Chapter 4

Thin shell construction of time-periodic geometries

4.1 Summary

As discussed in section 1.3 of chapter 1, there exists strong evidence in favor of the hypothesis that exactly periodic geometries in AdS$_{d+2}$ act as anchors of stability islands. We have already encountered several examples of these exacty periodic solutions [135][140]. Further cases include real massive scalar fields [195] as well as purely gravitational solutions within a cohomogeneity-two biaxial Bianchi IX ansatz in $d = 3$ [196]. In general, as discussed extensively in [196], the existence of time-periodic solutions is a common feature of nonlinear PDE systems on bounded domains.

In chapter 1 (subsection 1.2.7), we have also illustrated that thin shell spacetimes are extremely useful constructions to address trademark processes in gravitational physics in a tractable way. Therefore, we can ask ourselves if oscillatory geometries are also present wihin the thin shell formalism in global AdS$_{d+2}$. In this chapter, we are going to answer this question in the affirmative showing that, under mind dynamical assumptions, the existence of oscillating thin shell spacetimes is a generic property of asymptotically AdS$_{d+2}$ geometries.

This chapter is structured as follows. In section 4.2, we introduce our setup and obtain the shell equation of motion from the Israel juction conditions. We demonstrate that the shell trajectory follows from the motion of a point particle in a one-dimensional potential. This potential depends on the spacetime dimensionality, the shell equation of state, the asymptotic mass and the shell internal energy. Since it is known in closed form, in section 4.3 we provide semi-analytical expressions for the phase space region where oscillating thin shell solutions exist, and analyze their behavior in certain limits. The conclusions match in a natural way with similar results obtained in numerical simulations of realistic geometries supported by a masless scalar field. The three-dimensional case is separately analyzed due to the presence of the mass gap. Finally, in section 4.4 we discuss briefly the interpretation of our results in the light of the AdS/CFT correspondence and comment on possible future extensions.

4.2 Shell dynamics

We are considering a spherically symmetric thin shell of matter. The shell worldvolume Σ is a codimension-1 hypersurface that divides the $(d+2)$-dimensional background spacetime $\mathcal{M}$ in two distinct regions: outside, $\mathcal{M}_+$, and inside, $\mathcal{M}_-$. Due to the spherical symmetry of the problem, we know, by Birkhoff's theorem, that the spacetime metric takes the Schwarzschild-AdS form on both $\mathcal{M}_+$, $\mathcal{M}_-$. Choosing standard Schwarzschild coordinates $x_\pm = (t_\pm, r_\pm, \theta_1, ..., \theta_d)$ to cover $\mathcal{M}_\pm$, we find that, in this particular coordinate system

$$ds_\pm^2 = -f_\pm(r_\pm)dt_\pm^2 + f_\pm(r_\pm)^{-1}dr_\pm^2 + r_\pm^2 d\Omega_d^2 \tag{4.2.1}$$

where

$$f_\pm(r_\pm) = 1 + \frac{r_\pm^2}{l_\pm} - \frac{m_\pm}{r_\pm^{d-1}} \ . \tag{4.2.2}$$

As usual, $d\Omega_d^2$ is the metric of a unit round d-dimensional sphere, and the AdS radius l is related to the cosmological constant $\Lambda = -\frac{d(d+1)}{2l^2}$. In what follows, we will restrict ourselves to the case where the shell has no influence on the cosmological constant, so we are going to set $l_+ = l_- = l = 1$ by an appropriate choice of units. Furthermore, we assume that the spacetime inside the shell is empty AdS$_{d+2}$ and hence fix $m_- = 0$. In such case, $m_+ \equiv m$ sets the total ADM mass of the system.

Let the shell worldvolume Σ be parameterized with coordinates $y = (\tau, \theta_1, ..., \theta_d)$, where τ is the proper time of an comoving observer. The shell embedding in the ambient spacetime is given parametrically by the function

$$x_s(y) = (t_{\pm,s}(\tau), r_{\pm,s}(\tau), \theta_1, ..., \theta_d) \ . \tag{4.2.3}$$

The tangent space $\mathcal{T}_p\mathcal{M}$ of any point $p \in \Sigma$ admits a basis formed by $d+1$ vectors $e_a = e_a^\alpha \partial_{x^\alpha}$, tangent to Σ, and one vector $n = n^\alpha \partial_{x^\alpha}$, orthogonal to Σ. Explicitly,

$$e_{\tau,\pm} = \dot{t}_{\pm,s}\partial_{t_\pm} + \dot{r}_{\pm,s}\partial_{r_\pm} \tag{4.2.4}$$

$$e_{\theta_i,\pm} = \partial_{\theta_i} \tag{4.2.5}$$

$$n_\pm = + \left(f_{\pm,s}^{-1}\dot{r}_{\pm,s}\partial_{t_\pm} + f_{\pm,s}\dot{t}_{\pm,s}\partial_{r_\pm} \right) \tag{4.2.6}$$

The overall positive sign of $n_\pm$ is fixed by requiring that $n_\pm$ is always directed from $\mathcal{M}_-$ to $\mathcal{M}_+$[197].

The embedding (4.2.3) is not arbitrary: in order for the whole spacetime $\mathcal{M}$ to solve Einstein equations, the so called *Israel junction conditions* must be satisfied (see [197]). The first junction condition states that the induced metric h_{ab} on Σ must be continuous across Σ

$$[h_{ab}] = 0 \tag{4.2.7}$$

where the brackets stand for the jump. The second junction condition relates the jump of the extrinsic curvature K_{ab} with the matter composition of the shell,

$$[K_{ab} - h_{ab}K] = -8\pi G S_{ab} = -S_{ab} \tag{4.2.8}$$

where $K \equiv h^{ab}K_{ab}$, S_{ab} is the shell energy-momentum tensor and we have chosen units such that $8\pi G = 1$. Projecting g onto Σ to find the induced metric $h_{ab} = g_{\alpha\beta}e^{\alpha}_{a}e^{\beta}_{b}$ we get

$$dh^2_{\pm} = h_{\pm ab}dy^a dy^b = \left(-f_{\pm,s}\dot{t}^2_{\pm,s} + f^{-1}_{\pm,s}\dot{r}^2_{\pm,s}\right)d\tau^2 + r^2_{\pm,s}d\Omega^2_d\ . \tag{4.2.9}$$

The choice of τ as comoving time fixes $h_{\tau\tau} = -1$, whence it follows that

$$\dot{t}_{\pm,s} = \frac{\beta_{\pm}}{f_{\pm,s}} \tag{4.2.10}$$

with

$$\beta_{\pm} = \sqrt{f_{\pm,s} + \dot{r}^2_{\pm,s}}\ . \tag{4.2.11}$$

We have taken the positive root of $\dot{t}_{\pm,s}$, as we want the shell trajectory to be future oriented. Equation (4.2.10) together (4.2.11) accomplishes two tasks. It ensures that the $\tau\tau$ component of the first junction condition (4.2.7) is satisfied, and gives the correct normalisation to the vector n in (4.2.6), $n^2 = 1$. It also implies that it is imposible to cover the entire space-time $\mathcal{M}$ with a globally defined time-like Schwarzschild coordinate, as the embedding functions $t_{\pm,s}(\tau)$ will differ at the shell. On the other hand, the radial coordinate $r_{\pm}$ has to be continuous since $r_{+,s}(\tau) = r_{-,s}(\tau) \equiv r_s(\tau)$ must hold to signal unambiguously the shell's radial position. This condition, together with (4.2.10), ensures that all components of (4.2.7) are satisfied. From now on, we take these facts into account and change correspondingly our $\mathcal{M}_{\pm}$ coordinate system to $x_{\pm} = (t_{\pm}, r, \theta_i)$.

The extrisic curvature is the pullback of the Lie derivative of the ambient metric g along n. Several equivalent expressions can be found in the literature [197]:

$$K_{ab} = \frac{1}{2}e^{\alpha}_{a}e^{\beta}_{b}\left(\pounds_{n}g\right)_{\alpha\beta} = e^{\alpha}_{a}e^{\beta}_{b}\nabla_{\alpha}n_{\beta} = -n_{\mu}\left(\frac{\partial x^{\mu}_{s}}{\partial_{y^a}\partial_{y^b}} + \Gamma^{\mu}_{\alpha\beta}e^{\alpha}_{a}e^{\beta}_{b}\right) \tag{4.2.12}$$

where the orthogonality condition $e^{\alpha}_{a}n_{\alpha} = 0$ is used. In our particular setup (4.2.9), its non-zero components and trace are

$$K^{\tau}_{\pm,\tau} = \frac{\dot{\beta}_{\pm}}{\dot{r}_s} \qquad K^{\theta_i}_{\pm,\theta_i} = \frac{\beta_{\pm}}{r_s} \qquad K = \frac{\dot{\beta}_{\pm}}{\dot{r}_s} + d\frac{\beta_{\pm}}{r_s} \tag{4.2.13}$$

The diagonal nature of K^{a}_{b}, together with the second Israel junction condition (4.2.8), leave little room for the form of the shell stress-energy tensor S^{a}_{b}, which must be of the perfect fluid form

$$S^{a}_{b} = \mathrm{diag}(-\sigma, p, ..., p) \tag{4.2.14}$$

where σ will be the shell energy density and p the shell pressure. Due to spherical symmetry, p is independent of the particular angular direction considered. In components, (4.2.8) reads now

$$\left[K^{\theta_i}_{\theta_i}\right] = \frac{[\beta]}{r_s} \quad = \quad -\frac{1}{d}\sigma \tag{4.2.15}$$

$$\left[K^{\tau}_{\tau}\right] = \frac{\left[\dot{\beta}\right]}{\dot{r}_s} \quad = \quad p + \frac{d-1}{d}\sigma \tag{4.2.16}$$

With our choices for $f_\pm$, we always have $\beta_+ \leq \beta_-$ and, therefore, $\sigma \geq 0$. As usual, equations (4.2.15), (4.2.16) need to be supplemented with an equation of state which relates the shell energy density and pressure. At this point, we introduce a simplification by restricting our analysis to the case where this equation of state is linear. In AdS$_{d+2}$ we shall write

$$p = \frac{\alpha}{d}\,\sigma\ . \tag{4.2.17}$$

The parameter α determines the kind of matter the shell is made of. Taking $\alpha \in [0,1]$ it interpolates between dust ($\alpha = 0$) and conformal matter ($\alpha = 1$). This choice of equation of state, together with the positivity of σ, implies that $\sigma + p \geq 0$, so that the weak energy condition is respected. With the choice (4.2.17), equations (4.2.15), (4.2.16) can be solved explicitly. The final result is that the shell dynamics is fully equivalent to the one-dimensional motion of a particle in an effective potential V_{eff}

$$\dot{r}_s^2 + V_{eff} = 0 \tag{4.2.18}$$

where

$$V_{eff} = 1 + r_s^2 - \frac{1}{2} m r_s^{1-d} - \frac{m^2}{4M^2} r_s^{2\alpha} - \frac{1}{4} M^2 r_s^{-2(d-1+\alpha)}\,. \tag{4.2.19}$$

M is an integration constant that sets the shell's proper energy E, defined as $E \equiv vol(S_d) r_s^d \sigma = vol(S_d) d\, r_s^{-\alpha} M$, where $vol(S_d)$ is the volume of the d-dimensional unit sphere.

Notice that the potential V_{eff} is invariant under $m \to m$, $M \to \frac{m}{M}$ and $\alpha \to -(d-1+\alpha)$ so any result we may obtain is also going to hold in the range $\alpha \in [-d, -d+1]$, modulo the appropriate M redefinition. The weak energy condition will be still satisfied.

4.3 Oscillating solutions

From (4.2.18), we know that the region where the shell is allowed to move is the -possibly disconnected- set of radial intervals for which $V_{eff} \leq 0$. The asymptotic behaviour of V_{eff} is as follows:

- $V_{eff} \to -\infty$ as $r \to 0$, with $V_{eff} \sim -1/4M^2 r^{-2(d-1+\alpha)}$ for $r \ll 1$
- $V_{eff} \to \infty$ as $r \to \infty$, with $V_{eff} \sim r^2$ for $r \gg 1$

Oscillating shell trajectories, if they exist, are confined to an intermediate radial region where the potential V_{eff} develops a well. The turning points are given by two radii $r_\pm$ where $V_{eff}(r_\pm) = 0$ (subindices here do not refer to the inner or outer regions to the shell). The goal now is, fixing d, α and the space-time ADM mass m, find in what range of M oscillating solutions appear. It turns out that this M region is bounded by two shell rest energies $M_{l,u}$, with $M_l \leq M_u$, such that

- For $M = M_u$ there is a local minimum of V_{eff} touching the $V_{eff} = 0$ axis. This corresponds to a shell in equilibrium.

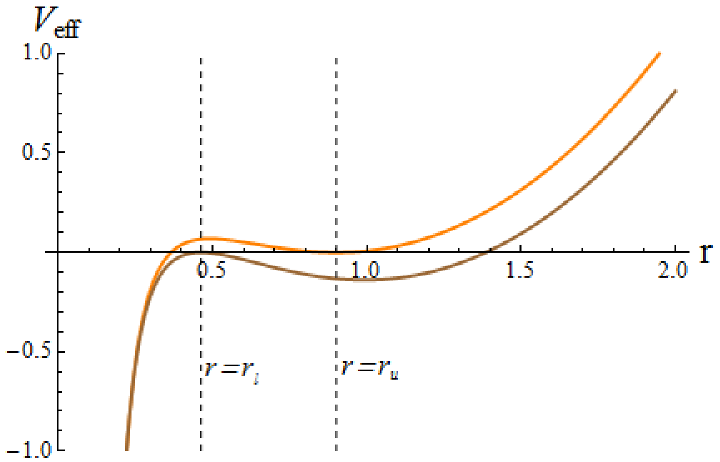

Figure 4.1: Typical form of the potential V_{eff} in the limiting cases that bound the oscillating shell existence region. In orange, the potential at $M = M_u$. In brown, the potential at $M = M_l$. Dashed black lines correspond to r_l and r_u. The parameter values are $d = 3$, $\alpha = 0.5$, $m = 0.1$, $M_u = 0.0359$, $M_l = 0.0346$, $r_l = 0.426$, $r_u = 0.901$.

- For $M = M_l$ there is a local maximum of V_{eff} touching the $V_{eff} = 0$ axis. This corresponds to the transition between oscillatory and collapsing behaviour.

Figure 4.1 depicts both limiting situations on AdS$_5$. To find the values of $M_{l,u}$, we have to solve the system of equations given by $V_{eff} = \partial_r V_{eff} = 0$. The solution is easily obtained in implicit form by taking $m = m(d, \alpha, r)$, $M = M(d, \alpha, r)$, which will be called the *existence curves*

$$m(d, \alpha, r) = \frac{4r^{d-1}(\alpha - (1-\alpha)r^2)(d - 1 + \alpha + (d+\alpha)r^2)}{(d - 1 + 2\alpha)^2\,(1 + r^2)} \tag{4.3.20}$$

$$M(d, \alpha, r) = \frac{2r^{d-1+\alpha}(\alpha - (1-\alpha)r^2)}{(d - 1 + 2\alpha)\sqrt{1 + r^2}} \tag{4.3.21}$$

As the $d = 1$ existence curves display peculiar properties we will discuss this case separately.

4.3.1 Oscillating shells in $d > 1$

The existence curves allow a straightforward computation of M_l and M_u. The procedure is illustrated in figure 4.2a. First, we choose some m and solve numerically the equation $m = m(d, \alpha, r)$ for r at fixed d and α. The output are two radii, r_l and r_u, such that $r_l < r_u$: r_u signals the position of the axis-touching minimum of $V_{eff}(d, \alpha, m, M_u)$, while r_l signals the position of the axis-touching maximum of $V_{eff}(d, \alpha, m, M_l)$ -see figure 4.1-. Inserting $r_{l,u}$ into equation (4.3.21) gives back the numerical values of $M_{l,u}$ and fixes completely the form the potential V_{eff}. For any $M \in (M_l, M_u)$, it is guaranteed that V_{eff} possesses an oscillating solution.

Looking at figure 4.2a, it is neatly seen that, at fixed d and α, there is a maximum mass, $m_{max}(d,\alpha)$, above which the construction just described cannot be performed. Therefore, oscillating shell trajectories only exist for sufficiently light shells; above $m_{max}(d,\alpha)$ there are only collapsing solutions. The fact that there are no oscillating geometries when the mass of the system surpasses a certain threshold is a feature that this simple model shares with more realistic setups, for instance, the massless scalar field studied in [130][142].

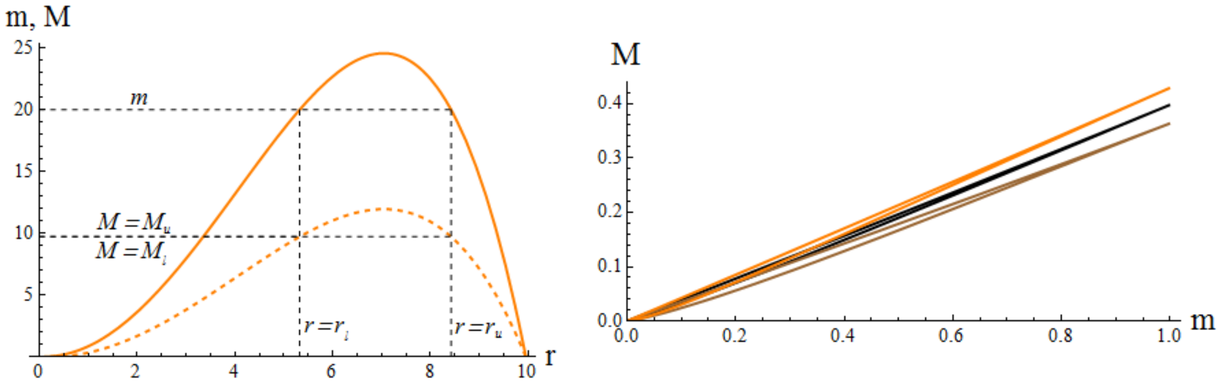

Figure 4.2: Left: existence curves for oscillating solutions in $d = 3$ and $\alpha = 0.99$. In solid orange, $m(d,\alpha,r)$. In dashed orange, $M(d,\alpha,r)$. The black dashed curves illustrate the construction described in the text. Notice that the range of M is so tiny that the two lines depicting M_l and M_u look coincident. Right: $M(3,\alpha,m)$ for $\alpha = 0.2, 0.5, 0.9$ -black, brown and orange curves respectively-. Any point within the region bounded by each curve corresponds to a particular oscillating solution. All quantities are measured in units of $m_{max}(d,\alpha)$.

Concerning M, it is important to stress that its value sets an energy scale that is independent of m. Tuning M deforms V_{eff} and, in particular, shifts the upper turning point r_+. Hence, one can think of this parameter in terms of the initial radius where the shell is released from rest and starts falling and, in consequence, M would be related to its potential energy.

In figure 4.2b we offer several parametric plots of $M(d,\alpha,r)$ as function of $m(d,\alpha,r)$. In each curve, the upper branch corresponds to M_u, while the lower branch corresponds to M_l. In the $m \to 0$ limit, the upper M_u branch asymptotes to a line,

$$M_u(\alpha,m) \sim \frac{1}{2}\,(1-\alpha)^{\frac{1-\alpha}{2}}\,\alpha^{\alpha/2} m \;. \tag{4.3.22}$$

Oscillating solutions exist for M in a narrow window around this upper branch of static shells. This window closes at $m_{max}(d,\alpha)$. If the two scales set by m and M were not independent, this finite-size region where oscillating solutions reside would degenerate into a line and they would cease to exist.

To start scanning the behavior of the existence region with respect to α, let us note that both $m(d,\alpha,r)$ and $M(d,\alpha,r)$ attain their maxima at the same radius

$$r_{max}(d,\alpha)=\frac{1}{\sqrt{2}}\frac{\sqrt{2\alpha(d-1+\alpha)-(d+1)+\sqrt{(d+1)^2-4(d-1)\alpha-4\alpha^2)}}}{\sqrt{(1-\alpha)(d+\alpha)}}\,. \tag{4.3.23}$$

which also controls $m_{max}(d,\alpha)$,

$$m_{max}(d,\alpha)=4r_{max}(d,\alpha)^{d+1}\frac{\sqrt{(d+1)^2-4(d-1)\alpha-4\alpha^2}-(d-1)}{(d-1+2\alpha)^2}\,. \tag{4.3.24}$$

In the conformal fluid limit $\alpha\to 1$, $r_{max}(d,\alpha)$ diverges as $r_{max}(d,\alpha)\sim\sqrt{\frac{d-1}{d+1}\frac{1}{\sqrt{1-\alpha}}}$, so we expect $m_{max}(d,\alpha)$ to be also divergent. In fact

$$m_{max}(d,\alpha)\sim\frac{8}{d^2-1}\left(\frac{d-1}{d+1}\right)^{\frac{1+d}{2}}(1-\alpha)^{\frac{1-d}{2}}\,. \tag{4.3.25}$$

This result shows that the maximum mass for which oscillating solutions exist grows unbounded as $\alpha\to 1$; for $d>1$, there are oscillating solutions with arbitrary high ADM energy as long as the shell matter is sufficiently near conformality. In the opposite limit (pressureless dust) $\alpha\to 0$

$$m_{max}(d,\alpha)\sim\frac{8}{(d-1)^2}\left(\frac{d-1}{d+1}\right)^{\frac{1+d}{2}}\alpha^{\frac{1+d}{2}}, \tag{4.3.26}$$

and the allowed region for oscillating trajectories shrinks down to zero. Physically, this means that there are no pressureless oscillating solutions, *i.e.* in order to be stable against gravitational collapse, the shell matter must have some self-interaction. As an aside, note that the limiting behaviour of $M(d,\alpha,r)$ as $\alpha\to 0,1$ just follows the behaviour of $m(d,\alpha,r)$, since

$$M(d,\alpha,r)=r^{\alpha}\frac{(d-1+2\alpha)\sqrt{1+r^2}}{2(d-1+\alpha+(d+\alpha)r^2)}m(d,\alpha,r)\,. \tag{4.3.27}$$

An important consistency check is to verify that r_- lies outside the position of the event horizon, r_h. Otherwise, instead of having an oscillating solution, the shell trajectory would represent direct gravitational collapse starting from r_+. As $r_-\geq r_l$, it is sufficient to show that $r_l\geq r_h$. The static event horizon location, $r_h(d,m)$, is the solution of the equation $1+r_h^2-mr_h^{1-d}=0$. Since we don't know explicitly $r_l=r_l(d,\alpha,m)$, but instead $m=m(d,\alpha,r_l)$, we are going to define correspondingly $m_h(d,r)\equiv r^{d-1}(1+r^2)$. It is easy to see that, if $m_h(d,r)-m(d,\alpha,r)\geq 0$ for all d,α,r, the consistency condition $r_l\geq r_h$ always holds -see figure 4.3-. We find that

$$m_h(d,r)-m(d,\alpha,r)=r^{d-1}\frac{\left(d-1+(d+1)r^2\right)^2}{\left(1+r^2\right)\left(d-1+2\alpha\right)^2} \tag{4.3.28}$$

which is positive definite. Thus, every oscillating shell trajectory found lies entirely outside the event horizon of the would-be black hole.

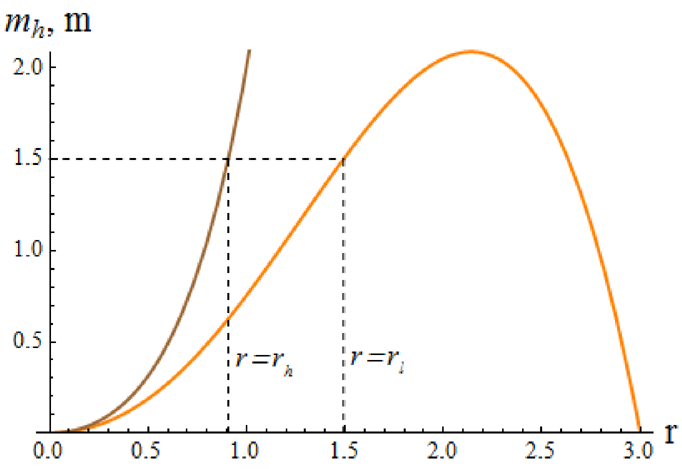

Figure 4.3: m_h -brown- versus mass existence curve -orange- in $d = 3$ for $\alpha = 0.9$. The line $m = 1.5$ is drawn -black dashed-, as well as its lowest intersection with the mass existence curve, r_l, and its intersection with m_h, r_h -both black dashed-.

4.3.2 Oscillating shells in $d = 1$

The case $d = 1$ is special because, as mentioned before, some general properties seen in $d > 1$ do not hold anymore. Representative existence curves are plotted in figure 4.4. The analytic form of $m(d, \alpha, r), M(d, \alpha, r)$ for $d = 1$ is

$$\begin{aligned} m(1,\alpha,r) \equiv m(\alpha,r) &= 1 + r^2 - \frac{r^4}{(1+r^2)\alpha^2} && (4.3.29) \\ M(1,\alpha,r) \equiv M(\alpha,r) &= r^{\alpha}\frac{\alpha-(1-\alpha)r^2}{\alpha\sqrt{1+r^2}} && (4.3.30) \end{aligned}$$

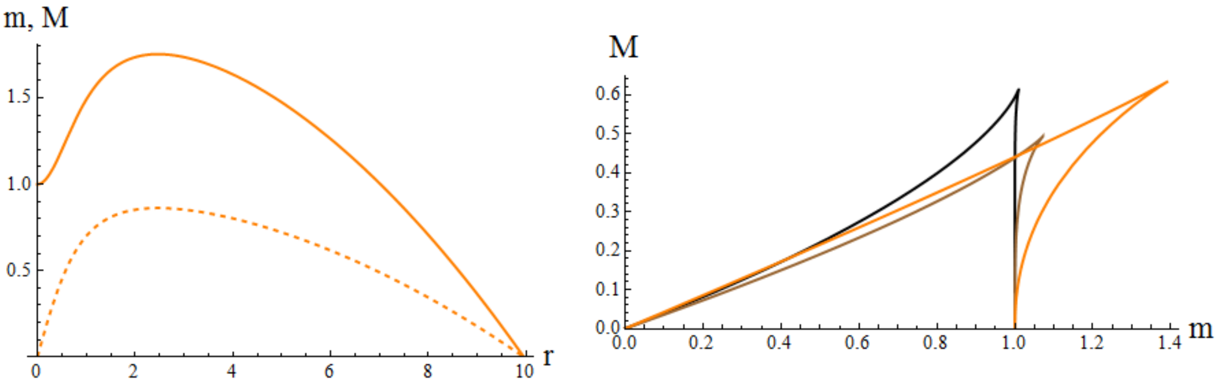

Figure 4.4: Left: existence curves for oscillating solutions in $d = 1$ and $\alpha = 0.99$. In solid orange, m as a function of r. In dashed orange, M. Right: $M(1, \alpha, m)$ for $\alpha = 0.2, 0.5, 0.9$ -black, brown and orange curves respectively-.

It is easy to prove that $r_l \geq r_h$, as equation (4.3.28) still holds. The major difference with respect to the $d > 1$ case comes when we evaluating the allowed mass range for oscillating shell trajectories. At $d = 1$

$$r_{max}(\alpha) = \left(\frac{1 + \sqrt{1 - \alpha^2}}{\alpha^2} - 1 \right)^{-\frac{1}{2}} \tag{4.3.31}$$

is still divergent as $\alpha \to 1$, although in a milder way, $r_{max}(\alpha) \sim (1 - \alpha)^{-\frac{1}{4}}$ instead of the $(1 - \alpha)^{-\frac{1}{2}}$ divergence in (4.3.23). However,

$$m_{max}(\alpha) = \frac{2}{1 + \sqrt{1 - \alpha^2}} \tag{4.3.32}$$

so, unlike the $d > 1$ case, for $d = 1$ the maximum allowed mass of an oscillating solution does not grow without bound as $\alpha \to 1$. Instead, it goes to a finite value, $m = 2$ (in our conventions). Note also that, in the $\alpha \to 0$ limit, the m-range does not close down. Instead, $m_{max}(\alpha) \to 1$ as $\alpha \to 0$. In AdS$_3$ there are oscillating shell solutions for any $m \leq 1$, even for dust made shells.

Looking at figure 4.4, we observe that there is a qualitative difference between shells of mass above and below the threshold $m = 1$. Each mass m belonging to the interval $[1, m_{max}(\alpha)]$ has two associated radii, r_l and r_u, such that, like in higher dimensions, r_l signals the position of the $V_{eff} = 0$ axis-touching maximum, while r_u signals the position of the axis-touching minimum. However, for $m < 1$ the axis-touching maximum disappears. This does not mean that shells with $m < 1$ are allowed to reach the point $r = 0$, because the potential barrier does not vanish at any finite M for $\alpha \neq 0$: as $M \to 0$, the maximum of the barrier gets radially displaced towards the origin and tends to a constant value. At the same time, r_+ grows unbounded. In the same way that oscillating shells cannot cross their Schwarzschild radius, in AdS$_3$ there is also a mechanism forbidding the possibility of reaching $r = 0$: the shells cannot form naked singularities. Again this is in parallel with the phenomenology shown by a massless scalar pulse in AdS$_3$ [159][198]. The behaviour of the barrier is depicted in figure 4.5.

It is easy to explain the behaviour of V_{eff} as $M \to 0$ in analytic terms. Let $r_{barrier}$ be the position of the maximum of the potential barrier. If $r \ll 1$, $\partial_r V_{eff} \sim \alpha \left(M^2 r^{-2\alpha} - \frac{m^2}{M^2} r^{2\alpha} \right)$, so

$$r_{barrier} \sim \left(\frac{M}{\sqrt{m}} \right)^{\frac{1}{\alpha}} . \tag{4.3.33}$$

Therefore, $r_{barrier} \to 0$ as $M \to 0$. At $r = r_{barrier}$, the potential is finite

$$V_{barrier} \equiv V_{eff}(r_{barrier}) \sim 1 - m . \tag{4.3.34}$$

Regarding the large r turning point, r_+, note that if V has a root r_+ such that $r_+ \gg 1$, we have that $V(r_+) \sim r_+^2 - \frac{m^2}{4M^2} r_+^{2\alpha} = 0$, which is solved by

$$r_+ = \left(\frac{m}{2M} \right)^{\frac{1}{1-\alpha}} . \tag{4.3.35}$$

This proves that $r_+ \to \infty$ as $M \to 0$.

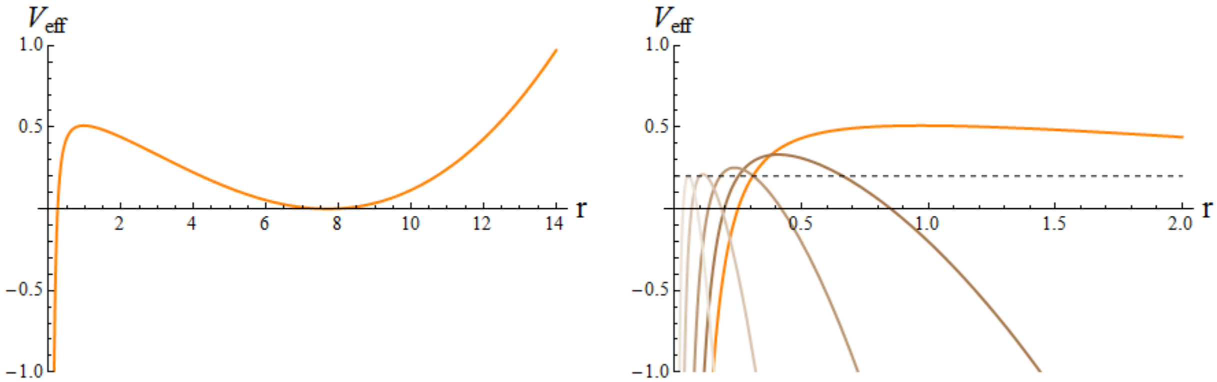

Figure 4.5: Left: for $\alpha = 0.99$ and $m = 0.8$, potential V_{eff} at $M = 0.3900$, which corresponds to a static shell located at $r_u = 7.699$. Right: evolution of the potential barrier for the oscillating shell at different M. The orange curve corresponds to V_{eff} on the left picture. From left to right, brown curves represent potentials with $M = 0.3$, $M = 0.2$, $M = 0.1$ and $M = 0.05$. Note that $r_{barrier}$ gets smaller as M does, while $V_{barrier} \to 1 - m = 0.2$ in this case -black dashed-

4.4 Final remarks

The homology constraint implies that the dual state to the oscillating thin shell geometries we are considering is pure. Furthermore, since at times $\tau_\pm$ such that $r_s(\tau_\pm) = r_\pm$ the effective potential $V_{eff}(r_\pm)$ vanishes, we have that $\dot{r}_s(\tau_\pm) = 0$ and the geometry is time-symmetric, i.e., $\partial_\tau g_{\mu\nu}|_{\tau=\tau_\pm} = 0$. Therefore, given a boundary cap $C(\tau_\pm)$, the bulk entangling surface $\sigma_{C(\tau_\pm)}$ is constraint to lie entirely on a constant time hypersuface and the time-independent RT prescription suffices to compute it. This readily implies that $S_{C(\tau)}$ is periodic, with a periodicity set by the shell oscillatory motion. If we made the natural assumption that the entanglement entropy is monotonous for $\tau \in [\tau_-, \tau_+]$, the amplitude of the entanglement entropy oscillations would be $\left|S_{C(\tau_+)} - S_{C(\tau_-)}\right|$.

Therefore, oscillating thin shell spacetimes provide extremely simple examples of CFT states that never thermalize. Strictly speaking, their existence is of dynamical origin: they are only allowed for specific equations of state and, in particular, they are forbidden if the shell is composed of pressureless matter. On the other hand, the fact that time-periodic thin shell solutions appear for any $\alpha \in (0, 1)$ points to the fact that the existence of exactly periodic solutions to the Einstein equation is a generic property of asymptotically global AdS spacetimes. Said otherwise, under mild dynamical assumptions (namely, the presence of pressure) the kinematical properties of Einstein gravity with global AdS asymptotics should guarantee the appearance of time-periodic spacetimes. In this regard it is intriguing to note that, had we performed our construction in *flat* AdS, the effective potential (4.2.19) would not had allowed for oscillating shells, irrespectively of the particular equation of state considered [199]. In the light of the AdS/CFT correspondence, the results of this chapter suggest that, under generic conditions, quantum revivals are to to be expected in holographic CFTs placed on spheres.

As we have stressed, the simple nature of the solutions found would allow a relatively easy calculation of holographic proxies of field theory quantities, that would help to characterize the non-thermalizing state. In this regard, the entanglement entropy computation in the three-dimensional case seems particularly easy to carry out. In this case, bulk geodesics are known in closed form, both in the interior and the exterior patch of the thin shell solution [200]. Furthermore, the matching conditions that determine how interior and exterior geodesics join have also been explicitly worked out in [117, 118].

Apart from exploiting the desirable features of our construction at the level of computing holographic probes, it is also mandatory to check the robustness of the results obtained. As several simplifying assumptions have been made, each one can be relaxed independently. For instance, more general equations of state, *i.e.* polytropes, can be considered. The requirement that the interior spacetime $\mathcal{M}_-$ is an empty AdS space with the same cosmological constant as the exterior one can also be lifted. Finally, going beyond spherical symmetry is a natural extension to consider, even though the addition of arbitrary angular deformations appears as a formidable challenge.

The fundamental question to answer is how the behavior of the thin shell is going to transition from periodic to either quasiperiodic or collapsing. Said otherwise, after these different deformations of our setup are taken into account, are quasiperiodic solutions going to occupy a nonzero measure of the phase space of the system?

It must also be mentioned that, after our original work [3] first appeared, [201] studied the dynamics of *two* spherically symmetric thin shells in global AdS$_4$ and found surprising agreement with the behavior of broad Gaussian initial data reported in [142]. At present, it is unknown if there exists a thin shell construction which shows a $t_c(m)$ that matches the behavior of the turbulently unstable families of initial data of [130]. This question is worth pursuing. To answer it, the protocol determining the shell interaction in [201] would probably need to be generalized.

Chapter 5

Stability of charged global AdS$_4$ geometries

5.1 Summary

In this chapter, we undertake the stability analysis of Einstein-Maxwell-scalar theory with global AdS$_4$ asymptotics, both at the linear and nonlinear level. For definiteness, we will consider a massless, complex scalar field that couples covariantly to the electromagnetic field. From the AdS/CFT perspective, this gravitational system describes a CFT$_3$ placed on a two-sphere where, besides the energy-momentum tensor T_{ab} and a marginal scalar operator $\mathcal{O}$, dual respectively to $g_{\mu\nu}$ and ϕ, there exists also a conserved global $U(1)$ current, J_μ, dual to the electromagnetic field A_μ. We present the model in section 5.2, discussing in detail its action, equations of motion, boundary conditions and computation of the conserved charges.

As we have discussed in 1, the fact that the scalar operator $\mathcal{O}$ is charged under the global internal $U(1)$ symmetry gives rise to a rich landscape of equilibrium solutions. At finite entropy and charge density, these include both normal phases, represented by AdS$_4$-Reissner-Nordström black hole, as well as superfluid phases, represented by hairy black holes. There also exists a new kind of statics solutions: the solitons. These are static, horizonless geometries supported by a nontrivial, normalizable scalar field profile. From the dual point of view, they correspond to pure states that should be identified with macroscopic Bose-Einstein condensates. The existence of this plethora of equilibrium states gives rise to a rich landscape of possible phase transitions, which we unravel both in the microcanonical and the grand-canonical ensembles.

In section 5.3, we construct the microcanonical phase diagram. Here, the thermodynamical potential to be extremized corresponds to the entropy. We demonstrate that, depending on the value of the electromagnetic coupling e, there exist three possible different structures for this diagram. Our findings build up in parallel with the achievements of [202] [203] where the landscape of static solutions was unraveled for five-dimensional case. We comment on the salient similarities and differences between our results and theirs. We analyze in detail the possible behaviors of the soliton solutions, and illustrate how they can be put into correspondence with planar geometries after a suitable blow up limit.

Section 5.4 focuses on the grand-canonical phase diagram. The structure is enriched by the fact that the free energy now can depend on two dimensionless parameters, μL and TL. We compute the grand-potential and perform a scan to elucidate how the structure of the phase diagram changes depending on their values. We uncover hairy black hole branches of negative specific heat and establish on firm grounds that they are always thermodynamically subdominant.

Then, in section 5.5, we discuss in detail the stability of our theory at the nonlinear level. We reviewed the recent research in the AdS instability problem in chapter 1, section 1.3. Let us remind the reader the major lessons obtained from this body of work that are of interest for the present chapter. The original numerical experiment of Bizon and Rostworowski in [130] showed that the nonlinear evolution of some family of arbitrarily small scalar field perturbations inevitably ended up in the collapse and formation of a black hole. Perturbatively, the problem was also examined [136] in the context of purely gravitational perturbations, and the importance of two ingredients was signalled: the presence of a fully resonant spectrum for the linearized perturbations, and the existence of time-periodic solutions that act as centers of stability islands in phase space. Back to the scalar field case, this suggestion received further backup from other contributions [135][134]. In this case, the periodic solutions were named oscillons, and indeed, the two previous observations became consistent in that the spectrum of linearized perturbations around an oscillon turns out not to be fully resonant. After some years of analytic and numerical work, it has become clear that there is a wealth of situations that one can encounter. One may choose to change either the dynamics (the action) or the kinematics (the boundary conditions). Generically, when departing from the easiest case of perturbations on pure AdS, the resonant property is lost [133].

In our case, to investigate the nonlinear stability of our Einstein-Mawell-scalar theory we must carry out a numerical analysis, searching for endpoints of the evolution in one of the possible static forms we discussed above. Performing these simulations with Dirichlet boundary conditions at the boundary is tantamount to studying the thermalization of the dual quantum system in the microcanonical ensemble.

The central question in this section is whether similar conclusions as those obtained in [130] can be extrapolated to the present situation. We consider Gaussian initial data families with different charges, generalizing the uncharged ones discussed in [130]. These initial conditions have an amplitude ϵ and a width σ. We find that for narrow initial pulses, a collapse protocol that shows a turbulent instability to black hole formation can be constructed. This fact confirms the expectation that places the origin of the turbulent cascade in the fully resonant character of the normal mode eigenfrequency spectrum, a fact that also upholds in the presence of a finite electromagnetic coupling. On the other hand, by analyzing the behavior of constant charge initial data, we have conclude that the turbulent instability is absent when the mass is sufficiently low. In the same way as pure AdS$_4$ controls the instability corner found in the previous case, we expect that soliton solutions are responsible for the nonlinear stability observed here, in the same vein as it happens at zero coupling for boson stars.

In order to confirm this picture, in section 5.6 we examine the linear and nonlinear stability of fluctuations placed on top of the soliton solutions. By a numerical computation, we show that their normal eigenfrequency spectrum is nonresonant. As expected, the linear instability, signaled by an imaginary eigenfrequency, is seen to appear as a result of a Chandrasekhar instability. For higher amplitude perturbations we resort to a full-fledged numerical simulation of the evolution of the system. In general, linear stability extends to nonlinear stability up to some threshold for the amplitude of the perturbation. Beyond that, the soliton is destroyed and collapses to a hairy black hole. We discover that the protection region where oscillations do not decay does not scale properly in the limit of large mass and charge to survive after blow up. This fact seems to point to the necessity of having a mass gap, and not just a mass scale, to find such oscillatory behaviors.

Finally, in section 5.7 we discuss the post-collapse relaxation of several one-point functions in our model, focusing on the vacuum expectation value of the marginal scalar operator. By employing the four-dimensional charged Vaidya model as a test example, we provide reliable evidence favoring the suitability of our coordinate system to address this issue. For initial data showing prompt collapse, we identified three different relaxation regimes that match perfectly the ones previously found in [103] for the four-dimensional, planar case (see chapter 1 for the statement of these results). We demonstrate that, for a given set of conserved charges, these relaxation regimes are independent on the particular form of the initial data considered, pointing towards their origin being in the structure of the quasinormal mode spectrum of the final black hole. To conclude, we comment on the late-time relaxation of the scalar operator for initial data that do show prompt collapse. We identify a new regime where long-lived oscillations seem to be present.

5.2 The model

5.2.1 Action and equations of motion

We are considering four-dimensional Einstein gravity with a negative cosmological constant in the presence of Maxwell electrodynamics and a charged complex scalar field with zero mass. For the sake of generality, let us treat the $d-$dimensional case with a nontrivial scalar potential. Our action is

$$S=\frac{1}{2\kappa^2}\int d^{d+1}x\sqrt{-g}\,(R-2\Lambda)-\int d^{d+1}x\sqrt{-g}\left(D_\mu\phi\bar{D}^\mu\phi^*+V(|\phi|)\right)-\frac{1}{4}\int d^{d+1}x\sqrt{-g}F_{\mu\nu}F^{\mu\nu}, \tag{5.2.1}$$

where $\kappa^2=8\pi G$, $\Lambda=-d(d-1)/2l^2$. We are working in length units such that $l=1$. The covariant derivative is given by

$$D_\mu\phi\equiv(\partial_\mu-ieA_\mu)\phi. \tag{5.2.2}$$

Note that the backreaction of the scalar field on the geometry is controlled by the electromagnetic coupling e, in such a way that $e\to\infty$ corresponds to the probe limit. The equations of motion that follow from (5.2.1) are

$$\begin{aligned} R_{\mu\nu} - \frac{1}{2} g_{\mu\nu} R + \Lambda g_{\mu\nu} &= \kappa^2 \left(T^{(\phi)}_{\mu\nu} + T^{(A)}_{\mu\nu} \right), && (5.2.3) \\ \frac{1}{\sqrt{-g}} D_\mu \left(\sqrt{-g} g^{\mu\nu} D_\nu \phi \right) &= \frac{\partial V(|\phi|)}{\partial \phi^*}, && (5.2.4) \\ \frac{1}{\sqrt{-g}} \partial_\mu (\sqrt{-g} F^{\mu\nu}) &= J^\nu, && (5.2.5) \end{aligned}$$

with the following energy-momentum tensor and charge currents

$$\begin{aligned} T^{(\phi)}_{\mu\nu} &= \left(\bar{D}_\mu \phi^* D_\nu \phi + \mu \leftrightarrow \nu \right) - g_{\mu\nu} \left(|D\phi|^2 + V(|\phi|) \right), && (5.2.6) \\ T^{(A)}_{\mu\nu} &= F_{\mu\alpha} F_\nu{}^\alpha - \frac{1}{4} g_{\mu\nu} F^2, && (5.2.7) \\ J^\nu &= ie \left(\phi^* D_\mu \phi - \phi (\bar{D}_\mu \phi^*) \right) g^{\mu\nu}. && (5.2.8) \end{aligned}$$

As usual, we restrict ourselves to spherically symmetric solutions and employ the ansatz

$$ds^2 = \frac{1}{\cos^2 x} \left(-f(t,x) e^{-2\delta(t,x)} dt^2 + f(t,x)^{-1} dx^2 + \sin^2 x \, d\Omega^2_{d-1} \right), \qquad (5.2.9)$$

$$A = A_t(t,x) dt, \qquad (5.2.10)$$

$$\phi = \phi(t,x). \qquad (5.2.11)$$

This ansatz leaves as residual gauge transformations

$$\phi \to e^{i\Lambda(t)} \phi, \qquad (5.2.12)$$

$$A_t \to A_t - ie \partial_t \Lambda(t), \qquad (5.2.13)$$

under which the equations of motion must be covariant. This motivates defining the following $U(1)-$covariant fields

$$\Phi(t,x) \equiv \phi'(t,x), \qquad (5.2.14)$$

$$\Pi(t,x) \equiv \frac{e^\delta}{f} D_t \phi. \qquad (5.2.15)$$

The first-order form of the Klein-Gordon equation is finally found to be

$$\begin{aligned} \dot{\Phi} &= \left(f e^{-\delta} \Pi + ie A_t \phi \right)', && (5.2.16) \\ \dot{\Pi} &= \frac{1}{\tan^{d-1} x} \left(\tan^{d-1} x f e^{-\delta} \Phi \right)' + ie A_t \Pi - \frac{1}{\cos^2 x} e^{-\delta} \partial_{\phi_c} V(\phi), && (5.2.17) \end{aligned}$$

while the $tt, xx-$components of the Einstein equation reduce to the two elliptic equations

$$\begin{aligned} f' &= \frac{d - 2 + 2\sin^2 x}{\sin x \cos x} (1 - f) - \frac{2\kappa^2}{d-1} \sin x \cos x \, f \, \left(|\Phi|^2 + |\Pi|^2 \right) && (5.2.18) \\ &\quad - \frac{\kappa^2}{(d-1)} e^{2\delta} \cos^3 x \sin x \, A_t'(t,x)^2 - \frac{2\kappa^2}{d-1} \tan x \, V(|\phi|), \\ \delta' &= -\frac{2\kappa^2}{d-1} \sin x \cos x \left(|\Phi|^2 + |\Pi|^2 \right). && (5.2.19) \end{aligned}$$

There is one additional equation coming from the $tx-$component of Einstein equation that yields the momentum constraint

$$\dot{f} = -\frac{4\kappa^2}{d-1} \sin x \cos x f^2 e^{-\delta} \, \mathrm{Re}(\Phi \Pi_c). \tag{5.2.20}$$

Concerning Maxwell's equations, let us define $C \equiv A_t'$, in such a way that from (5.2.5) we arrive to the following two equations

$$\begin{aligned} \left(e^{\delta} C\right)' &= 2e \frac{1}{\cos^2 x} \mathrm{Im}(\phi \Pi_c) - e^{\delta} C((d-3)\tan x + (d-1)\cot x), & (5.2.21) \\ (\dot{e^{\delta} C}) &= 2e \frac{e^{-\delta} f}{\cos^2 x} \mathrm{Im}(\phi \Phi_c) & (5.2.22) \end{aligned}$$

which can be easily shown to be compatible. The latter equation is the Gauss law constraint, while the former provides an elliptic equation that determines A_t. Indeed, assuming that A_t' is bounded at $x = x_0$, we can integrate (5.2.21) to find

$$A_t' = 2e \, e^{-\delta} \sin^{1-d} x \cos^{d-3} x \int_{x_0}^{x} \tan^{d-1} x \, \mathrm{Im}(\phi \Pi_c). \tag{5.2.23}$$

5.2.2 Boundary conditions

Solving equations (5.2.16)-(5.2.19),(5.2.21) in the domain $x \in [x_0, \pi/2]$ requires specifying appropriate boundary conditions. Let us define $\rho \equiv \pi/2 - x$. Focusing from now on the $V(|\phi|) = 0$ case, the following ultraviolet series expansions follow directly from the equations of motion

$$\begin{aligned} \phi(t,x) &= \phi_0(t) + \ldots + \phi_d(t)\rho^d + \ldots, & (5.2.24) \\ A_t(t,x) &= \mu + Q\rho^{d-2} + \ldots, & (5.2.25) \\ f(t,x) &= 1 + \ldots - M\rho^d + \ldots, & (5.2.26) \\ \delta(t,x) &= \delta_0(t) + \ldots + \delta_4(t)\rho^{d+1} + \ldots . & (5.2.27) \end{aligned}$$

We work boundary time gauge $\delta_0(t) = 0$; standard holographic renormalization then dictates that $\phi_0(t), \phi_d(t)$ determine the source and vacuum expectation value of scalar operator $\mathcal{O}$, while μ sets the dual CFT$_3$ chemical potential and Q the charge density of the state in question. M determines the state's energy density. In this chapter, we are solely considering out-of-equilibrium states set by the specification of initial data at $t = 0$ and, in consequence, for $t \geq 0$ we demand normalizability of the scalar field profile, $\phi_0(t) = 0$.

When the infrared end of the geometry corresponds to $x_0 = 0$, origin regularity enforces that $f(t,0) = 1, \Phi(t,0) = 0$ and, as usual, it follows that ϕ, f, δ and A_t are even functions of x. This condition upholds when considering a time-dependent situation or a static solitonic solution. For static black hole geometries, the condition that $x_0 = x_h$ corresponds to a horizon requires that $f(x_h) = 0$, while for A to be well-defined as a one-form when continuing analytically to Euclidean signature, we must demand that $A_t(x_h) = 0$. In this case, neither ϕ, f, δ nor A_t have a definite parity around x_h.

5.2.3 Conserved charges

As metioned, Q and M determine respectively the charge and energy densities of the dual field theory state. Owing to the form of equations (5.2.18)(5.2.21), it is possible to find an explicit integral expression for these quantities. Let us consider Q first. Notice that, with the ansatz we are considering, the electromagnetic current reads

$$J^\mu(t,x) = 2e\cos^2 x(-e^\delta\,\mathrm{Im}(\phi\Pi_c), f\,\mathrm{Im}(\phi\,\Phi_c), 0, 0) \tag{5.2.28}$$

and, therefore, the total charge of the spacetime is given by

$$\begin{aligned}\mathcal{Q} &= \int_{S_{d-1}} d\Omega_{S_{d-1}} \int_0^{\pi/2} dx\sqrt{-g}J^0(x) &(5.2.29)\\ &= -2eV_{S_{d-1}}\int_0^{\pi/2} dy\tan^{d-1} y\,\mathrm{Im}(\phi\Pi_c). &(5.2.30)\end{aligned}$$

Now, take (5.2.21) and notice that the following expression holds

$$\frac{(-1)^{d-3}}{(d-3)!}A_t^{(d-2)}(\pi/2) = 2e\int_0^{\pi/2}\tan^{d-1} y\,\mathrm{Im}(\phi\Pi_c) = \frac{-\mathcal{Q}}{V_{S_{d-1}}}. \tag{5.2.31}$$

In consequence, we find that

$$Q \equiv \frac{(-1)^{d-2}}{(d-2)!}A_t^{(d-2)}(\pi/2) = \frac{\mathcal{Q}}{(d-2)V_{S_{d-1}}}, \tag{5.2.32}$$

and finally

$$Q = -\frac{2e}{d-2}\int_0^{\pi/2}\tan^{d-1} y\,\mathrm{Im}(\phi\Pi_c). \tag{5.2.33}$$

Regarding M, from (5.2.18) and the boundary condition (5.2.26) it follows directly that

$$\begin{aligned}M &= \sin x_0\sec^3 x_0 e^{-\delta(x_0)} + &(5.2.34)\\ &+\kappa^2\int_{x_0}^{\pi/2}\left(\tan^d y\left(\Phi^2+\Pi^2\right)e^{-\delta} + \frac{1}{2}\sin^2 y A_t'^2 e^{\delta}\right), &(5.2.35)\end{aligned}$$

where we have allowed for the possibility that $x_0 = x_h$.

5.3 The microcanonical phase diagram

From the AdS/CFT perspective, our holographic CFT$_3$ contains an energy-momentum tensor operator T_{ab}, dual to the bulk metric $g_{\mu\nu}$, a conserved global $U(1)$ current J_a, dual to the electromagnetic field A_μ, and a marginal scalar operator $\mathcal{O}$, charged under the global $U(1)$ symmetry and dual to ϕ. As discussed in chapter 1, charged geometries correspond to CFT$_3$ states with finite charge density, $\langle J_t\rangle \neq 0$, that might or might not break spontaneously the global $U(1)$ symmetry, depending on whether $\langle\mathcal{O}\rangle \neq 0$ or $\langle\mathcal{O}\rangle = 0$. Restricting to normalizable and spherically symmetric configurations, the space of equilibrium states of the CFT$_3$ is composed of[1]

---

[1] See appendix 5.A.1 for a technical discussion of the numerical construction of these static solutions.

- The $M = Q = \langle \mathcal{O} \rangle = 0$ vacuum, holographically dual to AdS_4.
- $M \neq 0$, $Q = \langle \mathcal{O} \rangle = 0$ thermal states with finite entropy, holographically dual to AdS_4-Schwarzschild black holes.
- $M \neq 0$, $Q \neq 0$, $\langle \mathcal{O} \rangle = 0$ thermal states with finite entropy, holographically dual to AdS_4-Reissner-Nordström black holes, that do not break spontaneously the boundary global $U(1)$ symmetry.
- $M \neq 0$, $Q \neq 0$, $\langle \mathcal{O} \rangle \neq 0$ thermal states with finite entropy, holographically dual to AdS_4-hairy black holes, that do break spontaneously the boundary global $U(1)$ symmetry. They correspond to superfluid states in the dual CFT_3.
- $M \neq 0$, $Q \neq 0$, $\langle \mathcal{O} \rangle \neq 0$ Bose-Einstein condesates with zero entropy, holographically dual to soliton solutions.[2]

Therefore, at a given electromagnetic coupling e, the microcanonical phase diagram is parameterized by Q and M. If, for a given set of conserved quantities, several of the aforementioned static solutions coexist, the thermodynamically dominant solution corresponds to the one with higher entropy. Depending on e, there exist three different regimes for the micrcocanonical phase diagram. These regimes are separated by two threshold values, e_t and e_{sr}, that signal the appearance of two distinct linear instabilities affecting extremal Reissner-Nordström black holes:

- For $e \geq e_t$, extremal Reissner-Nordström black holes are subjected to a tachyonic instability. This instability is triggered by the fact that the nontrivial gauge field profile makes a negative contribution to the effective scalar field mass, lowering it below the Breitenlohner-Freedman bound of the AdS_2 factor of the near-horizon geometry. This tachyonic instability is the physical mechanism that allows for hair formation in the planar holographic superconductors introduced in [54][56]. In our setup, it is possible to show explicitly that[3]

  $$e_t^2 = \frac{4 + d(d - 4 + r_h^2(d-1))}{4r_h^2(d-1)(d(r_h^2+1)-2)}, \tag{5.3.36}$$

  where r_h is the event horizon radius of the extremal Reissner-Nordström black hole. Therefore, $r_h \to \infty$ black holes become unstable first, while the threshold (5.3.36) diverges as $r_h \to 0$, showing that small extremal Reissner-Nordström black holes are immune to the tachyonic instability.
- For $e \geq e_{sr}$, a new superradiant instability appears. This superradiant instability is triggered by the fact that, for $e\mu > \Delta = d$,[4] the imaginary part of the lowest quasinormal mode of a small Reissner-Nordström black hole becomes positive: scalar

---

[2] The fact that the soliton solution is regular at $x = 0$ implies that, in the light of the HEE prescription and due to the homology constraint, $S_A = S_{\bar{A}}$, and the dual CFT_3 state they represent is pure.

[3] We work in units where $\kappa^2 = L = 1$.

[4] Here Δ is the conformal dimension of the dual operator $\mathcal{O}$.

waves scatter off the black hole with a reflection coefficient $|R| > 1$. The instability follows then from the reflecting boundary conditions imposed at infinity. Since the chemical potential is always bounded by its value at extremality, the minimum charge e_{sr} at which the superrandiant instability can appear is

$$e_{sr}^2 = \frac{d^2(d-2)}{d-1}\left(1 - \frac{d}{2(d-2)}r_h^2 + \mathcal{O}(r_h^{3/2}) + \ldots\right), \tag{5.3.37}$$

where we assume that $r_h \ll 1$. Note that the condition (5.3.37) cannot be directly applied to large Reissner-Nordström black holes.

The values of these thresholds for AdS$_{d+1}$ with $d = 3, 4$ for $\kappa^2 = 1$ are:

	e_t^2	e_{sr}^2
AdS$_4$	$3/2$	$9/2$
AdS$_5$	3	$32/3$

In the remaining part of this section we summarize the phase diagram for the static solutions of our Einstein-Maxwell-scalar theory for values of the coupling lying on each interval, and discuss the associated soliton solutions. Our analysis follows [203], where the perturbative phase diagram originally uncovered in [202] for the five-dimensional case was extended into the nonlinear regime.

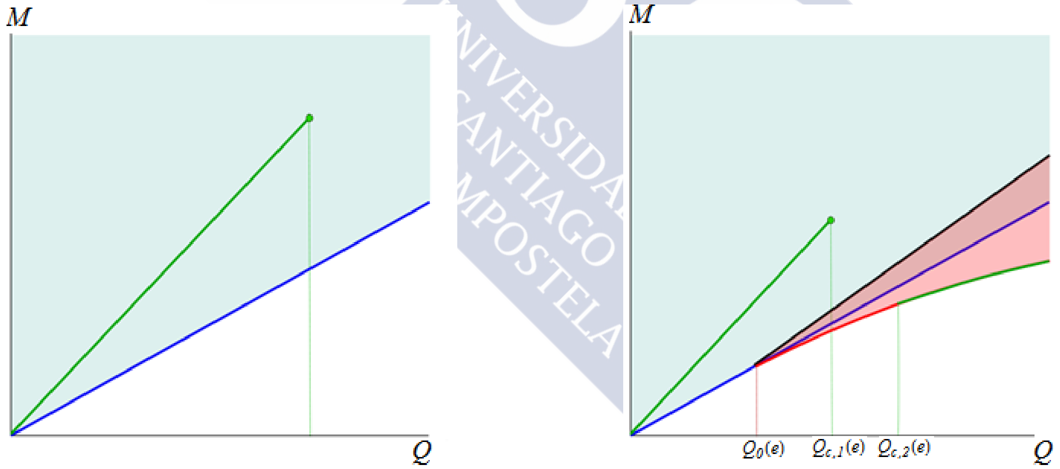

Figure 5.1: Left: microcanonical phase diagram for $e < e_t$. Right plot: microcanonical phase diagram for $e_t \leq e < e_{sr}$.

- $e < e_t$

  The only static solutions present are Reissner-Nordström black holes and solitons, which exist only below a Chandrasekhar limit $Q \leq Q_c(e)$, $M \leq M_c(e)$. In figure 5.1a, the green curve corresponds to the soliton family, the blue curve to extremal Reissner-Nordström black holes, and the blue shaded region to non-extremal Reissner-Nordström black holes.

- $e_t \leq e < e_{sr}$

  In this regime, in addition to Reissner-Nordström black holes and solitons, there exist hairy black holes in a band around extremality for $Q > Q_0(e)$ -red shaded region in figure 5.1b-. The red curve denotes extremal hairy black hole solutions and the black line marks the instability curve for the Reissner-Nordström solution. Solitons, depicted in green on figure 5.1, appear in two branches. One is vacuum connected and has bounded conserved charges, $Q \leq Q_{c,1}(e), M \leq M_{c,1}(e)$; the other one has unbounded conserved charges and is vacuum disconnected, since it only exists for $Q \geq Q_{c,2}(e), M \geq M_{c,2}(e)$. Both soliton branches merge, $Q_{c,2}(e) \to Q_{c,1}(e)$, as $e \to e_{sr}$. For $Q \geq Q_{c,2}(e)$, the lightest hairy black hole is no longer extremal. Numerical evidence suggests that its temperature is in fact divergent.

- $e_{sr} \leq e$

  Now hairy black holes exist for $Q > 0$ in a band around extremal Reissner-Nordström black holes. Concerning the solitonic solutions, the two branches observed for $e_t \leq e < e_{sr}$ merge into a single vacuum connected soliton branch with unbounded conserved charges. To our best numerical accuracy, the soliton line is the limit of $r_h \to 0$ hairy black holes with divergent temperature. The situation is similar to the five-dimensional setup [203]. However, in that case, a second critical charge was found, beyond which hairy black holes existed *below* the soliton line. We have found no trace of this particular behaviour in our numerical scan. This being said, it cannot be discarded that such a fine structure is present, but beyond the reach of our numerical accuracy. To settle this question, a perturbative analysis along the lines of [203] would be needed.

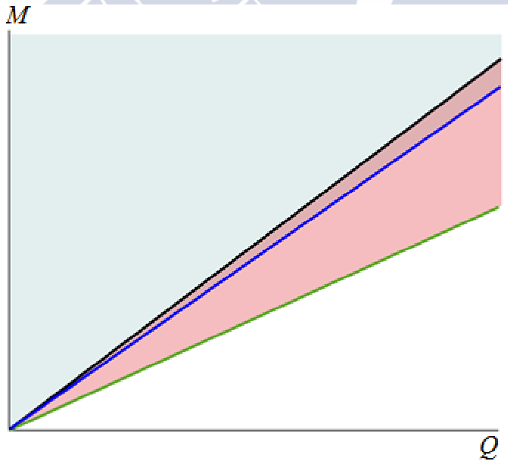

Figure 5.2: Microcanonical phase diagram for $e \geq e_{sr}$

5.3.1 The soliton branches

Let us describe the soliton solutions in more detail. They are fully-backreacted, horizonless solutions sourced by a normalizable scalar field profile $\phi_s(x)$. Equilibrium is attained by an exact compensation of gravitational and electrostatic forces. They come in one-parameter families that can be indexed by the central value $\phi_0 \equiv \phi_s(x = 0)$.

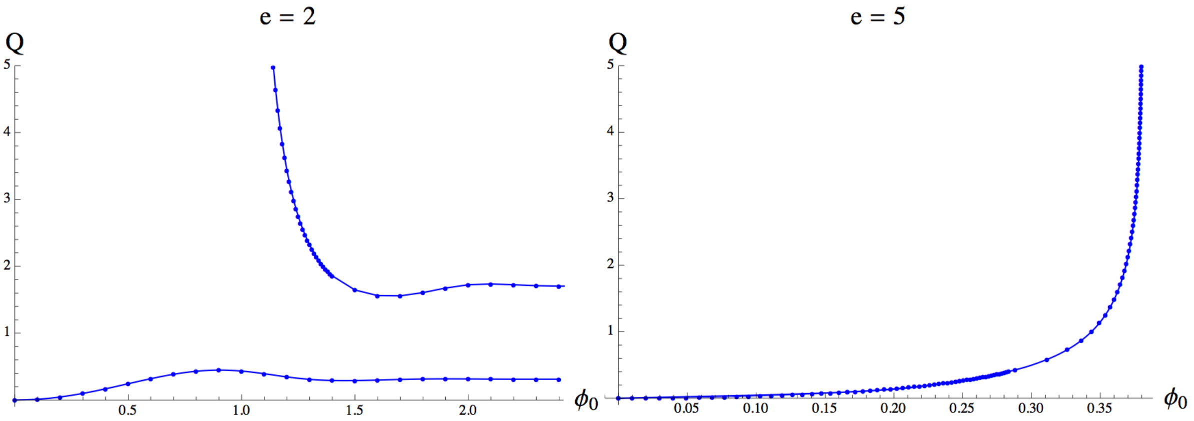

Figure 5.3: Left: charge of vacuum connected and disconnected soliton branches against ϕ_0 for $e = 2$. Right: soliton charge against ϕ_0 for $e = 5$.

Depending on the value of the coupling e, soliton families display different aspects:[5]

- For $e < e_t$, there exists a single soliton branch. It is continuously connected to the AdS$_4$ vacuum, in the sense that, for $\phi_0 \to 0$, it reduces to global AdS$_4$. Therefore, for $\phi_0 \ll 1$, this soliton family admits a perturbative construction, and can be described as a $\omega = 0$ scalar normal mode dressed nonlinearly. Besides this fact, the trademark property of this branch is the existence of a critical value $\phi_0 = \phi_{c,1}$ at which both the soliton mass $M(\phi_0)$ and the soliton charge $Q(\phi_0)$ attain a maximum. When $\phi_0 > \phi_{c,1}$, M and Q spiral around a limiting value that is reached at $\phi_0 \to \infty$.

- For $e_t \leq e < e_{sr}$, there exist two different soliton branches. The first one, connected with the vacuum, was already present in the $e < e_t$ case. The second one, disconnected from the vacuum, is not amenable to a perturbative construction. In this branch, solitons exist for ϕ_0 larger than some critical value $\phi_{c,2a}$, at which the conserved charges M, Q diverge. They decrease for $\phi_0 > \phi_{c,2a}$ until they reach a minimum value at some $\phi_0 = \phi_{c,2b} > \phi_{c,2a}$. In parallel with the first soliton branch, for $\phi_0 > \phi_{c,2b}$, M and Q show damped oscillations around a limiting value that is attained in the $\phi_0 \to \infty$ limit. Representative plots of the behavior just described are provided in figure 5.3a.

- For $e \geq e_{sr}$, the two soliton branches described in the previous item fuse into a single soliton family that is vacuum connected (see figure 5.3b). Again, there exists a critical $\phi_{c,3}$ such that M and Q seem to diverge in the $\phi_0 \to \phi_{c,3}$ limit.

---

[5] Our results agree essentially with the ones presented in [204] for the $m^2 = -2$ case.

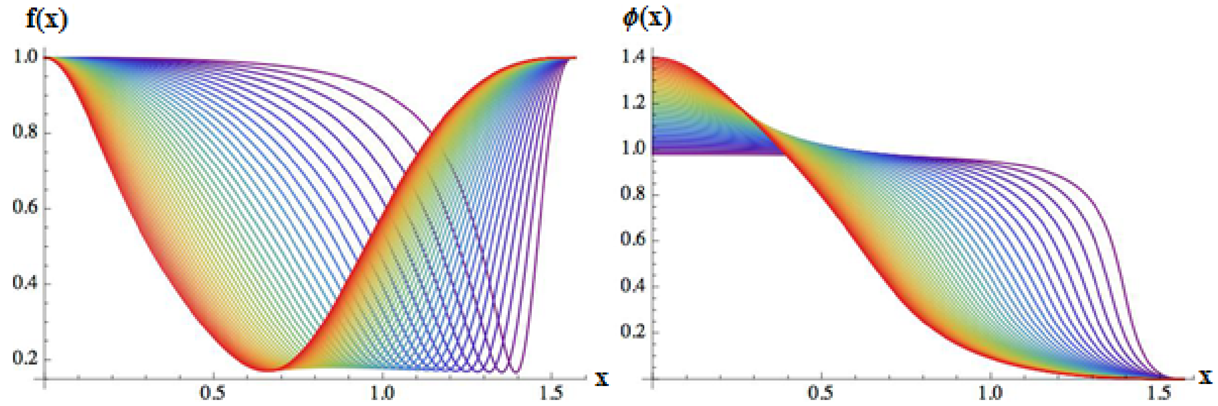

Figure 5.4: Fields for the vacuum disconnected soliton branch at $e = 2$ from $\phi_0 = 1.4$ (red) to $\phi_0 = 0.98$ (purple) in steps of $\delta\phi_0 = -0.01$.

5.3.2 The blow up limit

In figure 5.4 we plot f_s and ϕ_s for representative soliton solutions in the vacuum disconnected branch at $e = 2$. We start at $\phi_0 = 1.4$ (reddest curve), and decrease ϕ_0 in steps of $\delta\phi_0 = -0.01$ up to $\phi_0 = 0.98$ (bluest cuve). By inserting these values into the $Q - \phi_0$ plot of figure 5.3a, it is clearly appreciated that the field gradients become more localized in the near-boundary region as the conserved charges of the soliton become larger.

As emphasized in [204], the fact that solitons come in one-parameter families with unbounded conserved charges allows taking a *blow up* limit that maps onto a solution with planar geometry. The procedure starts by looking at the near-boundary expansion

$$\phi(t,r) = \frac{\phi_3}{r^3} + O(r^{-4}) \tag{5.3.38}$$

$$A = A_t(t,r)dt = \left(\mu - \frac{Q}{r}\right)dt + O(r^{-2}) \tag{5.3.39}$$

$$ds^2 = -\left(r^2 + 1 - \frac{m}{r}\right)dt^2 + \frac{dr^2}{r^2 + 1 - \frac{m}{r}} + r^2 d\Omega_2^2 + O(r^{-2})\,. \tag{5.3.40}$$

Introducing new coordinates

$$r = \lambda\hat{r} \quad t = \frac{\hat{t}}{\lambda} \quad \theta = \frac{\hat{\theta}}{\lambda} \quad \varphi = \hat{\varphi} \tag{5.3.41}$$

and redefinitions

$$M = \lambda^3\hat{m}(\lambda) \quad Q = \lambda^2\hat{q}(\lambda) \quad \mu = \lambda\hat{\mu}(\lambda) \quad \phi_3 = \lambda^3\hat{\phi}_3(\lambda)\,, \tag{5.3.42}$$

(5.3.38)-(5.3.40) become

$$\phi = \frac{\hat{\phi}_3}{\hat{r}^3} + O(\hat{r}^{-4}) \tag{5.3.43}$$

$$A = A_t d\hat{t} = \left(\hat{\mu} - \frac{\hat{q}}{\hat{r}}\right) d\hat{t} + O(\hat{r}^{-2}) \tag{5.3.44}$$

$$\begin{aligned} ds^2 = &-\left(\hat{r}^2 + \frac{1}{\lambda^2} - \frac{\hat{m}}{\hat{r}}\right) d\hat{t}^2 + \left(\hat{r}^2 + \frac{1}{\lambda^2} - \frac{\hat{m}}{\hat{r}}\right)^{-1} d\hat{r}^2 \\ &+ \hat{r}^2 \left(d\hat{\theta}^2 + \lambda^2 \sin\left(\frac{\hat{\theta}}{\lambda}\right)^2 d\hat{\varphi}^2\right) + O(\hat{r}^{-2}) \,. \end{aligned} \tag{5.3.45}$$

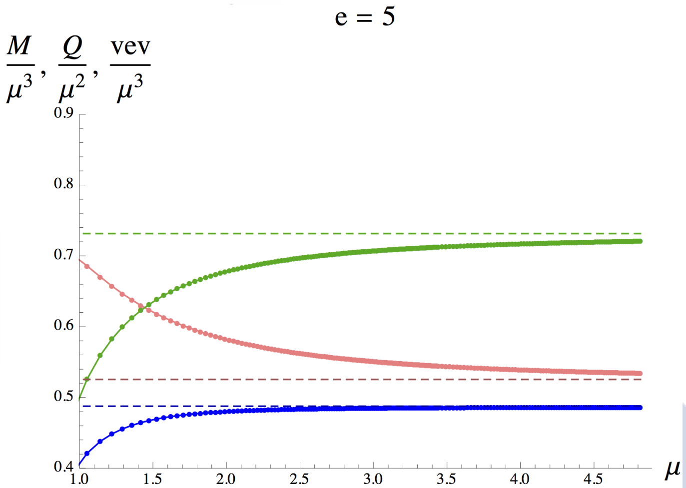

Figure 5.5: Scaling ratios (5.3.46) for the $e = 5$ soliton branch. Blue, green and pink colors correspond to the scaling ratios of the mass, charge and vev, respectively. Dashed lines correspond to the same ratios computed in the asymptotic planar geometry reached upon blow up.

So far, this is only a reparametrization of our initial solution. However, if we now take the singular limit $\lambda \to \infty$ and, simultaneously, move along the soliton branch in such a way that the vector of rescaled quantities $\vec{\chi}(\lambda) \equiv (\hat{m}(\lambda), \hat{q}(\lambda), \hat{\mu}(\lambda), \hat{\phi}_3(\lambda))$ remains finite, we obtain a planar geometry[6] characterized by the hatted quantities. For example, identifying the parameter λ with μ, the dimensionless ratios

$$\frac{M}{\mu^3}, \quad \frac{Q}{\mu^2}, \quad \frac{\phi_3}{\mu^3} \tag{5.3.46}$$

must tend to constant quantities when $\mu \to \infty$ for the planar limiting geometry to have finite energy, charge and vev densities, respectively. In figure 5.5 the ratios (5.3.46) are plotted for the soliton branch at $e = 5$. The planar geometry obtained after the blow up limit is taken clearly matches the extremal hairy black brane geometry studied in [205], at the given

---

[6] Note that the boundary sphere maps onto a two-dimensional plane in the $\lambda \to \infty$ limit, with its metric written in polar coordinates.

e.[7] Incidentally, this observation explains why there does not exist a second soliton branch when $e < e_t$. In that case, in planar AdS, there is no near-horizon tachyonic instability that can trigger hair condensation, so there is no limiting extremal hairy black hole to which this hypothetical branch could map on.

5.4 Grand-canonical phase diagram

Section 5.3 provides a classification of static solutions in the microcanonical ensemble. Since we are considering a holographic CFT at finite volume, the thermodynamically dominant phase can change depending on the particular ensemble we are in. Recall that, for global asymptotics, Schwarzschild black hole solutions split into two different kinds, small and large, with negative and positive specific heat respectively. In our setup, large Reissner-Nordström or hairy black holes are to be put into correspondence with stable quantum states in the canonical or grand-canonical ensembles. In addition to these finite-entropy thermal states, we must also consider the thermal gas represented by Euclidean AdS$_4$ and the Bose-Einstein condensates dual to the the soliton solitons. These different geometries are the building blocks of a rich landscape of first- and second-order phase transitions.

In this section, we analyze the grand-canonical phase diagram of the Einstein-Maxwell-scalar system for a coupling $e = 3$. For any $e > e_t$, the results are qualitatively identical. Instead, below e_t the situation changes, since the only building blocks for obtaining a phase transition are Reissner-Nordström black holes and soliton solitons. In this regard, our setup differs from the one analysed in [204][206], where the scalar field is tachyonic.

5.4.1 Small and large hairy black holes

The thermodynamics of Reissner-Nordström black holes, both in the canonical and grand-canonical ensembles, has been examined with great care in [61][62]. Here, we focus on the thermodynamical behavior of hairy solutions. The Hawking temperature is given by

$$T = \frac{1}{8\pi}\Big((6 - A_t'(x_h)^2\cos^4 x_h)\tan x_h + 2\cot x_h\Big) \tag{5.4.47}$$

and the entropy is

$$S = 2\pi A_h = 8\pi^2 \tan(x_h)^2, \tag{5.4.48}$$

where A_h is the area of the event horizon horizon.

In figure 5.6a, we plot $|\langle\mathcal{O}\rangle|$ for fixed chemical potential $\mu = 1.5$ as a function of T. The observed behaviour is typical when the gravitational solution corresponds to a small hairy black hole: condensation appears for $T > T_c$. This phenomenon, dubbed retrograde condensation in the literature, has appeared in different contexts [207][208]. We will show that

---

[7] We have indeed verified that, in the time-independent case, our equations of motion reduce to those on [205] after the blow up limit if we set $\kappa^2 = 1/2$ so field normalizations agree.

this condensed phase is not physically relevant because it is thermodynamically subdominant with respect to the Reissner-Nordström and soliton solutions. Note that the negative specific heat of this branch can be readily infered from figure 5.6b.

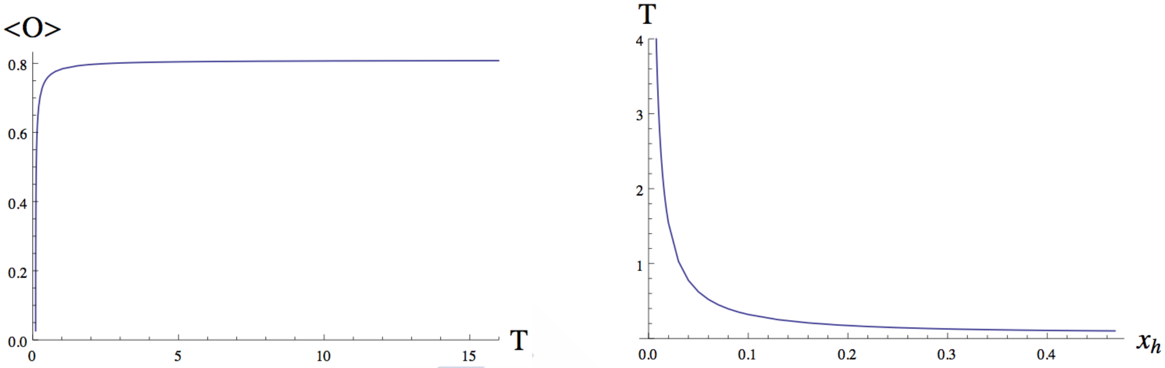

Figure 5.6: Condensate (left) and temperature (right) for hairy black holes with $\mu = 1.5$.

In order to exemplify small/large hairy black hole coexistence, we rise the value of the chemical potential up to $\mu = 3$. Figure 5.7a shows the behavior of $|\langle\mathcal{O}\rangle|$ as a function of T. The lower/upper curve corresponds to large/small hairy black hole solutions, as can be read from figure 5.7b. We will show that, upon lowering T, the system will undergo a second-order normal-superfluid phase transition involving the large hairy black hole branch, with the small one staying subdominant. In this regard, notice that for $T \to T_c^-$, $|\langle\mathcal{O}\rangle|$ shows the standard mean field theory scaling $|\langle\mathcal{O}\rangle| \propto (T_c - T)^{\frac{1}{2}}$.

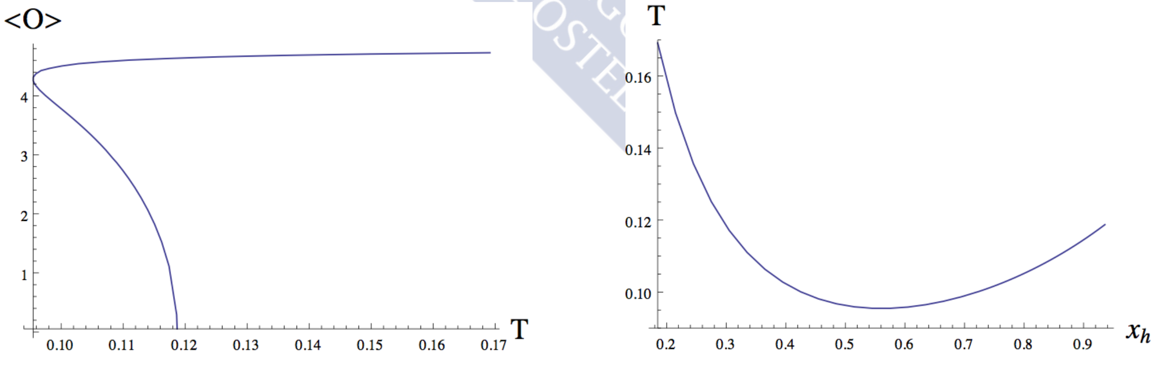

Figure 5.7: As figure 5.6, but for $\mu = 3$.

Further increasing the chemical potential, we observe the behaviour shown in figure 5.8 for $\mu = 15$. The same second-order normal-superfluid phase transition will happen here, but the small black hole branch has now disappeared.

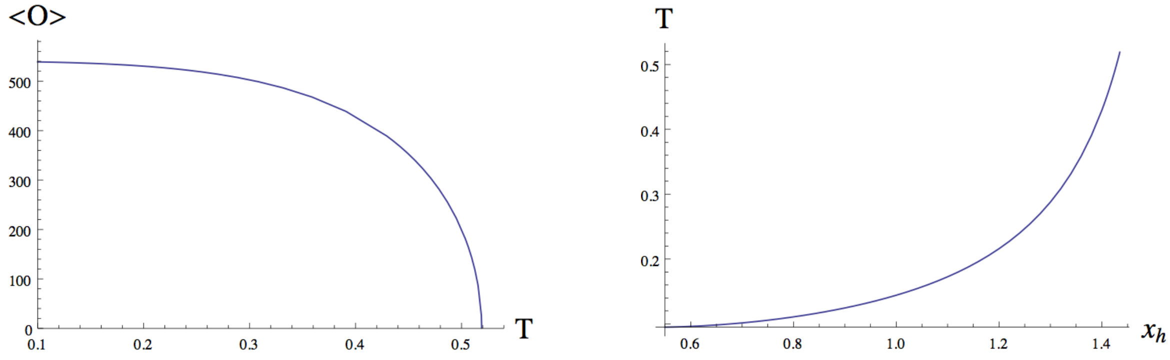

Figure 5.8: As figure 5.6, but for $\mu = 15$.

5.4.2 Grand-potential

Linear stability of the previous solutions amounts to the minimization of certain ensemble-dependent thermodynamical potential. In the grand-canonical ensemble this is the grand-potential $\Omega(T, \mu)$, which the AdS/CFT correspondence identifies with the on-shell renormalized Euclidean action $\Omega = TS_{\text{on-shell}}$.

In figure 5.9, we plot Ω and the entropy S as functions of T for $\mu = 1.5$. As mentioned, the hairy black hole curve, having negative specific heat, is thermodynamically subdominant. At $T = T_c$ we have a first-order phase transition with a net entropy reduction between the normal phase, which is represented by the Reissner-Nordström black hole and dominates for $T > T_c$, and a Bose-Einstein condensate, which corresponds to the soliton solution and dominates for $T < T_c$.

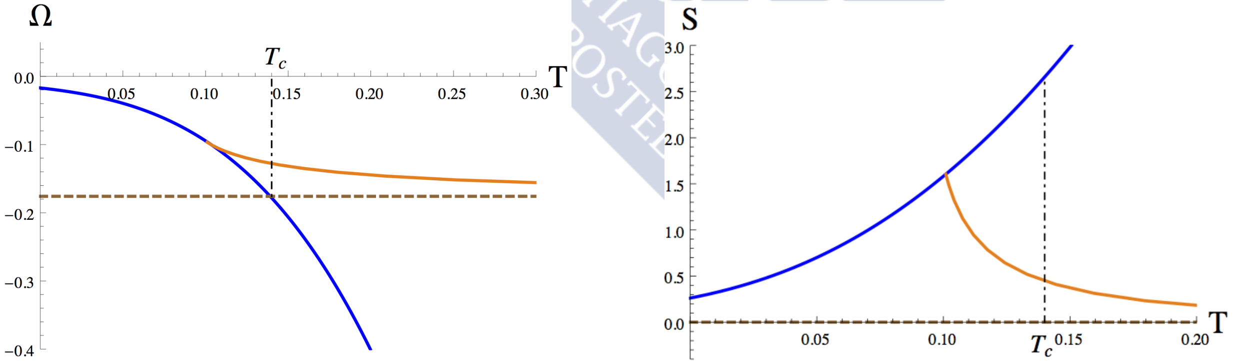

Figure 5.9: For $\mu = 1.5$, free energy (left) and entropy (right) against temperature for the different saddles involved in the determination of the grand-canonical phase diagram: Reissner-Nordström black holes (blue), hairy black holes (orange) and solitons (brown dashed).

At $\mu = 3$ (figure 5.10), there exist two different hairy black hole branches. Small hairy black holes continue to be thermodynamically subdominant at any T. For $T > T_{c_1}$, the system is in the normal phase. At $T = T_{c_1}$, there is a second-order phase transition with no entropy production from the normal phase to the superfluid one, holographically dual to the large hairy black hole. This superfluid phase continues to dominate the grand-canonical ensemble up to $T = T_{c_2}$, where there is a first-order phase transition with a net entropy reduction to the Bose-Einstein condensate.

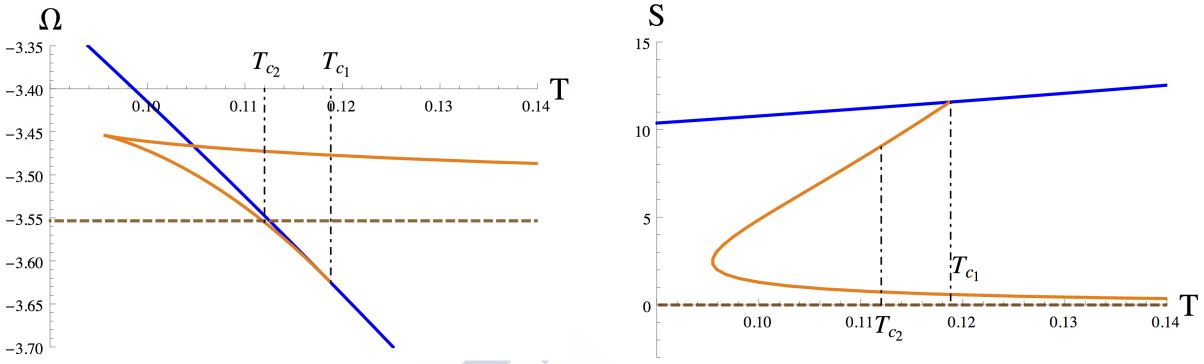

Figure 5.10: As figure 5.9, but for $\mu = 3$.

Finally, at $\mu = 15$ (figure 5.11), we observe that the grand-canonical phase diagram has the same structure as for the $\mu = 3$ case, the only difference being the disappearance of the small hairy black hole branch.

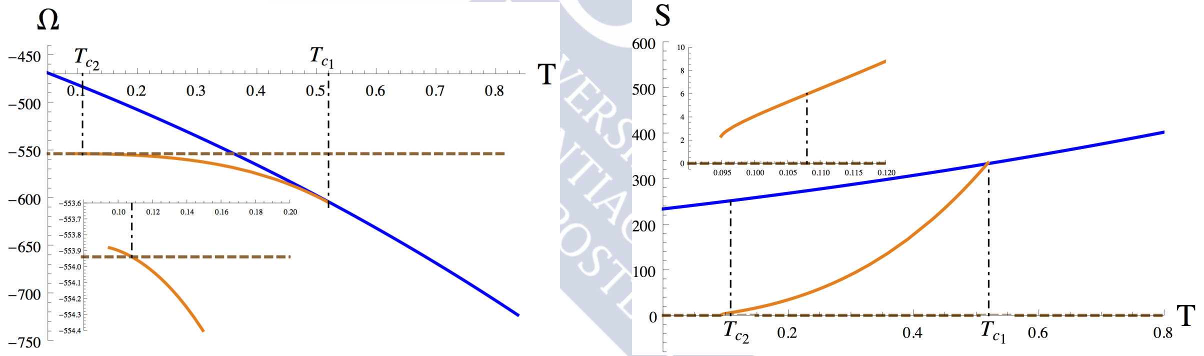

Figure 5.11: As figure 5.9, but for $\mu = 15$.

5.5 AdS nonlinear stability

The above sections have relied on a combination of analytical and numerical arguments. The construction of static solutions is performed by solving a nonlinear ODE system and setting up a shooting procedure. It involves fixing, for example, the event horizon radius of the desired solution and the value of the scalar field ϕ_o at such radius. Then the value of $A_t'(x_o)$ is also varied until one obtains a solution with vanishing source $\phi_b = 0$ and non vanishing vev $\phi_{b,3} \neq 0$. The end result is scrutinized to find the actual value of the mass M

and the charge Q of the obtained stationary solution. If more than one solution is available, a thermodynamical potential is to be invoked in order to select the correct groundstate in the ensemble under consideration. In a sense, this strategy relies on a certain amount of guesswork. Prior to the construction of hairy black holes in [54], the space of known static vacua consisted of either pure AdS or Reissner-Nordström black holes. Later on, solitons where first inferred, and then constructed [202] from a limit whereby the hairy black hole's horizon is shrunk to zero size.

In this section we will use a complementary approach. A numerical code for simulating the time evolution of a given non-equilibrium geometry is the closest one can get to a real experiment.[8] In this spirit, the approach starts from the other end: one devises a certain initial radial profile for the bulk fields, with a given total mass M and charge Q, and lets it evolve under a scheme that preserves these values. If the evolution settles down to a certain stationary state, it must necessarily be one in the list above. And if two of them are available with the same values of M and Q, the evolution will select the ground state in the microcanonical ensemble.[9] By evolving an initial condition below the blue curve in figure 5.2 this would have shown that black holes with abelian hair exist in global AdS, had this work been done prior to 2008. Furthermore, imagine there were another exotic type of black hole that nobody has constructed yet using static methods and suppose it had larger entropy than the known phases. The collapse simulation would *smell* its existence and the fields decay to that solution after exploring large portions of phase space. We must admit we have not found any new such solution using this, admittedly expensive, method.

In figure 5.12 we have plotted some snapshots of a typical collapse process to a hairy black hole. For the values of Q, M, and coupling e used in this simulation there is no Reissner-Nordström black hole available. Nevertheless at $t = 14.8$ the scalar develops a spike at a point where the metric approaches an apparent horizon, signalled by a zero of the function f (blue curve). Even if the zero value is never reached, the dynamics close to this point becomes extremely slowed down in terms of the boundary time. At later times, the outer oscillations of the scalar field start piling up on top of the first spike, and the metric function f tries to reach zero at higher values of the coordinate x (see inset). A very high precision and up to 2^{17} grid points are needed to push this numerical evolution safely, and resolve the region close to the collapse with enough accuracy, in particular monitoring the constancy of M and Q values throughout the process. The exponentially decaying ringdown ends up in a static solution where the outside hair profile resembles the ones in figure 5.4 for the soliton solutions.

We move now onto showing and commenting the results of uniparametric families of collapses that scan across the (Q, M) plane. The first protocol will involve a set of initial conditions, parameterized with some amplitude ϵ. Consider the following family of gaussian initial data

---

[8] See appendix 5.A.2 for a technical discussion of our simulation code and some convergence tests.

[9] This could proceed in a direct way or through a number of different steps. There are situations where prethermalization to some excited intermediate state followed by further relaxation to the true final equilibrium state can be observed [209]. It would be interesting to study in detail the possible existence of such metastable attractors in the present context.

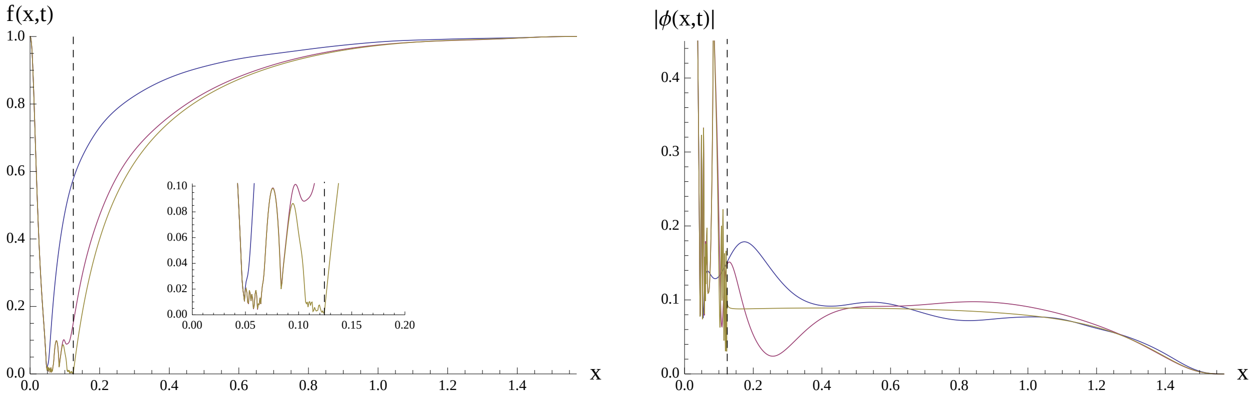

Figure 5.12: For coupling $e = 20$, we plot three snapshots of a collapse with mass $M = 2$ and charge $Q = 2.9$ at times $t = 14.8, 17.3$ and 28.1 (blue, magenta and yellow). At this time, the solution has become an almost static hairy black hole. The evolution exhibits the typical ring down whereby apparent horizon builds up while capturing successive oscillations of the scalar field. They fold behind the accumulation point of the vanishing locus of $f(t,x)$, hence the position of the event horizon

that initially fall from the boundary:

$$\Phi = \epsilon \cos\beta \, \frac{2}{\pi} \cos^2 x \exp\left(-\frac{4\cot^2(x)}{\pi^2\sigma^2}\right), \tag{5.5.49}$$

$$\Pi = i\epsilon \sin\beta \, \frac{2}{\pi} \cos^3 x \exp\left(-\frac{4\cot^2(x)}{\pi^2\sigma^2}\right). \tag{5.5.50}$$

Here, the angle β is fixed, and ϵ will decrease monotonically towards zero. The cases $\beta = 0, \pi/2$ corresponds to the uncharged initial conditions studied in [130], albeit with an initial pulse that starts infalling from the boundary [1], a fact that is inspired from the physics of a quench. For $\beta \neq 0, \pi/2$ we are dealing with a shell of charged scalar and gauge field collapsing together.

As extensively argued in [136], a resonant eigenfrequency spectrum for the scalar fluctuations around a reference solution is a necessary condition for the existence of the turbulent instability at the nonlinear level. This requirement is met for scalar fluctuations around AdS$_4$ at $e = 0$. A natural question is if this condition is preserved when a finite electromagnetic coupling is introduced. The answer turns out to be positive. In order to see this note that, over AdS$_4$, $O(\epsilon)$ scalar field perturbations source electromagnetic field ones only at order $O(\epsilon^2)$ and, in consequence, at $O(\epsilon)$ there exists a gauge where $A_t = O(\epsilon^2)$ and the covariant derivative (5.2.2) reduces to an ordinary derivative, leaving the original $e = 0$ eigenfrequency spectrum invariant. In consequence, we expect that, in the $\epsilon \to 0$ limit, initial data (5.5.49)-(5.5.50) with sufficiently small σ are still subjected to the turbulent instability, even if their charge density does not vanish. The only effect that a finite e bears is that the scalar eigenfrequency spectrum is not a gauge invariant object: the action of the residual gauge symmetry $\phi \to e^{-i\mu e t}\phi$, $A_t \to A_t + \mu$ over the original $e = 0$ scalar fluctuations, $\phi_n(t,x) = e^{i\omega_n^{(e=0)}t}e_n(x)$, $\omega_n^{(e=0)} = 3+2n$, $A_t^{(e=0)} = 0$ is implementing the change $\omega_n^{(e=0)} \to \omega_n^{(e)} = 3 - \mu e + 2n$, $A_t^{(e=0)} \to A_t^{(e)} = \mu$. Therefore, the condition $\partial_n \omega_n^{(e)} = 2$ is gauge-independent, while the absolute value of $\omega_n^{(e)}$ is not.

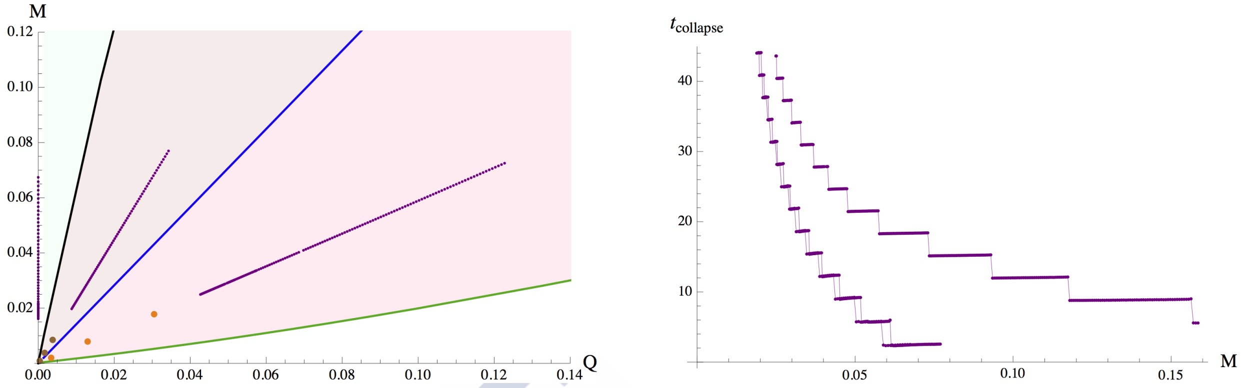

Figure 5.13: Collapses with $\sigma = 0.1$ and $e = 20$. In the left plot, the phase space and color coding is the same as in figure 5.2. The dotted purple lines represent three series of initial conditions with $\beta = 0°$, $45°$ and $82°$ from left (vertical) to right (most bended). For each line we have taken 3 points deep in the low ϵ limit with $\epsilon = 6, 4$ and 2, and performed very long time simulations in order to test the scaling hypothesis (see figure 5.15). Right plot: time for collapse for each of the three lines in the left plot, in the same order from left to right, as a function of the mass M. The time for collapse increases with the closeness to the soliton line, i.e. for fixed mass M, at higher charge Q.

In figures 5.13 and 5.16 we exhibit series of simulations for initial conditions of the form (5.5.49)(5.5.50) for $\sigma = 0.1$ and 0.2, and several values of β. The cases examined in [130] would lie on the vertical axis $Q = 0$ (uncharged case). Notice that we have searched for peculiar behaviours in different domains of the phase space in this microcanonical ensemble. Above the instability line where only Reissner-Nordström solutions exist, we find little or no difference with the case of zero charge. Below this line, the final state of the evolution is a hairy black hole. We have included two lines of collapse that bend towards the soliton line (the green line), in the region where hairy black holes exist, both above and below the line of extremal Reissner-Nordström (in blue).

We want to stress that it is by no means easy to engineer initial conditions that come close to the line of soliton solutions. In particular, within the family of gaussians spelled out in (5.5.49) and (5.5.50), by letting β sweep from 0 to $\pi/2$, the lines incline up to some point, for some β_0, where the initial conditions approaches maximally the soliton line, and then turn back towards the vertical. These values are, for example, $\beta_0 = 82°$ for $\sigma = 0.1$ and $\beta_0 = 75°$ for $\sigma = 0.2$. In principle one can engineer initial conditions that come closer to the soliton line by starting from the other end: namely, by perturbing a soliton, and this will be the subject of the next section. Most remarkable is the fact that is seems impossible to even write initial data whose charge, Q, and mass, M, give a point below the soliton line (white region). This seems to point out that soliton solutions extremize certain positive definite functional that can be derived from the action, even though they are not BPS solutions since, along the soliton line, $dM(Q)/dQ$ is a nontrivial function of Q.

Collapse time is one of the important observables in the game. We can see in figure 5.13 the case of sharp pulses with $\sigma = 0.1$ and $\beta = 0°$, $48°$ and $82°$. The horizontal axis represents the initial mass, M, which, for fixed σ, grows with ϵ^2. On the right, the times for collapse for each family are plotted. When moving along an individual series from right to left, the plateaux reflect the number of oscillations that the system undergoes before the final collapse is reached. We see that the behaviour points towards the existence of a corner of instability at the origin of the (Q, M) plane even in the charged situation, i.e., no sign of a threshold for stability is appreciated. This seems to confirm the expectation coming from the resonant character of the linearized approximation. From the figure 5.13b we also draw the important conclusion that, at fixed mass, charged configurations take longer time to collapse. This is in sharp contrast with the case without gauge field where charged initial conditions were collapsing sooner than neutral ones of the same mass (see figure 6 in [142]). Note that this behavior is to be expected, since it implies that electric repulsion counteracts gravitational attraction.

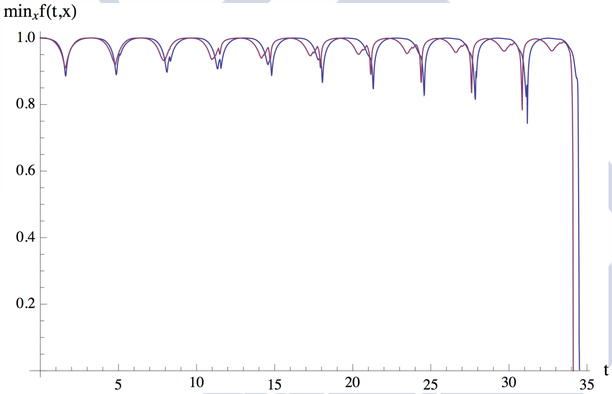

Figure 5.14: Plot of the minimum of $f(t, x)$ as a function of time for two simulations with similar histories in the lines $\beta = 45°$ (blue) and $\beta = 82°$ (magenta) in figure 5.13 (left). The roughness of the profile in the second case reveals that the scalar pulse is not smooth but fractures into ripples. This, presumably, is an effect of the electrostatic repulsion in action.

Like in [142], in the present situation the charge of the scalar pulse also adds to the defocusing. Still, what figure 5.13 says is that, for $\sigma = 0.1$, this is not enough to erase the instability corner, even for the most charged gaussians that one can device (the right most blue magenta diagonal). Both plots for collapse time scale with $1/M \sim 1/\epsilon^2$ in the $\epsilon \to 0$ limit. However, a closer look at the evolution of the scalar field reveals that, for $\beta = 89°$, the initial gaussian develops subpulses. A reflection of this can be observed in figure 5.14 which plots the minimum of the blackening factor $f(t, x)$, $\min_x f(t, x)$, as a function of time. The evolution still exhibits a quasiperiodic structure where the action of the turbulent cascade is apparent in that the minima become sharper and deeper until finally collapse takes over.

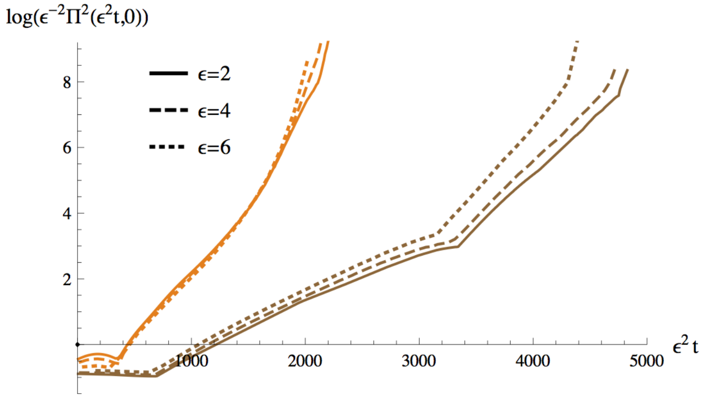

Figure 5.15: Evolution of the maxima of the Ricci scalar at the origin upon rescaling of the time and the initial amplitude. The six simulations correspond to the six dots in figure 5.13 with $\sigma = 0.1$ and $\beta = 45°$ (brown) and $82°$ (orange).

The existence of a instability corner centered on the AdS$_4$ vacuum is also manifest in the $1/\epsilon^2$ scaling of the maxima of the Ricci scalar at the origin when $\epsilon \to 0$, as depicted in figure 5.15, which should be compared with figure 2 in reference [130]. The orange curves correspond to the orange dots in figure 5.13 and the same is true for the brown curves and dots.

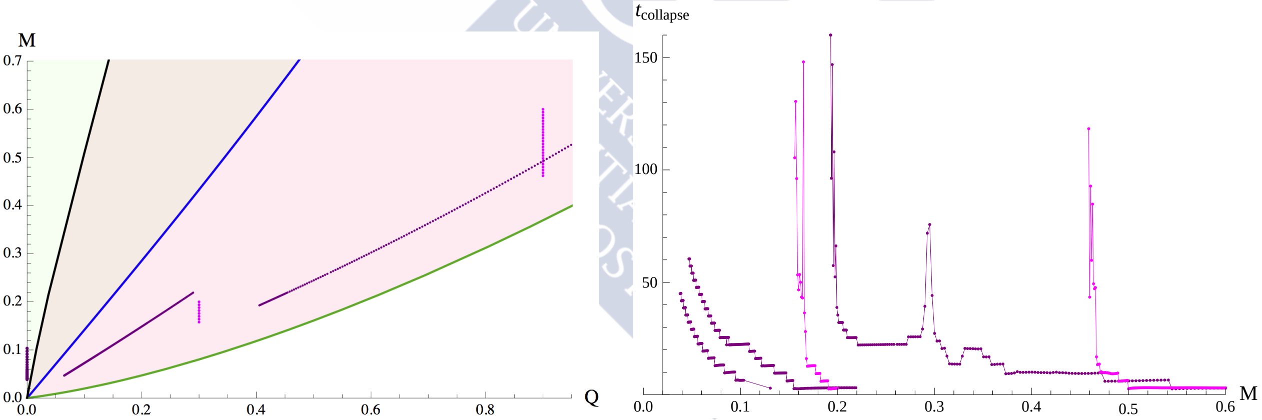

Figure 5.16: Collapses with $\sigma = 0.2$ and $e = 20$. The dotted purple lines represent three series with $\beta = 0°, 45°$ and $63°$. Vertical magenta lines represent collapse series at constant $Q = 0.3$ and 0.9. On the right plot the associated time curves are in direct correspondence from left to right.

After the works in [139, 146, 148], it has become clear that both focusing and defocusing dynamics (i.e. direct and inverse cascade) seem to be in action and in a delicate equilibrium. For very sharp initial data, small σ, focusing wins. In figure 5.16, collapse times for initial width $\sigma = 0.2$ are plotted. For vanishing charge $\beta = 0, \pi/2 \Rightarrow Q = 0$, they show the expected $1/\epsilon^2$ scaling as ϵ decreases, as for sharper pulses. However, as soon as some charge is added, we start seeing a seemeling divergent $t_{collapse}$ at finite values of ϵ. This is exactly the same effect encountered in [135], but here it appears for smaller values of σ than in that case. Note that for constant Q initial data, represented by the vertical magenta lines in figure 5.16a, the collapse time diverges at a critical M above the soliton line, and the instability corner present for $Q = 0$ disappears. In the next section, we will show that linearized fluctuations around a soliton solution have a nonresonant eigenfrequency spectrum. This fact, when combined with the divergent collapse time, provides a nontrivial check of the hypothesis put forward in [136].

5.6 Soliton stability

If the existence of a resonant eigenfrequency spectrum for the linearized fluctuations around a given solution is a necessary condition for the presence of an instability corner, the results presented in figure 5.16 strongly suggest that this condition is not satisfied for the soliton solutions. In this section, we address this issue by an explicit numerical computation. A parallel analysis has been put forward in [134], where it was shown at the perturbative level that the eigenfrequency spectrum of linearized fluctuations around boson stars is just asymptotically resonant, a fact that the authors found to be in direct correlation with the erasure of the instability corner they observed numerically.

5.6.1 Linear stability properties

Besides finding out the if the soliton eigenfrequency spectrum is resonant or not, another of the the aims of this subsection is to demonstrate that, whenever the soliton mass $M(\phi_0)$ attains an extremum, the solutions become linearly unstable, signaling the appearance of a Chandrasekhar instability we discussed in section 5.3.

We are considering linearized radial perturbations of the solitonic solutions with an harmonic time dependence of the form $\cos\omega t$. Before delving into the details it is useful to notice that, as we are considering a nondissipative problem, ω^2 is going to be purely real. In this way, an exponentially growing mode that signals an instability appears whenever $\omega^2 < 0$. We start by fixing our perturbations to be of the form[10]

$$\delta(t,x) = \delta_s(x) + \epsilon\delta_1(t,x), \tag{5.6.51}$$
$$f(t,x) = f_s(x)(1 + \epsilon f_1(t,x)), \tag{5.6.52}$$
$$A(t,x) = A_s(x) + \epsilon A_1(t,x), \tag{5.6.53}$$
$$\phi(t,x) = \phi_s(x) + \epsilon(\phi_1(t,x) + i\phi_s(x)\partial_t\phi_2(t,x)), \tag{5.6.54}$$

with real ϕ_1, ϕ_2. Since, due to spherical symmetry, the metric carries no degrees of freedom in our setup, the perturbations defined by (5.6.51)-(5.6.54) are not independent. In fact, the reason for having chosen this particular form for the scalar field perturbation is that it

---

[10] The strategy adopted here is an adaptation of the method employed in [135][210] to study boson star stability.

allows to solve for δ_1 and f_1 in terms of ϕ_1, ϕ_2 and A_1, by making use of the momentum and Maxwell constraints (5.2.20),(5.2.22) linearized in ϵ. Specifically, we get that

$$\delta_1(t,x) = -\frac{\partial_x A_1(t,x)}{A_s'(x)} - \frac{2ef_s(x)e^{-2\delta_s(x)}\phi_s(x)\partial_x\phi_2(t,x)}{\cos(x)^2 A_s'(x)} + C_\delta(x), \tag{5.6.55}$$

$$f_1(t,x) = -\sin(2x)\left(\phi_s'(x)\phi_1(t,x) - eA_s(x)\phi_s(x)^2\partial_x\phi_2(t,x)\right) + C_f(x), \tag{5.6.56}$$

where C_δ, C_f are integrating functions that must be fixed by the correct choice of boundary conditions. For harmonic perturbations, set

$$(\delta_1(t,x), f_1(t,x), A_1(t,x), \phi_1(t,x), \phi_2(t,x)) = (\hat{\delta}_1(x), \hat{f}_1(x), \hat{A}_1(x), \hat{\phi}_1(x), \hat{\phi}_2(x))\cos\omega t \tag{5.6.57}$$

which forces C_δ, C_f to be zero. Then, we can obtain the equations of motion for $\hat{\phi}_2$ and $\hat{A}_1$ by linearizing in ϵ the equations for δ and A, (5.2.19) and (5.2.21) (the linearized equation for f is not independent). The remaining equation for $\hat{\phi}_1$ comes from equation (5.2.17) for ϕ, linearized in ϵ, after making use of both the $\hat{\phi}_2$ and $\hat{A}_1$ equations. The final expression of the equations of motion for the perturbations is not particularly illuminating. Defining

$$\vec{Z} = \left(\hat{\phi}_1, \hat{\phi}_2, \hat{A}_1\right)^T, \tag{5.6.58}$$

the perturbation equations are of the form

$$\vec{Z}''(x) + M^1(x)\vec{Z}'(x) + \left(M_a^0(x) + \omega^2 M_b^0(x)\right)\vec{Z}(x) = 0, \tag{5.6.59}$$

where $M^1, M^0_{a,b}$ are matrix-valued functions that depend exclusively on the background solution. In order to solve (5.6.59), we have to choose appropriate boundary conditions for $\vec{Z}$. At $x = 0$ we demand regularity. As for the background soliton, this forces $\vec{Z}$ to be even at $x = 0$. At $x = \pi/2$, boundary conditions are

$$\hat{\phi}_1(x) = O(\rho^3), \tag{5.6.60}$$

$$\hat{\phi}_2 = \hat{\phi}_{2,0} + O(\rho^2), \tag{5.6.61}$$

$$\hat{A}_1 = O(\rho^2). \tag{5.6.62}$$

The first two conditions come from imposing normalizability on the scalar field perturbation (5.6.54). The last condition demands a more thoughtful explanation. Let us consider the most general near boundary expansion for $\hat{A}_1$,

$$\hat{A}_1(x) = \hat{A}_{1,0} + \hat{A}_{1,1}\rho + O(\rho^2). \tag{5.6.63}$$

In this case, it can be shown that we have $\hat{\delta}_1(\pi/2) \propto \hat{A}_{1,1}$ and, in consequence, if we want to maintain our gauge choice for the time coordinate, we must set $\hat{A}_{1,1} = 0$. This is tantamount to demanding that the frequency ω is the one measured by a boundary observer.[11] On the other hand, nothing prevents us from allowing that $\hat{A}_{1,0} \neq 0$ i.e., perturbations that don't

---

[11] Under a shift $\delta(x) \to \delta(x) + c$, ω changes as $\omega \to \omega e^{-c}$ so as to maintain the ωt phase of the perturbation invariant.

keep fixed the soliton chemical potential. However, examining the explicit form of equation (5.6.59) we discover that any solution is invariant under the change $\hat{\phi}_1 \to \hat{\phi}_1$, $\hat{\phi}_2 \to \hat{\phi}_2 + \alpha$ and $\hat{A}_1 \to \hat{A}_1 + \beta$, provided that $\alpha\omega^2 + e\beta = 0$. Therefore, we can employ this residual symmetry[12] to set $\hat{A}_{1,0} = 0$ with no loss of generality, fixing it completely along the way.[13]

Before discussing how equation (5.6.59) was solved numerically, let us make a last general comment. The boundary conditions (5.6.60)-(5.6.62) and the relations (5.6.55)-(5.6.56) imply that the perturbations here considered don't change the charge and the mass of the soliton at linear order. This observation allows for a better understanding of the relation between the soliton linear stability properties and the fact that the mass curve, $M(\phi_0)$, encounters an extremum at $\phi_0 = \phi_{0,c}$.[14] First, let us mention that, whenever $M'(\phi_{0,c}) = 0$, we also find that $Q'(\phi_{0,c}) = 0$. Therefore, around $\phi_{0,c}$, two infinitesimally close solitons, parameterized respectively by $\phi_{0,c}$ and $\phi_{0,c} + \Delta\phi$, have the same mass and charge, up to $O(\Delta\phi^2)$ corrections. This implies that there must be a time-independent linear radial perturbation that connects these static configurations and, in consequence, equation (5.6.59) admits a solution with $\omega_1^2(\phi_{0,c}) = 0$, i.e. a zero mode in the soliton spectrum. For $\omega_1^2(\phi_0)$ at least a C^2 function around $\phi_{0,c}$, we find

$$\omega_1^2(\phi_0) = \omega_1^2(\phi_{0,c}) + \partial_{\phi_0}\omega_1^2(\phi_{0,c})(\phi_0 - \phi_{0,c}) + ... = \partial_{\phi_0}\omega_1^2(\phi_{0,c})(\phi_0 - \phi_{0,c}) + ... \qquad (5.6.64)$$

which becomes negative on one side of the mass curve extremum, signalling an instability. On the remaining part of this section we are going to proceed by solving (5.6.59) numerically, confirming this expectation. For this task we employed Tchebychev pseudospectral collocation method. Inserting expansions

$$\hat{\phi}_1(x) = \cos(x)^3 \sum_{k=0}^{N-1} c_{1,k} T_k(1 - 4/\pi x), \qquad (5.6.65)$$

$$\hat{\phi}_2(x) = \sum_{k=0}^{N-1} c_{2,k} T_k(1 - 4/\pi x), \qquad (5.6.66)$$

$$\hat{A}(x) = \cos(x)^2 \sum_{k=0}^{N-1} c_{3,k} T_k(1 - 4/\pi x), \qquad (5.6.67)$$

into equation (5.6.59) and evaluating on a collocation grid $\{x_k, k = 1...N\}$

$$x_k = \frac{\pi}{4}\left(1 - \cos\left(\left(k - \frac{1}{2}\right)\frac{\pi}{N}\right)\right), \qquad (5.6.68)$$

---

[12] This residual symmetry stems from the fact that equation (5.6.59) is a linear ODE that admits an algebraic solution of the form $\vec{Z} = (0, \alpha, \beta)^T$ with the aforementioned coefficient choice. This algebraic solution, on the other hand, is nothing but the action of a linearized gauge transformation on the trivial $\vec{Z} = 0$ solution.

[13] We have checked explicitly that the numerical results presented further on are independent of the particular way this symmetry is fixed. They are also equivalent to the ones obtained when this symmetry is left unbroken.

[14] See also the related discussion in [211].

an algebraic generalized eigenvalue problem is to be solved which gives the numerical values of the first soliton normal modes.[15]

As for the results, first, the spectrum thus found is not resonant. In the spirit of [136], this should entail the absence of a turbulent cascade in the fully nonlinear regime. In figure 5.17, we plot the first eight normal frequencies for the soliton branch at coupling $e = 5$. As $\phi_0 \to 0$, they consistently reduce to their vacuum values in the presence of the chemical potential $\mu = 3/e$, which is nothing but the first contribution to the soliton chemical potential in a ϕ_0-expansion. A remarkable feature is the mode splitting that occurs for $k \geq 3$.[16] This is common to every vacuum connected soliton branch we have analyzed. If the spectrum were exactly resonant, we would have that, for $k \geq 2$,

$$|\omega_{k+1}| = |\omega_1| + k(|\omega_2| - |\omega_1|). \tag{5.6.69}$$

We plot the right hand side of (5.6.69) for each k in figure 5.17 (blue-dashed). It is clearly seen that the equality is not satisfied away from $\phi_0 = 0$. A similar exercise can be performed only between the lower or upper splitted eigenfrequencies, choosing as reference the difference between any two consecutive ones, with identical conclusion.

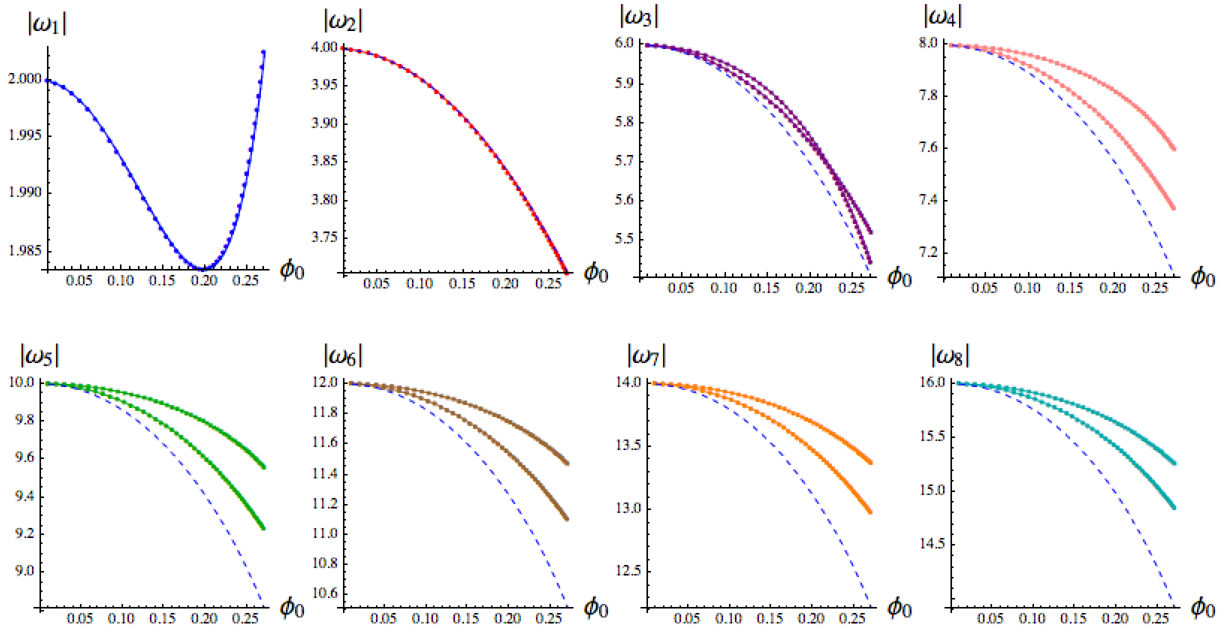

Figure 5.17: Soliton scalar eigenfrequencies for $e = 5$.

Let us consider the intermediate region $3/2 \leq e^2 \leq 9/2$. In figure 5.18a, we plot $\omega_1^2(\phi_0), \omega_2^2(\phi_0)$

---

[15] We discard the values that don't converge when N is increased. See appendix 5.A.3 for a convergence test.

[16] We remind the reader that a mode splitting was previously found in the perturbative computation of [134].

for the vacuum connected soliton branch at $e = 2$, together with the rescaled $Q(\phi_0)$ curve. We clearly see that a zero mode develops precisely at the point where $Q(\phi_0)$ reaches its first maximum and that, past this point, the solutions become linearly unstable.[17] The same phenomenon can be clearly appreciated on the vacuum disconnected soliton branch after $Q(\phi_0)$ attains its first minimum (figure 5.18b). The general pattern we find is that, when $Q(\phi_0)$ hits a new extremum, a new normal mode crosses zero.[18]

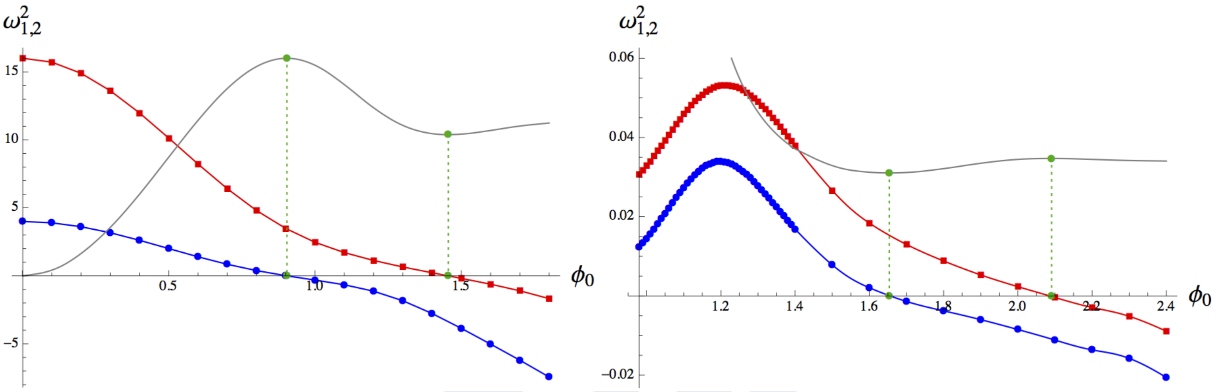

Figure 5.18: Left: ω_1^2 (blue) and ω_2^2 (red) versus ϕ_0 for the vacuum connected soliton branch at $e = 2$. In grey we show the rescaled charge curve $Q(\phi_0)$. Right: ω_1^2 (blue) and ω_2^2 (red) versus ϕ_0 for the vacuum disconnected soliton branch at $e = 2$. In grey we show the rescaled charge curve $Q(\phi_0)$. Green vertical lines correspond to the position of the charge curve extrema.

As an additional comment, note that, regarding the vacuum disconnected branch, and in the $Q \gg 1$ regime, $\omega_1^2(Q)$ is a decreasing function of Q that stays finite in the $Q \to \infty$ limit (figure 5.19a). Instead, in order for the phase of the harmonic perturbation ωt to remain finite in the blow up limit (5.3.41), the frequency should scale as $\omega \sim \mu \sim Q^{\frac{1}{2}}$. We conclude that harmonic linear perturbations die off when the blow up limit is taken. This is consistent with the fact that the soliton branch maps onto a $T = 0$ hairy black brane, for which linearized perturbations correspond to quasinormal rather than normal modes. The discussion goes through in parallel to the regime $e > e_{sr}$ (see figure 5.19b for $\omega_1^2(Q)$ at $e = 5$).

After having discussed the linear stability properties of the solitons, in the next section we move on to the study of their nonlinear stability.

---

[17] With a resolution of $\delta\phi_0 = 10^{-3}$, we have determined that the maximum lies at $\phi_{0,c} = 0.904$. Our pseudospectral code produces the values $\omega_1^2(\phi_0 = 0.903) = 0.0031$ and $\omega_1^2(\phi_0 = 0.905) = -0.0037$, in perfect agreement with expectations.

[18] This is a nontrivial result obtained from the computation, since apparently nothing prevents the other option, where some normal mode oscillates up and down, crossing zero at every extremum of the charge curve.

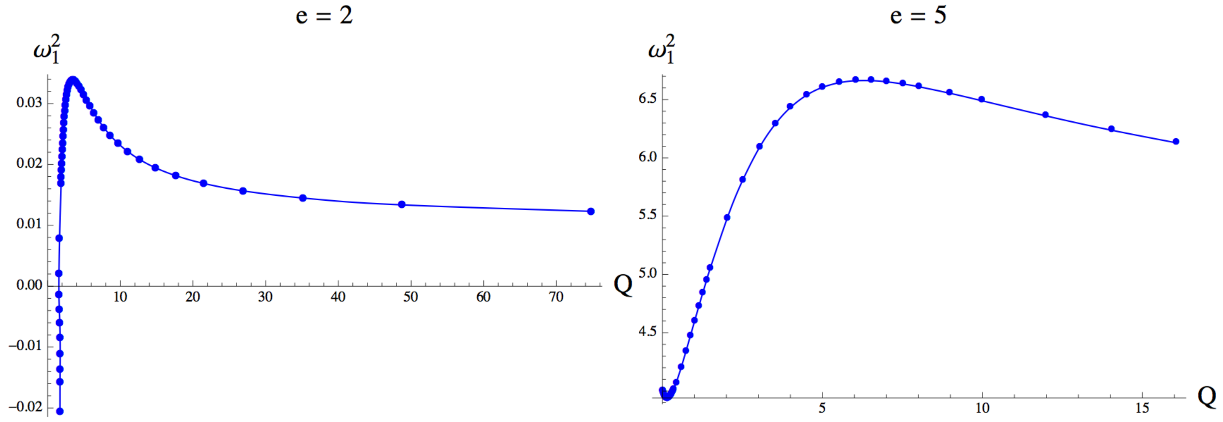

Figure 5.19: Left: ω_1^2 (blue) versus Q for the vacuum connected soliton branch at $e = 2$. Right: ω_1^2 (blue) versus Q for the vacuum disconnected soliton branch at $e = 5$.

5.6.2 Nonlinear stability properties

We consider now the effect that a localized scalar field perturbation has on the soliton. We will stick to the same family of initial conditions that were used to perturb the AdS_4 vacuum (5.5.49)(5.5.50) but in a purely real setup. Concretely, our initial condition will be $\phi_s + \phi$ with $\phi(0, x) = 0$ and

$$\Pi(0, x) = \epsilon \frac{2}{\pi} \exp\left(-\frac{4\cot^2(x)}{\pi\sigma^2}\right) \cos^3(x). \tag{5.6.70}$$

As this configuration has zero charge (see (5.2.33)), the family of perturbed solitons that we use to start with spans a vertical line in the (Q, M) plane above the unperturbed soliton solution ϕ_s, like the magenta vertical sets in figure 5.16a. The difference now is that this set of initial conditions explores down to the bottom green line as $\epsilon \to 0$.

Despite the fact that placing a perturbation like (5.6.70) on top of the AdS vacuum or on top of a soliton leads to very different initial conditions, the phenomenology we discover is remarkably similar. Namely, the magenta lines found in figure 5.16b are qualitatively reproduced here. Indeed, for high enough ϵ prompt collapse is observed. Below some threshold mass M_c we have a delayed collapse and a number of oscillations are completed before the system finally undergoes gravitational collapse. This number, and with it the final time for collapse, diverges rapidly at some value of the mass above the soliton curve. Hence we don't see any trace of a nonlinear instability corner centered at the soliton solution (instead of the AdS vacuum). This is presumably again a symptom of the nonresonant character of the spectrum of soliton perturbations.

The possible survival of this oscillating region in the blow up limit is a relevant question. More precisely, we are interested in establishing whether its width $M_c - M_s$ has a finite size relative to M_s

$$M_c - M_s \sim M_s \sim Q_s^{2/3}. \tag{5.6.71}$$

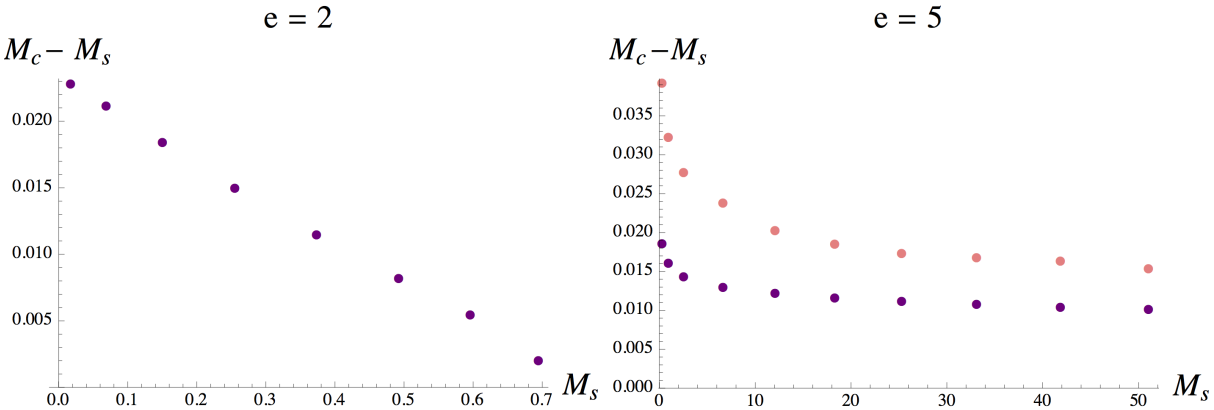

Figure 5.20: Left: limit of the prompt collapse region for the vacuum connected $e = 2$ soliton branch for $\sigma = 0.05$ (purple). Right: limit of the prompt collapse region for the $e = 5$ soliton branch for $\sigma = 0.1$ (magenta) and $\sigma = 0.05$ (purple).

In figure 5.20b we plot the location of the mass threshold $M_c - M_s$ for prompt collapse for the $e = 5$ family of solitons of mass M_s. We consider perturbations of the form (5.6.70) with $\sigma = 0.1$ and $\sigma = 0.05$. We see that, despite having finite width for large mass, the region of oscillations does not have the appropriate scaling to survive in the blow up limit. In this case, for $M_s \gg 1$, entering the oscillating regime requires to fine-tune the initial perturbation (5.6.70) in such a way that its relative contribution to the system energy goes to zero. The behaviour just described is fairly natural given that, in the blow up limit, the soliton branch we are perturbing reduces to an extremal hairy black brane with an AdS$_4$ near-horizon geometry. It is not unreasonable that, above this background, any perturbation localized in the near-boundary region, regardless of its amplitude, leads to direct collapse to a $T \neq 0$ black brane, in the same vein as it happens for zero charge [98].

It remains to be seen if this is also the pattern in other matter models. Our educated guess is that, for any theory that displays an unbounded soliton branch, the blown up extension of the oscillatory regime is finite whenever the theory can support a gapped spectrum of scalar fluctuations in the planar limit. Theories of this kind are not unknown. Consider, for instance, the model recently analysed in[212][213], or related Improved Holographic QCD models [214, 215]. There, the planar geometry dual to the field theory groundstate is sourced by a nontrivial, infrared-divergent scalar field profile, and contains a naked singularity at $r = 0$.[19] When considered in the fully nonlinear regime, weak perturbations localized near the boundary may be noncollapsing and forever oscillating, since the singularity would repel them from the infrared, so as they never reach their Schwarzschild radius. This behavior has been explicitly seen in more crude models of gapped field theories in planar AdS, such as a scalar field in a hard wall geometry [161] or the AdS-soliton [162]. It would be interesting to classify, in generic terms, which Einstein-Maxwell-scalar theories support a soliton branch with a gapped planar limit and check if this is correlated with a nonvanishing width for the

---

[19] This, and what follows in the main text, is true at least for some specific classes of scalar potentials.

oscillatory regime upon blow up. As a final remark, note that obtaining these nakedly singular backgrounds as the blow up limit of a *regular* soliton family could provide an alternative and useful way of dealing with their infrared behavior at the practical level.[20]

We have also determined the boundary of the prompt collapse region for the vacuum connected soliton branch at coupling $e = 2$, upon scalar fluctuations of the form (5.6.70) with $\sigma = 0.05$ (figure 5.20, left). In accordance with the fact that soliton solutions become linearly unstable when the mass curve reaches its maximum, here we find that the width of the oscillation region shrinks to zero in a linear fashion.

5.7 Post-collapse dynamics

So far, and apart from the numerical simulation presented in figure 5.12, we have focused on the time evolution of our Einstein-Maxwell-scalar theory before a horizon first forms. In this section, we want to comment on the post-collapse dynamics exhibited by our system. This section is divided in two parts. In the first one, we illustrate how our Schwarzshchild coordinate system sufficies to describe the part of the dynamical geometry located outside the apparent horizon that is generated, taking the four-dimensional charged Vaidya model as a test example. In the second, we comment on the post-collapse relaxation of $\mu(t)$ and $\langle\mathcal{O}(t)\rangle$ in a collapse protocol at fixed Q. We shall focus on initial data exhibiting prompt collapse, discussing briefly our numerical findings for initial data collapsing to small radius hairy black holes at the end.

5.7.1 Post-collapse dynamics in the charged Vaidya model

In the uncharged case, the Vaidya model has been extremely useful as a simple toy model of a holographic quench. As mentioned in chapter 1, the planar Vaidya geometry describes the realistic process of massless scalar field collapse at leading order in a perturbative expansion [110]. With our unit conventions, the four-dimensional charged Vaidya geometry is described by the line element

$$ds^2 = \sec^2 x \left(-F(v,x)dv^2 + 2dvdx + \sin^2 x d\Omega_2^2\right), \tag{5.7.72}$$

$$F(v,x) = 1 - M(v)\cos^3 x \csc x + \frac{1}{2}Q(v)^2\cos^4 x \csc^2 x, \tag{5.7.73}$$

where the mass $M(v)$ and charge $Q(v)$ injection functions are in principle arbitrary.[21]

Going from the Eddington-Finkelstein coordinate system (v, x, θ, φ) to the Schwarzschild coordinate system (t, x, θ, φ) we are employing involves finding the location of the spacelike

---

[20] For instance, in order to deal numerically with the infared divergences of the vacuum geometry, a black hole was introduced as a regulator in [212][213], and this put the system into a regime where the confinement scale had little impact on the thermalization process of the dual theory.

[21] See [216] for a very interesting discussion of the relation between the null energy condition and the strong subadditivity of HEE in this model.

hypersurfaces of constant $t = t_0$ in the (v, x) plane. Let $t = t(v, x)$. After this coordinate change, the line element 5.2.9 takes the form (5.7.72) if the following conditions hold

$$\partial_v t = -\exp(\delta), \tag{5.7.74}$$

$$\partial_x t = \exp(\delta) f^{-1}, \tag{5.7.75}$$

$$F = f. \tag{5.7.76}$$

Note that, in particular, the condition $\partial_v t + F^{-1}\partial_x t = 0$ is satisfied. Let the constant time $t(v, x) = t_0$ hypersurface be parametrized by $v_{t_0}(\lambda), x_{t_0}(\lambda)$. From $dt(v_{t_0}(\lambda), x_{t_0}(\lambda))/d\lambda = 0$, we get that $v_{t_0}(\lambda)$ and $x_{t_0}(\lambda)$ are related as $v'_{t_0}(\lambda) = F^{-1}x'_{t_0}(\lambda)$. If we assume that $x_{t_0}(\lambda)$ increases monotonically with λ, we can trade one parameter for the other. Thus, we get the following equation for the location of the constant t slices on the (v, x) plane

$$v'_{t_0}(x) = \left(1 - M(v_{t_0}(x))\cos^3 x \csc x + \frac{1}{2}Q(v_{t_0}(x))^2 \cos^4 x \csc^2 x\right)^{-1}. \tag{5.7.77}$$

This equation is solved numerically by a shooting procedure starting from the asymptotic boundary. A representative example is plotted in figure 5.21.

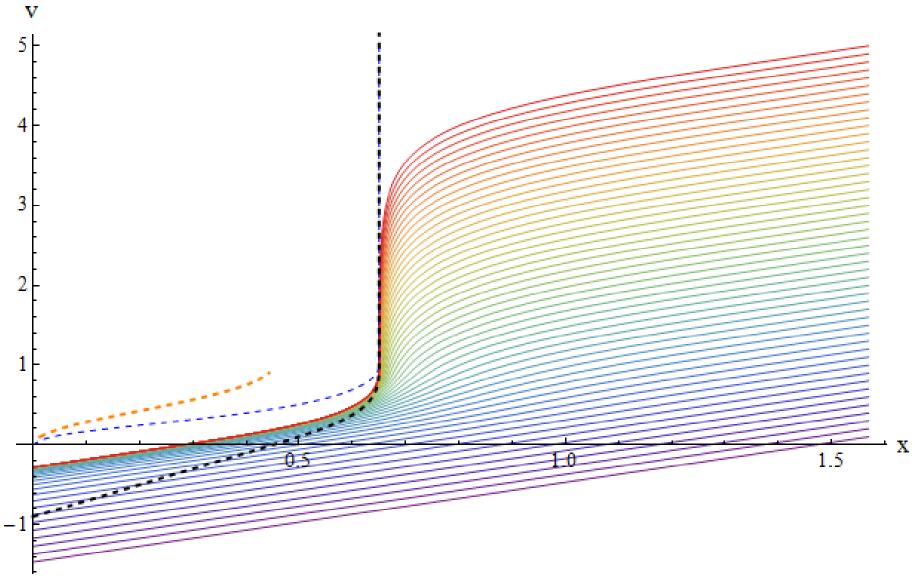

Figure 5.21: Constant t slices of the charged Vaidya geometry described in the main text (rainbow colors, with t increasing with the color wavelength from bottom up). The dashed orange, blue and black lines mark the location of the critical surface for the violation of the null energy condition, the apparent and the event horizon.

In this example, we have considered the mass and charge functions given by

$$M(v) = \Theta(v)\left[\Theta(\alpha - v)M\sin^2\left(\frac{\pi}{2\alpha}v\right) + \Theta(v - \alpha)M\right], \tag{5.7.78}$$

$$Q(v) = \Theta(v)\left[\Theta(\alpha - v)Q\sin^2\left(\frac{\pi}{2\alpha}v\right) + \Theta(v - \alpha)Q\right], \tag{5.7.79}$$

that represent a process of energy and charge injection on the dual field theory during the time $t \in [0, \alpha]$. Figure 5.21 has $\alpha = 1$. We also have fixed $M = 1.85664, Q = 1$ as the mass and charge of the Reissner-Nordström black hole formed by this collapse process. In figure 5.21, rainbow-colored curves correspond to constant t slices, with t increasing with the color wavelength. The black dashed curve marks the location of the event horizon, while the blue dashed one represents the position of the apparent horizon. Finally, the orange dashed line corresponds to the critical x_c below which, at constant v, the null energy condition is violated.

We can draw several relevant observations from figure 5.21. First, the apparent horizon is always located inside the event horizon, and only coincides with it in the $t \to \infty$ limit. Second, the region where the null energy condition is violated is always contained inside the apparent horizon. Finally, and most importantly, constant t hypersurfaces never cross the apparent horizon but, however, always cross the event horizon after a critical value of t.[22] This implies that the $t = 0$ hypersurface is actually a Cauchy surface for the exterior of the event horizon and, as a consequence, specifying initial data at $t = 0$ determines completely this part of the time-dependent geometry.[23] Note also that in Schwarzschild coordinates one would only detect strict apparent horizon formation, signalled by a vanishing f, in the $t \to \infty$ limit.

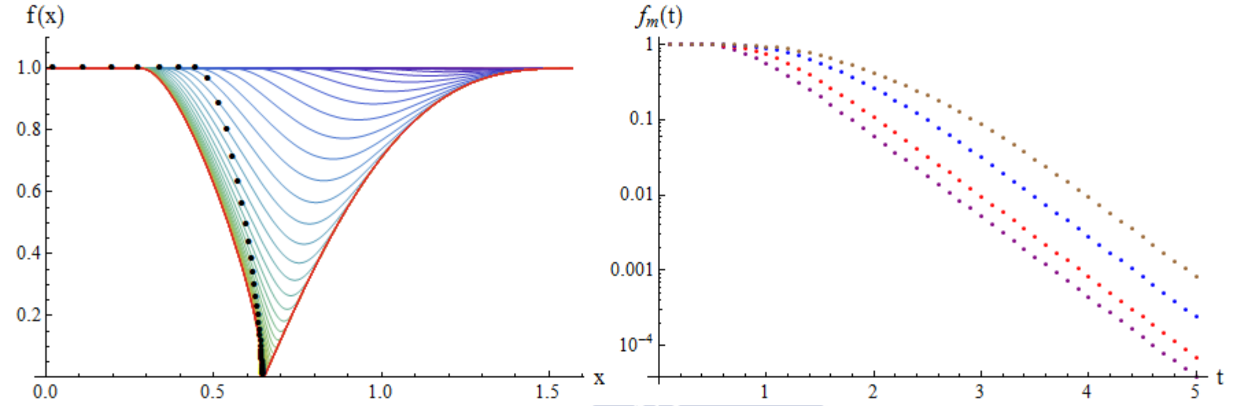

Figure 5.22: Left: the function $f(t, x)$ for the constant t hypersurfaces shown in figure 5.21. The black dots mark the f value at the location of the event horizon. Right: $f_m(t)$ for the injection process (5.7.78)-(5.7.79) with $M = 1.85664$ and $Q = 1$. The purple, red, blue and brown dots correspond respectively to $\alpha = 0.25, 0.5, 1$ and 2.

In order to illustrate this last point explicitly, in figure 5.22b we plot $f_m(t)$, as defined by the projection of $F(v, x)$ on the constant t hypersurfaces, $f_m(t) = \min_x F(v_t(x), x)$, for different injection processes of duration $\alpha = 0.25, 0.5, 1, 2$ with the same final mass, $M = 1.85664$, and charge, $Q = 1$. After a transient early-time regime that increases with α, an exponential

---

[22] The reason for this is that, as $t \to \infty$, constant t surfaces accumulate at a value of v that is greater than the v at which the event horizon appears.

[23] Of course, we mean that this surface can be pictured as a Cauchy surface after suitable boundary conditions have been prescribed at $x = \pi/2$.

decay to zero sets in. This shows faithfully that $f_m(t)$ cannot vanish in finite time. The $f(t,x) = F(v_t(x),x)$ projections associated with the constant t hypersufaces depicted in figure 5.21 are presented in figure 5.22a. For each projection, we have signaled with a black dot the value of the x coordinate where the constant t surface intersects the event horizon.

It is interesting to note that in figure 5.22b the relaxation rate

$$\Gamma \equiv -\partial_t \log f_m(t) \tag{5.7.80}$$

of $f_m(t)$ to zero looks independent of α. This entails that Γ depends solely on the properties of the final Reissner-Nordström black hole created by the injection process, and not on the specific injection protocol driving the dual CFT out-of-equilibrium. Therefore, we must have $\Gamma = \Gamma(M,Q)$ or, alternatively, $\Gamma = \Gamma(x_h,T)$, where x_h is the event horizon radius of the final black hole and T its temperature. This fact strongly suggests that the exponential decay of $f_m(t)$ could be explained by some universal properties of the map between Eddington-Finklestein and Schwarzschild coordinates when the apparent horizon is sufficiently close to its final location. In this sense, it is a kinematical effect.

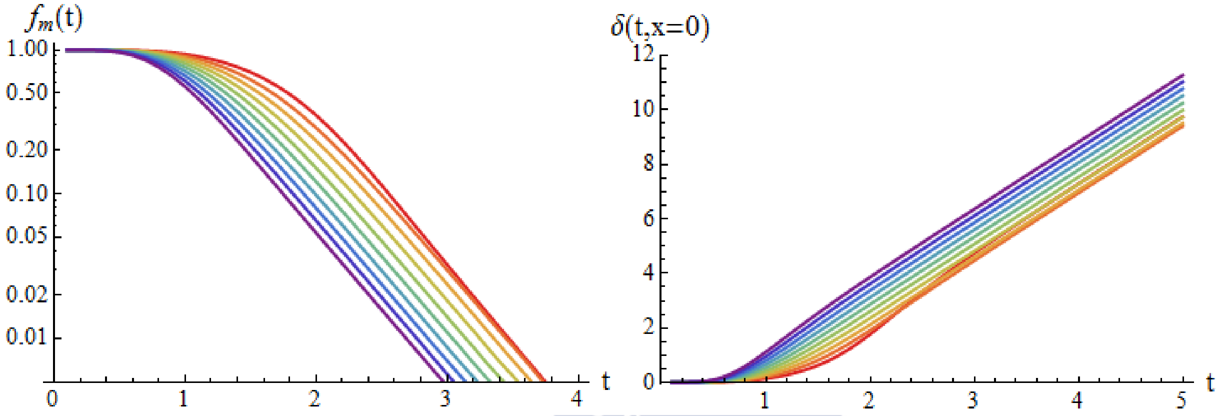

Figure 5.23: Left: $f_m(t)$ for different injection processes with $M(v), Q(v)$ as given in (5.7.78)-(5.7.79) with $\alpha = 0.5$. The temperature is $T = 0.19545$, and r_h increases in steps of $\delta r_h = 0.1$ from $r_h = 0.2$ to $r_h = 1.1$ from top down. The wavelength of the curves reflects this last fact. Left: same as right plot, but for $\delta(t, x = 0)$.

It turns out that the observation on the last paragraph can be sharpened even further. In figure 5.23a, we plot $f_m(t)$ for different injection processes with varying values of M and Q, that we constrain to give the same final T. We choose this temperature to be the same as in the example provided in figures 5.215.22. Note that, even if T does not change, x_h does. Again, our injection profiles $M(v), Q(v)$ are the ones given in (5.7.78)-(5.7.79), and we fix $\alpha = 0.5$. It is clearly seen that, irrespectively of the x_h considered, Γ remains the same. Therefore, for this family of injection processes, we have that

$$\Gamma(x_h, T) \approx \Gamma(T). \tag{5.7.81}$$

This readily implies that Γ must be determined by a perturbative expansion around the apparent horizon location at late times. Actually, the numerical evidence we have collected is compatible with the relation $\Gamma(T) = 4\pi T = f'(r_h)$. It would be interesting to investigate this analytically.

To conclude our analysis, let us point out that the origin-to-boundary redshift in Schwarzschild slices, $\exp\delta(t, x = 0)$, can be computed from

$$\delta(t,0) = -\log\left(\partial_t v_t(x=0)\right), \tag{5.7.82}$$

and also shows an exponential divergence with t; equivalently, $\delta(t,0)$ diverges linearly. This is due to the exponential approach of the constant t hypersurfaces to their accumulation point on the $x = 0$ axis, as can be clearly appreciated in figure 5.21. In figure 5.23b, we plot $\delta(t,0)$ for the the family of injectionprocecess we have employed to build figure 5.23a. At late times, the slope of $\delta(t,0)$ is found to be weakly dependent on x_h, and is mostly controlled by T.

Based on the observations of the last paragraphs, we expect that the different properties we have uncovered in this subsection are universal and, as a consequence, hold in realistic models of gravitational collapse when described in Schwarzschild coordinates.[24] In fact, for the time-dependent geometries we have simulated, we also observe the exponential decrease of $f_m(t)$ to zero, as well as the linear divergence of $\delta(t,0)$. Not only that, but we also find that the dynamics inside the radial position of the minimum of f, $x_m(t)$, progressively freezes out as $f_m(t)$ decreases. In consequence, we find likely that in our setup the initial $t = 0$ hypersurface is a Cauchy surface for the exterior of the event horizon. This entails that analyzing the gravitational collapse process in Schwarzschild coordinates suffices to study the relaxation of one-point functions in holography, as they are determined by the asymptotic fall-off of bulk fields. In principle, we don't need to make further assumptions about the behavior of our probes, as we were forced to in chapter 2.

Having made these clarifications, in the next subsection we discuss the post-collapse relaxation of $\langle\mathcal{O}(t)\rangle$ and $\mu(t)$ in our Einstein-Maxwell-scalar theory.

5.7.2 Post-collapse dynamics in Einstein-Maxwell-scalar theory

In this subsection, we consider initial data configurations Π_0, Φ_0 that share the same electric charge Q. The algorithm employed to build a given one-parameter family of profiles with the same Q is the following. First, we fix the functional form of our profiles to be:

$$\Pi_0 = -i\frac{2}{\pi}\epsilon_1 \exp\left(-\frac{4}{\pi\sigma^2}\tan(x)^2\right)\cos(x)^3 \tag{5.7.83}$$

$$\Phi_0 = \frac{2}{\pi}\epsilon_2 \exp\left(-\frac{4}{\pi\sigma^2}\tan(x)^2\right)\cos(x)^2 \tag{5.7.84}$$

---

[24] But note that have not established a direct correspondence neither numerically nor from a first-principles computation.

The parameters (ϵ_1, ϵ_2) are fixed by the condition $\epsilon_1\epsilon_2 Q_0 = Q$, where Q_0 is the electric charge associated to the profiles (5.7.83)-(5.7.84) when $\epsilon_1 = \epsilon_2 = 1$. After solving this condition for ϵ_2, we perform a scan in ϵ_1, so as to get a one-parameter family of solutions that span a vertical line, $(Q, M(\epsilon_1))$, in the (Q, M) phase diagram. Typically, the inverse function $\epsilon_1(M)$ is double-valued and, therefore, for each mass we are able to obtain two different initial profiles (Π_0, Φ_0) wih the same charge.

We are going to focus on the dynamical evolution of a family of the form (5.7.83)-(5.7.84) with $\sigma = 0.5$ and $Q = 1$ at coupling $e = 3$. These initial data show prompt collapse and, as a consequence, after a short transitionary regime, one-point functions such as $\langle\mathcal{O}(t)\rangle$, $\mu(t)$ start to relax to their final equilibrium values. The final equilibrium values[25] of $\langle\mathcal{O}\rangle$, μ are shown in figure 5.24. We observe that there is a critical mass M_c where the final state changes from a Reissner-Nordström black hole to a hairy solution. When $M \to M_c^-$, the vacuum expectation value of $\mathcal{O}$ in the final state vanishes, and we expect a standard mean field theory exponent, $\langle\mathcal{O}(M)\rangle_f \sim |M - M_c|^{\frac{1}{2}}$. Note that, since we are in the microcanonical ensemble, this phase transition is entropy-driven an does not correspond to the standard grand-canonical one we discussed in section 5.4.

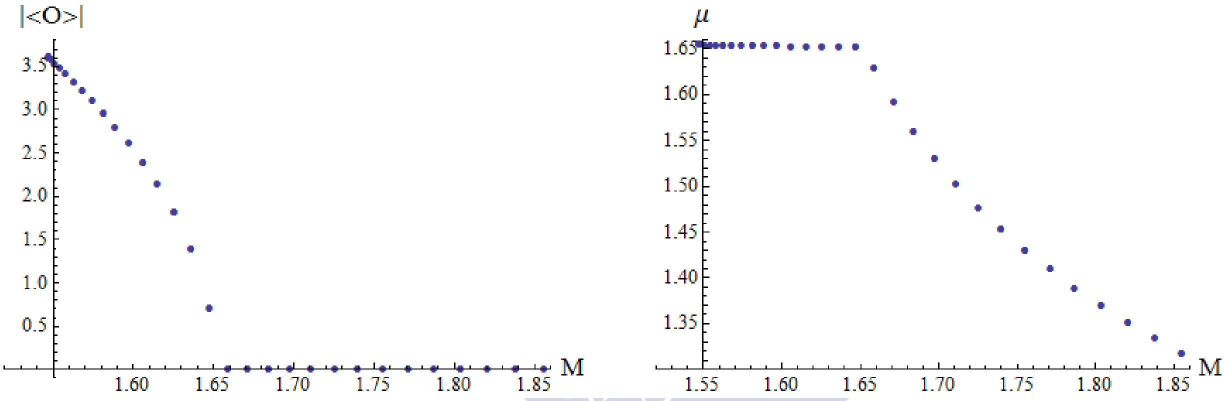

Figure 5.24: Right: equilibrium value of $\langle\mathcal{O}\rangle$. Left: equilibrium value of μ.

The full nonlinear time evolution of $\langle\mathcal{O}(t)\rangle$, $\mu(t)$ is shown in figure 5.25.We clearly distinguish three different regimes of post-collapse evolution. For $M > M_c$ (regime *a*), the final state is a Reissner-Nordström black hole and the vev relaxes exponentially to zero. As has been mentioned before, below M_c the final state is a hairy black hole with $\langle\mathcal{O}\rangle_f \neq 0$. A new mass scale M^* appears, in such a way that, for $M_c \geq M > M^*$, relaxation is overdamped (regime *b*), while it becomes underdamped for $M^* \geq M$ (regime *c*). The vev late-time evolution can thus be subsumed into an equation of the form

$$|\langle\mathcal{O}(t)\rangle| \sim \left|\langle\mathcal{O}\rangle_f + A\exp(-i\omega t)\right|, \tag{5.7.85}$$

---

[25] These are the values associated to the entropy-maximizing static black hole solution with the same conserved charges as the initial data.

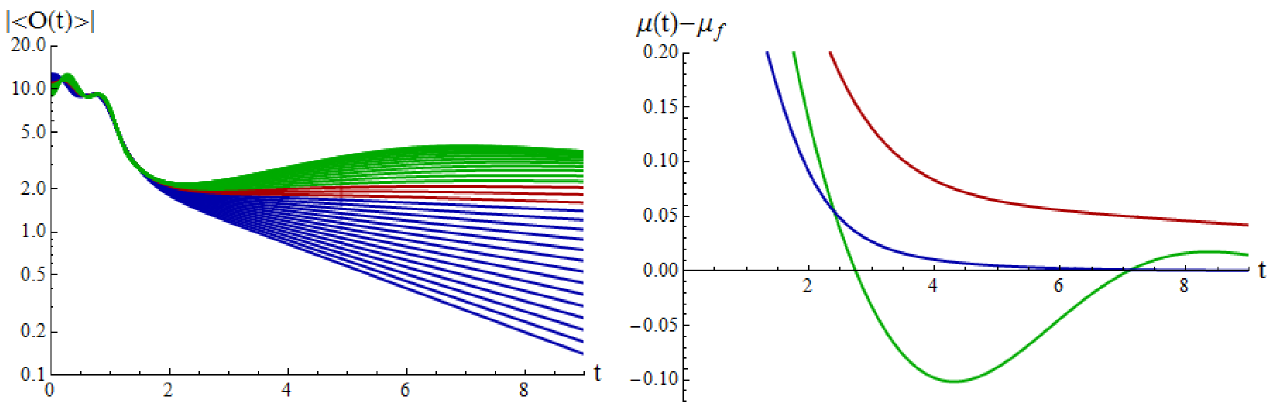

Figure 5.25: Left: Time evolution of $\langle O(t)\rangle$. Curves belonging to regimes a, b and c have been respectively marked blue, brown and green. The mass decreases from bottom up. Right: Time evolution of $\mu(t)-\mu_f$ for a representative solution in each one of the three regimes discussed in the main text. The color coding is as in the left figure.

where ω must correspond to the frequency of the lowest quasinormal mode of the final black hole. The existence of three different kinds of late-time relaxation must be related to the facts that *i)* in regime a any ω with Im $\omega \neq 0$ leads to overdamped relaxation since $\langle\mathcal{O}\rangle_f = 0$, *ii)* ω is purely imaginary in regime b and *iii)* ω has a non-zero real part in regime c. Before going on, let us refer to figure 5.26, where we plot $\delta(t,0)$ for the one-parameter family of initial data we are considering. The linear divergence found in the charged Vaidya model is also present in the realistic collapse processes we are analyzing here, and we expect the physical origin of both to be the same.

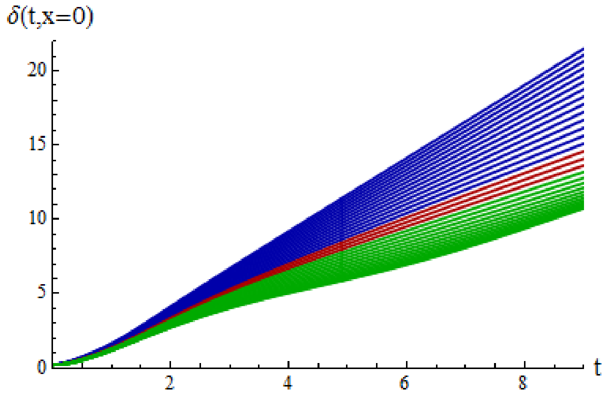

Figure 5.26: $\delta(t,x=0)$, for the one-parameter family of initial data discussed in the main text. The color coding is as in figure 5.25a.

In reference [103], a $m^2=-2$ scalar field was employed to quench a four-dimensional hairy black brane at fixed charge density. As we discussed in chapter 1, it was found that, depending on the quench amplitude, three different relaxation regimes analogous to the ones described here appeared. Despite this observed matching, our setup and the one studied in [103] couldn't be more distinct: we are considering a field theory that is placed on a manifold with different topology, and we don't even start from a thermal superfluid state, but rather from a pure out-of-equilibrium state that evolves unitarily. The reason for the coincidence stems from the fact that, as previously mentioned, the late time relaxation of one-point functions is solely controlled by the qualitative behavior of the quasinormal modes of the final state. This behavior must agree between our system and the setup studied in [103], providing strong evidence in favor of the universality conjectured there.

Since we are in the microcanonical ensemble, the observations of the last paragraph imply that different initial data with the same conserved charges should display identical patterns of late-time relaxation. In order to check if this expectation is correct, we take advantage of the fact that our procedure for building initial data automatically provides two different (Π_0, Φ_0) profiles with the same M at fixed Q. In figure 5.27, we show the evolution of $|\langle\mathcal{O}(t)\rangle|$ for the two inequivalent families of initial data obtained with this method. We clearly observe that, even if the early-time transitionary regime differs between them, post-collapse relaxation proceeds in an identical fashion.

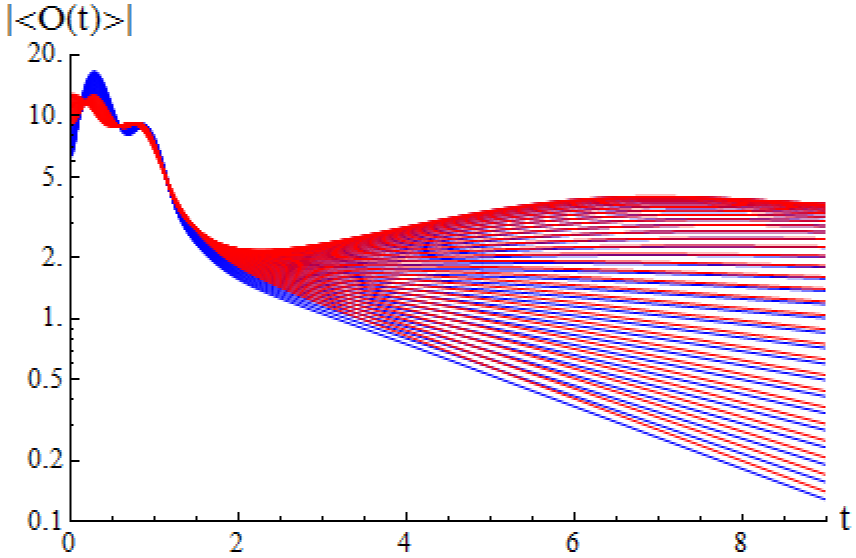

Figure 5.27: Time evolution of $\langle O(t)\rangle_1$, $\langle O(t)\rangle_2$ for the two initial data families described in the main text (new one in blue, old one in red)

We want to close this chapter by reporting on some preliminary results. We have also analyzed the post-collapse relaxation of one-point functions in bouncing geometries. These are geometries that do not collapse directly into a black hole, but rather exhibit an extended pre-collapse phase. The example we provide in figure 5.28 corresponds to a coupling $e = 20$ and initial data of the form (5.7.83)-(5.7.84) with $\sigma = 0.1$, $Q = -0.2015$ and $M = 0.1213$. The simulations we report on have been performed with discretization grids of $N = 2^{16} + 1$,

$N = 2^{17} + 1$ points.[26]

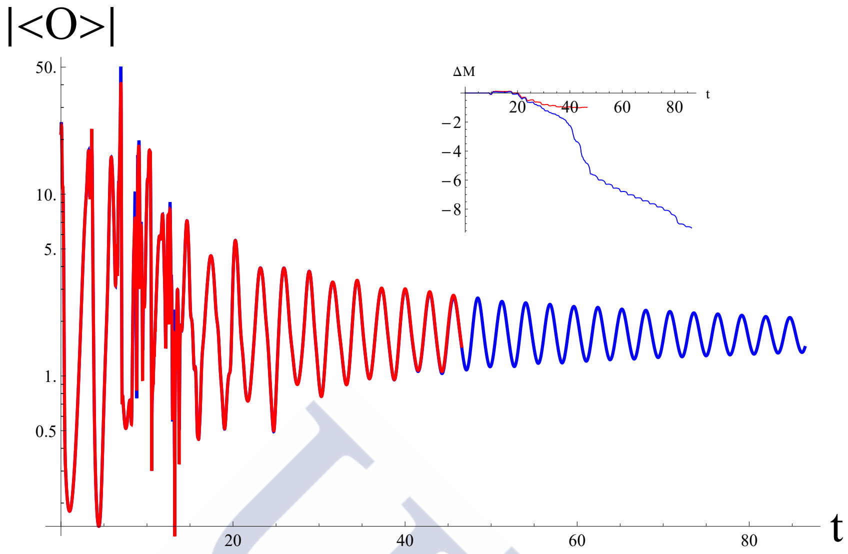

Figure 5.28: Time evolution of $\langle O(t)\rangle$ for initial data (5.7.83)-(5.7.84) with $\sigma = 0.1$, charge $Q = -0.2015$ and mass $M = 0.1213$ at $e = 20$. Blue curves corresponds to the $N = 2^{16} + 1$ simulation, while red curves correspond to the $N = 2^{17} + 1$ one. The inset shows the relative mass loss of (%) with respect to the initial mass.

$\langle \mathcal{O}(t)\rangle$ relaxes in an underdamped way to its final equilibrium value, as prompt-collapse initial data belonging to regime c do. The novelty here arises from the fact that its oscillations around this value are hardly suppressed. Said otherwise, the final hairy black hole formed by the gravitational collapse process supports long-lived excitations.

As we are discussing in chapter 7, a pressing direction for future research is elucidating the nature of these long-lived oscillations. Several comments are in order now.

By looking just at the $N = 2^{16} + 1$ simulation (blue curves in figure 5.28), we could think that these long-lived oscillations are a numerical artifact, due to the poor grid resolution. This expectation is also motivated by taking into account that they seem to be correlated with a substantial relative mass loss. In order to confirm or discard their existence, we performed the additional, higher resolution simulation with $N = 2^{17} + 1$ grid points (red curves in figure 5.28). By comparing both, we observe clearly that the relative mass loss is subtantially reduced in the latter one, as expected.[27] However, and more remarkably, the long-lived oscillation pattern agrees between them.

This fact could seem to vindicate that these oscillations are not a numerical artifact; however, this is a rather premature conclusion. It could be that both $N = 2^{16}+1$, $N = 2^{17}+1$ grids are insufficient to resolve the actual post-collapse dynamics of the system, regarding

---

[26] They have been extremely demanding at the resources level. The one with higher resolution took O(1) months, running in parallel on 24 cores.

[27] Even though it must be said that it still stays at the one percent level.

in particular the absortion of the scalar field by the emerging horizon at sufficiently late times. The long-lived oscillations could still be a finite-size effect linked to the finiteness of the discretization grid, and not to the fact that our holographic CFT is at finite volume. In this regard, the purpose of mentioning this result is pointing out that long-lived excitations *could* exist in holographic superfluids at finite volume, not claiming that they *actually* exist, although the evidence reported here seems compelling, to say the least.

In order to establish faithfully the existence of this kind of relaxation, we need further technical improvements and independent consistency checks. These are discussed in chapter 7. Let us just mention now what could be a natural physical mechanism behind these long-lived oscillations. As demonstrated in [84] for AdS-Schwarzschild black holes in global AdS$_4$, the quasinormal mode spectrum reduces continuously to the normal mode one as the black hole radius tends to zero. In our case, when the radius of the final hairy black hole vanishes, we recover a soliton solution. In parallel with [84], we can argue that the hairy lowest quasinormal mode, which controls the post-collapse dynamics, also reduces continuously to the fundamental normal mode of this soliton in the zero radius limit. In this way, when a hairy black hole of charge Q_h is sufficiently close to its corresponding $Q_s = Q_h$ soliton, we can expect that the imaginary part of this quasinormal mode is correspondingly small. This would provide a natural mechanism to account for these long-lived oscillations.

If this hypothesis turns out to be correct, by taking into account our discussion in subsection 5.6.2 we can conjecture the structure of the different late-time relaxation regimes of our system. Take initial data at fixed Q, and assume that M is sufficiently large. Our initial data would collapse prompty to a Reissner-Nordström black hole, and the vev relaxation would fall into regime a. Upon lowering the initial mass, the final state would eventually correspond to a hairy black hole: the system would enter first into regime b, and then transition to regime c. In our setup, the novelty with respect to the planar case seems to be that the imaginary part of the quasinormal frequency ω controlling the late-time underdamped relaxation of the vev must become progressively smaller as the mass is lowered. However, the existence of the stability band shows that, at some critical mass, black hole formation would be halted and the system would not thermalize. As a consequence, the vev would exhibit persistent oscillations. It would be interesting to elucidate the late-time dynamics of the vev at the critical mass separating these two last regimes.

5.A Appendix

In this appendix, we provide a technical discussion of the different numerical methods that have been employed in the main part of the chapter.

5.A.1 The static solutions

In order to build both the hairy and the soliton solutions, we resort either to a shooting or to a pseudospectral algorithm. Both methods give identical results. We take the gauge choice Im $\phi = 0$, and set to zero the time-derivatives of f, δ, A_t and ϕ. We obtain the following equations

$$
\begin{aligned}
&\phi''(x) + \left((d-1)\csc(x)\sec(x) + \frac{f'(x)}{f(x)} - \delta'(x) \right) \phi'(x) + e^2 \frac{e^{2\delta(x)} A(x)^2 \phi(x)}{f(x)^2} = 0, \\
&A''(x) + \left((d-1)\cot(x) + (d-3)\tan(x) + \delta'(x) \right) A'(x) - e^2 \frac{2\sec(x)^2 A(x) \phi(x)^2}{f(x)} = 0, \\
&f'(x) - \frac{d-2+2\sin(x)^2}{\sin(x)\cos(x)} (1-f(x)) - f(x)\delta'(x) + \frac{1}{2}\cos(x)^3 \sin(x) e^{2\delta(x)} A'(x)^2 = 0, \\
&\delta'(x) + \cos(x)\sin(x) \left(\phi'(x)^2 + e^2 \frac{e^{2\delta(x)} A(x)^2 \phi(x)^2}{f(x)^2} \right) = 0. \qquad (5.A.1)
\end{aligned}
$$

As we mentioned in section 5.2, we refer to the infrared end of the radial coordinate as x_o, with either $x_o = 0$ for solitonic solutions, or $x_o = x_h > 0$ for the horizon of a black hole. The infrared series expansions read

$$
\begin{aligned}
\phi(x) &= \phi_o + \phi_{o,1}(x - x_o) + \ldots, && (5.A.2) \\
A_t(x) &= A_o + A_{o,1}(x - x_o) + \ldots, && (5.A.3) \\
\delta(x) &= \delta_o + \delta_{o,1}(x - x_o) + \ldots, && (5.A.4) \\
f(x) &= f_o + f_{o,1}(x - x_o) + \ldots. && (5.A.5)
\end{aligned}
$$

where it should be noted that regularity of solutions at the origin demands $f_o = 1$ and forces every odd term of (5.A.2)-(5.A.5) to be zero. In the black hole case, the existence of a horizon and regularity of the gauge field one-form implies

$$
f_h = A_h = 0\,. \qquad (5.A.6)
$$

Each static solution of the equations of motion is completely characterized by its infrared series expansion which, in turn, is totally fixed in terms of a finite number of parameters. In the absence of a horizon, these parameters are the values of the scalar and gauge fields at $x_o = 0$, (ϕ_0, A_0). A soliton geometry is dual to a field theory state with spontaneously, and not explicitly, broken symmetry. This further demands that the source ϕ_b vanishes, which provides a nonlinear relation between (ϕ_0, A_0) that determines completely A_0 in terms of ϕ_0. A family of soliton solutions is therefore one-parametric. The same reasoning goes through to the black hole case. Now, each black hole solution is totally determined by the triplet $(x_h, \phi_h, A_{h,1})$ and, again, the condition $\phi_b = 0$ links ϕ_h and $A_{h,1}$ at the given x_h. In this way, a family of black hole solutions is two-parametric.

The shooting algorithm starts from a choice of x_h, ϕ_h and $A_{h,1}$ in the hairy black hole case, or ϕ_0 and A_0 in the soliton case. We introduce infrared and ultraviolet cutoffs $x_{IR} = x_o + \epsilon$, $x_{UV} = \pi/2 - \epsilon$, with $\epsilon \ll 1$. Initial conditions for f, δ, A and ϕ are specificied at x_{IR} by means of the series expansions (5.A.2)-(5.A.5). Then, equations (5.A.1) are solved by Mathematica's NDSolve routine. The value of $\phi(\pi/2)$ is computed by a interpolation from x_{UV} with the help of the asymptotic series expansions (5.2.24)-(5.2.27). It is generically different from zero. Its vanishing is enforced by performing a binary search in A_0 or $A_{h,1}$, that lasts until $\phi(\pi/2)$ drops below an user-defined cutoff.

The pseudospectral code involves a choice of the spatial eigenfunction basis and the discretization grid. We choose to work with the ones employed to find the soliton eigenfrequency spectrum, *i.e.*, we decompose our fields in a basis of Tchebyshev polynomials of the first kind as in (5.6.65), and take the collocation grid defined by equation (5.6.68). This procedure results in a system of coupled, nonlinear algebraic equations that we solve by means of a Newton-Raphson algorithm implemented in Mathematica.

It is mandatory to have a consistency check on the static solutions found numerically. Our standard approach is verifying if they satisfy the First Law,

$$dM - TdS - \mu dQ = 0. \tag{5.A.7}$$

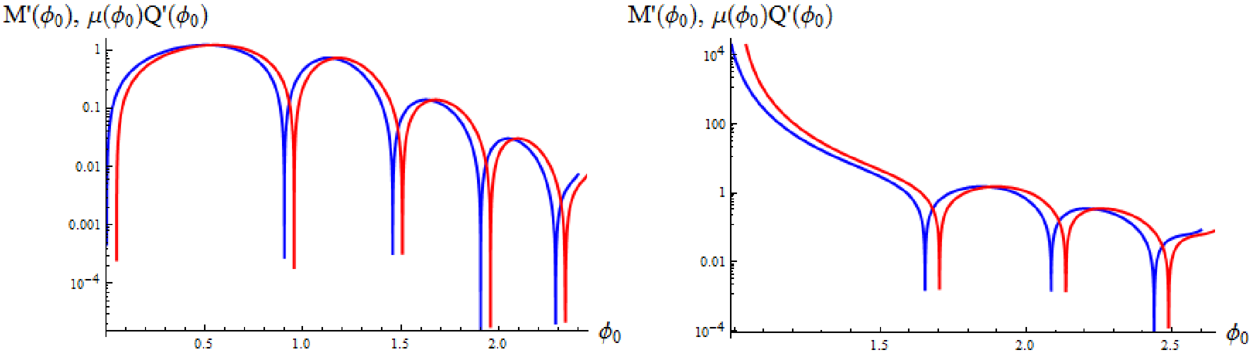

Figure 5.29: Left: $M'(\phi_0)$ (blue) and $\mu(\phi_0)Q'(\phi_0)$ (red) for the vacuum connected soliton branch at $e = 2$. The red curve has been displaced to the left for the sake of comparison. Right: same as left plot, for the vacuum disconnected soliton branch at $e = 2$.

For instance, for a one-parameter family of soliton solutions ($S = 0$), we must have that

$$\frac{dM(\phi_0)}{d\phi_0} = \mu(\phi_0)\frac{dQ(\phi_0)}{d\phi_0}. \tag{5.A.8}$$

In figure 5.29 we plot the left and right hand sides of the identity above for the soliton branches at $e = 2$. Figure 5.29a corresponds to the vacuum connected branch, and figure 5.29b to the vacuum disconnected one. The blue curve corresponds to $M'(\phi_0)$, while the red one to $\mu(\phi_0)Q'(\phi_0)$. The red curve has been artificially displaced to the left for the sake of comparison. Excellent agreement is found between both curves, implying that the soliton solutions we have constructed numerically do satisfy the First Law.

5.A.2 The time evolution code

It is a virtue of the coordinate system (5.2.9) that the Einstein and Maxwell equations appear as constraints (5.2.18), (5.2.19) and (5.2.21) that can be solved at each instant of time. The evolution of the system is then driven by the scalar field equations (5.2.16) and (5.2.17). Starting from given nonequilibrium initial data, such as (5.5.49) and (5.5.50), we have solved these equations numerically by resorting to a fourth-order accurate finite-difference evolution code.

Time evolution is performed by an explicit Runge-Kutta method. In order to deal with the high-frequency noise generated due to the finiteness of the discretization grid, we implement standard Kreiss-Oliger dissipation. By setting $\delta(\pi/2) = 0$ we obtain stable evolutions with a constant Courant factor λ with no need of local mesh refinement in time. The simulations presented in the main part of the chapter have $\lambda = 0.1$. On the other hand, spatial derivatives are discretized by employing a centered, fourth-order finite-difference stencil, while integrations are handled by a specifically designed routine, based on local polynomial interpolation. Dealing with the boundary conditions at $x = 0, \pi/2$ requires some detailed procedures that can be found in [131]. These procedures are essential for obtaing both numerical stability and convergence.

The major difficulty in the present setup stems from the fact that, upon evolution, the scalar profile develops very spiky features that demand a high resolution. To resolve these sharp features, which are apparent in figure 5.12, we used global mesh refinement in space, eventually reaching $2^{17} + 1$ grid points to discretize the interval $x \in [0, \pi/2]$. This has required a parallel implementation that employs the MPI infrastructure to run the code on a computer cluster. Optimal results have been obtained for ~ 30 nodes running in parallel. Smarter solutions involving local space mesh refinement are left for the future.

The quality control parameters employed to activate the refinement process are both the norm of the momentum contraint (5.2.20), as well as the relative mass loss at each time step. As a matter of fact, only at late times in the simulation are such mentioned fine resolutions required. The code stops at a time t_f when the minimum value of $f(t, x)$ reaches below an user-defined cutoff f_c.[28] This is the time that is meant in the right figures 5.13 and 5.16. Of course, as discussed in 5.7, the apparent horizon will only form in the infinite future $\lim_{t_f \to \infty} \min[f(t_f, x)] = 0$ in the our coordinate gauge.

To illustrate the convergence properties of our time evolution code, we consider the functional

$$\Delta_n[g](t) \equiv \|g_n(t,x) - g_{n+1}(t,x)\| = \left(\int_0^{\pi/2} \tan(x)^2 (g_n(t,x) - g_{n+1}(t,x))^2 \right)^{1/2} , \qquad (5.A.9)$$

where g_n refers to any function computed on a discretization grid of spatial resolution $h = \pi/2^{n+1}$. Fourth-order convergence then implies that

$$\Delta_{n+1}[g](t) = 2^{-4} \Delta_n[g](t). \qquad (5.A.10)$$

In figure 5.30a, we plot $\Delta_n[\Phi_1](t), \Delta_n[\Phi_2](t)$ at $n = 11, 12, 13$ for simulations with initial data

$$\Phi = \epsilon_1 \frac{2}{\pi} \sin x \exp\left(-\frac{4\tan^2(x)}{\pi^2 \sigma^2} \right) , \qquad (5.A.11)$$

$$\Pi = i\epsilon_2 \frac{2}{\pi} \exp\left(-\frac{4\tan^2(x)}{\pi^2 \sigma^2} \right) , \qquad (5.A.12)$$

---

[28] For the simulations shown in sections 5.5 and 5.6, we have set $f_c = 0.02$.

where $\epsilon_1 = \epsilon_2 = 12$, $\sigma = 0.1$ and $e = 5$. The scalar field completes seven bounces before collapse is achieved at $t_f = 23.47$. From figure 5.30b, we see that relation (5.A.10) is precisely fulfiled.[29]

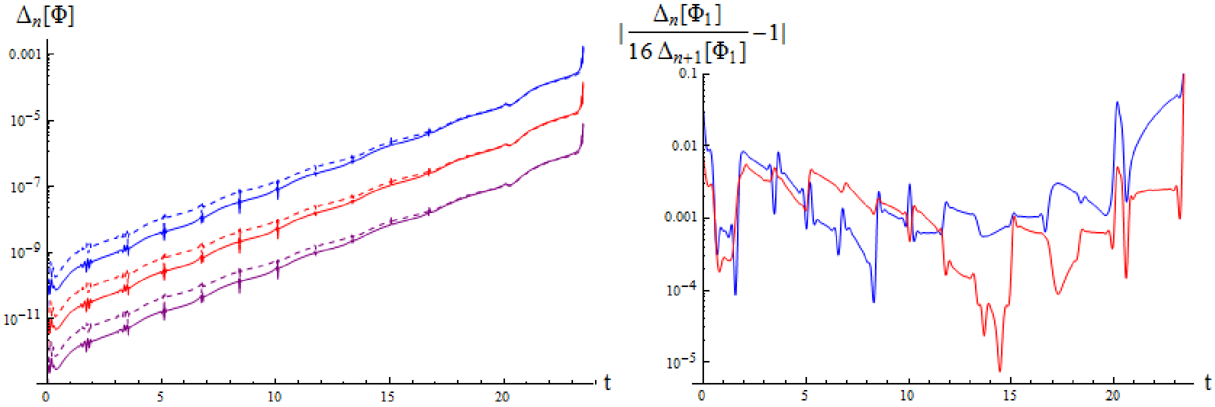

Figure 5.30: Left: $\Delta_n[\Phi]$ for $n = 11$ (blue), $n = 12$ (red) and $n = 13$ (purple). Solid lines correspond to Φ_1, while dashed ones to Φ_2. The error norm decreases with increasing grid resolution. Right: Absolute value deviation of the quotient $\frac{\Delta_n[\Phi_1]}{2^4\Delta_{n+1}[\Phi_1]}$ from 1 for $n = 11$ (blue) and $n = 12$ (red). The error norm converges to zero at the right order.

5.A.3 Soliton eigenfrequencies pseudospectral code

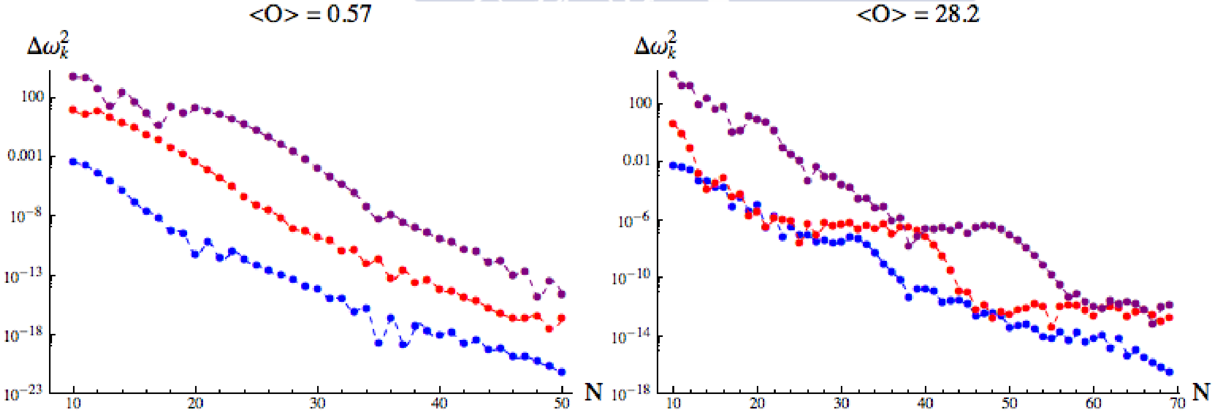

Figure 5.31: Left: At $e = 5$, and for a soliton with $\langle\mathcal{O}\rangle = 0.57$, we plot the errors $\Delta\omega_1^2$ (blue), $\Delta\omega_{10}^2$ (red), $\Delta\omega_{20}^2$ (purple) on a collocation grid ranging from $N = 10$ to $N = 50$. It is seen that the error tends exponentially to zero as the resolution N is increased. Right: The same quantities for the e = 5, $\langle\mathcal{O}\rangle = 28.2$ soliton, on a collocation grid ranging from $N = 10$ to $N = 70$.

---

[29] We have deactivated the global mesh refinement algorithm, and thus we observe deviations from exact fourth-order convergence right before collapse.

For the computation of the normal modes on top of a soliton background, we have resorted to the pseudospectral method described in the section 5.6. As mentioned, the output of this procedure are the first N soliton normal modes. For pseudospectral methods, we expect exponential convergence, since the scalar field eigenmodes are analytic functions.

In order to determine the convergence properties of the method, in figure 5.31 we show the quantity $\Delta\omega_k^2(N)$,

$$\Delta\omega_k^2(N) = \left|\omega_k^2(N+1) - \omega_k^2(N)\right| . \tag{5.A.13}$$

Here, $\omega_k(N)$ is the frequency of the k-th eigenmode, computed on a grid of N collocation points. The fact that $\Delta\omega_k^2(N) \to 0$ exponentially as $N \to \infty$ implies that the sequence $\{\omega_k^2(N), N = N_0, N_0+1, ...\}$ converges as anticipated.

Chapter 6

Holographic quenches in global AdS

6.1 Summary

Quenching an isolated quantum system reveals valuable information about its nature. In this chapter, we are studying holographic quenches with global asymptotics. We will consider the Einstein-scalar model of [130], where now we allow for a nontrival source, $\phi_0(t) \neq 0$. Although simple, extracting nontrivial results from this system generically demands resorting to numerical simulations. This technical complication can be avoided in two opposite limits. The first one corresponds to the *fast-but-smooth* quenches extensively studied in recent years (see [217] and references therein). The second one corresponds to *adiabatic* quenches. We will demonstrate that, for a sufficiently small *pumping* $\phi_0(t) = \alpha t$, the system dynamics is controlled by the *pumping solution.*[1] This is a solution endowed with a static metric, and its only time dependence comes from the nontrivial, non-normalizable mode excited by the source. Therefore, although being non-normalizable, these pumping solutions are remarkably similar to the solitons we studied in chapter 5.

This chapter is structured as follows. In section 6.2, we introduce the ultraviolet series expansion in the presence of a nontrivial source and discuss the holographic renormalization of our model. Then, in section 6.3, we present the four-dimensional pumping solution. First, we show that there exists a critical $\alpha_{\max}$ above which no pumping solution can be found. As a consequence, we identify this value with an intrinsic adiabaticity threshold for our system. Second, we demonstrate that, for a given $\alpha < \alpha_{\max}$, there exist two different pumping solutions, *i.*e., pumping solutions come in two branches, which meet at $\alpha = \alpha_{\max}$. The first branch is vacuum connected, in the sense that it reduces to empty AdS$_4$ when $\alpha \to 0$, and it always has negative mass. The second branch is vacuum disconnected, and the mass has a not well-defined sign within it.

The fact that the mass of the pumping solution can be negative raises an obvious concern regarding its stability. With this motivation, in section 6.4 we study the linear and nonlinear stability properties of the two branches. By a numerical normal mode computation, we establish that the first branch is linearly stable, while the second one is linearly unstable.

---

[1] We inform the reader that a cousing of the pumping solution had been previously identified in the hard-wall model [161].

In this sense, the $\alpha_{\max}$ theshold controls the apperance of a Chandrasekhar instability in the system. We also analyze how the linear stability properties we have uncovered uplift to the nonlinear level. First, we demonstrate that pumping solutions in the first branch are nonlinearly stable. This follow from the fast that this branch contain the pumping solutions that appear as an intermediate attractor in an adiabatic quench protocol. We confirm their nonlinear stability by studying also normalizable perturbations over them. For the second branch, we could expect that, owing to its linearly unstable nature, infinitesimal perturbations would lead directly to black hole formation. However, we identify a regime in which this phenomenon does not take place. The pumping solution, once perturbed, decays to a limiting cycle instead of collapsing gravitationally. We provide compelling evidence in favor of the hypothesis that these limiting cycle solutions are not a numerical artifact.

Motivated by the existence of the limiting cycle solutions, in section 6.5 we show that the pumping $\phi_0(t) = \alpha t$ can support exactly periodic solutions. They can be thought of as finite-α deformations of the oscillon solutions introduced in [140] that we discussed in section 1.3. We construct these novel time-periodic solutions both by means of a double perturbative expansion and a full-fledged numerical computation. We find agreement between the results we have obtained when the applicability regimes of both methods overlap.

In section 6.6, we revisit the status of the stable pumping solution as an intermediate attractor of an adiabatic quench protocol. We establish that no boundary observer would measure a negative energy density when the source becomes time-independent, focusing on the process of quenching off the pumping solution. We uncover universal scaling properties of the mass when this process is sufficiently fast, and discuss their relation with related previous observations in the vacuum case [217].

Finally, in section 6.7 we analyze the three-dimensional pumping solution. Our findings vindicate that this solution is remarkable, since it is possible to show that, under a series of duality maps, it can be put into correspondence with other known solutions of three-dimensional gravity, including charged black branes. This allows us to obtain an analytical expression for the three-dimensional pumping solution in closed form.

6.2 Holographic quench basics

As mentioned, we are considering a Einstein-scalar system with action (1.3.169). Focusing on spherically symmetric solutions, we employ our standard metric ansatz (1.3.173), which results in the hyperbolic scalar field equations (1.3.175),(1.3.176) and the elliptic constraint equations (1.3.177),(1.3.178) we reviewed in section 1.3 of chapter 1. Regarding the boundary conditions, we find that origin regularity still enforces a definite parity on ϕ, δ and f. However, due to the nontrivial source $\phi_0(t)$, the asymptotic series expansions get modified as

$$\delta(t, \pi/2 - x) = \frac{\kappa^2}{4}\dot{\phi}_0^2\rho^2 + \frac{\kappa^2}{48}(-4\dot{\phi}_0^2 + 9\kappa^2\dot{\phi}_0^4 + 6\ddot{\phi}_0^2 - 6\dot{\phi}_0\dddot{\phi}_0)\rho^4 + \ldots, \tag{6.2.1}$$

$$f(t, \pi/2 - x) = 1 - \frac{\kappa^2}{2}\dot{\phi}_0^2\rho^2 - a_3(t)\rho^3 + \frac{\kappa^2}{6}\left(-2\dot{\phi}_0^2 + 3\kappa^2\dot{\phi}_0^4 + 3\ddot{\phi}_0^2 - 3\dot{\phi}_0\dddot{\phi}_0\right)\rho^4 + \ldots, \tag{6.2.2}$$

$$\phi(t, \pi/2 - x) = \phi_0 + \frac{1}{2}\ddot{\phi}_0\rho^2 + \phi_3(t)\rho^3 + \frac{1}{24}(8\dot{\phi}_0 - 9\kappa^2\dot{\phi}_0^2\ddot{\phi}_0 + 3\dddot{\phi}_0)\rho^4 + \ldots \tag{6.2.3}$$

We are working in the boundary time gauge $\delta(t, \pi/2) = 0$, and we remind the reader that $\kappa^2 = 8\pi G$ and that our units choice is such that $l = 1$. In contrast with the normalizable case, the parameter a_3 is no longer time-independent. The momentum constraint provides a nontrivial link between this parameter, ϕ_0 and ϕ_3:

$$\dot{a}_3(t) + 3\kappa^2 \dot{\phi}_0(t)\phi_3(t) = 0. \tag{6.2.4}$$

With this choice, the asymptotic series expansion of the momentum constraint vanishes at every order. How are these parameters to be interpreted in the light of the AdS/CFT correspondence? As usual, the bulk massless scalar field corresponds to a marginal scalar operator $\mathcal{O}$: the GKPW relation implies that ϕ_0 implements the lagragian deformation (1.2.80). It remains to obtain the dual role of a_3, ϕ_3.

The holographic renormalization of a massless scalar field with finite backreaction has been discussed in [46], and recently reviewed in [218]. The results of [46] readily apply to our case. Going to Fefferman-Graham coordinates and expanding around $z = 0$,

$$ds^2 = \frac{dz^2}{z^2} + \frac{h_{ab}dy^a dy^b}{z^2}, \tag{6.2.5}$$

$$h_{ab} = \eta_{ab} + h^{(3)}_{ab} z^3 + \ldots, \tag{6.2.6}$$

$$\phi = \phi_0 + \ldots + \phi_3 z^3 + \ldots \tag{6.2.7}$$

the holographic renormalization procedure instructs us to identify $\langle T_{ab}\rangle = 3/(2\kappa^2)h^{(3)}_{ab}$ and $\langle \mathcal{O}\rangle = 3\phi_3$.[2] This results in the following expectation value for the dual QFT energy-momentum tensor

$$\langle T_{ab}\rangle = \frac{1}{\kappa^2}\text{diag}\left(a_3(t), \frac{1}{2}a_3(t), \frac{1}{2}a_3(t)\sin^2\theta\right). \tag{6.2.8}$$

and scalar operator vev

$$\langle \mathcal{O}\rangle = 3\phi_3(t). \tag{6.2.9}$$

We observe that $\langle T^a_a\rangle = 0$, implying that the dual QFT is conformal invariant. This is expected, since i) the scalar operator $\mathcal{O}$ dual to ϕ is marginal and ii) in odd boundary dimensions there are no gravitational conformal anomalies. The energy density of the dual CFT state is then given by $\langle T_{tt}(t)\rangle = \kappa^{-2}a_3(t)$, and the relation (6.2.4) reduces to

$$\partial_t \langle T_{tt}(t)\rangle + \dot{\phi}_0(t)\langle \mathcal{O}\rangle = 0, \tag{6.2.10}$$

which is nothing but the CFT differomorphism Ward identity, $\nabla^a \langle T_{ab}\rangle = \langle \mathcal{O}\rangle \partial_a\phi_0$. We define $m = \langle T_{tt}\rangle$ as the energy density of the dual field theory. From now on, we set $\kappa^2 = d - 1$.

Finally, let us perform one last observation. We are interested in the following scenario: at $t = 0$, we place ourselves in the vacuum AdS$_4$ geometry, driving the system away from its initial groundstate by specifying a particular ϕ_0 function. In principle, the functional form of ϕ_0 looks arbitrary. However, expasions (6.2.1)-(6.2.3) imply that this is not the case;

---

[2] At leading order, $z = \rho$, so this coefficient is the one appearing in (6.2.3).

for instance, if $\phi_0^{(n)}(0) \neq 0$ for some n, a nonzero term would appear in the f expansion at $O(\rho^{2n})$, violating the assumption that the initial geometry is AdS$_4$. Said otherwise, consistency of our initial data with the asymptotic expansions demands that every derivative of ϕ_0 is vanishing at $t = 0$: the function ϕ_0 is necessarily non-analytic.

6.3 The four-dimensional pumping solution

The expansions (6.2.1)-(6.2.3) suggest that, for the pumping source $\phi_0(t) = \alpha t$, the metric is time-independent. In fact, if we introduce the pumping ansatz $\Phi(t,x) = 0, \Pi(t,x) = \Pi_\alpha(x) = \alpha e^{\delta_\alpha(x)} f_\alpha(x)^{-1}$ into the equations of motion for the metric, we arrive at

$$\delta'_\alpha(x) + \sin x \cos x \alpha^2 e^{2\delta_\alpha(x)} f_\alpha(x)^{-2} = 0, \tag{6.3.11}$$

$$f'_\alpha(x) + \frac{1 + 2\sin^2 x}{\sin x \cos x}(1 - f_\alpha(x)) + \sin x \cos x \alpha^2 e^{2\delta_\alpha(x)} f_\alpha(x)^{-1} = 0, \tag{6.3.12}$$

while the scalar field equations of motion are trivially satisfied. This coupled system of nonlinear ODEs determines the pumping solution metric. As we will show in section 6.6, the $d = 2$ counterpart of these equations admits an analytic solution; for $d \geq 3$, they must be solved numerically. If we work in the boundary time gauge $\delta(t, \pi/2) = 0$, we find that there is a maximum value of α, $\alpha_{\max}$, such that, for $\alpha > \alpha_{\max}$, no solution exists. Therefore, $\alpha_{\max}$ corresponds to an intrinsic adiabaticity threshold present in our system.

Actually, it turns out that equations (6.3.11)(6.3.12) cannot be univocally solved: there exist two different pumping solutions with the same α. This non-uniqueness can be exposed by going momentarily to the origin time gauge, $\delta(t, 0) = 0$. The origin time is given by[3]

$$t_o = e^{-\delta_b(0)} t_b, \tag{6.3.13}$$

where δ_b corresponds to our original pumping solution in the boundary time gauge. Under this transformation, α_b transforms contravariantly,

$$\alpha_o = e^{\delta_b(0)} \alpha_b, \tag{6.3.14}$$

in such a way that ϕ_0 is invariant, $\phi_0 = \alpha_b t_b = \alpha_o t_o$. It is obvious that the relation $\alpha_o = \Pi_b(x = 0)$ provides a diffeomorphic invariant definition of α_o. When expressed in this gauge, equations (6.3.11)(6.3.12) allow for a single pumping solution for a given $\alpha_o \in \mathbb{R}^+$. We plot representative examples in figure 6.1. We denote with $\alpha_{o,\text{thr}}$ the value of α_o that corresponds to $\alpha_{\max}$.

Let us pause here an discuss why the existence of the pumping solutions is remarkable. On general grounds, the pumping source $\phi_0(t) = \alpha t$ is expected to be associated with a process of energy injection that leads to a time-dependent geometry that eventually may collapse gravitationally. However, the Ward identity (6.2.10) readily implies that, if the

---

[3] In the following, we will denote boundary time quantities with a b subindex, while the subindex o will refer to quantities in origin time

pumping source is accompanied by a vanishing vev, $\langle \mathcal{O}(t) \rangle = 0$, the energy density remains constant, $\dot{m}(t) = 0$. This is precisely the situation in the pumping solution, since $\Phi(t,x) = 0$. Notice that the physical mechanism behind the existence of the pumping solutions could also be the reason of its physical irrelevance: the question of whether the pumping solution is infinitely fine-tuned needs to be explicitly addressed. Said otherwise, we must determine if any infinitesimal perturbation with $\Phi(t,x) \neq 0$ leads to a process of energy exchange that destroys the pumping solution.

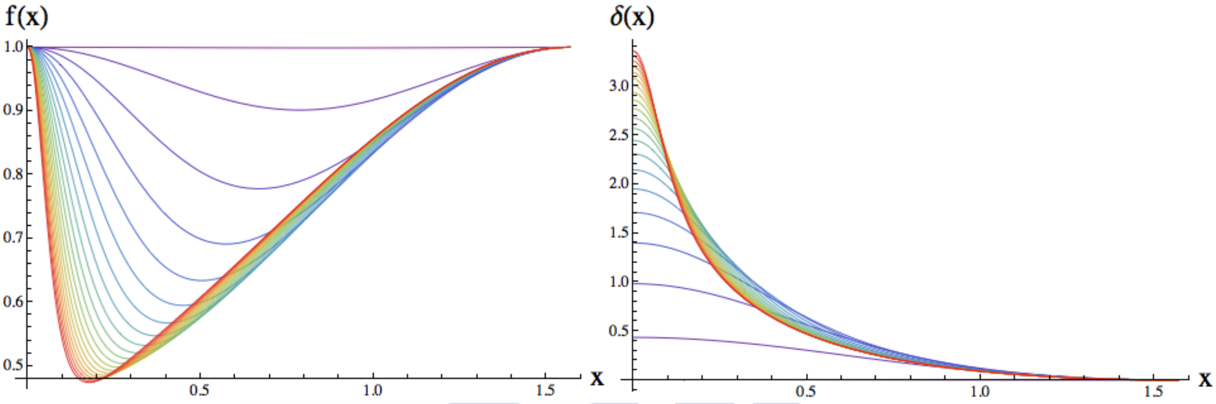

Figure 6.1: Pumping solutions for $\alpha_o \in [0, 20]$, the color wavelength grows with growing α_o.

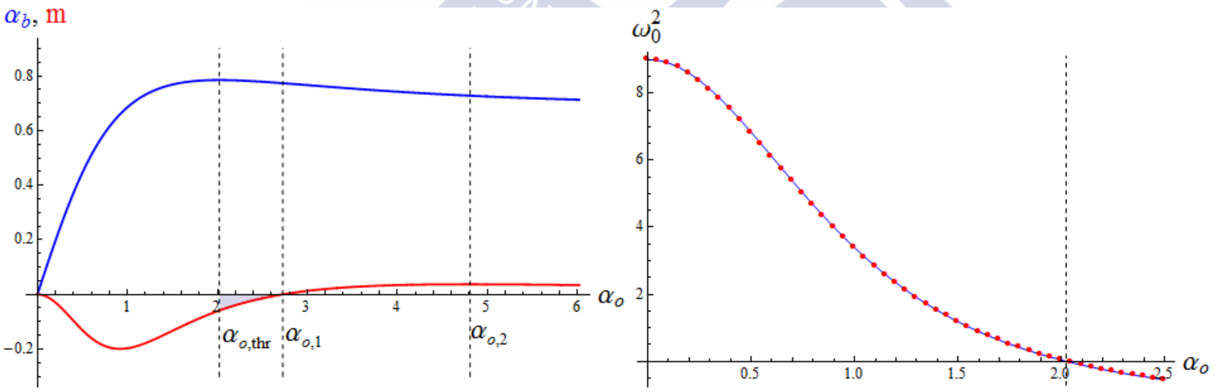

Figure 6.2: Left: α_b (blue) and energy density (red) of the pumping solution in terms of α_0. The left dashed vertical line signals the first α_b maximum, while the right one marks the maximum of the energy density. The shaded region corresponds to the linearly unstable pumping solutions of negative energy density. Right: frequency of the fundamental mode of a linear radial fluctuation of the pumping solution. The linear instability threshold is signaled by the dashed vertical line.

We can compute the energy density of the pumping solutions, and perform two important observations (see figure 6.2a). The first one is that there exist a threshold value $\alpha_{o,1}$ such that, for $\alpha_o < \alpha_{o,1}$, m is *negative*. As with other gravitational background with negative mass this raises a concern regarding stability [219]. The second one is that there exists yet another threshold value $\alpha_{o,2} > \alpha_{o,1}$ where the energy density curve $m(\alpha_o)$ reaches an extremum. According to the discussion in chapter 5, we may naively think that $\alpha_{o,2}$ signals a Chandrasekhar instability. Both issues will be addressed in the next section.

6.4 Linear and nonlinear stability of the pumping solution

Let us start by pointing out that, at $\alpha_o = \alpha_{o,2}$, a linearized radial fluctuation cannot connect two infinitesimally-close pumping solutions if its normalizable, since $\alpha_b'(\alpha_o)|_{\alpha_o=\alpha_{o,2}} \neq 0$. In order for this to happen, we would need a vanishing $\alpha_b'(\alpha_o)$: we must place ourselves at $\alpha_b = \alpha_{\max}$. For linearized fluctuations around the pumping solution contained in our original ansatz, an explicit computation show that, indeed, at $\alpha_o = \alpha_{o,\mathrm{thr}}$, a zero mode appears in the eigenfrequency spectrum (see figure 6.2b). Therefore, pumping solutions with $\alpha_o > \alpha_{o,\mathrm{thr}}$ are linearly unstable. This entails that, in principle, only pumping solutions with $\alpha_o \leq \alpha_{o,\mathrm{thr}}$ can be prepared by a quasistatic quench starting from the AdS$_4$ vacuum.

Two questions naturally arise at this point. The first one is if the linear stability of the $\alpha_o \leq \alpha_{o,\mathrm{thr}}$ pumping solutions translates into nonlinear stability. The second one concerns the final state reached by the $\alpha_o > \alpha_{o,\mathrm{thr}}$ pumping solutions once perturbed.

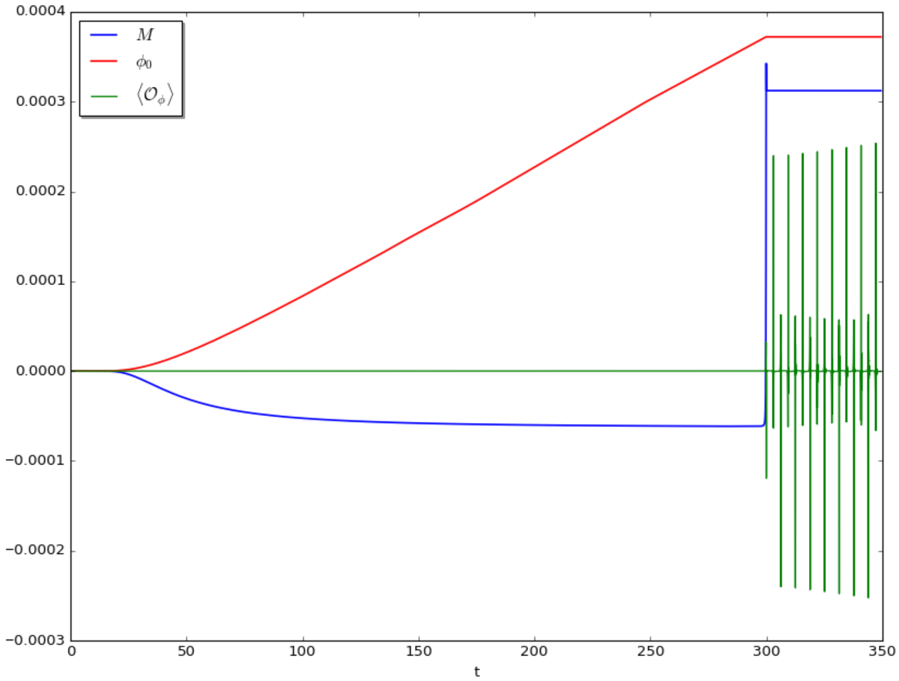

Figure 6.3: Generation of a pumping solution by means of a quasistatic quench. After the initial transient regime, the energy density stabilizes to a time-independent negative value corresponding to the pumping solution associated with the slope of $\phi_0(t)$. At late times, the pumping source is turned off and the system enters into a dynamical regime. ϕ_0, m and $\langle \mathcal{O} \rangle$ have been rescaled to fit into the same figure.

Let us address the first question. Notice first that, by virtue of the Ward identity (6.2.10), even if a linear eigenmode has a nonzero $\langle\mathcal{O}(t)\rangle$, since its time dependence is harmonic, the energy density it generates would also oscillate periodically with a $\pi/2$ phase shift with respect to $\langle\mathcal{O}(t)\rangle$. Nonlinear perturbations, being generically nonharmonic, might trigger a nonlinear instability due to the existence of a finite $\Phi(t,x)$ with arbitrary time dependence, which results in a net energy exchange that eventually leads to gravitational collapse. There exist two complementary ways of establishing the absence of this potential nonlinear instability. The first one is realizing that pumping solutions below $\alpha_{o,\mathrm{thr}}$ can be explicitly accessed by a quasistatic quench. Indeed, we have simulated the time-dependent geometry generated by a source $\phi_0(t)$ such that $\phi_0(t<0)=0$, $\ddot{\phi}_0/\dot{\phi}_0^{\,2} \ll 1$ and $\lim_{t\to\infty}\phi_0/t=\alpha_b$, and have checked that, at sufficiently late times, it settles down into the linearly stable pumping solution corresponding to α_b. In consequence, these solutions play a nontrivial role at the nonlinear level. If they were nonlinearly unstable, the system would never relax to them. We provide one example of this process in figure 6.3.

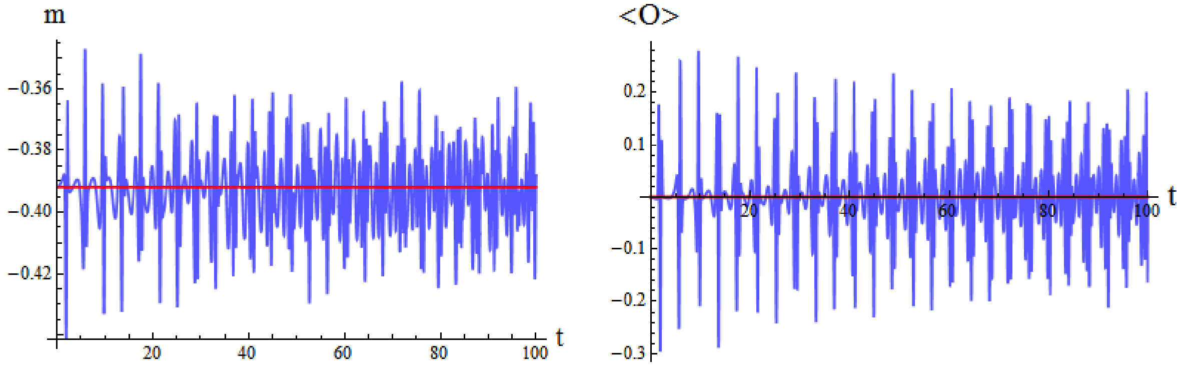

Figure 6.4: Energy density (left, blue) and vev (right, blue) for the a $\epsilon=1, \sigma=0.1$ gaussian perturbation of a pumping solution with $\alpha_0=1$. Red curves denote the initial values of each plotted quantity. In this simulation, the absolute error in the Ward identity is bounded by 10^{-4} for a grid resolution $N=2^{11}$.

The second approach we followed in order to determine whether linearly stable pumping solutions are also nonlinearly stable was to take, as initial data at $t=0$,

$$\Phi(0,x)=0, \tag{6.4.15}$$

$$\Pi(0,x)=\Pi_b(x)+\frac{2\epsilon}{\pi}\exp\left(-\frac{4\tan^2 x}{\pi^2\sigma^2}\right), \tag{6.4.16}$$

and simulate their subsequent time evolution. An example is depicted in figure 6.4, for $\alpha_0=1$, $\epsilon=1$ and $\sigma=0.1$. Due to the gaussian perturbation, the initially negative $m(0)$ does not remain constant: its time derivative perfectly satisfies the Ward indentity in the presence of the nontrivial $\langle\mathcal{O}(t)\rangle$ that is generated. Both quantities, $m(t)$ and $\langle\mathcal{O}(t)\rangle$, are found to oscillate around their respective initial values. In fact, we find that the time-averaged energy density, $\langle m\rangle_t = t^{-1}\int_0^t m(t')dt'$, rapidly reaches a constant value and the system absorbes/loses no net energy density. Therefore, no sign of the new potential nonlinear instability is found.

6.4.1 The linearly unstable branch

This situation changes dramatically for the linearly unstable branch of pumping solutions. In fact, repeating the procedure just described for finite ϵ, a black hole promptly forms. Initializing the simulation code with $\epsilon = 0$ puts us exactly on top of an $\alpha_o > \alpha_{o,\mathrm{thr}}$ pumping solution, up to numerical error. Being linearly unstable, this unavoidable numerical error drives the system away from the original geometry. However, for $\alpha_{o,\mathrm{thr}} < \alpha_o \leq \alpha_{o,c}$, despite entering a time-dependent regime, the system does not undergo gravitational collapse, but rather decays into a limiting cyle that, for $\alpha_o - \alpha_{o,\mathrm{thr}} \ll 1$, seems to be time-periodic.[4]

Let us perform two different checks that help establishing that this limiting cycle solution is not a numerical artifact. First, since the departure from the original unstable pumping solution is noise-driven, the transient time needed to reach the limit cycle solution should be proportional to the grid resolution. We find that this is precisely what happens (figure 6.5).

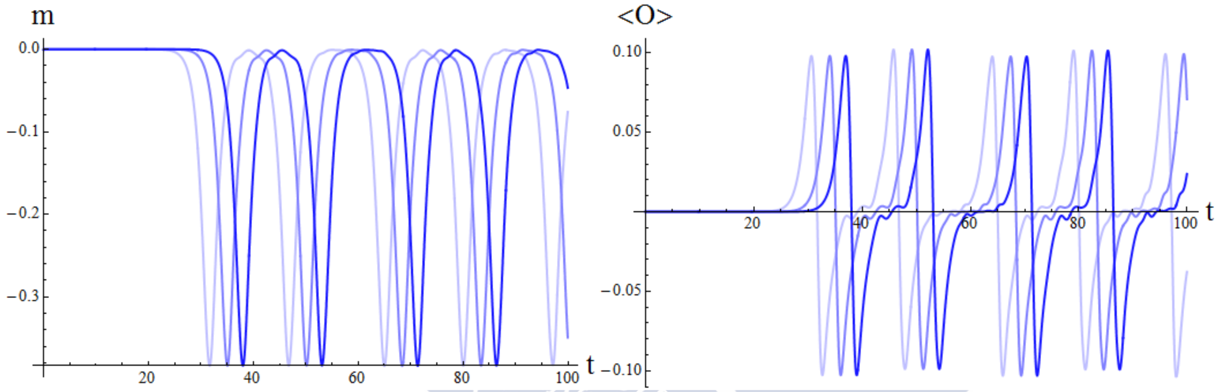

Figure 6.5: Time evolution of the mass (left) and vev (right) for the oscillatory solution with $\alpha_0 = 2.71$. The colouring encodes the three spatial resolutions $N = 2^{10}$, 2^{11}, 2^{12} employed to build the initial data and perform the simulation. Consistently, the transition to a time-dependent solution happens at later times for increasing N. On the contrary, the periodicity is resolution-independent. This means that the system reaches the same limiting cycle at different times depending on the initial conditions.

As a second check, we wait until the system has decayed into the limiting cycle solution, and take the $\Phi(t_{ref}, x), \Pi(t_{ref}, x)$ profiles at the reference time t_{ref} as initial data of another numerical simulation where the deformation

$$\Phi(t_{ref}, x) \to \Phi(t_{ref}, x) + \epsilon \cos^2 x \sin x \tag{6.4.17}$$

is implemented. Then, we perform a scan in ϵ, with the aim of seeing if the perturbed limiting cycle solution collapses gravitationally. The results of this analysis for the unstable pumping solution with $\alpha_b = 0.78497$ can be found in figure 6.6. The collapse time $t_c(\epsilon)$ looks

---

[4] The quantity $\alpha_{o,c}$ is close to, but distinct from the value $\alpha_{o,1}$ that marked the sign change of the energy density of the pumping solution.

divergent at a critical ϵ_c and, for $\epsilon \leq \epsilon_c$, no black hole forms within the times computationally accessed. This phenomenology agrees with the one previously found for $\sigma > \sigma_c$ Gaussian initial data in [135], and provides strong evidence favoring the hypothesis that the limiting cycle solution is nonlinearly stable.

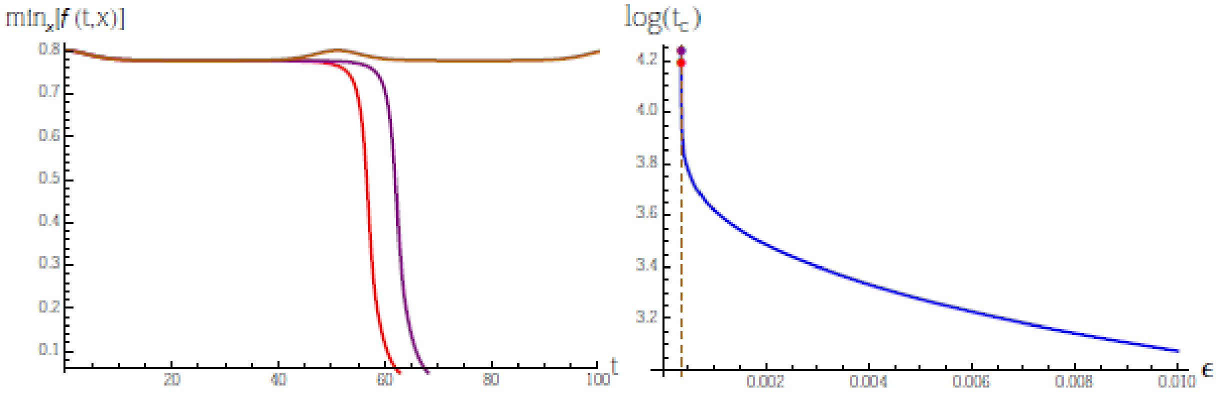

Figure 6.6: Left: $\min_x f(t,x)$ for the perturbed limit cycle solution for three deformations of the form (6.4.17) close to ϵ_c, two above (red and purple) and one below (brown). Right: $t_c(\epsilon)$ for the perturbed limit cycle solution (blue). The purple and red dots correspond to the purple and red simulations depicted on the left figure. The brown dashed line represents the brown simulation on the left, for which no collapse is found.

6.5 Time-periodic pumping solutions

As said before, for $\alpha_{o,\text{thr}} \leq \alpha_o < \alpha_{0,c}$ the endpoint of the unstable branch is limiting cycle. For $\alpha_o - \alpha_{o,\text{thr}} \ll 1$ this limiting cycle is apparently time-periodic. This fact came as totally unexpected, and prompted us to look for exactly periodic solutions with a pumping source. Time-periodic solutions in global AdS supported by a real massless scalar field with zero source were originally presented in [140]. We now show that, for $\alpha_b \neq 0$, each such solution branches into a family of exactly periodic solutions with a linear source. The existence of this new kind of solutions can be first proven at the perturbative level and later corroborated with a numerical approach.

6.5.1 Peturbative construction

Let Ω be the frequency of the periodic solution we aim at. Rescale the time coordinate as $\tau \equiv \Omega\, t$ and introduce the following ansatz

$$\phi(\tau,x) = \alpha_b \frac{\tau}{\Omega(\alpha_b,\epsilon)} + \epsilon\cos^3 x \sin\tau + \sum_{n=1}^{\infty}\sum_{k=0}^{2n+1} \varphi_{2n+1-k,k}(\tau,x)\alpha_b^{2n+1-k}\epsilon^k, \tag{6.5.18}$$

$$\delta(\tau,x) = \sum_{n=1}^{\infty}\sum_{k=0}^{2n} d_{2n-k,k}(\tau,x)\alpha_b^{2n-k}\epsilon^k, \tag{6.5.19}$$

$$f(\tau,x)=1+\sum_{n=1}^{\infty}\sum_{k=0}^{2n}a_{2n-k,k}(\tau,x)\alpha_b^{2n-k}\epsilon^k, \tag{6.5.20}$$

$$\Omega(\alpha_b,\epsilon)=3+\sum_{n=1}^{\infty}\sum_{k=0}^{2n}\omega_{2n-k}\alpha_b^{2n-k}\epsilon^k. \tag{6.5.21}$$

At first order in α_b and ϵ we are just considering the linear superposition of the pumping solution $\phi_\alpha(t,x)=\alpha_b t$ and the fundamental eigenmode of the scalar field[5] $\phi_\epsilon=\epsilon\sin\tau\cos^3 x$ over global AdS$_4$. Higher order corrections determine how the seed $\phi_\alpha+\phi_\epsilon$ is dressed nonlinearly. We are solving the ansatz (6.5.18)-(6.5.21) with the following boundary conditions:

- Normalizability of the scalar field, $\varphi_{2n+1-k,k}(\tau,\pi/2)=0$.
- Regularity of the scalar field at $x=0$, $\lim_{x\to 0}x\,\varphi_{2n+1-k,k}(\tau,x)=0$.
- Regularity of the blackening factor at at $x=0$, $\lim_{x\to 0}x\,a_{2n-k,k}(\tau,x)=0$.
- Preservation of the boundary time gauge, $d_{2n-k,k}(\tau,\pi/2)=0$.

Furthermore, we also demand that $\phi(0,x)=0$. Note that, when $\epsilon=0$, the ansatz (6.5.18)-(6.5.21) must reduce to the pumping solution. Therefore, we must have $\varphi_{2n+1,0}=\partial_t a_{2n,0}=\partial_t d_{2n,0}=0$. On the other hand, for $\alpha_b=0$, we must recover the perturbative expansion of the exactly periodic solution branching from the fundamental eigenmode of global AdS$_4$ [196].[6]

Substituting (6.5.18)-(6.5.21) into the equations of motion and expanding to order $n=1$, we get the following equations for the metric

$$a_{2,0}'+(3\tan x+\cot x)\,a_{2,0}+\cos x\sin x=0, \tag{6.5.22}$$
$$a_{1,1}'+(3\tan x+\cot x)\,a_{1,1}+6\sin x\cos^4 x\cos t=0, \tag{6.5.23}$$
$$a_{0,2}'+(3\tan x+\cot x)\,a_{0,2}+\frac{9}{5}\sin x\cos^5 x\,(1+\cos 2x\cos 2\tau)=0, \tag{6.5.24}$$
$$d_{2,0}'+\cos x\sin x=0, \tag{6.5.25}$$
$$d_{1,1}'+6\sin x\cos^4 x\cos\tau=0, \tag{6.5.26}$$
$$d_{0,2}'+\frac{9}{5}\sin x\cos^5 x\,(1+\cos 2x\cos 2\tau)=0, \tag{6.5.27}$$

---

[5] Recall that scalar eigenmodes in global AdS have a frequency spectrum given by $\omega_n=\Delta+2n$, where Δ is the conformal dimension of the dual scalar operator. For a massless scalar field in AdS$_4$, $\Delta=3$.

[6] The comparison of our results with [196] is not immediate, since there the origin time gauge was employed.

which are solved by

$$a_{2,0}(x) = \frac{1}{2}\cot^2 x \sin 2x(x - \tan x), \tag{6.5.28}$$

$$a_{1,1}(\tau, x) = -\sin x \sin 2x \cos^2 x \cos\tau, \tag{6.5.29}$$

$$a_{0,2}(\tau, x) = -\frac{3}{2}\sin^2 x \cos^6 x \cos 2\tau + \frac{9}{64}\cot x \cos^2 x(\sin 4x - 4x), \tag{6.5.30}$$

$$d_{2,0}(x) = \frac{1}{2}\cos^2 x, \tag{6.5.31}$$

$$d_{1,1}(\tau, x) = \frac{6}{5}\cos^2 x \cos\tau, \tag{6.5.32}$$

$$d_{0,2}(\tau, x) = \frac{3}{16}\cos^6 x\left(4 + (3\cos 2x - 1)\cos 2\tau\right), \tag{6.5.33}$$

where the aforementioned boundary conditions have been imposed. Regarding the scalar field, the equation for $\varphi_{3-k,k}$ takes the form

$$\varphi''_{3-k,k} + 2\csc(x)\sec(x)\varphi'_{3-k,k} - 9\ddot{\varphi}_{3-k,k} - S_{3-k,k} = 0\ . \tag{6.5.34}$$

The differential operator acting on $\varphi_{3-k,k}$ is nothing but the AdS$_4$ Laplacian, expressed in $\tau = 3t$ and x coordinates, and the non-homogeneous source $S_{3-k,k}$ depends on lower-order corrections. Explicitly,

$$S_{3,0} = 0, \tag{6.5.35}$$

$$\begin{aligned} S_{2,1} =& 3\cos^2 x(2\cos x(\omega_{2,0} + 3(d'_{2,0} - a'_{2,0}))+ \\ & \sin x(d'_{2,0} - a'_{2,0}))\sin\tau + 9\cos^3 x(\dot{a}_{2,0} - \dot{d}_{2,0})\cos\tau + \dot{a}_{1,1} - \dot{d}_{1,1}, \end{aligned} \tag{6.5.36}$$

$$\begin{aligned} S_{1,2} =& 3\cos^2 x(2\cos x(\omega_{1,1} + 3(d'_{1,1} - a'_{1,1}))+ \\ & \sin x(d'_{1,1} - a'_{1,1}))\sin\tau + 9\cos^3 x(\dot{a}_{1,1} - \dot{d}_{1,1})\cos\tau + \dot{a}_{0,2} - \dot{d}_{0,2}, \end{aligned} \tag{6.5.37}$$

$$\begin{aligned} S_{0,3} =& 3\cos^2 x(2\cos x(\omega_{0,2} + 3(d'_{0,2} - a'_{0,2}))+ \\ & \sin x(d'_{0,2} - a'_{0,2}))\sin\tau + 9\cos^3 x(\dot{a}_{0,2} - \dot{d}_{0,2})\cos\tau. \end{aligned} \tag{6.5.38}$$

When solving any one of the nontrivial equations above, the requirement that $\varphi_{3-k,k}$ is both regular at $x = 0$ and unsourced can only be satisfied if the frequency correction appearing in $S_{3-k,k}$ takes a particular value. We have that $\omega_{2,0} = -7/4$, $\omega_{1,1} = 0$ and $\omega_{0,2} = -135/128$. The most general solutions compatible with the boundary conditions that we find are:

$$\begin{aligned} \varphi_{2,1}(\tau, x) =& \frac{3}{20}\cos^3 x(19\cos^2 x + 5x(2(x + \cot x) + \sin 2x))\sin\tau + \\ & C_{2,1}\cos^3 x \sin\tau, \end{aligned} \tag{6.5.39}$$

$$\begin{aligned} \varphi_{1,2}(\tau, x) =& -\frac{1}{17920}\cos^2 x \cot x(-3240x + 5760x\cos 2x - 3600x\cos 4x + \\ & 1345\sin 2x + 4394\sin 4x + 381\sin 6x)\sin 2\tau \\ & + C_{1,2}\cos^3 x \sin\tau, \end{aligned} \tag{6.5.40}$$

$$\begin{aligned}\varphi_{0,3}(\tau,x) =& \frac{3}{896}\cos^3 x(108\cos^4 x - 88\cos^6 x + 12\cos^8 x - \\ & 252x(x+2\cot x) + 63\cos^2 x(4x\cot x - 1))\sin\tau - \\ & \frac{1}{64}\cos^9 x(1+9\cos 2x)\sin(3\tau) + C_{0,3}\cos^3 x\sin\tau + \\ & \frac{D_{0,3}}{64}\cos^3 x(-2+6\cos 2x - 3\cos 4x + 4\cos 6x)\sin(3\tau).\end{aligned} \tag{6.5.41}$$

We observe that regularity and normalizability by themselves are not enough to fix the undetermined constants $C_{1,2}, C_{2,1}, C_{0,3}, D_{0,3}$. Notice also that, up to this point, ϵ remains as a formal expansion parameter. By adscribing a physical meaning to it we can reduce the four undetermined integration constants to one. Let us identify

$$\lambda \equiv \langle \mathcal{O}(\tau = \pi/2)\rangle = 3\epsilon. \tag{6.5.42}$$

Higher order corrections would modify this relation unless $C_{1,2} = 0, C_{2,1} = -3/8\pi^2$ and $C_{0,3} = 3/128(9\pi^2 - 10D_{0,3})$. The integration constant $D_{0,3}$ cannot be fixed at this order of the perturbative expansion.[7] It turns out that, when computing the $\varphi_{0,5}$ correction, regularity and normalizability enforce that $D_{0,3} = 305/808$. With the definition (6.5.42), the seed frequency $\Omega_0 = 3$ is modified to

$$\Omega = \Omega_0 - \frac{15}{128}\lambda^2 - \frac{7}{4}\alpha_b^2, \tag{6.5.43}$$

The introduction of a finite pumping has nontrivial consequences regarding the Fourier decomposition of the exactly periodic solution in time. To wit, while in the $\alpha_b = 0$ case only odd multiples of the oscillation frequency Ω appear, for $\alpha_b \neq 0$ even multiples are also present, as exemplified by the $\varphi_{1,2}$ correction. It is mandatory to take this fact into account when designing a pseudospectral code able to find these solutions numerically.

6.5.2 Numerical construction

To close the gap between the perturbative and the fully nonlinear regime, one needs to resort to numerical methods. In particular, since the eigenmodes of the AdS$_4$ Laplacian do not satisfy the boundary conditions (6.2.3)[8], we have adapted the pseudospectral method described in [196] to our present setup.

We start by decomposing our dynamical fields as

$$\Pi(\tau,x) = \alpha_b + \frac{3}{2}\alpha_b^3\cos^2 x + \cos^2 x\hat{\Pi}(\tau,x), \tag{6.5.44}$$

$$\Phi(\tau,x) = \cos x\hat{\Phi}(\tau,x), \tag{6.5.45}$$

---

[7] This phenomenon is solely due to the $\alpha_b = 0$ sector of the perturbative expansion and has been previously pointed out in [196].

[8] A finite mass breaks the parity that the scalar field near-boundary expansion exhibits at the normal mode level.

in such a way that $\hat{\Pi}, \hat{\Phi}$ satisfy the boundary conditions $\hat{\Pi}(\tau, \pi/2) = \hat{\Phi}(\tau, \pi/2) = 0$ with nonzero first-order spatial derivatives. The equations of motion are correspondingly modified. Taking into account the appearance of both odd and even multiples of the fundamental frequency at the perturbative level, we Fourier decompose our rescaled fields in time as

$$\hat{\Pi}(\tau, x) = \sum_{k=0}^{N_k} \cos(k\tau) P_k(x), \qquad \hat{\Phi}(\tau, x) = \sum_{k=0}^{N_k} \sin((k+1)\tau) Q_k(x), \tag{6.5.46}$$

where we have allowed for a nontrivial zero-mode $P_0(x)$ in $\hat{\Pi}$, that would take care of the fact that, when $\epsilon = 0$, Π must reduce to the field corresponding to the pumping solution at the given α_b. N_k is a numerical cutoff in the total mode number. The functions $\{P_k, Q_k, k = 0 ... N_k\}$ must be further decomposed into a convenient spatial basis. A suitable choice was provided in [220] and exploited in-depth in [196] in the spherically symmetric and sourceless case. For completeness, let us elaborate a bit on this choice. We largely follow [196], and we refer the reader to that useful reference for further information.

First, let us take $y = \frac{2}{\pi} x$, in such a way that $y \in [0, 1]$; then notice that, since origin regularity imposes a definite parity on the fields of our problem, we might extend them to the domain $y \in [-1, 0]$ in a univocal way. Define $\bar{y} \in [-1, 1]$, and focus on the extended functions $\{\bar{P}_k(\bar{y}), \bar{Q}_k(\bar{y}), k = 0 ... N_k\}$. We introduce Lagrange interpolating polynomials $\{l_j(\bar{y}), j = 0 ... 2N_j + 1\}$ that satisfy $l_j(\bar{y}_k) = \delta_{j,k}$ for some extended collocation grid $\{\bar{y}_j, j = 0 ... 2N_j + 1\}$. We can write a polynomial approximation to any function $f : [-1, 1] \to \mathbb{R}$ as

$$\mathcal{I}_{2N_j+1} f(\bar{y}) = \sum_{j=0}^{2N_j+1} f(\bar{y}_j) l_j(\bar{y}) \equiv \sum_{j=0}^{2N_j+1} \bar{f}_j l_j(\bar{y}). \tag{6.5.47}$$

Explicitly, the interpolating polynomials are given by

$$l_j(\bar{y}) = \frac{w_j}{\bar{y} - \bar{y}_j} \left(\sum_{l=0}^{2N_j+1} \frac{w_l}{\bar{y} - \bar{y}_l} \right)^{-1}, \tag{6.5.48}$$

where the weights $\{w_j, j = 0 ... 2N_j + 1\}$ are defined as $w_j = \left(\prod_{j=0, j \neq l}^{2N_j+1} (\bar{y}_j - \bar{y}_l) \right)^{-1}$ in terms of the extended collocation grid. So far, the extended collocation grid we are referring to remains arbitrary. A convenient choice is provided by the Chebyshev collocation grid of the second kind

$$\bar{y}_j = \cos\left(\frac{\pi j}{2N_j + 1} \right), j = 0 ... 2N_j + 1. \tag{6.5.49}$$

Notice that the boundary $x = \pi/2$ (*i.e.* $\bar{y} = 1$) is included in the collocation grid, while the origin is avoided. This last feature is convenient in two regards. First, it allows to impose the boundary conditions at $\bar{y} = \pm 1$ on the functions $\{\bar{P}_k(\bar{y}), \bar{Q}_k(\bar{y}), k = 0 ... N_k\}$ in a straighforward way. Second, it implies that the singular behavior of some terms present in the equations of motion at $x = 0$ (*i.e.* $\bar{y} = 0$) is no longer a concern in the discretized version of the problem. Furthermore, with this choice, the approximant (6.5.47) satisfies

$$I_{2N_j+1}f(\bar{y}) = \sum_{j=0}^{2N_j+1} \hat{f}_j T_j(\bar{y}), \tag{6.5.50}$$

where $\{T_j(\bar{y}), j = 0...2N_j + 1\}$ are Chebyshev polynomials of the first kind. Standard optimization theorems in polynomial approximation then apply immediately to our case. As a final benefit, it turns out that the grid choice (6.5.49) allows for a simple analytic expression of the w_j weights [220]. The n-th derivative of the function f can be approximated by the n-th derivative of (6.5.47). We have that

$$\frac{d^n}{d\bar{y}^n}\mathcal{I}_{2Nj+1}(\bar{y}_j) = \sum_{l=0}^{2Nj+1} D^{(n)}_{j,l}\bar{f}_l \ , \tag{6.5.51}$$

where the explicit form of the $2(N_j+1)\times 2(N_j+1)$ differentiation matrix $\mathbf{D}^{(n)}$ can be found in [196]. Now the crucial point comes into play. Since we are working with functions of definite parity around $x = 0$, $P_k(-x) = P_k(x), Q_k(-x) = -Q_k(x)$, we have that, being f any one of these functions and p its parity under $x \to -x$,

$$\bar{f}_{2N_j+1-j} = (-1)^p\bar{f}_j \equiv (-1)^p f_j, j = 0...N_j \ , \tag{6.5.52}$$

in such a way that the differentiation matrix $\mathbf{D}^{(n)}$ splits into four $(N_j+1)\times(N_j+1)$ blocks. Defining $\mathbf{f} = (f_0, ..., f_{N_j})$, $\bar{\mathbf{f}} = (f_0, \ldots, f_{N_j}, (-1)^p f_{N_j}, \ldots, (-1)^p f_0)$ we have that

$$\bar{\mathbf{f}} = \begin{pmatrix} \mathbf{1} & \mathbf{0} \\ (-1)^p\mathbf{R} & \mathbf{0} \end{pmatrix}\begin{pmatrix} \mathbf{f} \\ \mathbf{0} \end{pmatrix}, \tag{6.5.53}$$

where $\mathbf{R}$ is a $(N_j+1)\times(N_j+1)$ exchange matrix. In consequence

$$\mathbf{D}^{(n)}\bar{\mathbf{f}} = \begin{pmatrix} \mathbf{D}^{(n)}_{++} & \mathbf{D}^{(n)}_{+-} \\ \mathbf{D}^{(n)}_{-+} & \mathbf{D}^{(n)}_{--} \end{pmatrix}\begin{pmatrix} \mathbf{1} & \mathbf{0} \\ (-1)^p\mathbf{R} & \mathbf{0} \end{pmatrix}\begin{pmatrix} \mathbf{f} \\ \mathbf{0} \end{pmatrix} = \begin{pmatrix} (\mathbf{D}^{(n)}_{++} + (-1)^p\mathbf{D}^{(n)}_{+-}\mathbf{R})\mathbf{f} \\ (\mathbf{D}^{(n)}_{-+} + (-1)^p\mathbf{D}^{(n)}_{--}\mathbf{R})\mathbf{f} \end{pmatrix}, \tag{6.5.54}$$

and we find that the parity-adapted n-th derivative operator acting on the physical $y > 0$ part of the extended grid is

$$\mathbf{D}^{(n)}_p \equiv \mathbf{D}^{(n)}_{++} + (-1)^p\mathbf{D}^{(n)}_{+-}\mathbf{R} \ . \tag{6.5.55}$$

Therefore, for functions of well-defined parity around $x = 0$, if we restrict ourselves to the original spatial domain $x \in [0, \pi/2]$ but employ the rescaled collocation grid

$$x_j = \frac{\pi}{2}\cos\left(\frac{\pi j}{2N_j+1}\right), j = 0...N_j \ , \tag{6.5.56}$$

and discretize derivatives with the just defined operator $\mathbf{D}^{(n)}_p$, the desirable features of working with a Chebyshev spectral decomposition are kept while the boundary conditions at $x = 0$ are also automatically incorporated into the discretized problem.

Having clarified our strategy, we take the final ansatz

$$\hat{\Pi}(\tau, x_j) = \sum_{k=0}^{N_k} \sum_{j=0}^{N_j} \cos(k\tau) p_{k,j} \ , \tag{6.5.57}$$

$$\hat{\Phi}(\tau, x_j) = \sum_{k=0}^{N_k} \sum_{j=0}^{N_j} \sin((k+1)\tau) q_{k,j} \ , \tag{6.5.58}$$

so we work in mode space in τ, but real space in x. As a collocation grid in the time domain, we choose

$$\tau_k = \frac{2\pi(k-1/2)}{2N_k+3}, k = 1 \ldots N_k + 1 \ , \tag{6.5.59}$$

At each τ_k, it is convenient to define the variables $\{\delta_{k,j}, c_{k,j}\}$, where $\delta_{k,j} = \delta(\tau_k, x_j)$ and $c_{k,j} = f(\tau_k, x_j)\exp(-\delta(\tau_k, x_j))$, which are then expressed in terms of $\{p_{k,j}, q_{k,j}\}$ by discretizing the corresponding constraint equations and inverting the resulting discretized differential operators. Imposing the boundary conditions $\delta_{k,0} = 0$ and $c_{k,0} = 1$ ensures that we are working in the boundary time gauge and renders the above mentioned discretized differential operators invertible. Once this expressions are known, the first-order dynamical equations for the scalar field can be solved by means of a Newton-Raphson algorithm that we implement in Mathematica. We impose the boundary conditions $p_{k,0} = q_{k,0} = 0$, that follow from the linear independence of the Fourier modes of the time decomposition and $\hat{\Pi}(\tau, \pi/2) = \hat{\Phi}(\tau, \pi/2) = 0$.

As a last comment, notice that we have $2(N_k+1) \times (N_j+1) + 1$ dynamical variables, that correspond to $\{p_{k,j}, q_{k,j}\}$ and the oscillation frequency Ω, but the discretization of the equations of motion for $\hat{\Pi}, \hat{\Phi}$ on the two-dimensional collocation grid provides just $2(N_k+1) \times (N_j+1)$ equations. The remaining equation comes from normalizing some relevant physical quantity to a prescribed numerical value. We choose to set

$$\langle \mathcal{O}(\pi/2) \rangle = \lambda \ , \tag{6.5.60}$$

where λ is an user-defined value for the vev. Since we have defined $\langle \mathcal{O}(\tau) \rangle = -1/2\phi'''(\tau, \pi/2) = \hat{\Phi}''(\tau, \pi/2)$, this extra boundary condition is discretized as

$$\sum_{k=0}^{N_k} \sin((k+1)\pi/2) \sum_{l=0}^{N_j} D^{(2)}_{0,l} q_{k,l} = \lambda \ . \tag{6.5.61}$$

Finally, a given family of time-periodic pumping solutions is found iteratively: we place ourselves at $\lambda, \alpha_b \ll 1$ and employ the perturbative solution as an initial seed to start the relaxation algorithm. Then, we move in discrete steps along the $(\alpha_b(\eta), \lambda(\eta))$ curve in the two-dimensional phase space of time-periodic solutions, taking the one found in the previous step as the initial guess for the next step. The results shown in the following have been obtained for a $N_k = N_j = 20$ grid; the time it took to find each solution along the curve was $O(5)$ min.

6.5.3 Results

Let us perform two different checks on the time-periodic pumping solutions found numerically. In figure 6.7, we plot $\Omega(\alpha_b, \lambda)$ for two orthogonal directions in the phase space of exactly periodic solutions, and compare it with (6.5.43). In each case, excellent agreement is found between the perturbative and the numerical result in the $\alpha_b, \lambda \ll 1$ regime.

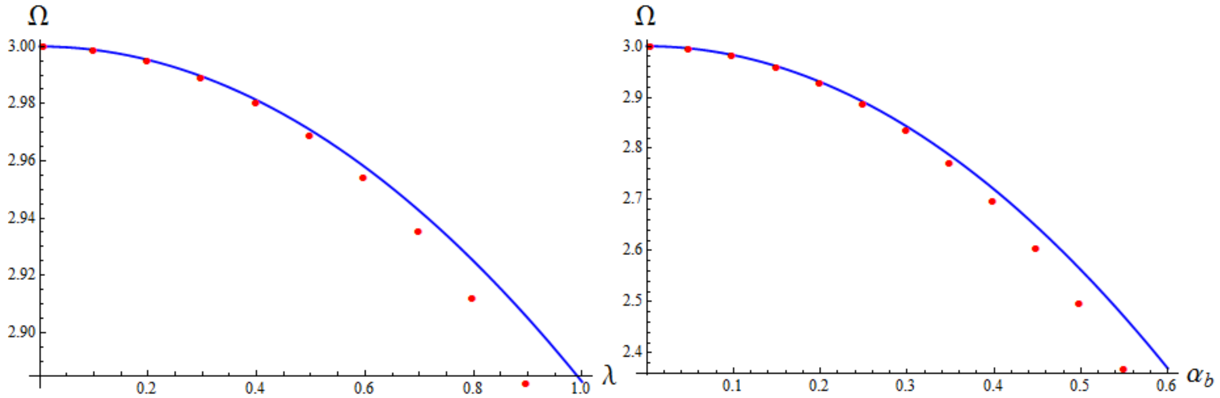

Figure 6.7: Left: $\Omega(0.0005, \lambda)$ as determined numerically (red dots) and perturbatively (blue line). Right: $\Omega(\alpha_b, 0.001)$ as determined numerically (red dots) and perturbatively (blue line).

As a further consistency check, we perform a simulation starting from the initial data $\Pi(t = 0, x) = \Pi_0(x)$ and $\Phi(t = 0, x) = 0$ as determined by the pseudospectral algorithm and study their subsequent time evolution. We provide one example in figure 6.8. It is observed that the time development of the initial data perfectly agrees with the output of the pseudospectral code, providing a highly nontrivial check of our numerical procedures.

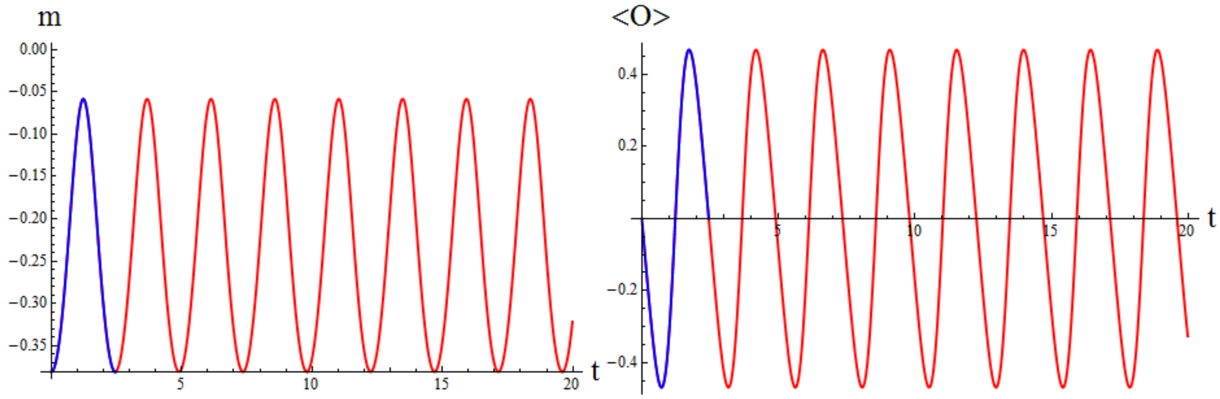

Figure 6.8: Energy density and vev for an exactly periodic pumping solution with $\alpha_b = 0.45$, $\lambda = -0.45$ as obtained from the pseudospectral generating code (blue) and the simulated time evolution of the initial data (red).

6.6 Quenching off the pumping solution

In this section, we will demonstrate that no boundary observer will measure a negative energy density when the scalar source $\phi_0(t)$ is time-independent. Let us perform the following numerical experiment. At $t = 0$, we start with a stable pumping solution and, suddenly, turn off the scalar source. Naively, one could think that a regular solution with negative energy density has been generated. However, this is not the case. We turn off the scalar source by means of a smooth interpolation of time span δ between the pumping boundary condition $\dot\phi_0(t = 0) = \alpha_b$ and a time-independent $\dot\phi_0(t \geq \delta) = 0$. One example can be found in figure 6.3. The remarkable result is that, for any interpolating function and any δ employed, the final geometry always displays a positive energy density at times $t \geq \delta$. In fact, in the $\delta \to \infty$ limit, the end result recovers the original AdS$_4$ vacuum with $m = 0$. More abrupt interpolations result in a time-dependent geometry with positive mass. Finally, in the $\delta \to 0$ limit, the energy density peaks so violently that a black hole forms right away.

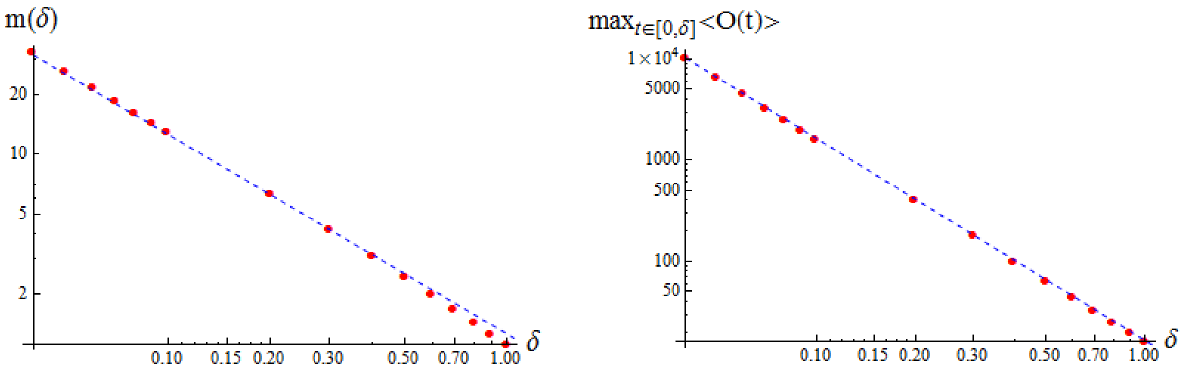

Figure 6.9: Left: log-log plot of $m(\delta)$ (red dots) and the fitting curve $m(\delta) \propto \delta^{-1}$ (blue dashed) for a quench off the $\alpha_0 = 1$ pumping solution with interpolating function (6.6.62). Right: log-log plot of $\max_{t\in[0,\delta]} \langle \mathcal{O}(t) \rangle$ (red dots) and the fitting curve $\max_{t\in[0,\delta]} \langle \mathcal{O}(t) \rangle \propto \delta^{-2}$ (blue dashed) for the same quench process as in the left figure.

Let us discus this last behavior in more detail. In figure 6.9, we plot $m(\delta)$ and $\max_{t\in[0,\delta]} \langle \mathcal{O}(t) \rangle$ for a quench off the $\alpha_0 = 1$ pumping solution with the interpolating function

$$\dot\phi_0(t) = \frac{1}{2}\alpha_b \left(1 + \tanh\left(\frac{\delta}{t} + \frac{\delta}{t-\delta}\right)\right), \quad t \in [0, \delta]. \tag{6.6.62}$$

For $\delta \lesssim 1$, both $m(\delta)$ and $\max_{t\in[0,\delta]} \langle \mathcal{O}(t) \rangle$ display a well defined scaling with respect to δ, $m(\delta) \propto \delta^{-1}$ and $\max_{t\in[0,\delta]} \langle \mathcal{O}(t) \rangle \propto \delta^{-2}$, confirming that both diverge in the $\delta \to 0$ limit.
A natural question is if the observed scaling is related to the fact that we are quenching off the pumping solution, or is rather determined by the particular form of the interpolating function (6.6.62). To answer this question, in figure 6.10 we plot $m(\delta)$ and $\max_{t\in[0,\delta]} \langle \mathcal{O}(t) \rangle$ for a quench with $\phi_0(t)$ given by the time-reversed version of (6.6.62) acting over the AdS$_4$ vacuum,

$$\dot\phi_0(t) = \frac{1}{2}\alpha_b \left(1 - \tanh\left(\frac{\delta}{t} + \frac{\delta}{t-\delta}\right)\right), \quad t \in [0, \delta]. \tag{6.6.63}$$

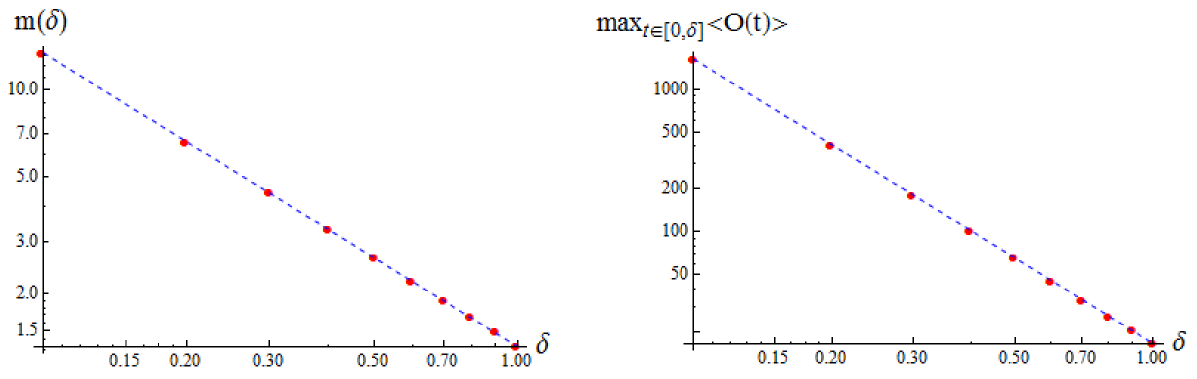

Figure 6.10: Left: log-log plot of $m(\delta)$ (red dots) and the fitting curve $m(\delta) \propto \delta^{-1}$ (blue dashed) for the quench profile (6.6.63) with α_b as in (6.6.62). Right: log-log plot of $\max_{t\in[0,\delta]} \langle \mathcal{O}(t) \rangle$ (red dots) and the fitting curve $\max_{t\in[0,\delta]} \langle \mathcal{O}(t) \rangle \propto \delta^{-2}$ (blue dashed) for the same quench process as in the left figure.

We observe that the former scaling relations $m(\delta) \propto \delta^{-1}$, $\max_{t\in[0,\delta]} \langle \mathcal{O}(t) \rangle \propto \delta^{-2}$ uphold, showing that the scaling is solely determined by the precise non-analytic behavior of the source in the $\delta \to 0$ limit; in this limit, both (6.6.62) and (6.6.63) correspond to quench profiles $\phi_0(t)$ that are continuous but non-differentiable. In particular, the scaling displayed by $m(\delta)$ and $\max_{t\in[0,\delta]} \langle \mathcal{O}(t) \rangle$ under (6.6.63) differs from the one that would be present if the *rhs* of (6.6.63) were applied directly to $\phi_0(t)$, rather than to $\dot{\phi}_0(t)$. In this case, in the $\delta \to 0$ limit the source shows a jump discontinuity, resulting in a $m(\delta) \propto \delta^{-3}$, $\max_{t\in[0,\delta]} \langle \mathcal{O}(t) \rangle \propto \delta^{-3}$ behavior, as expected on purely dimensional grounds [221]. We plot representative results of this behavior in figure 6.11.

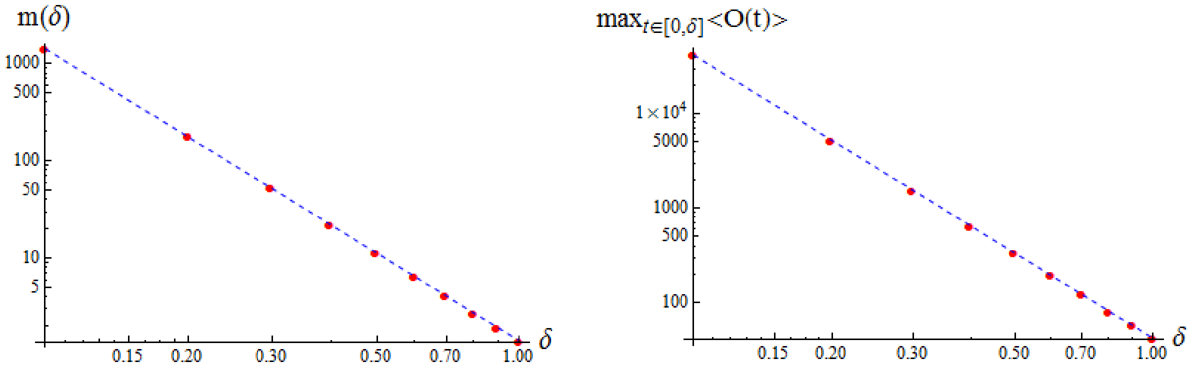

Figure 6.11: Left: log-log plot of $m(\delta)$ (red dots) and the fitting curve $m(\delta) \propto \delta^{-3}$ (blue dashed) for a quench profile given by the *rhs* of (6.6.63) applied to $\phi_0(t)$. Right: log-log plot of $\max_{t\in[0,\delta]} \langle \mathcal{O}(t) \rangle$ (red dots) and the fitting curve $\max_{t\in[0,\delta]} \langle \mathcal{O}(t) \rangle \propto \delta^{-3}$ (blue dashed) for the same quench process as in the left figure.

As a final observation, we would like to point out that the process of quenching on/quenching off a pumping solution we discussed embodies an irreversible character: the system displays an intrinsic hysteresis. Imagine slowly building up the value of $\dot{\phi}_0(t)$ from zero to a constant final value in a time span δ, staying there for a long time, and finally switching back $\dot{\phi}_0(t) \to 0$ using the same δ-smeared step function, but time-reversed. Even if both the equations of motion and the boundary conditions are time reversal invariant, the end result will always have $m(t=\infty) \geq m(t=0) = 0$, and only $m(t=\infty) = 0$ in the quasistatic limit $\delta \to \infty$ for both steps.

6.7 Pumping solution over AdS$_3$

In this section we shall investigate the three dimensional case. It turns out that the pumping solution over AdS$_3$ is related to a number of other solutions known in the literature via a series of mappings that includes double Wick rotations and/or Hodge dualities. This observation allows us to give an analytic expression for the pumping solution.

Let us consider a three-dimensional charged black brane with negative cosmological constant [156, 157]. The metric and the electromagnetic potential are given by

$$
\begin{aligned}
ds^2 &= -h(r)dt^2 + \frac{dr^2}{h(r)} + r^2 dx^2, && (6.7.64)\\
h(r) &= r^2 - M - Q_e^2 \log(r), && (6.7.65)\\
A(r) &= \left[\mu + Q_e \log(r)\right] dt. && (6.7.66)
\end{aligned}
$$

In the expressions above, $r \in [0, \infty)$ and $t, x \in \mathbb{R}$. M and Q_e determine respectively the mass and the electric charge of the black brane geometry. From now on, we focus on the one-parameter family of charged black branes with $M = 1$ and $\mu = 0$. Note that the outer horizon is located at $r = r_h = 1$ for $Q_e < \sqrt{2}$. The temperature is

$$
T = \frac{1}{2\pi}\left(1 - \frac{1}{2}Q_e^2\right). \qquad (6.7.67)
$$

At $Q_e = \sqrt{2}$ the black brane is extremal. For $Q_e > \sqrt{2}$, the hypersurface $r = 1$ actually corresponds to the inner horizon, and (6.7.67) does not represent the real temperature of the back brane. By performing the coordinate change $r^2 = 1 + R^2$, the exterior region of the charged black brane can be parametrized as

$$
\begin{aligned}
ds^2 &= -h(R)dt^2 + \frac{R^2}{(1+R^2)h(R)}dr^2 + (1+R^2)dx^2, && (6.7.68)\\
h(R) &= R^2 - \frac{1}{2}Q_e^2 \log(1+R^2), && (6.7.69)\\
A &= \frac{1}{2}Q_e \log(1+R^2)dt. && (6.7.70)
\end{aligned}
$$

with $R \in [0, \infty)$. Now, let us perform the double Wick rotation defined by

$$
t \to i\varphi, \quad x \to it, \quad Q_e \to -iQ_m, \qquad (6.7.71)
$$

in a such a way that the geometry and electromagnetic potential of the exterior region are mapped to the following solution of three-dimensional Einstein-Maxwell theory with a negative cosmological constant

$$\begin{aligned} ds^2 &= -(1+R^2)dt^2 + \frac{R^2}{(1+R^2)h(R)}dR^2 + h(R)d\varphi^2, && (6.7.72)\\ h(R) &= R^2 + \frac{1}{2}Q_m^2 \log(1+R^2), && (6.7.73)\\ A &= \frac{1}{2}Q_m \log(1+R^2)d\varphi. && (6.7.74) \end{aligned}$$

This is a horizonless geometry. It can be explicitly shown that the coordinate φ must be identified with period $\beta = 2\pi/(1+Q_m^2/2)$ in order to avoid a conical singularity at $R=0$. On the other hand, this period is nothing but the analytic continuation of the inverse temperature of the original charged black brane under the double Wick rotation. The geometry (6.7.72), (6.7.73) is supported by the radial magnetic field associated to (6.7.74), and we will refer to it as the *magnetic* AdS_3 solution.[9]

We want to map the magnetic solution to the pumping solution. To this purpose we will rely on Hodge duality. However we have still to massage the magnetic solution: let us rescale our coordinates as $t = \beta/(2\pi)\tilde{t}$, $R = 2\pi/\beta\tilde{R}$ and $\varphi = \beta/(2\pi)\tilde{\varphi}$, in such a way that $\tilde{\varphi} \sim \tilde{\varphi} + 2\pi$.[10] In this new coordinate system,[11] we have that

$$\begin{aligned} ds^2 &= -\left[\left(\frac{\beta}{2\pi}\right)^2 + R^2\right]dt^2 + \frac{R^2}{\left[\left(\frac{\beta}{2\pi}\right)^2 + R^2\right]h(R)}dR^2 + h(R)d\varphi^2, && (6.7.75)\\ h(R) &= R^2 + \frac{1}{2}\tilde{Q}_m^2 \log\left[\left(\frac{\beta}{2\pi}\right)^2 + R^2\right] + \tilde{\mu}\tilde{Q}_m, && (6.7.76)\\ A &= \left\{\tilde{\mu} + \frac{1}{2}\tilde{Q}_m \log\left[\left(\frac{\beta}{2\pi}\right)^2 + R^2\right]\right\}d\varphi, && (6.7.77) \end{aligned}$$

where we have defined

$$\tilde{Q}_m \equiv \frac{\beta}{2\pi}Q_m = \frac{Q_m}{1+\frac{1}{2}Q_m^2} \qquad , \qquad \tilde{\mu} \equiv \tilde{Q}_m \log\frac{2\pi}{\beta}\ . \qquad (6.7.78)$$

The field strength corresponding to the magnetic solution is

$$F = \tilde{Q}_m \frac{R}{\left(\frac{\beta}{2\pi}\right)^2 + R^2}\ dR \wedge d\varphi. \qquad (6.7.79)$$

---

[9] This background was originally found in references [222, 223, 224]. In [224], the authors introduced the double Wick rotation we discussed here. See [225, 226] for the construction of the general magnetic solution with angular momentum, the computation of its conserved charges and a proposed physical interpretation. The physical nature of the magnetic solution was further elucidated in [227].

[10] The rescaling of the t and R coordinates follows from the requirement that $\lim_{\tilde{R}\to\infty} \tilde{R}^{-2}ds^2 = -d\tilde{t}^2 + d\tilde{\varphi}^2$. This corresponds to the standard flat space metric as the representative of the conformal structure of the boundary where we have chosen $\Omega(\tilde{R}) = \tilde{R}^{-2}$ as conformal factor. Note also that this is the same procedure we would have employed were we on the vacuum state.

[11] We drop the tildes from now on.

Under Hodge duality, the magnetic AdS$_3$ solution can be put into correspondence with the three-dimensional pumping solution. Recall that the vacuum Maxwell equations are $dF = d(\star F) = 0$, where $\star$ is the Hodge operator. In three dimensions, the Hodge dual of a two-form corresponds to a one-form. Hence F can be alternatively expressed as $F = \star d\phi$, where ϕ is a massless scalar field. The Bianchi identity $dF = 0$ transforms into the scalar field equation of motion, $-\star\, d(\star d\phi) = \nabla^2\phi = 0$, while the dynamical Maxwell equation reduces to the trivial statement $d^2\phi = 0$. The map leaves the metric invariant and, as a consequence, a metric supported by a given electromagnetic field can be thought of as being sourced by the dual scalar field defined by this procedure.

Let us consider explicitly how the Hodge duality works at the level of the solution. Take the three-dimensional pumping solution with $\phi(t, r) = \alpha t$. Under Hodge duality, we find that the scalar field profile maps to

$$F = \alpha \frac{r e^{\delta(r)}}{f(r)} dr \wedge d\varphi, \tag{6.7.80}$$

where we have parametrized the pumping solution geometry in standard Schwarzschild coordinates,

$$ds^2 = -f(r) e^{-2\delta(r)} dt^2 + \frac{dr^2}{f(r)} + r^2 d\varphi^2. \tag{6.7.81}$$

Note that the radial coordinates of the magnetic AdS$_3$ solution and the pumping solution are related by

$$r^2 = h(R), \tag{6.7.82}$$

as it emerges from comparing the $\varphi\varphi$-component of the metric (6.7.72) and (6.7.81). From a comparison of the radial components of (6.7.72) and (6.7.81), we have that r and R must also satisfy

$$\frac{dr^2}{f(r)} = \frac{R^2 dR^2}{\left[\left(\frac{\beta}{2\pi}\right)^2 + R^2\right] h(R)}. \tag{6.7.83}$$

Deriving (6.7.82) and substituting into the expression above, we obtain the relation

$$f(r(R)) = \left[\left(\frac{\beta}{2\pi}\right)^2 + R^2\right]\left(1 + \frac{1}{2}\frac{\tilde{Q}_m^2}{\left(\frac{\beta}{2\pi}\right)^2 + R^2}\right)^2, \tag{6.7.84}$$

where the explicit form of $h(R)$ provided by equation (6.7.76) has been employed. Note that, when $R = 0$, (6.7.76) implies that $r = h(0) = 0$. As a consequence, from (6.7.84) and the definitions of β and $\tilde{Q}_m$, it follows that $f(0) = 1$, a fact that shows the absence of a conical singularity at the origin in a manifest way. By identifying now the tt-components of the metrics (6.7.72) and (6.7.81), we get that

$$\left(\frac{\beta}{2\pi}\right)^2 + R^2 = f(r) e^{-2\delta(r)}. \tag{6.7.85}$$

Employing equation (6.7.84), we finally obtain

$$\delta(r(R)) = \log\left(1 + \frac{1}{2}\frac{\tilde{Q}_m^2}{\left(\frac{\beta}{2\pi}\right)^2 + R^2}\right). \tag{6.7.86}$$

Notice that $\delta(\infty)=0$, which means that the parametrization of the magnetic solution corresponds to the boundary time gauge (see section 6.3).

With the help of equations (6.7.82), (6.7.84) and (6.7.86) we can express the field strength dual (in the Hodge sense) to the pumping solution in R coordinates, namely

$$F=\alpha\frac{R}{\left(\frac{\beta}{2\pi}\right)^2+R^2}\,dR\wedge d\varphi. \tag{6.7.87}$$

Comparing (6.7.87) with (6.7.79) we find that the pumping solution corresponds to a magnetic solution such that

$$\alpha=\tilde{Q}_m=\frac{Q_m}{1+\frac{1}{2}Q_m^2}, \tag{6.7.88}$$

or, alternatively,

$$Q_m=\frac{1\pm\sqrt{1-2\alpha^2}}{\alpha}. \tag{6.7.89}$$

From (6.7.89), we have that the reality of Q_m implies that α is restricted to the domain $\alpha\in\left[0,\frac{1}{\sqrt{2}}\right]$. Furthermore, a given α has two associated Q_m parameters, $Q_\pm$, in a self-explaining notation. The Q_+ branch is restricted to the domain $Q_+\in[\sqrt{2},\infty)$, with limits respectively attained at $\alpha=1/\sqrt{2}$, $\alpha=0$. The Q_- branch satisfies $Q_-\in[0,\sqrt{2}]$, and its limits correspond to $\alpha=0,\alpha=1/\sqrt{2}$. We observe that both branches merge at the critical value $\alpha^*\equiv 1/\sqrt{2}$.

The two-branch structure of (6.7.89) is particularly interesting. Indeed, as we will show in the next subsection through an explicit computation, the Q_- branch of magnetic solutions corresponds to the branch of linearly stable pumping solutions, while the Q_+ branch maps onto the linearly unstable branch (see section 6.4). Remembering how the magnetic solution has been obtained performing the double Wick rotation (6.7.71) on the three-dimensional charged black brane solution (6.7.64), (6.7.65), (6.7.66), we bring into attention that $|Q_e|=|Q_m|$. Therefore, for $Q_m=Q_+\geq\sqrt{2}$, the linear instability of this branch of pumping solutions seems to be related to the fact that our original $r^2=1+R^2$ expansion is performed with respect to the wrong horizon (see comments below (6.7.67)). In the next subsection we also show that α^*, *i.e.* the critical value where the two branches of (6.7.89) merge, corresponds to $\alpha_{\max}$.[12] This is an important and exact result emerging directly from the chain of mappings illustrated above.[13]

The different maps we have uncovered so far are not the end of the story. Another interesting geometry can be brought into the game. In [228], Andrade and Withers (AW) introduced a beautifully simple holographic model of momentum relaxation. It involved charged black branes with nontrivial axion profiles along the spacelike boundary directions,

---

[12] We remind the reader that $\alpha_{\max}$ is the maximum value of α_b for which pumping solutions exist, see section 6.3.

[13] It would be interesting to repeat the argument in higher dimensionality and get an exact value for the adiabatic threshold $\alpha_{\max}$ starting from an extremal charged AdS black hole in 3+1 dimensions.

that broke translational invariance at the level of the solution as a whole, but keeping the metric and the electromagnetic field translationally invariant. In three dimensions, the corresponding AW solution would involve a neutral massless scalar field $\phi(x) = \gamma x$. Focusing on the uncharged case, the metric of the AW solution would be given by

$$ds^2 = -f(r)dt^2 + f(r)^{-1}dr^2 + r^2dx^2, \tag{6.7.90}$$

$$f(r) = r^2 - M - \gamma^2 \log(r), \tag{6.7.91}$$

$$\phi(x) = \gamma x \ . \tag{6.7.92}$$

By Hodge duality, the scalar field is associated with the field strength

$$F = \star d\phi = \gamma \star dx = \frac{\gamma}{r} dt \wedge dr, \tag{6.7.93}$$

that comes from the potential $A = -\gamma \log(r)dt$. If we identify $|\gamma| = |Q_e|$, we find that the charged black brane and the neutral three-dimensional AW solution are dual to each other. Of course, we must take $M = 1$ after the duality map to land on the one-parameter family of charged black branes (6.7.64), (6.7.65) and (6.7.66). It is also possible to show that, by performing again the coordinate change $r^2 = 1+R^2$, double Wick rotating as $x \to it, t \to i\varphi$, $\gamma \to -i\gamma$ and rescaling our coordinates, the pumping solution is obtained.

Let us summarize the structure of duality mappings through the following diagram,[14]

$$\begin{tikzcd}
\text{charged black brane} \arrow[r, "DW"] \arrow[d, "\star"'] & \text{magnetic AdS}_3 \arrow[d, "\star"] \\
\text{Andrade-Withers} \arrow[r, "DW"] & \text{pumping solution}
\end{tikzcd}$$

where DW stands for the double Wick rotation.

6.7.1 Analytic pumping solution in AdS$_3$

As promised, we can employ the relation (6.7.82) to obtain an analytic expression for the three-dimensional pumping solution. Let us set $R = R(r)$, identify $\tilde{Q}_m = \alpha$ and recall that $\beta(\alpha) = 2\pi/(1+Q_\pm^2/2) = \pi(1 \mp \sqrt{1-2\alpha^2})$. It turns out that (6.7.82) can be explicitly solved, yielding

$$R(r)^2 = -\frac{\beta(\alpha)^2}{4\pi^2} + \frac{1}{2}\alpha^2 W\left(\frac{\beta(\alpha)^2}{2\pi^2\alpha^2} e^{\frac{2r^2}{\alpha^2} + \frac{\beta(\alpha^2)}{2\pi^2\alpha^2}}\right), \tag{6.7.94}$$

where W is the Lambert W-function, which solves the transcendental equation $W(x)e^{W(x)} = x$. We consistently find that $R(r)^2 \geq 0$, with equality only at $r = 0$, a fact that is guaranteed by $W(xe^x) = x$. By taking (6.7.94) and substituting it in (6.7.84),(6.7.86), we obtain the three-dimensional pumping solution in a closed form. It can be straightforwardly checked that the resulting expressions for $f(r)$ and $\delta(r)$ solve the equations of motion of the pumping solution in Schwarzschild coordinates. Alternatively, if we take the relations (6.7.84),(6.7.86)

---

[14] We emphasize that the duality map between the electrically charged black hole and the magnetic solution has already been discussed in [224].

and introduce them into the equations of motion for the pumping solution with $R = R(r)$ unknown, we arrive to the equation

$$R'(r) - \frac{r(\beta(\alpha)^2 + 4\pi^2 R(r)^2)}{R(r)(2\pi\alpha^2 + \beta(\alpha)^2 + 4\pi^2 R(r)^2)} = 0, \tag{6.7.95}$$

for which (6.7.94) is the only solution such that $R(r=0) = 0$.

As a final consistency check, let us note that equation (6.7.86) implies that

$$\delta(0) = \log\left(1 + \frac{1}{2}Q_\pm^2\right) = \log\left(\frac{1 \pm \sqrt{1-2\alpha^2}}{\alpha^2}\right). \tag{6.7.96}$$

In figure 6.12, we plot $\delta(0)$ against α,[15] as obtained from the numerical solution of the equations of motion, and compare it with the expression (6.7.96). We plot both the stable and the unstable branches. The agreement is perfect. For example, the numerically determined maximum of $\delta(0)$ for the stable branch is located at $\alpha = 0.7071067$, where $\delta(0) = 0.693148$. The expected results are $\alpha = 1/\sqrt{2} = 0.7071068$ and $\delta(0) = \log(2) = 0.693147$.

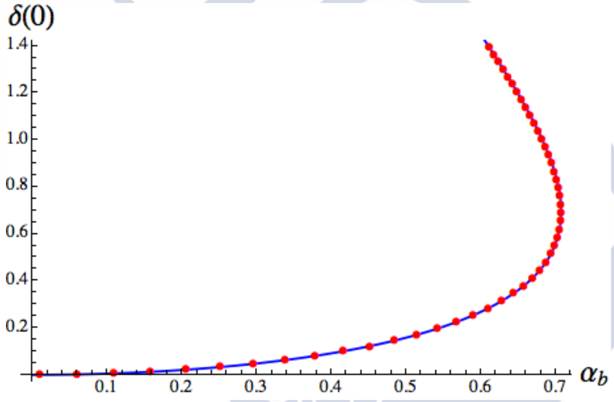

Figure 6.12: $\delta(0)$ vs α, numerical (red dots) and analytical (blue curve).

---

[15] Recall that $\alpha = \alpha_b$, since the map between the magnetic and the pumping solutions has been obtained in the boundary time gauge.

Chapter 7

Conclusions and future prospects

The question of how macroscopic, isolated quantum systems driven out-of-equilibrum thermalize has been under intense survey in recent years. A vast ammount of works have focused on this question, by employing tools that range from integrability to numerical simulations. Recently, it has become feasable to address it also from the experimental point of view. A major lesson of this research is that the landscape of possible routes to final equilibration is surprisingly rich.

On the other hand, Holography has provided a stunning way to look at the same problem in strongly-coupled systems, by studying the dual counterpart as being gravitational collapse in asymptotically global AdS spacetimes. In recent years, we have similarly learned that there is an equally rich landscape of possible routes to final black hole formation, depending upon the underlying dynamics and the initial conditions.

Therefore, the natural program that arises is trying to establish solid conections between these two landscapes, as an extension of the holographic dictionary in the out-of-equilibrium regime. It is the hope of this author that the work presented in this thesis has contributed to this aim, at least infinitesimally. The essential philosophy has been to unravel robust features that can be clearly identified from both sides.

In the planar case, the research in real-time Holography is a mature subject, that has already delivered poweful lessons. They range from the discoverement of the almost-perfect fluid nature of holographic matter at thermal equilibrium to its fast hydrodynamization. These results have made contact with real-world phenomena and have sparked deep developments in other areas of Physics. Real-time holography has also been instrumental in the study of entanglement propagation in time-dependent processes and has allowed to conjecture new bounds on its speed, in certain regimes.

Compared to this state of affairs, the research about holographic thermalization in the global case its still at its infancy, but also in rapid development and intense scrutiny. We have clearly established in this work that the presence of finite-size effects naturally allows for new phenomena, such as delayed thermalization processes, in which an ergodic stage is not reached right away, full-fledged collapses and revivals of the system state, possibly new late-time forms of relaxation for non-conserved quantities, or rich dynamics at adiabaticity. Smoking guns like the ones already obtained in the planar case are still needed to establish if the study of this new field is more than a theoretical curiosity.

This author would like to close the main part of this manuscript by commenting on the different research directions that unfold immediately from the results presented in it.[1]

- **The stability band**

  As we have argued several times, a common feature of holographic QFTs whose black hole spectrum is separated from the vacuum by a mass gap is the existence of a stability band. This stability band consists of a region where kinematically allowed processes of black hole formation are dynamically forbidden, at least during the times accessed on the different numerical experiments that have been performed. At present, there is evidence of its existence in the hard wall model [161], the AdS-soliton [162], five-dimensional Einstein-Gauss-Bonnet gravity [229, 194], and AdS$_3$ gravity ([160] and the work presented here in chapter 3). The stability band lies at the transition between fast thermalization, represented by prompt black hole formation, and a regime where the gravitational system cannot undergo gravitational collapse to a black hole on kinematic grounds.[2] Just above the stability band, the thermalization time is generically non-monotonic.

  Several question arise. The most obvious one is if the stability band is indeed a region where thermalization is halted or, on the other hand, the system collapses, but at so late times that this collapse has never been observed experimentally. Simulating reliably and efficiently the evolution of the system up to such long times will require the development of improved numerical algorithms: as we have exemplified in chapter 3, the very existence of this region stems from the fact that the initial data break into one or more extremely sharp subpulses. Resolving them with the appropriate accuracy calls for a local mesh refinement technique, that surpasses the global one we have employed in this work.

  Once these techniques are developed, we could perform a detailed scan of the thermalization time in terms of the mass above the gap, so as to find out if this magnitude displays a self-similar structure at some intervals in the transition region between fast and frustrated thermalization (preliminar evidence in favor of this was provided in [194] for the case of Einstein-Gauss-Bonnet gravity in five dimensions). It is particularly interesting to disentangle how kinematic (the existence of the gap, the dimension of the spacetime) and dynamic effects (the precise form of the action) interact with each other to determine the properties of this region.

  We close this item by stressing two facts. The first one is that, since the geometries falling within this transition region present suprisingly sharp features, perhaps a thin shell analysis along the lines of [230, 201] could shed light on the questions raised above. The second fact is that there exists yet another theory where the stability band phenomenon can be looked for. Reference [231] analyzed in detail which $D-$dimensional Lovelock theories allow for a single AdS$_D$ vacuum. It was found that, in D dimensions,

---

[1] The discussion is not going to include other interesting directions related to them in a more indirect way.

[2] Although it may equilibrate in finite time to other static solution in some cases, see [194].

there exist $\left\lfloor \frac{D-1}{2} \right\rfloor$ of such theories, that can be indexed by the highest power of the curvature in the Lovelock action, k. The case $k = 1$ corresponds thus to Einstein-Hilbert gravity in any dimensionality. For odd D, the $k = \left\lfloor \frac{D-1}{2} \right\rfloor$ theory is actually a Chern-Simons theory, *i.e.*, the Lovelock Lagrangian is given by the Chern-Simons form of the AdS group. The cases with $D = 3$ and $D = 5$ correspond respectively to three-dimensional Einstein gravity and five-dimensional Einstein-Gauss-Bonnet gravity. In any odd D, these Chern-Simons theories share the property of having a mass gap in their black hole spectrum, which ends on a critical black hole with vanishing entropy and zero temperature. Furthermore, above the gap black holes always have positive specific heat. To this author's knowledge, a numerical study of gravitational collapse in the $D = 7$ Chern-Simmons theory has never been performed.

- **Long-lived oscillations?**

  In chapter 5, we provided premilinar evidence of long-lived oscillations in the late-time relaxation of the scalar vev. Establishing their existence on firm grounds is a mandatory and pressing direction of future research. As an immediate step, we must scan the phase space of the system by performing additional high-resolution numerical experiments that help to elucidate how accurate this phenomenon is. In this regard, the development of new numerical methods able to manage efficiently the problem is mandatory. We should consider the possibility of implementing local, instead of global, mesh refinement algorithms or evaluate if it is convenient to describe the collapse process in a horizon-penetrating coordinate system.

  Apart from that, and as we already suggested in chapter 5, we should try to understand these long-lived oscillations in terms of the quasinormal modes of the final black hole, so as to find out if the slow relaxation we observe is in part due to a quasinormal frequency pair of very small imaginary part. This can be achieved by adapting the techniques we employed to compute soliton normal modes. Further light on this issue can be shed by performing a real-time analysis of a linearized scalar fluctuation over the static hairy solution, as was done in [232] for the case of Kerr-AdS black holes. This would require the use of infalling coordinates. Of course, this procedure can be carried out also for nonlinear perturbations (see for instance [233] for a study of the superradiant instability of Reissner-Nordström black holes along these lines).

  Finally, if our results prove to be robust, we can try to look for long-lived oscillations in other holographic superfluids with extra length scales, apart from the temperature and the chemical potential. It is worth mentioning that this kind of relaxation dynamics has already been reported in the context of five-dimensional charged magnetic black brane solutions to Einstein-Maxwell-Chern-Simons theory [234].

- **Holographic quenches with global asymptotics**

  The numerical techniques we have developed to obtain the results presented in chapter 6 promise to be fruitful in the near future. A immediate direction sprouts from the observation that the Einstein-scalar theory we have analyzed is a special example of a wider class. Indeed one could consider complex, instead of real, massless bulk scalar fields. These still correspond to marginal deformations, with many intriguing features such as cousins of the pumping solution with a nontrivial radial scalar profile and a natural connection to periodically-driven systems. They also provide an intermediate step to study relevant deformations in a similar setup.

It is mandatory to employ the numerical control we have achieved over this kind of processes to determine how entanglement entropy is generated during the quench. Finally, it is also worth realizing that the numerical techniques we have developed can be employed to compute retarded correlators in generic time-dependent geometries, following a proposal that was recently put forward in [235].

Chapter 8

Summary

Thermalization, strongly-coupled matter and String Theory

Consider an isolated macroscopic system in equilibrium. The Second Law guarantees that, for the given extensive variables characterizing the system -such as total energy E, volume V, total electric charge Q...- the equilbrium state maximizes the entropy S. Understanding how a perturbed macroscopic system attains the final equilibrium state predicted by Thermodynamics is the problem of *thermalization*. The nontrivial nature of this problem is made manifest when we observe that physical evolution laws, both in the classical and in the quantum realm, are *unitary*. Given some initial state, no information it contains is lost during time evolution: the microscopical dynamics of the system are time-reversal invariant. Threfore, where does the time-asymmetry implied by the Second Law come from?

Irreversibility can only come from *coarse-graining*: certain information pertaining the exact description of the system must be kept away from the macroscopic observer. For a non-isolated system, this information loss is certainly expected, since the effective description of the system neglects the environmental degrees of freedom. However, for an isolated system, the situation is richer: the own microscopic dynamics of the system is to be held responsible for the apparent information loss.

A nice example of this last observation can be found in classical statistical mechanics. For an isolated system with energy E, confined in a volume V, the familiar thermodynamic description of the equilibrium state can be obtained straightforwardly by assuming the principle of equal a priori probabilities. This principle poses that any microscopic state with energy E is equally realizable by the macroscopic system. Secretly, it is a dynamical assumption: in phase space, the microscopic time evolution equations must be such that, on the long run, the time t the system spends in a region ω of the constant-energy manifold $\Omega(E)$ is proportional to the volume of this region, $t \propto \mathrm{Vol}(\omega)$. Said otherwise, the microscopic dynamics must be such that the time average of a given observable agrees with the microcanonical average: it must be *ergodic*.

With the advent of classical chaos, the ergodic hypothesis gained a firm ground. Consider a chaotic system that is, at $t = 0$, in a phase space region $\alpha(E; 0) \subset \Omega(E)$ such that $\mathrm{Vol}(\alpha(E; 0)) \ll \mathrm{Vol}(\Omega(E))$. The trajectories associated to two initial states in $\alpha(E; 0)$ flow appart exponentially as time passes. On the other hand, the Liouville theorem guarantees that the phase space volume occupied by the system remains invariant, $\mathrm{Vol}(\alpha(E; 0)) = \mathrm{Vol}(\alpha(E; t))$. As a consequence, on the long run, $\alpha(E; t)$ is a region with fractal-like structure that, when viewed with finite resolution, reduces to $\Omega(E)$. For a system with this mixing behavior, ergodicity follows.

This qualitative picture cannot be fundamental, for one reason: Nature is essentially quantum-mechanical and, in quantum physics, time-evolution is not only unitary, but also *linear*. If we cannot rely on chaotic behavior, how is even thermalization going to be achieved?

Providing a definitive answer to this question has been in the theoretical physicist to-do list since the advent of quantum mechanics in the first half of the 20th century. However, and rather surprisingly, it was not until recently that this question gained widespread attention. These efforts culminated in the so called *Eigenstate Thermalization Hypothesis* (ETH), which we will introduce latter. The ETH is believed to be the fundamental mechanism behind thermalization in the quantum realm. Understanding its regime of validity, and the possible exceptions to it, has reveled a great deal of valuable information about the out-of-equilibrium physics of isolated quantum systems.

The fundamental reason behind this delay is that not until modern times isolated quantum systems of physical interest were accessible by experiment. Nowadays, optical lattices can be efficiently employed to manipulate cold atom sytems in the laboratory, while keeping them in a very good degree of isolation. Different perturbations can be introduced and the possible routes to thermal equilibrium, or its absence, can be monitored. Away from non-relativistic many-body physics, great attention has been also paid to the question of how relativistic QFTs thermalize. One paradignamtic example is provided by inflation and the subsequent re-heating. The other one, which is currently under intense experimental survey, is the quark-gluon plasma (QGP). Advances in accelerator technology have made possible to collide heavy ions so as to overcome confinement and recreate this novel phase of matter, that permeated the Universe shortly after inflation. Quantifying the dynamics of the QGP formation, relaxation and final dissipation into the hadron shower experimentally detected forces us to deepen into our understanding of QFTs out-of-equilibrium.

In parallel with these developments, novel phases of fermionic matter have been found in the condensed matter realm; most famously, high-T_c superconductors. These phases defy the standard description in terms of weakly-coupled quasiparticles: they are apparently strongly-coupled systems, where these entities cannot even be defined. In fact, the QGP itself is believed to be a strongly-coupled liquid above/but close to the deconfinement transition, which is the relevant energy regime for the experiments carried on at RHIC and LHC.

If so, we face a problem. Standard perturbative QCD techniques are certainly not valid at strong-coupling: a collective medium in this regime is not ammenable to a kinetic description. Furthermore, even if Lattice QCD allows one to perform explicit computations at any coupling, the sign problem prevents any attempt to study real-time processes, since numerical control demands working with the Euclidean version of the theory. The finite resolution unavoidable in any numerical approximation implies that the analitycal continuation of Lattice QCD answers to real-time is an ill-defined procedure. Not even transport coefficients in linear response theory can be efficiently accessed, even though they are of the uttermost importance in order to characterize the time-evolution of the QGP when it enters into the hydrodynamical regime.

Far from being specific to the QGP, these caveats apply to the first-principles study of any dynamical process in a strongly-coupled phase of matter with no quasiparticles. We soon realize that the standard field theorist arsenal has no weapon that can take down this problem. This would be a sad endpoint, if it were not for one of the most remarkable triumphs of the human endeavor: string/M-theory.

Originally proposed as a theory of the strong interaction in the sixties, string theory was soon after recognized as a viable theory of quantum gravity (QG), at the same time that is was being surpassed by QCD in its original goal. Latter research, culminating in the First Superstring Revolution in the eighties, showed that string theory included the necessay ingredients to generate four-dimensional, anomaly free non-abelian gauge theories with the right properties to describe Nature and, furthermore, consistently coupled to gravity. The nineties witnessed the discoverement of new objects of extended nature, called D-branes. At the same time, it was discovered that the five different string theories known from the First Superstring Revolution where secretly related by a web of non-perturbative dualities. This observation sparked the Second Superstring Revolution, that changed completely the previous perspective on the theory. Rather than being independent, the different superstring theories were different perturbative limits of a fundamental theory, whose final nature is still waiting to reveal herself in its full splendor: M-theory.

It is in this context where the holographic duality first appears. Introduced by Maldacena in 1997 by carefully examining a system of D-branes, the holographic duality postulates that certain non-abelian gauge theories, without gravity, are secretly string theories living in a higher-dimensional spacetime. From a rethorical perspective, the higher-dimensional string theory is a hologram, encoded by the lower-dimensional QFT. The strongly-coupled and large-N regime of these holographic QFTs is shown to be equivalent to the classical, pointlike limit of their string theory counterparts. As these strings theories are consistent theories of QG, this limit is nothing but General Relativity in a higher-dimensional spacetime. More concretely, the QFT has an ultraviolet fixed point: it is a conformal field theory (CFT) at high energies. In accordance with this fact, the spacetime in which its dual gravitational theory lives is asymptotically anti-de Sitter (AdS). In this way, the duality usually goes under the name of AdS/CFT correspondence. Asymptotically AdS spacetimes are endowed with a timelike boundary at infinity, and the dual CFT can be pictured as living on it.

In the light of the discussion above, we realize that AdS/CFT is a first-principles tool to study out-of-equilibrium processes at strong-coupling, at least in certain QFTs. We just have to map the QFT setup we are interested in into a classical gravitational construction. In this way, considering a strongly-coupled QFT at thermal equilibrium involves putting a stationary black hole in the gravity theory. Wonderfully, classical black hole thermodynamics is mapped to the standard thermodynamical description of a QFT plasma. Moreover, black hole perturbations encode both the linear and the hydrodynamical response of this plasma.

Transport coefficients can be easily computed, and the limits of validity of the hydrodynamic expansion can be addressed. Most famously, it was found that the shear-viscosity to entropy-density ratio of these holograhic plasmas was lower than the one present in any system ever observed in the laboratory. More remarkably, compatible with the value experimentally measured for the QGP at RHIC.

This observation bolstered a rapidly developing line of research, that tries to understand the fully out-of-equilibrium regime of the QGP by employing holographic QFTs as toy models. Starting from some excited state, the formation of an equilibrated plasma in the holographic QFT is nothing but a process of black hole formation in familiar General Relativity. Our originally intractable problem is thus reduced to solving a coupled system of non-linear PDEs, a task that can be undertaken by standard numerical techniques. This corner of the AdS/CFT landscape goes under the name of Numerical Holography. Far from being restricted to an effective modeling of the QGP, Numerical Holography has proven to be useful in a wide variety of different physical setups. These include, for instance, quantum turbulence or quantum quenches in strongy-coupled systems.

This thesis focuses on the study of this last kind of process in the case where the holographic QFT lives on a finite-sized space. The interplay of finite size effects with the strong-coupling limit of a quantum theory out-of-equilibrium leads to a rich landscape of possible routes to thermalization, or even to its absence thereof. Charting and, more importantly, understanding these routes is a challenging endeavor, both from the theoretical and from the purely computational perspective.

The entanglement entropy

The partition functions and the Hlbert spaces of the CFT and the gravitational theory are identified by the duality. This identification provides a way of accessing the partition function of the strongly-coupled CFT in terms of the partition function of the classical gravitational theory, allowing for an explicit computation of n-point correlation functions or entanglement entropies in the CFT.

Consider a quantum system described by some Hilbert space $\mathcal{H}$, that we factorize in two subsystems, A e $\bar{A}$, as $\mathcal{H} = \mathcal{H}_A \otimes \mathcal{H}_{\bar{A}}$. The *entanglement entropy* of A, S_A, is defined as the von Neumann entropy of the reduced density matrix of the subsystem,

$$S_A = -\mathrm{tr}(\rho_A \log \rho_A),$$

and provides a measure of the ammount of correlation between A and $\bar{A}$. In QFT, the subsystem A typically corresponds to a spacelike region in a Cauchy surface.

In the case of a holographic CFT, this region lives in the boundary of an asymptotically AdS spacetime. Let us consider a spacelike codimension-two hypersurface σ_A which, departing from the boundary of A, penetrates inside this spacetime. From the set of hypersurfaces σ_A of this kind, take the one that minimizes its area, γ_A. The entanglement entropy of A is given by the area of this extremal hypersurface from a relation analogous to the Bekenstein-Hawking formula computing the entropy of a black hole

$$S_A = \frac{1}{4G}\text{Area}(\gamma_A).$$

This formula is known as the holographic prescription for the entanglement entropy, or HEE prescription for short [63, 64, 65]. The HEE prescription also applies in the case where the CFT state, and as a consequence the dual geometry, are time dependent. Therefore, it allows accessing the dyamical evolution of the entanglement entropy in a thermalization process.

Thus, the entanglement entropy is an quantity extremely useful to characterize how an out-of-equilibrium system relaxes. The main problem it presents is that its computation cannot be carryed out in a generic situation. The existence of the HEE prescription shows that holoraphic CFTs are an exception to this observation. However, they are not the only one. The entanglement entropy can be also computed explicitly in $1+1$-dimensional CFTs, with the help of the so-called replica trick. Calabrese and Cardy were the first to employ this method to obtain the entanglement entropy of a one-dimensional system that had been taken out of equilibrium by a quantum quech.

Quantum quenches

Let us consider a Hamiltonian H_0 that depends on an external parameter λ_0, and image that the system is in the groundstate. A quantum quench consists on the sudden change $\lambda_0 \to \lambda_1 = \lambda_0 + \delta\lambda$. With respect to the new Hamiltonian H_1, the original groundstate of H_0 is a highly excited state. Its subsequent time evolution with respect to H_1 must lead in a natural way to the final thermalization of the system.

Calabrese and Cardy were the first to compute the entanglement entropy evolution in a process of this type [22]. They started with the groundstate of a $1+1$-dimensional theory with a mass gap, that lived on an infinite line. By erasing suddenly the mass gap, this groundstate becomes a highly excited state in a conformal theory. Calabrese and Cardy observed that, during the time evolution of this excited state, the expectation values of non-conserved quantities relaxed exponentially fast to their thermal equilibrium value. However, the relaxation of the entanglement entropy of a segment on length l displayed a totally different behavior. There exists a horizon time, $t_h = l/2$, such that i) for times $0 \leq t < t_h$, the entanglement entropy growth linearly, $S_l \propto t$ and ii) for times $t \geq t_h$, the entanglement entropy saturates at its thermal equilibrum value, $S_l = l s_{th}$, where s_{th} is the thermodynamical entropy density of the system.

In their original work, Calabrese and Cardy explained the existence of the horizon effect in terms of a simple heuristic picture. They assumed that the sudden removal of the original mass gap resulted in the creation of a homogeneous distribution of pointlike entangled quasiparticle pairs and that, after the quench, these quasiparticles traveled in opposite directions at the speed of light. This picture explains in a natural way both the existence of regimes i) and ii) as well as the particular value of t_h.

In a remarkable way, in [26] it was shown that in $1+1$-dimensional holographic CFTs, the computation of the entanglement entropy in the simplest model of gravitational collapse available precisely reproduced the horizon effect, even though we are in a strongly-coupled theory. This spacetime is the Vaidya solution, which represents the gravitational collapse of a distribution of null dust or incoherent radiation.

Thermalization in finite-size systems

Whe considering a finite-sized system, new ways of relaxation to thermal equilibrium may appear. Already at the classical level, the Fermi-Pasta-Ulam-Tsingou paradox (FPUT paradox) demonstrated that the existence of finite size effects enriches significantly the possible routes to equilibration the system has at its disposal.

The FPUT paradox was the foundational numerical experiment of the field of computational physics. FPUT started from a one-dimensional chain of particles coupled harmonically at first neighbours. This system is integrable, as the energy-per-mode is a conserved quantity. In this case, the initial energy of the system cannot be redistributed between the different normal modes, in such a way that equipartition is impossible and thermalization cannot be achieved in a standard sense. Fermi's original expectation was that the introduction of small aharmonic couplings between the particles would result in an ergodic behavior, that would finally lead to the equipartition of the initial energy. Starting from an initial state in which only the fundamental mode was excited, the simulations performed showed that, at short times, this expectation was correct: energy started to flow to higher normal modes. However, at sufficiently long times, it was observed that most part of the energy came back again to the fundamental mode: the initial state was reconstructed in a quasiperodic way.

The FPUT paradox consists of the observation that nonlinearity is not a sufficient condition for ergoidicity. Understanding the physics behind this paradox contributed decisevely to some of the most important breaktroughs of the XXth century in classical mechanics, as soliton theory an chaos theory. Even today, there exist aspects of the FPU paradox that await to be fully understood as, for instance, its persistence in the thermodynamic limit.

The experimental evidence available clearly shows that macroscopic, isolated and finite-sized quantum systems also display a rich phenomenology. There exists a plethora of routes to final equlibration that depend both on the microscopic interactions and the inital state, and it has even been veryfied that in somes cases an ergodic behavior is not quickly established. For certain integrable systems, the initial momentum distribution frozens and the memory of the initial state is conserved. A paradigmatic example of this phenomenon is the quantum Newton's cradle [170]. In quasi-integrable systems, thermalization may not happen right away, but rather the system can go through a mestastable intermediate phase known as pre-thermalization. For other systems, the time needed for the loss of quantum coherence is greater than the characteristic propagation time of the excitations, and the initial state can be partially reconstructed several times before thermalization finally takes place.

This reconstruction of the initial state is named a *quantum revival*. A well-known experimental example of this phenomenon is provided by a three-dimensional Bose gas in an optical lattice [184]. At the theoretical level, quantum revivals have been recently studied by Cardy in the context of $1+1$-dimensional rational CFTs [187] and are trivially present in free theories. For instance, in [178] Takayanagi and Ugajin computed the time evolution of the entanglement entropy of a free Dirac fermion on a circle of lenght 2π after a quantum quench. The entanglement entropy turned out to be periodic, coming back to its initial value every π seconds. In the light of this observation, Takayanagi and Ugajin proposed that that this process could be represented holographically as the periodic formation and evaporation of a quantum black hole.

The natural question is if there exist a process analogous to the Takayanagi and Ugajin one at strong coupling. Under the AdS/CFT correspondence, answering this question just ammounts to finding out if there exist oscillating geometries in General Relativity in an asymptotically global AdS spacetime. The answer is affirmative, and represents the focus of chapters 2, 3 and 4 of this work.

Quantum revivals in Holography

Even though the Vaidya solution considered in [26] can be trivially generalized to the global case, the fact that the radiation supporting it is incoherent implies that the matter wavefront does not have an internal pressure able to counteract the attractive force of gravity. Therefore, this solutions represents a process of direct gravitational collapse to a black hole. Obtaining an oscillating geometry implies considering coherent radiation.

The simplest example of coherent radiation is provided by a massless scalar field. The study of gravitational collapse processes triggered by scalar fields is an old subject in numerical General Relativity. Already at the level of asymptotically flat spacetimes, the pioneering work of Choptuik in this area allow establishing the existence of critical phenomena in gravity [158]. Choptuik observed that, depending on its total energy, a spherically symmetric scalar pulse could face two distinguished fates. At energies above some threshold energy, the pulse collapse directly to a black hole. However, at energies below this threshold, collapse did not take place: the pulse implosioned and the dispersed to future null infinity. The fundamental discoverement of Choptuik lies between these two possibilities: at the threshold energy, the scalar pulse evolves to an universal solution that contains a naked singularity at its center. The existence of this solution explains the critical behavior of the mass of the black holes formed by scalar pulses just above threshold.

This numerical experiment can be repeated in an asymptotically global AdS spacetime. For scalar pulses energetic enough, the results agree with the original ones of Choptuik. However, for scalar pulses below threshold, the phenomenology changes radically. After implosioning and dispersing, the scalar pulse reaches the spacetime boundary in a finite time, where it is reflected. This reflection results in a new implosion. The natural question that arises is what happens next. This problem was addressed by Bizon and Rostworowski in 2011 [130]. For the scalar pulse shape they considered, their observations vindicated that, independently of the initial energy, the evolution after the first implosion always results in gravitational collapse; there exists a sequence of critical energies $\{M_n, n \in \mathbb{N}\}$ such that, if the energy M of the scalar pulse lies in the range $M_{n+1} < M < M_n$, a black hole forms after n rebounds against the AdS boundary.

The merchanism underlying the existene of the sequence of critical energies is a turbulent instability: by decomposing the scalar field in normal modes, it is found that the initial energy flow from low to high frequencies, until a power-law spectrum is eventually established.

In real space, after each implosion, part of the scalar pulse focuses. This focusing results in an increment of the local energy density, that eventually is concentrated enough to form a black hole.

In the light of the holographic duality, in chapter 2 we propose that oscillating geometries that eventually end up forming a black hole are correspond to macroscopical states in the dual CFT that experience a series of quantum revivals before thermalizing completely. We focus on four-dimensional oscillating geometries, reproducing different results previously obtained in the literature and introducing some new ones. We support our proposal in an explicit numerical computation of the entanglement entropy, following the HEE prescription. We analyze in detail the different regimes that the entanglement entropy goes through during its time evolution, as well as their dependence on the initial state considered.

In chapter 3 we discuss three-dimensional oscillating geometries. General Relativity in asymptotically AdS_3 spacetimes is essentially different from its higher-dimensional counterparts. The fundamental reason behind this difference stems from the fact that global AdS_3 is separated by the static black hole solutions by a mass gap. Within this gap, the static geometries correspond to horizonless conical singularities. The study of dynamical scalar fields in these spacetimes was initiated by Pretorius and Choptuik in the context of critical phenomena in gravitation [160], and was revisited recently by Bizon and Jalmuzana with the focus on the possible existence of the turbulent instability and is consequences for cosmic censorship. They determined that, even though the instability is still present, it never leads to a cosmic censorship violation, as it does not form a conical singularity in finite time.

Our focus in this chapter is discussing the entanglement entropy evolution in these three-dimensional oscillating geometries, which we compare with the results obtained in chapter 2. We demonstrate that, in three dimensions, these geometries represent quantum revival processes with an apparently arbitrary periodicity, in stricking contrast with their higher-dimensional counterparts. We analyze in detail the dependence of this period with respect to the energy density of the initial state and the scalar pulse shape, and discuss the physics behind its increase. Finally, we comment on simple quantu systems where this phenomenon also takes place.

Nowadays, there is solid evidence favoring that the existence of oscillating geometries in asymptotically global AdS spacetimes is a generic phenomenon. Up to this point, we have only mentioned nonlinearly unstable oscillating geometries, that eventually end up collapsing into a black hole. However, this is not the only possibility. There exist cases in which the turbulent instablity is not at work [135]. Instead of thermalizing, the dual CFT remains forever in a quasiperiodic state, keeping the memory of the initial one.

The natural question that arises is which is the physical mechanism that underlyes this inhibition of the turbulent instability. One answer can be found in [136], where it was emphasized that the existence of the turbulent instability herself relies on the fact that the eigenfrequency spectrum of the normal modes of the scalar field over global AdS is exactly resonant, *i.e.*, it has a linear dispersion relation. In this way, an oscillating solution could be immune to the turbulent instability if, instead of being a perturbation of global AdS, could be regarded as a perturbation of an attractor that breaks the linearity of the dispersion relation. Do these attractors exist?

Already in the original work of Bizon and Rostworowski, it was suggested that a scalar normal mode over AdS_4 allows for a nonlinear extension to an exactly periodic geometry. These geometries were constructed numerically by Maliborski and Rostworowski in [140], and were previously known for a complex scalar field [210]. In this last case, in [134] it was shown that the normal mode eigenfrequency spectrum of the complex scalar field over the exactly periodic solution is non-resonant, as well as that this property is directly correlated with the absence of the turbulent instablity for perturbations of this solution. Assuming that the nonlinearity of the dispersion relation holds also in the real case, the nonlinear stability of the oscillating geometries constructed in [135] can be explained by this argument [141].

Far from being restricted to spherically symmetric setups, exactly periodic geometries also appear in the purely gravitational case, where they are known as geons [167]. Collecting the experimental evidence available so far, the existence of exactly periodic geometries seems to be a common feature of asymptotically global AdS spacetimes.

In chapter 4 we check that, under mild dynamical assumptions, this kind of solutions exist in the simplest setup imaginable: we consider a spherically symmetric thin shell with a linear equation of state. The shell interior is given by a global AdS spacetime, while the exterior corresponds to a global AdS-Schawarzschild spacetime with a mass equal to that of the shell. The shell equation of motion is determined by the Israel junction conditions, which guarantee that the Einstein equation is well-defined in a distributional sense.

By scanning over the spacetime dimensionality we establish that, in any dimension, our construction supports thin shells that oscillate periodically between a maximum and a minimum radius, as long as the matter they are made of has a nonzero pressure. We check that the shell never crosses its Schwarzschild radius, and illustrate how this simple exactly periodic solutions present similar properties to the solutions we discussed in the previous paragraphs.

Holographc thermalization at finite charge density

In chapter 5 we undertake the study of the turbulent instability in situations where there exist an additional conserved quantity in the CFT: the charge density. With this aim, we consider a gravitational theory in global AdS_4 that contains a massless, complex scalar field, covariantly coupled to an electromagnetic field.

The electromagnetic field is dual to a conserved current. Therefore, our CFT is endowed with a global $U(1)$ internal symmetry. The fact that the scalar field is charged implies that its dual operator also has a nontrivial charge under this global symmetry. The possible equilibrium states the CFT has at its disposal are significantly enriched. When the expectation value of the scala operator vanishes, the gravitational solution corresponding to an equilibrium state at finite temperature with a nonzero charge density is a Reissner-Nordström black hole. However, this is not the only solution at finite charge density. There exists also the possibility of obtaining states where the global $U(1)$ symmetry is spontaneously broken: the dual scalar operator adquires a nonzero expectation value. From the CFT point of view, these states are superfluids. From the gravitational theory point of view, they correspond to hairy black holes, where a nontrivial scalar field profile exists outside the horizon. Furthermore, there is also possible to obtain other horizonless solutions with this property. These geometries are dubbed solitons, and are static configurations supported by a nontrivial scalar field. Their very existence relies of the fact that the presence of electrostatic repulsion is able to compensate exactly the attractive force of gravity. From the dual point of view, they correspond to pure states that must be pictured as macroscopic Bose-Einstein condensates.

The existence of these different equilibrium states leads to a rich phase diagram, that we construct both in the microcanonical and grand-canonical ensembles. When several phases coexist, the dominant one corresponds to the solution that extremizes the appropriate thermodynamical potential. In the microcanonical ensemble, this potential is the entropy, which must be maximized; in the grand-canoncial ensemble, this potential corresponds to the Gibbs free energy. Depending on the value of the electromagnetic coupling, there exist three well differentiated structures for the microcanonical phase diagram, which we discuss in detail.

Once the landscape of equilibrium states the theory could thermalize into is understood, we perform a study of the holographic thermalization is this model. We check that the eigenfrequency spectrum of the scalar field normal modes over global AdS_4 is exactly resonant, and we demonstrate that the turbulent instability is still present for small perturbations of the vacuum, even at finte charge density. These results validate the hypothesis proposed in [136]. We also consider collapse protocols at constant charge density, and we show that for sufficiently small masses the turbulent instability is inhibited. This suggest that the nonlinear stability of the initial data considered is controlled by a soliton with a nonresonant eigenfrequency spectrum.

With this expectation in mind, we undertake the stability analysis of the soliton, both at the linear and at the nonlinear level. We argue that when the mass of the solution reaches an extremum in terms of its central energy density a linear instability appears, and we confirm this hypothesis by means of a numerical computation of the soliton normal modes. The results we obtain also show that, indeed, the eigenfrequency spectrum is non-resonant.

Having confirmed our previous expectations, we study the nonlinear stability of the soliton. We identify a region where neutras perturbations of the soliton never result in gravitational collapse, and bound its extension in the microcanonical phase diagram by finding the critical mass curve below which the perturbation considered requires at least one rebound against the AdS boundary to form a black hole. This critical mass curve does not show the right scaling properties to survive in the planar limit, and therefore we argue that oscillating geometries disappear in this limit. We put forward the hypothesis that the critical mass curve can only survive if, under this limit, the soliton maps to a solution that breaks the infrared conformal symmetry of the theory, *i*.e., if the dual theory has a mass gap.

Finally, we study the post-collapse relaxation of the expectation value of the scalar operator and the chemical potential. In the case here the initial perturbation collapses directly to a black hole, we identify three different relaxation regimes, that we put into correspondence with previous discoverements in the planar case [103]. The agreement between the results of [103] and our observations, given the manifest difference between our constructions, signals that that the existence of these three regimes in our case relies on the mechanism proposed in [103] and points to its universality. Finally, we also consider the post-collapse relaxation of the expectation value of the scalar operator in oscillating geometries. This problem is extremely demanding from the numerical point of view but, nevertheless, we are able to identify a novel relaxation regime, where this quantity displays long-lived oscillations.

Holographic quenches

Up to this date, studies of holographic thermalization in global AdS startfrom an out-of-equiibrium state, specified by some initial data, and do not address the question of how this initial state can in principle be produced. In chapter 6, we undertake, for the first time, the study of quantum quenches in Holography in the global context.

We consider homgeneous holographic quenches implemented by a deformation of the CFT Lagrangian by means of a marginal scalar operator. In this way, our gravitational theory coincides with the one discussed in 2. Our quench is implemented by turning on a non-normalizable mode of the scalar field. Recently, the fast quench limit has been under an intense theoretical survey [217]. In holographic constructions, it has been possible to show that the energy injected by the quench satisfies simple scaling laws in terms of its time span. Afterward, these results have been confirmed in conformal perturbation theory.

However, our focus in this chapter are not the fast, but the adiabatic quenches. We consider an injection process in which the non-normalizable mode of the scalar field increases linearly with time. Surprisingly, for small enough slopes, the system, instead of ending up forming a black hole, relaxes to an attractor that we identify: the pumping solution. This solution is endowed with a static metric, and its only nontrivial time dependence comes from the scalar field. We discuss the fundamental properties of these pumping solutions, demonstating that they only exist for linear injection processes with a slope below a maximum, that indicates the presence of an intrinsic adiabaticity threshold in our system. Below this threshold, we show that the pumping solution is not univocally determined by the contour conditions of our problem, as there exist two different branches. The first one is linearly stable and has a negative mass, while the second is linearly unstable and, within it, the mass does not have a well-defined sign. Having established the linear stability properties of the pumping solution, we undertake the analysis of its nonlinear stability. We argue that, for the linearly stable branch, the stability is mantained at the nonlinear level. The case of the linearly unstable branch is more complex. We provide evidence in favor of the existence of two different scenarios, in such a way that this branch is divided into two subbranches. The second one, upon any perturbation, collapses directly into a black hole. However, the first one does not collapse gravitationally, but it rather decays into a new attractor that correponds to a limiting cycle. We perform different checks that favor both the existence as well as the nonlinear stability of this new solution.

Motivated by the existence of this new kind of solution we build, both at the perturbative and the numerical level, solutions in which, even though the non-normalizable mode of the scalar field continues to increase linearly with time, both the expectation value of the dual scalar operator and the mass of the system are exactly periodic. This solutions are natural extensions of the time-periodic solutions uncovered in [140] to the case of a nontrivial non-normalizable mode.

Being able to employ the negative mass pumping solutions to obtain a normalizable geometry that shares this property raises an obvious concern regarding the stability of the AdS vacuum itself. We close our analysis of the four-dimensional pumping solution by demonstrating that, by turning off the source, a boundary observer can never devise a normalizable solution with a negative mass. We focus on the process when this turning off is sufficiently fast, uncovering simple scaling relations for the final positive mass attained by the system, and discussing their similarities and differences with respecto to similar results already known in the literature for fast quenches over the vacuum.

Finally, we discuss the three dimensional pumping solution. We demonstrate that, in this case, this solution can be put into correspondence with other solutions previously knwn in the literature by means of a series of duality maps. These already known solutions include charged black hole, purely magnetic solutions, or solutions that break invariance under spatial translations. With the help of this duality chain, we are able to find an exact analytical expression for the three-dimensional pumping solution and establish that, in this case, the intrinsic adiabaticity threshold can be put into correspondence with the extremal limit of a charged black hole.

Chapter 9

Resumo

Termalización, materia fortemente acoplada e Teoría de Cordas

Consideremos un sistema macroscópico isolado e en equilibrio. A Segunda Lei da Termodinámica garante que, para as variábeis extensivas caracterizando o sistema -tais como a enerxía total E, o volume V, a carga eléctrica Q, etc.- a entropía S é maximizada. Endenter como un sistema macroscópico perturbado acada o estado de equilibrio final predito pola Termodinámica é o problema da *termalización.* A natureza non trivial deste problema ponse de manifesto cando observamos que as leis de evolución físicas, tanto a nivel cuántico como clásico, son unitarias. Dado un estado inicial arbitrario, nengunha parte da información que este contén pérdese durante a evolución temporal: a dinámica microscópica do sistema é invariante baixo inversión temporal. Por tanto, de onde procese a asimetria temporal implicada pola Segunda Lei?

A irreversibilidade só pode proceder dun proceso de graulado: certa información referente á descrición exacta do sistema ten que permanecer inaccesíbel para o observador macroscópico. Para sistemas non isolados, esta perda de información é certamente esperada, dado que a descrición efectiva do sistema obvia os graos de liberdade do seu entorno. Porén, no caso dun sistema isolado, a situación enriquécese: a propia dinámica microscópica do sistema ten que ser responsábel da aparente perda de información.

Un belo exemplo desta última observación pode atoparse na mecánica estatística clásica. Para un sistema isolado de enerxía E, confinado nun volume V, a descrición termodinámica usual do estado de equilibrio final pode obterse de forma inmediata asumindo o postulado de iguais probabilidades a priori: calquer estado microscópico con enerxía E é igualmente realizábel polo sistema macroscópico. Este principio é, en segredo, unha asunción dinámica. Situémonos no espazo de fases do sistema a enerxía constante, que denotamos por $\Omega(E)$. As leis de evolución temporal microscópicas deben ser tais que, a longo prazo, o tempo t que o sistema pasa nunha rexión $\omega \in \Omega(E)$ é proporcional ao volume de dita rexión, $t \propto \mathrm{Vol}(\omega)$: a dinámica microscópica do sistema debe ser ergódica.

Co descobrimento do caos clásico, a hipótese ergódica gañou fundamentos sólidos. Consideremos que o sistema está, a $t = 0$, nunha rexión $\alpha(E; 0) \in \Omega(E)$ de volume infinitesimal. Para un sistema caótico, o efecto bolboreta implica as diferentes traxectorias que o sistema segue no espazo de fases separánse exponencialmente a medida que o tempo transcorre, mentres que o teorema de Liouville garante que o volume do espazo de fases ocupado polo sistema permanece invariante, $\mathrm{Vol}(\alpha(E; 0)) = \mathrm{Vol}(\alpha(E; t))$. Como consecuencia, a longo prazo, $\alpha(E; t)$ é unha rexión de estrutura fractal que, observada con resolución finita, redúcese a $\Omega(E)$. A ergodicidade do sistema séguese deste simple razonamento.

Esta imaxe cualitativa non pode ser fundamental, por unha razón: a Natureza é esencialmente cuántica e, en física cuántica, a evolución temporal non é soamente unitaria, mais tamén linear. Se non podemos confiar no caos, como ten lugar a termalización?

Proporcionar unha resposta definitiva a esta pregunta leva na lista de tarefas pendentes do físico teórico desde o nacimento da mecánica cuántica na primeira metade do século XX. Porén, e quizá de xeito sorprendente, non fai atá recentemente que esta pregunta gañou extensa atención. Estes esforzos culminaron na chamada Hipótese da Termalización de Autoestados. Actualmente, crese que esta hipótese describe o mecanismo fundamental detrás da termalización no reino cuántico. Entender o seu rexime de aplicabilidade, así como as suas posíbeis excepcións, ten relevado valiosa información sobre a física fóra do equilibrio de sistemas cuánticos isolados.

A razón fundamental detrás desta tardanza é que só en tempos recentes sistemas cuánticos isolados de interés físico foron accesíbeis experimentalmente. Actualmente, redes ópticas poden ser empregadas eficazmente para manipular sistemas de átomos frios no laboratorio cun razoble grao de isolamento. Diferentes perturbacións poden ser introducidas, e as diferentes rutas que conducen até o equilibrio térmico, ou a súa ausencia, poden monitorizarse. Lonxe da física de moitos corpos non relativista, tamén se prestou grande atención ao proceso de termalización en teoría cuántica de campos (TCC). Un exemplo paradigmático é o proporcionado pola inflación e o subsecuente re-aquecimento. Outro, que se atopa actualmente baixo un intenso escrutinio experimental, é o plasma de quarks e gluóns (PQG). Avances tecnolóxicos no campos dos aceleradores de partículas teñen feito posíbel recrear esta nova fase de materia mediante a colisión de ións pesados. Cuantificar a dinámica da formación, evolución e final disipación do PQG na chuvia de hadróns detectada experimentalmente fórzanos a profundizar no noso entendimento das TCC fóra do equilibrio.

De xeito parelelo a estes avances, novas fases de materia fermiónica tamén foron atopadas no campo da materia condensada, sendo o caso máis coñecido os supercondutores de alta temperatura crítica. Estas fases novidosas desafían a descrición estándar en termos de cuasepartículas debilmente interactuantes. Aparentemente, son sistemas fortemente acoplados, onde estas entidades non poden ser definidas. De feito, o propio PQG semella ser un líquido fortemente acoplado xusto acima da transición ao deconfinamento, que é o réxime de enerxía relevante para os experimentos levados a cabo nos modernos aceleradores.

Deste xeito, enfrontámonos a un problema. As técnicas perturbativas estándar en cromodinámica cuántica non poden aplicarse directamente a acoplamento forte: un medio colectivo neste réxime non se axusta a unha descrición de tipo cinético. Ademais, aínda que a Cromodinámica Cuántica no Retículo permita realizar cálculos explicítios a calquer acoplamento, o problema do signo imposibilita calquer intento de estudar procesos en tempo real, xa que para obter control numérico é preciso traballar na versión euclídea da teoría. A resolución finita inevitábel en calquer experimento numérico fai que continuar as respostas obtidas nesta aproximación a tempo real sexa un procedimento indefinido. Nen sequer pode accederse de xeito eficaz aos coeficientes de transporte do PQG en teoría de resposta linear, a pesar de que son dunha importancia fundamental á hora de caracterizar a evolución temporal to PQG unha vez este entra no réxime hidrodinámico.

Lonxe de ser específicas ao PQG, estas reservas aplican a xenericamente a calquer estudo que, partindo de primeiros principios, pretenda abordar un proceso dinámico nunha fase da materia fortemente acoplada sen cuase-partículas. A caixa de ferramentas estándar do físico teórico carece dun instrumento capaz de atacar este problema. Este sería un punto e final certamente triste, de non ser por un dos triunfos máis salientábeis do intelecto humano: a teoría de cordas ou teoría M.

Orixinalmente proposta como unha teoria da interacción forte nos anos sesenta do século XX, a Teoría de Cordas foi rapidamente recoñecida como unha teoría viábel da Gravidade Cuántica (GC), ao mesmo tempo que era sobrepasada pola Cromodinámica Cuántica no seu obxectivo orixinal. Investigación posterior, que culminou na chamada *primeira revolución das supercordas* nos anos oitenta, amosou que a Teoría de Cordas incorpora de xeito automático os ingredientes precisos para construir TCC non abelianas libres de anomalías capaces de describir a Natureza e, ademais, consistentemente acopladas á gravidade. Os anos noventa foron testigos do descobrimento de novos obxectos de natureza extensa, denominados D-branas. Ao mesmo tempo, decubriuse que as cinco teorías de cordas coñecidas desde a primeira revolución das supercordas estaban relacionadas en segredo por unha rede de dualidades non perturbativas. Esta observación, que foi a semente da *segunda revolución das supercordas*, cambiou de raíz a perspectiva anterior sobre a teoría. En lugar de ser independentes, as diferentes teorías de cordas son diferentes límites perturbativos dunha única teoría máis fundamental, cuxa naturaleza final aínda agarda a ser revelada en todo o seu esplendor: a teoría M.

É neste contexto cando a dualidade holográfica aparece por primeira vez. Introducida por Maldacena no ano 1997 mediante a análise coidadosa dun sistema de D-branas, a correspondencia postula que certas teorías gauge non abelianas, sen gravidade, son en segredo teorías de cordas que habitan un espazo-tempo de dimensión máis alta. Desde unha perspectiva retórica, a teoría de cordas en dimensión superiores é un holograma, codificado na teoría gauge. O aspecto máis poderoso da dualidade holográfica é a súa natureza forte/débil: cando o grupo de simetría gauge da TCC ten un rango infinito, e o acoplamento é forte, a teoría de cordas dual atópase no límite clásico e puntual. Dado que a teoría de cordas é unha teoría consistente de GC, este límite non e máis que Relatividade Xeral estándar nun espazo-tempo multidimensional. Máis concretamente, a teoría cuántica de campos posúe un punto fixo ultravioleta: é unha teoría cuántica de campos conforme a altas enerxías (unha *conformal field theory* ou CFT). De acordo con este feito, o espazotempo no que habita a súa teoría gravitatoria dual é asintóticamente anti-de Sitter ou AdS. Deste xeito, a dualidade recibe habitualmente o nome de correspondencia AdS/CFT. Os espazotempos asintoticamente AdS posúen unha fronteira de tipo tempo no infinito, e pode imaxinarse que nela habita a CFT dual.

Á luz do anterior, vemos que AdS/CFT é unha ferramenta de primeiros principios para estudar procesos fóra do equilibrio a acoplamento forte, polo menos en certas TCC. Soamente é preciso atopar a construción graviatotoria dual ao proceso en TCC no que estexamos interesados. Deste modo, considerar unha TCC a acoplamento forte en equilibrio térmico impica incluír un buraco negro estacionario na teoría gravitatoria. De xeito marabilloso, a termodinámica de buracos negros é posta en correspondencia coa descrición termodinámica estándar dun plasma equlibrado en TCC. Ademais, as diferentes perturbacións deste buraco negro codifican tanto a resposta linear como a resposta hidrodinámica deste plasma. Os coeficientes de transporte do plasma poden ser calculados eficazmente, e pode accederse aos límites de validez da expansión hidrodinámica. Un famoso resultado é que o ratio entre a visocidade e a densidade de entropía do plasma holográfico é menor que o de calquer fluido xamais observado no laboratorio e, de forma máis salientable aínda, da orde de magnitude do valor determinado experimentalmente para o PQG.

Esta observación cimentou unha liña de investigación en rápido densenvolvimento, que intenta comprender o réxime fóra do equlibrio do PQG empregando TCC holográficas como modelos de xoguete. Partindo dun certo estado excitado, a formación dun plasma equilibrado na TCC holográfica é nada máis que un proceso de colapso gravitatorio na imaxe dual. Este proceso de termalización, orixinalmente intratábel, é por tanto mapeado nun sistema non linear de ecuacións en derivadas parciais acopladas, que pode resolverse con técnicas numéricas estándar. Esta esquina da paisaxe da correspondencia AdS/CFT coñécese como *holografía numérica*. Lonxe de estar restrinxida a unha modelización efectiva do PQG, a holografía numérica ten demostrado ser útil nunha grande variedade de problemas físicos. Estes inclúen, por exemplo, turbulencia cuántica ou quenches cuánticos en sistemas fortemente acoplados.

Esta tese ocúpase do estudo deste último tipo de procesos, no caso no que a TCC holográfica habita nun espazo de tamaño finito. A interrelación entre efectos de tamaño finito e o límite de acoplamento forte dunha teoría cuántica fóra do equilibrio da lugar a unha rica paisaxe de rutas cara a termalización, ou incluso á sua ausencia. Clasificar e, de xeito máis importante, entender estas rutas supón un desafío, tanto desde unha perspectiva teórica como puramente computacional.

A entropía de entrelazamento

As funcións de partición e os espazos de Hilbert da CFT e da teoría gravitatoria identifícanse baixo a dualidade. Esta identificación proporciona a posibilidade de acceder á función de partición da CFT fortemente acoplada en termos da función de partición da teoría gravitatoria clásica, permitindo o cálculo de funcións de correlación a n-puntos ou de entropías de entrelazamento na CFT.

Consideremos un sistema cuántico descrito por un espazo de Hilbert $\mathcal{H}$, que factorizamos en dous subsistemas A e $\bar{A}$ como $\mathcal{H} = \mathcal{H}_A \otimes \mathcal{H}_{\bar{A}}$. A *entropía de entrelazamento* de A, S_A, defínise como a entropía de von Neumann da matriz densidade reducida do subsistema,

$$S_A = -\mathrm{tr}(\rho_A \log \rho_A),$$

e proporcion unha medida do grado de correlación existente entre A e $\bar{A}$. En TCC, o subsistema A é tipicamente unha rexión espacial nunha superficie de Cauchy.

No caso dunha CFT holográfica, a rexión A habita na fronteira dun espazotempo asintóticamente AdS. Consideremos unha hipersuperficie tipo espazo σ_A que, partindo da fronteira de A, se introduce no interior deste espazotempo. De entre todas as posíbeis hipersuperficies σ_A deste tipo, tomemos a que extremiza a súa área, γ_A. A entropía de entrelazamento de A ven entón dada pola área desta hipersuperficie extremal en termos dunha fórmula análoga á relación de Bekenstein-Hawking para a entropía dun buraco negro,

$$S_A = \frac{1}{4G}\mathrm{Area}(\gamma_A).$$

Esta fórmula coñécese como prescrición holográfica para a entropía de entrelazamento ou prescrición HEE [63, 64, 65]. A prescrición HEE aplica tamén no caso de que o estado da CFT, e por tanto a xeometría dual, dependen do tempo. Por tanto, permite acceder á evolución dinámica da entropía de entrelazamento nun proceso de termalización.

A entropía de entrelazamento é por tanto unha cantidade extremadamente útil para caracterizar cómo un sistema fóra do equilibrio se relaxa. O principal problema que presenta é que o seu cálculo non pode levarse a cabo nunha situación xeral. A existencia da prescrición HEE amosa que as CFTs holográficas son unha excepción a esta observación. Porén, non son a única. A entropía de entrelazamento pode tamén calcularse explicitamente en CFTs 1+1-dimensionais, empregando o chamado truco da réplica. Calabrese e Cardy foron os primeiros en empregar este método para obter a entropía de entrelazamento dun sistema unidimensional que foi levado fóra do equilibrio mediante un quench cuántico.

Quenches cuánticos

Tomemos un Hamiltoniado H_0 que depende dun parámetro externo λ_0, e imaxinemos que o sistema se encontra no estado fundamental. O quench cuántico consiste no cambio súbito $\lambda_0 \to \lambda_1 = \lambda_0 + \delta\lambda$. Con respeito ao novo Hamiltoniano H_1, o estado fundamental de H_0 no que o sistema se atopaba orixinalmente convértese nun estado altamente excitado. A súa evolución temporal posterior con respeito a H_1 debe levar, de xeito natural, á termalización final do sistema.

Calabrese e Cardy foron quen de calcular a evolución da entropía de entrelazamento nun proceso deste tipo [22]. Eles partiron do estado fundamental dunha teoría 1+1-dimensional cun intervalo de masa, que habita nunha liña de extensión infinita. Eliminando o intervalo de masa súbitamente, este estado fundamental pasa a ser un estado altamente excitado nunha teoría conforme. Calabrese e Cardy observaron que, durante a evolución temporal deste estado excitado, os valores esperados de cantidades non conservadas se relaxan exponencialmente ao seu valor en equilibrio térmico. Porén, a relaxación da entropía de entrelazamento dun segmento de lonxitude l amosa un comportamento diferente. Existe un tempo de horizonte, $t_h = l/2$, tal que i) para tempos $0 \leq t < t_h$, a entropía de entrelazamento do intervalo medra de xeito linear, $S_l \propto t$ e ii) para tempos $t \geq t_h$, a entropía de entrelazamento satura ao seu valor en equilibrio térmico, $S_l = l s_{term}$, onde s_{term} e a densidade de entropía termodinámica do sistema.

No seu traballo orixinal, Calabrese e Cardy explicaron a existencia deste efecto horizonte mediante unha sinxela imaxe heurística. Asumiron que a eliminación súbita do intervalo de masa orixinal resultou na creación dunha distribución homoxénea de pares puntuais de cuase-partículas entrelezadas e que, após o quench, as cuase-partículas viaxan en direccións opostas á velocidade da luz. Esta imaxe explica de xeito natural tanto a existencia dos réximes i) e ii) como o valor particular de t_h.

De xeito sorprendente, en [26] demostrouse que en CFTs holográficas en 1+1-dimensións, o cálculo da entropía de entrelazamento no modelo de colapso gravitatorio máis sinxelo dispoñíbel reproduce de forma precisa o efecto horizonte, a pesar de que nos encontremos nunha teoría fortemente acoplada. Este espazotempo é a solución de Vaidya, que representa o colapso gravitatorio dunha distribución de polvo nulo ou radiación incoherente.

Termalización en sistemas de tamaño finito

Cando consideramos un sistema de tamaño finito, novas formas de relaxación ao equilibrio térmico poden aparecer. Xa a nivel clásico, a paradoxa de Fermi, Pasta, Ulam e Tsingou (paradoxa FPUT) amosou que a existencia de efectos de tamaño finito enriquece significativamente as posíbeis rutas cara a equilibración das que dispón o sistema.

A paradoxa FPUT foi o experimento numérico fundacional do campo da física computacional. FPUT partiron dunha cadena unidimensional finita de partículas acopladas harmonicamente a primeiros veciños. Este sistema é integrable, xa que a enerxía por modo normal é unha cantidade conservada. Neste caso, a enerxía inicial do sistema non pode redistribuirse entre os modos normais, a equipartición é imposíbel, e por tanto a termalización nun sentido estándar non pode darse. A expectativa orixinal de Fermi era que a introdución de pequenos acoplamentos nonlineares entre as partículas resultaría nunha dinámica ergódica que finalmente conduciría á equipartición da enerxía inicial. Partindo dun estado inicial no que únicamente o modo fundamental do sistema estaba excitado, as simulación realizadas amosaron que, a tempos curtos, esta expectativa era correcta: a enerxía comezaba a fluir a modos normais superiores. Porén, a tempos suficientemente longos, observouse que a maior parte da enerxía regresaba de novo ao modo fundamental: o estado inicial reconstruíase de forma cuase-periódica.

A paradoxa de FPUT consiste na observación de que a nonlinearidade non é condición suficiente para a termalización. Comprender a física detrás desta paradoxa contribuiu decisivamente a algúns dos avances máis importantes do século XX en mecánica clásica, como son a teoría de solitóns ou a teoría do caos. Aínda a día de hoxe, existen aspectos da paradoxa FPUT que agardan ser totalmente entendidos, como son súa pervivencia no límite termodinámico.

A evidencia experimental dispoñíbel demostra claramente que sistemas cuánticos macroscópicos, isolados e de tamaño finito tamén posúen unha rica fenomenoloxía. Existe unha plétora de rutas cara a equilibración final que dependen tanto das interaccións microscópicas como do estado inicial, e tense comprobado que en certos casos non se estabelece rapidamente un comportamento ergódico. Para certos sistemas integrábeis, a distribución de momentos conxélase e a memoria do estado inicial consérvase. Un exemplo paradigmático deste fenómeno é o péndulo de Newton cuántico [170]. En sistemas cuase-integrábeis, a termalización pode non suceder de maneira directa, senón que o sistema pode atravesar unha fase metaestábel intermedia denominada pre-termalización. Para outros sistemas, o tempo de perda da coherencia cuántica é maior que o tempo de propagación característico das excitacións, e o estado inicial pode reconstruirse parcialmente varias veces antes de que a termalización final teña lugar.

Esta reconstrución do estado inicial do sistema denomínase *resurximento cuántico*. Un coñecido exemplo experimental deste comportamento é o proporcionado por un gas de Bose tridimensional nunha rede óptica [184]. A nivel teórico, os resurximentos cuánticos foron estudados recentemente por Cardy no contexto de CFTs racionais en 1+1-dimensións [187] e están trivialmente presentes en teorías libres. Por exemplo, en [178] Takayanagi e Ugajin calcularon a evolución temporal da entropía de entrelazamento dun fermión de Dirac libre nunha circunferencia de lonxitude 2π após un quench cuántico. A entropía de entrelezamento resultou ser periódica, regresando ao seu valor inicial cada π segundos. Á luz desta observación, Takayanagi e Ugajin propuxeron que o seu quench podía representarse holograficamente como a formación e evaporación periódica dun buraco negro cuántico no espazotempo dual.

A pregunta natural é se existe un análogo do proceso de Takayanagi e Ugajin a acoplamento forte. Baixo a dualidade AdS/CFT, responder a esta pregunta redúcese a averiguar se existen xeometrías oscilantes en Relatividade Xeral nun espazotempo asintóticamente AdS global. A resposta é afirmativa, e constitúe o foco dos capítulos 2, 3 e 4 deste traballo.

Resurximentos cuánticos en Holografía

Se ben a solución de Vaidya considerada en [26] pode xeralizarse trivialemente ao caso global, o feito de que a radiación que lle da soporte sexa incoherente implica que a fronte de onda non dispón dunha presión interna capaz de se sobrepor á forza atractiva da gravitatición. Deste xeito, esta solución representa un proceso de colapso gravitatorio directo a un buraco negro. Obter unha xeometría oscilante implica considerar radiación coherente.

O exemplo máis sinxelo de radiación coherente é o proporcionado por un campo escalar real. O estudo de procesos de colapso gravitatorio soportados por un campo escalar é unha vella asignatura en Relatividade Xeral numérica. Xa a nivel de espazotempos asintóticamente planos, o pioneiro traballo de Choptuik neste eido permitiu estabelecer a existencia de fenómenos críticos en gravitación [158]. Choptuik observou que, dependendo da súa enerxía total, un pulso escalar esfericamente simétrico podía afrontar dous destinos ben diferentes. A enerxías superiores a unha enerxía umbral, o pulso colapsaba directamente a un buraco negro. Porén, a enerxías inferiores, o colapso non tiña lugar: o pulso implosionaba sobre si mesmo e posteriormente dispersábase ao infinito nulo futuro. O descubrimento fundamental de Choptuik sitúase na transición entre estas dúas posibilidades: á enerxía umbral o pulso escalar evolúe até unha solución universal que contén unha singularidade desnuda no seu centro. A existencia desta solución universal explica o comportamento crítico da masa dos buracos negros formados por pulsos escalares xusto por riba do umbral.

Este experimento numérico pode ser repetido nun espazotempo asintóticamente AdS global. Para pulsos escalares suficientemente enerxéticos, os resultados coinciden cos atopados orixinalmente por Choptuik. Porén, para pulsos escalares por debaixo do umbral, a fenomenoloxía cambia radicalmente. Tras implosionar sobre si mesmo e dispersarse, o pulso escalar alcanza a fronteira do espazotempo nun tempo finito, onde é reflexado. Isto resulta nunha nova implosión. A pregunta natural que surxe é que sucede a continuación. Este problema foi abordado por Bizon e Rostworowski en 2011 [130]. Para a forma do pulso escalar que consideraron, observaron que, independentemente da enerxía inicial, a evolución posterior á primeira implosión sempre resulta nun colapso gravitatorio: existe unha secuencia de enerxía críticas $\{M_n, n \in \mathbb{N}\}$ tais que, se a enerxía M do pulso escalar se atopa no rango $M_{n+1} < M < M_n$, un buraco negro se forma tras n rebotes contra a fronteira de AdS.

O mecanismo que subxace á existencia da secuencia de enerxías críticas e unha inestabilidade turbulenta: descopoñendo o campo escalar en modos normais, obsérvase que a enerxía inicial flúe de baixas a altas frecuencias, até que eventualmente se estabelece un espectro polinómico. No espazo real, tras cada implosión sobre si mesmo, parte do pulso escalar se focaliza. Esta focalización resulta no incremento da densidade local de enerxía, que eventualmente está o suficientemente concentrada como para formar un buraco negro.

Á luz da dualidade holográfica, no capítulo 2 propoñemos que as xeometrías oscilantes que eventualmente rematan colapsando nun buraco negro son duais a estados macroscópicos na CFT dual que experimentan unha serie de resurximentos cuánticos antes de termalizar definitivamente. Centrámonos en xeometrías oscilantes catro-dimensionais, reproducindo diferentes resultados previamente obtidos na literatura e introducindo algúns novos. Apoiamos a nosa proposta nun cálculo numérico explícito da entropía de entrelazamento seguindo a prescrición HEE. Analizamos en detalle tanto os diferentes réximes que atravesa a entropía de entrelazamento na súa evolución temporal como a súa dependencia do estado inicial.

No capítulo 3 discutimos as xeometrías oscilantes tridimensionais. A Relatividade Xeral en espazos asintóticamente AdS_3 é esencialmente diferente da súa contrapartida en dimesións superiores. A razón fundamental detrás desta diferenza é que AdS_3 global está separado dos buracos negros estáticos por un intervalo de masa. Dentro deste intervalo, as xeometrías estaticas son singularidades cónicas sen horizonte. O estudo de campos escalares dinámicos nestes espazotempos foi inciado por Pretorius e Choptuik no contexto dos fenómenos críticos en gravitación [160], e foi revisitado recentemente por Bizon e Jalmuzna coa atención posta na posíbel existencia da inestabilidade turbulenta e as súas consecuencias [159]. Neste traballo determinouse que, aínda que a inestabilidade segue estando presente, esta non resulta nunha violación da censura cósmica, dado que non conduce á formación dunha singularidade cónica nun tempo finito.

O noso foco neste capítulo é discutir a evolución da entropía de entrelazamento nas xeometrías oscilantes tridimensionais, que comparamos cos resultados obtidos no capítulo 2. Demostramos que, en tres dimensións, estas xeometrías representan procesos de resurximento cuántico que poden presentar unha periodicidade aparentemente arbitraria, en marcado contraste co que sucede en dimensións superiores. Analizamos en detalle a dependencia deste periodo con respeito á densidade de enerxía do estado inicial e a forma do pulso escalar, e discutimos a física detrás do seu elongamento. Finalmente, comentamos sobre sistemas cuánticos sinxelos nos que este fenómeno tamén ten lugar.

Actualmente existe evidencia sólida a favor de que a existencia de xeometrías oscilantes en espazotempos asintóticamente AdS é un fenómeno xenérico. Até o momento, soamente temos discutido xeometrías oscilantes nonlinearmente inestábeis, que eventualmente rematan colapsando nun buraco negro. Porén, esta non é a única situación que se pode dar. Existen casos nos que a inestabilidade turbulenta non está activa [135]. A teoría dual, en lugar de termalizar, permanece para sempre nun estado cuase-periódico, conservando a memoria do estado inicial.

A pregunta natural que surxe é cal é o mecanismo físico que subxace a esta inhibición da inestabilidade turbulenta. Unha resposta pode atoparse en [136], onde se enfatizou que a mesma existencia da inestabilidade turbulenta descansa no feito de que o espectro de autofrecuencias dos modos normais do campo escalar sobre AdS global é exactamente resonante, i.e., ten unha relación de dispersión linear. Deste xeito, unha solución oscilante podería ser inmune á inestabilidade turbulenta se, en lugar ser unha perturbación sobre AdS global, fose unha perturbación dun atractor que rompa a linearidade da relación de dispersión. Cales son estes atractores?

Xa no traballo orixinal de Bizon e Rostworowski se suxeriu que un modo normal escalar sobre AdS$_4$ admite unha extensión nonlinear a unha xeometría exactamente periódica. Estas xeometrías foron construídas numericamente por Maliborski e Rostworowski en [140] para o campo escalar real, e xa eran previamente coñecidas no caso dun campo escalar complexo [210]. Para este último exemplo, en [134] demostrouse que o espectro de autofrecuencias dos modos normais do campo escalar sobre a solución exactamente periódica é non resonante, así como que este feito está directamente correlacionado coa ausencia da inestabilidade turbulenta para perturbacións desta solución. O cálculo análogo para o caso real non foi realizado, pero asumindo que a nonlinearidade da relación de dispersión se mantén, a estabilidade nonlinear das xeometrías oscilatorias construídas en [135] pode explicarse por medio deste argumento [141].

Lonxe de estar restinxidas a situacións esféricamente simétricas, xeometrías exactamente periódicas tamén aparecen no caso puramente gravitatorio, onde se coñecen como xeóns [167]. Xuntando a evidencia experimental dispoñíbel, a existencia de solucións exactamente periódicas semella ser unha propiedade común dos espazotempos asintóticamente AdS.

No capítulo 4 comprobamos que, baixo asuncións dinámicas moi febles, este tipo de solucións existen na situación máis sinxela imaxinable: consideramos unha cáscara delgada de materia cunha ecuación de estado linear e esfericamente simétrica. O interior da cáscara ven dado por un espazotempo AdS global, mentres que o exterior se corresponde cun espazotempo AdS-Schwarzschild cunha masa igual á enerxía da cáscara. A ecuación de movimento da cáscara é determinada polas condicións de pegado de Israel, que se obteñen demandando que a ecuación de Einstein estexa ben definida nun senso distribucional.

Realizando un barrido na dimensionalidade total do espazotempo demostramos que, en calquer dimensión, a nosa construción soporta cáscaras delgadas que oscilan periodicamente entre un radio máximo e un radio mínimo, sempre e cando a materia que as conforma posúa unha presión distinta de cero. Comprobamos que a cáscara nunca atravesa o seu radio de Schwarzschild, e ilustramos como estas solucións exactamente periódicas tan sinxelas presentan propiedades semellantes ás das solucións que discutimos nos parágrafos anteriores.

Termalización holográfica a densidade de carga finita

No capítulo 5 abordamos o estudo da inestabilidade turbulenta en situacións nos que existe unha cantidade conservada adicional na CFT: a densidade de carga. Con este fin, consideramos unha teoría graviatoria asintóticamente AdS$_4$ global que contén un campo escalar complexo sen masa, covariantemente acoplado a un campo electromagnético.

O campo electromagnético é dual a unha corrente global conservada. Por tanto, a nosa CFT posúe unha simetría $U(1)$ global interna. O feto de que o campo escalar estexa cargado implica que o seu operador marxinal dual ten unha carga non trivial baixo esta simetría global. Os posíbeis estados de equilibrio dos que dispón a CFT enriquécense significativamente. Cando o valor de expectación do operador escalar dual é nulo, a solución gravitatoria que se corresponde cun estado de equilibrio a temperature finita no que densidade de carga non é nula é un buraco negro de Reissner-Nordström. Porén, esta non é a única solución a densidade de carga finita. Existe tamén a posibilidade de obter estados nos que a simetría U(1) global se rompe espontaneamente: o operador escalar dual adquire un valor de expectación distinto de cero. Desde o punto de vista da CFT, estes estados son superfluidos. Desde o punto de vista da teoría gravitatoria, corresponden a buracos negros con pelo, nos que existe un perfil nontrivial do campo escalar fóra do horizonte. Ademais, tamén é posíbel obter solucións sen horizonte con esta propiedade. Estas xeometrías denomínanse solitóns, e son configuracións estáticas soportadas por un campo escalar nontrivial. A súa mesma existencia descansa sobre o feito de que a presenza da repulsión electrostática é capaz de compensar exactamente a forza atractiva da gravidade. Desde o punto de vista dual, correspóndense a estados puros que deben ser visualizados como condensados de Bose-Einstein macroscópicos.

A existencia destas diferentes estados de equilibrio da lugar a un rico diagrama de fases, que construímos tanto no colectivo microcanónico como no gran-canónico. Cando varias fasen coexisten, a dominante correspóndense coa solución que minimiza o potencial termodinámico apropiado. No colectivo microcanónico, este potencial é a entropía; no grancanónico, é a enerxía libre de Gibss. Dependendo do valor do acoplamento electromagnético, existen tres estruturas ben diferentes no diagrama de fases microcanónico, que discutimos en detalle.

Unha vez comprendida a paisaxe de estados de equilibrio nos que pode termalizar a teoría, realizamos un estudo da termalización holográfica neste modelo. Amosamos que o espectro de autofrecuencias dos modos normais do campo escalar sobre AdS$_4$ é exactamente resonante, e comprobamos como a inestabilidade turbulenta segue estando presente para pequenas perturbacións do vacío incluso a carga finita. Estes resultados validan a hipótese proporsta en [136]. Ao mesmo tempo, consideramos protocolos de colapso a carga constante, e comprobamos que a masas suficientemente pequenas a inestabilidade turbulenta inhíbese.

Isto suxire que a estabilidade nonlinear dos datos iniciais considerados está controlada por un solitón cun espectro de autofrecuencias non resonante.

Con esta expectación de fondo, pasamos a estudar tanto estabilidade linear como nonlinear do solitón. Argumentamos que cando a masa da solución alcanza un extremo con respeito á densidade de enerxía no seu centro unha inestabilidade linear aparece, e confirmamos esta hipótese mediante un cálculo numérico dos modos normais do solitón, empregando para elo un método pseudospectral. Os resultados obtidos amosan que, efectivamente, o espectro de autofrecucias non é resonante.

Tendo confirmado as nosas expectativas previas, pasamos ao estudo da inestabilidade nonlinear do solitón. Identificamos unha rexión na que perturbacións neutras do solitón nunca resultan nun colapso gravitatorio, e acotamos a súa extensión no diagrama de fases microcanónico atopando a curva de masa crítica por debaixo da cal a perturbación considerada necesita polo menos un rebote contra a fronteira de AdS para formar un buraco negro. Esta curva de masa crítica non manifesta as propiedades de escaleado necesarias para sobrevivr no límite planar, e por tanto argumentamos que as xeometrías oscilantes desaparecen nese límite. Propoñemos a hipótese de que esta curva de masa crítica só pode sobrevivir se, baixo este límite, o solitón se transforma nunha solución que rompe a simetría conforme do infravermello da teoría, é dicir, se a teoría dual ten un intervalo de masa.

Finalemente, estudamos a relaxación post-colapso do valor esperado do operador escalar e do potencial químico. No caso de que a perturbación colapse directamente a un buraco negro, identificamos tres réximes de relaxación diferentes, que poñemos en correspondencia con descubrimentos previos no caso planar [103]. O acordo entre os resultados de [103] e as nosas observacións, a pesar da diferenza manifesta entre as nosas construcións, sinalan que a existencia destes tres réximes no noso caso descansa no mecanismo proposto en [103] e apuntan á universalidade do mesmo. Por último, consideramos tamén a relaxación post-colapso do valor esperado do operador escalar en xeometrías oscilantes. Este problema é extremadamente demandante desde o punto de vista numérico, pero a pesar disto somos quen de idenficar un réxime de relaxación novidoso, no que esta cantidade amosa osilacións de longa vida media.

Quenches holográficos

Até o momento, os estudos de termalización holográfica en AdS global parten dun estado fóra do equilibrio especificado no instante inicial, pero non abordan como este estado é orixinalmente producido. No capítulo 6 tratamos por vez primeira quenches cuánticos en Holografía no contexto global.

Consideramos quenches holográficos homoxéneo implementado mediante unha deformación do Lagranxiano da CFT por medio dun operador escalar marxinal. Deste xeito, a nosa teoría gravitaria coincide ca discutida no capítulo 2. O quench impleméntase por medio da activación no modo non-normalizábel do campo escalar. Recentemente, o límite de quenches rápidos estivo baixo un intenso escrutinio teórico [217]. En construcións holográficas, foi posible amosar que a enerxía inxectada polo quench satisface relacións de escala en termos da súa duración. Posteriormente, estes resultados for confirmados en teoría de perturbacións conforme.

O noso foco de atención, porén, non os quenches rápidos, senón os quenches adiabáticos. Consideramos un proceso de inxección no que o modo non-normalizábel do campo escalar se incrementa linearmente co tempo. De xeito sorprendente, para pendentes suficientemente pequenas o sistema, en lugar de rematar colapsando, reláxase a un atractor que idenficamos: a solución de bombeo. Esta solución posúe unha métrica estática, e a súa única dependencia temporal non trivial provén do propio campo escalar. Discutimos as propiedades fundamentais destas solucións de bombeo, demostrando como soamente existen para procesos de inxeción lineares cunha pendente por debaixo dun máximo, que indica a existencia dun umbral de adiabaticidade intrínseco presente no sistema. Por debaixo deste umbral, amosamos que a solución non está univocamente determinada polas condicións de contorno do problema, xa que existen dúas posíbeis ramas. A primeira é linearmente estábel é ten masa negativa, mentres que a segunda é linearmente inestábel e nela a masa non ten un signo definido. Tendo estabelecido a estabilidade linear da solución de bombeo, pasamos ao estudo da súa estabilidade nonlinear. Argumentamos que, para a rama linearmente estábel, a estabilidade mantense a nivel nonlinear. O caso da rama linearmente inestábel é máis complexo. Amosamos evidencia a favor da existencia de dous escenarios diferentes, de modo que a rama se divide en dúas subramas. A segunda, perante calquer perturbación, decae directamente a un buraco negro. Porén, a primeira non colapsa gravitatoriamente, senón que decae a un novo atractor, que se corresponde cun ciclo límite. Realizamos diferentes comprobacións que favorecen tanto a existencia como a estabilidade nonlinear deste novo tipo de solución.

Motivados pola existencia deste novo tipo de solucións contruímos, tanto a nivel perturbativo como numérico, solucións nas que, a pesar de que o modo non-normalizábel do campo continúa a se incrementar linearmente co tempo, tanto o valor de expectación do operador escalar dual como a masa do sistema son exactamente periódicos. Estas solucións son extensións naturais das xeometrías descubertas en [140] ao caso dun modo non-normalizábel non trivial.

Poder empregar a solucións de bombeo de masa negativa para obter unha xeometría normalizable que comparta esta propiedade da lugar a unha preocupación obvia con respecto á estabilidade do propio vacío AdS. Fechamos a nosa análise da solución de bombeo catrodimensional demostrando que, apagando a fonte, un observador na teoría dual non pode crear unha solución normalizábel de masa negativa. Centrámonos no caso en que este proceso de apagado é suficientemente rápido, descubrindo sinxelas relacións de escala para a masa final positiva que acada o sistema, e discutimos as similitudes e diferenzas con respeito a resultados semellantes xa coñecidos na literatura para quenches rápidos sobre o vacío.

Por último, discutimos a solución de bombeo en tres dimensións. Demostramos que, neste caso, esta solución pode relacionarse por medio dunha serie de dualidades con outras solucións previamente coñecidas na literatura. Estas solucións inclúen buracos negros cargados, solucións puramente magnéticas, ou solucións que rompen invarianza baixo traslacións espaciais. Ca axuda desta cadea de dualidades, atopamos unha expresión analítica exacta para a solución de bombeo e establecemos que, nesta caso, o límite intrínseco de adiabaticidade pode ser posto en correspondencia co límite extremal dun buraco negro cargado.

Bibliography

[1] J. Abajo-Arrastia, E. da Silva, E. Lopez, J. Mas, and A. Serantes, "Holographic Relaxation of Finite Size Isolated Quantum Systems," *JHEP*, vol. 05, p. 126, 2014.

[2] E. da Silva, E. Lopez, J. Mas, and A. Serantes, "Collapse and Revival in Holographic Quenches," *JHEP*, vol. 04, p. 038, 2015.

[3] J. Mas and A. Serantes, "Oscillating Shells in Anti-de Sitter Space," *Int. J. Mod. Phys.*, vol. D24, no. 09, p. 1542003, 2015.

[4] R. Arias, J. Mas, and A. Serantes, "Stability of charged global AdS_4 spacetimes," *JHEP*, vol. 09, p. 024, 2016.

[5] P. Carracedo, J. Mas, D. Musso, and A. Serantes, "Adiabatic pumping solutions in global AdS," 2016.

[6] L. D'Alessio, Y. Kafri, A. Polkovnikov, and M. Rigol, "From quantum chaos and eigenstate thermalization to statistical mechanics and thermodynamics," *Adv. Phys.*, vol. 65, no. 3, pp. 239–362, 2016.

[7] M. Van Raamsdonk, "Lectures on Gravity and Entanglement," 2016.

[8] T. Hartman, "Lectures on quantum gravity and black holes," 2015.

[9] D. W. Robinson and D. Ruelle, "Mean entropy of states in classical statistical mechanics," *Communications in Mathematical Physics*, vol. 5, no. 4, pp. 288–300, 1967.

[10] O. E. Lanford III and D. W. Robinson, "Mean entropy of states in quantum-statistical mechanics," *Journal of Mathematical Physics*, vol. 9, no. 7, pp. 1120–1125, 1968.

[11] E. H. Lieb and M. B. Ruskai, "Proof of the strong subadditivity of quantum-mechanical entropy," *Journal of Mathematical Physics*, vol. 14, no. 12, pp. 1938–1941, 1973.

[12] H. ARAKI and E. H. LIEB, "Entropy inequalities," *Commun. math. Phys*, vol. 18, pp. 160–170, 1970.

[13] A. B. Zamolodchikov, "Irreversibility of the flux of the renormalization group in a 2d field theory," *JETP lett*, vol. 43, no. 12, pp. 730–732, 1986.

[14] J. L. Cardy, "Is there a c-theorem in four dimensions?," *Physics Letters B*, vol. 215, no. 4, pp. 749–752, 1988.

[15] R. C. Myers and A. Sinha, “Seeing a c-theorem with holography,” *Phys. Rev.*, vol. D82, p. 046006, 2010.

[16] R. C. Myers and A. Sinha, “Holographic c-theorems in arbitrary dimensions,” *JHEP*, vol. 01, p. 125, 2011.

[17] H. Casini and M. Huerta, “On the RG running of the entanglement entropy of a circle,” *Phys. Rev.*, vol. D85, p. 125016, 2012.

[18] C. Holzhey, F. Larsen, and F. Wilczek, “Geometric and renormalized entropy in conformal field theory,” *Nucl. Phys.*, vol. B424, pp. 443–467, 1994.

[19] P. Calabrese and J. L. Cardy, “Entanglement entropy and quantum field theory,” *J. Stat. Mech.*, vol. 0406, p. P06002, 2004.

[20] M. M. Wolf, F. Verstraete, M. B. Hastings, and J. I. Cirac, “Area laws in quantum systems: mutual information and correlations,” *Physical review letters*, vol. 100, no. 7, p. 070502, 2008.

[21] P. Calabrese, J. Cardy, and E. Tonni, “Entanglement entropy of two disjoint intervals in conformal field theory II,” *J. Stat. Mech.*, vol. 1101, p. P01021, 2011.

[22] P. Calabrese and J. L. Cardy, “Evolution of entanglement entropy in one-dimensional systems,” *J. Stat. Mech.*, vol. 0504, p. P04010, 2005.

[23] P. Calabrese and J. L. Cardy, “Time-dependence of correlation functions following a quantum quench,” *Phys. Rev. Lett.*, vol. 96, p. 136801, 2006.

[24] J. Cardy, “Quantum Quenches to a Critical Point in One Dimension: some further results,” *J. Stat. Mech.*, vol. 1602, no. 2, p. 023103, 2016.

[25] E. H. Lieb and D. W. Robinson, “The finite group velocity of quantum spin systems,” in *Statistical Mechanics*, pp. 425–431, Springer, 1972.

[26] J. Abajo-Arrastia, J. Aparicio, and E. Lopez, “Holographic Evolution of Entanglement Entropy,” *JHEP*, vol. 11, p. 149, 2010.

[27] J. M. Deutsch, “Quantum statistical mechanics in a closed system,” *Physical Review A*, vol. 43, no. 4, p. 2046, 1991.

[28] M. Srednicki, “Chaos and quantum thermalization,” *Physical Review E*, vol. 50, no. 2, p. 888, 1994.

[29] A. Dymarsky, N. Lashkari, and H. Liu, “Subsystem ETH,” 2016.

[30] N. Lashkari and J. Simon, “From state distinguishability to effective bulk locality,” *JHEP*, vol. 06, p. 038, 2014.

[31] P. Francesco, *Conformal Field Theory.* New York, NY: Springer New York, 1997.

[32] E. S. Fradkin and M. Y. Palchik, *Conformal quantum field theory in D-dimensions*, vol. 376. Springer Science & Business Media, 1996.

[33] J. M. Maldacena, "The Large N limit of superconformal field theories and supergravity," *Int. J. Theor. Phys.*, vol. 38, pp. 1113–1133, 1999. [Adv. Theor. Math. Phys.2,231(1998)].

[34] G. 't Hooft, "A Planar Diagram Theory for Strong Interactions," *Nucl. Phys.*, vol. B72, p. 461, 1974.

[35] J. D. Bekenstein, "Universal upper bound on the entropy-to-energy ratio for bounded systems," *Physical Review D*, vol. 23, no. 2, p. 287, 1981.

[36] G. 't Hooft, "Dimensional reduction in quantum gravity," in *Salamfest 1993:0284-296*, pp. 0284–296, 1993.

[37] L. Susskind, "The World as a hologram," *J. Math. Phys.*, vol. 36, pp. 6377–6396, 1995.

[38] J. Polchinski, "Introduction to Gauge/Gravity Duality," in *Proceedings, Theoretical Advanced Study Institute in Elementary Particle Physics (TASI 2010). String Theory and Its Applications: From meV to the Planck Scale: Boulder, Colorado, USA, June 1-25, 2010*, pp. 3–46, 2010.

[39] J. Solana, *Gauge/string Duality, hot QCD and heavy ion collisions.* Cambridge: Cambridge University Press, 2014.

[40] V. E. Hubeny, "The AdS/CFT Correspondence," *Class. Quant. Grav.*, vol. 32, no. 12, p. 124010, 2015.

[41] K. Papadodimas and S. Raju, "Remarks on the necessity and implications of state-dependence in the black hole interior," *Phys. Rev.*, vol. D93, no. 8, p. 084049, 2016.

[42] C. Fefferman and C. R. Graham, "The ambient metric," *ArXiv e-prints*, Oct. 2007.

[43] D. Marolf, M. Rangamani, and T. Wiseman, "Holographic thermal field theory on curved spacetimes," *Class. Quant. Grav.*, vol. 31, p. 063001, 2014.

[44] S. S. Gubser, I. R. Klebanov, and A. M. Polyakov, "Gauge theory correlators from noncritical string theory," *Phys. Lett.*, vol. B428, pp. 105–114, 1998.

[45] E. Witten, "Anti-de Sitter space and holography," *Adv. Theor. Math. Phys.*, vol. 2, pp. 253–291, 1998.

[46] S. de Haro, S. N. Solodukhin, and K. Skenderis, "Holographic reconstruction of spacetime and renormalization in the AdS / CFT correspondence," *Commun. Math. Phys.*, vol. 217, pp. 595–622, 2001.

[47] K. Skenderis, "Lecture notes on holographic renormalization," *Class. Quant. Grav.*, vol. 19, pp. 5849–5876, 2002.

[48] P. Breitenlohner and D. Z. Freedman, “Positive Energy in anti-De Sitter Backgrounds and Gauged Extended Supergravity,” *Phys. Lett.*, vol. B115, pp. 197–201, 1982.

[49] P. Breitenlohner and D. Z. Freedman, “Stability in Gauged Extended Supergravity,” *Annals Phys.*, vol. 144, p. 249, 1982.

[50] A. V. Ramallo, “Introduction to the AdS/CFT correspondence,” *Springer Proc. Phys.*, vol. 161, pp. 411–474, 2015.

[51] I. R. Klebanov and E. Witten, “AdS / CFT correspondence and symmetry breaking,” *Nucl. Phys.*, vol. B556, pp. 89–114, 1999.

[52] S. W. Hawking and D. N. Page, “Thermodynamics of Black Holes in anti-De Sitter Space,” *Commun. Math. Phys.*, vol. 87, p. 577, 1983.

[53] E. Witten, “Anti-de Sitter space, thermal phase transition, and confinement in gauge theories,” *Adv. Theor. Math. Phys.*, vol. 2, pp. 505–532, 1998.

[54] S. S. Gubser, “Breaking an Abelian gauge symmetry near a black hole horizon,” *Phys. Rev.*, vol. D78, p. 065034, 2008.

[55] S. A. Hartnoll, C. P. Herzog, and G. T. Horowitz, “Building a Holographic Superconductor,” *Phys. Rev. Lett.*, vol. 101, p. 031601, 2008.

[56] S. A. Hartnoll, C. P. Herzog, and G. T. Horowitz, “Holographic Superconductors,” *JHEP*, vol. 12, p. 015, 2008.

[57] S. S. Gubser and S. S. Pufu, “The Gravity dual of a p-wave superconductor,” *JHEP*, vol. 11, p. 033, 2008.

[58] M. Ammon, J. Erdmenger, V. Grass, P. Kerner, and A. O’Bannon, “On Holographic p-wave Superfluids with Back-reaction,” *Phys. Lett.*, vol. B686, pp. 192–198, 2010.

[59] S. A. Hartnoll, “Lectures on holographic methods for condensed matter physics,” *Class. Quant. Grav.*, vol. 26, p. 224002, 2009.

[60] J. McGreevy, “Holographic duality with a view toward many-body physics,” *Adv. High Energy Phys.*, vol. 2010, p. 723105, 2010.

[61] A. Chamblin, R. Emparan, C. V. Johnson, and R. C. Myers, “Charged AdS black holes and catastrophic holography,” *Phys. Rev.*, vol. D60, p. 064018, 1999.

[62] A. Chamblin, R. Emparan, C. V. Johnson, and R. C. Myers, “Holography, thermodynamics and fluctuations of charged AdS black holes,” *Phys. Rev.*, vol. D60, p. 104026, 1999.

[63] S. Ryu and T. Takayanagi, “Holographic derivation of entanglement entropy from AdS/CFT,” *Phys. Rev. Lett.*, vol. 96, p. 181602, 2006.

[64] S. Ryu and T. Takayanagi, "Aspects of Holographic Entanglement Entropy," *JHEP*, vol. 08, p. 045, 2006.

[65] V. E. Hubeny, M. Rangamani, and T. Takayanagi, "A Covariant holographic entanglement entropy proposal," *JHEP*, vol. 07, p. 062, 2007.

[66] A. Lewkowycz and J. Maldacena, "Generalized gravitational entropy," *JHEP*, vol. 08, p. 090, 2013.

[67] X. Dong, A. Lewkowycz, and M. Rangamani, "Deriving covariant holographic entanglement," *JHEP*, vol. 11, p. 028, 2016.

[68] C. T. Asplund, "Holographic entanglement entropy beyond coherent states," 2012.

[69] T. Faulkner, A. Lewkowycz, and J. Maldacena, "Quantum corrections to holographic entanglement entropy," *JHEP*, vol. 11, p. 074, 2013.

[70] M. Headrick and T. Takayanagi, "A Holographic proof of the strong subadditivity of entanglement entropy," *Phys. Rev.*, vol. D76, p. 106013, 2007.

[71] P. Hayden, M. Headrick, and A. Maloney, "Holographic Mutual Information is Monogamous," *Phys. Rev.*, vol. D87, no. 4, p. 046003, 2013.

[72] A. Almheiri, X. Dong, and D. Harlow, "Bulk Locality and Quantum Error Correction in AdS/CFT," *JHEP*, vol. 04, p. 163, 2015.

[73] X. Dong, D. Harlow, and A. C. Wall, "Reconstruction of Bulk Operators within the Entanglement Wedge in Gauge-Gravity Duality," *Phys. Rev. Lett.*, vol. 117, no. 2, p. 021601, 2016.

[74] M. Headrick, V. E. Hubeny, A. Lawrence, and M. Rangamani, "Causality & holographic entanglement entropy," *JHEP*, vol. 12, p. 162, 2014.

[75] J. D. Brown and M. Henneaux, "Central Charges in the Canonical Realization of Asymptotic Symmetries: An Example from Three-Dimensional Gravity," *Commun. Math. Phys.*, vol. 104, pp. 207–226, 1986.

[76] J. Polchinski and M. J. Strassler, "The String dual of a confining four-dimensional gauge theory," 2000.

[77] I. R. Klebanov and M. J. Strassler, "Supergravity and a confining gauge theory: Duality cascades and chi SB resolution of naked singularities," *JHEP*, vol. 08, p. 052, 2000.

[78] M. Kruczenski, D. Mateos, R. C. Myers, and D. J. Winters, "Towards a holographic dual of large N(c) QCD," *JHEP*, vol. 05, p. 041, 2004.

[79] T. Sakai and S. Sugimoto, "Low energy hadron physics in holographic QCD," *Prog. Theor. Phys.*, vol. 113, pp. 843–882, 2005.

[80] J. Kaplan, “Lectures on ads/cft from the bottom up.”

[81] V. E. Hubeny and M. Rangamani, “A Holographic view on physics out of equilibrium,” *Adv. High Energy Phys.*, vol. 2010, p. 297916, 2010.

[82] G. T. Horowitz and V. E. Hubeny, “Quasinormal modes of AdS black holes and the approach to thermal equilibrium,” *Phys. Rev.*, vol. D62, p. 024027, 2000.

[83] A. Buchel, M. P. Heller, and R. C. Myers, “Equilibration rates in a strongly coupled nonconformal quark-gluon plasma,” *Phys. Rev. Lett.*, vol. 114, no. 25, p. 251601, 2015.

[84] N. Jokela, A. Pönni, and A. Vuorinen, “Small black holes in global AdS spacetime,” *Phys. Rev.*, vol. D93, no. 8, p. 086004, 2016.

[85] N. Iqbal and H. Liu, “Universality of the hydrodynamic limit in AdS/CFT and the membrane paradigm,” *Phys. Rev.*, vol. D79, p. 025023, 2009.

[86] G. Policastro, D. T. Son, and A. O. Starinets, “The Shear viscosity of strongly coupled N=4 supersymmetric Yang-Mills plasma,” *Phys. Rev. Lett.*, vol. 87, p. 081601, 2001.

[87] G. Policastro, D. T. Son, and A. O. Starinets, “From AdS / CFT correspondence to hydrodynamics,” *JHEP*, vol. 09, p. 043, 2002.

[88] S. Bhattacharyya, V. E. Hubeny, S. Minwalla, and M. Rangamani, “Nonlinear Fluid Dynamics from Gravity,” *JHEP*, vol. 02, p. 045, 2008.

[89] S. Bhattacharyya, V. E. Hubeny, R. Loganayagam, G. Mandal, S. Minwalla, T. Morita, M. Rangamani, and H. S. Reall, “Local Fluid Dynamical Entropy from Gravity,” *JHEP*, vol. 06, p. 055, 2008.

[90] M. Rangamani, “Gravity and Hydrodynamics: Lectures on the fluid-gravity correspondence,” *Class. Quant. Grav.*, vol. 26, p. 224003, 2009.

[91] V. E. Hubeny, S. Minwalla, and M. Rangamani, “The fluid/gravity correspondence,” in *Black holes in higher dimensions*, pp. 348–383, 2012. [,817(2011)].

[92] P. Romatschke, “Do nuclear collisions create a locally equilibrated quark-gluon plasma?,” *Eur. Phys. J.*, vol. C77, no. 1, p. 21, 2017.

[93] P. M. Chesler and L. G. Yaffe, “Boost invariant flow, black hole formation, and far-from-equilibrium dynamics in N = 4 supersymmetric Yang-Mills theory,” *Phys. Rev.*, vol. D82, p. 026006, 2010.

[94] L. Keegan, A. Kurkela, P. Romatschke, W. van der Schee, and Y. Zhu, “Weak and strong coupling equilibration in nonabelian gauge theories,” *JHEP*, vol. 04, p. 031, 2016.

[95] M. P. Heller, R. A. Janik, and P. Witaszczyk, “Hydrodynamic Gradient Expansion in Gauge Theory Plasmas,” *Phys. Rev. Lett.*, vol. 110, no. 21, p. 211602, 2013.

[96] M. P. Heller, A. Kurkela, and M. Spalinski, “Hydrodynamization and transient modes of expanding plasma in kinetic theory,” 2016.

[97] P. M. Chesler and L. G. Yaffe, “Horizon formation and far-from-equilibrium isotropization in supersymmetric Yang-Mills plasma,” *Phys. Rev. Lett.*, vol. 102, p. 211601, 2009.

[98] B. Wu, “On holographic thermalization and gravitational collapse of massless scalar fields,” *JHEP*, vol. 10, p. 133, 2012.

[99] B. Wu, “On holographic thermalization and gravitational collapse of tachyonic scalar fields,” *JHEP*, vol. 04, p. 044, 2013.

[100] A. Buchel, L. Lehner, and R. C. Myers, “Thermal quenches in N=2* plasmas,” *JHEP*, vol. 08, p. 049, 2012.

[101] A. Buchel, L. Lehner, R. C. Myers, and A. van Niekerk, “Quantum quenches of holographic plasmas,” *JHEP*, vol. 05, p. 067, 2013.

[102] A. Buchel, R. C. Myers, and A. van Niekerk, “Nonlocal probes of thermalization in holographic quenches with spectral methods,” *JHEP*, vol. 02, p. 017, 2015. [Erratum: JHEP07,137(2015)].

[103] M. J. Bhaseen, J. P. Gauntlett, B. D. Simons, J. Sonner, and T. Wiseman, “Holographic Superfluids and the Dynamics of Symmetry Breaking,” *Phys. Rev. Lett.*, vol. 110, no. 1, p. 015301, 2013.

[104] M. P. Heller, R. A. Janik, and P. Witaszczyk, “The characteristics of thermalization of boost-invariant plasma from holography,” *Phys. Rev. Lett.*, vol. 108, p. 201602, 2012.

[105] P. M. Chesler and L. G. Yaffe, “Holography and colliding gravitational shock waves in asymptotically AdS$_5$ spacetime,” *Phys. Rev. Lett.*, vol. 106, p. 021601, 2011.

[106] J. Casalderrey-Solana, M. P. Heller, D. Mateos, and W. van der Schee, “From full stopping to transparency in a holographic model of heavy ion collisions,” *Phys. Rev. Lett.*, vol. 111, p. 181601, 2013.

[107] A. Adams, P. M. Chesler, and H. Liu, “Holographic turbulence,” *Phys. Rev. Lett.*, vol. 112, no. 15, p. 151602, 2014.

[108] R. Wald, *General relativity.* Chicago: University of Chicago Press, 1984.

[109] P. Figueras, V. E. Hubeny, M. Rangamani, and S. F. Ross, “Dynamical black holes and expanding plasmas,” *JHEP*, vol. 04, p. 137, 2009.

[110] S. Bhattacharyya and S. Minwalla, “Weak Field Black Hole Formation in Asymptotically AdS Spacetimes,” *JHEP*, vol. 09, p. 034, 2009.

[111] V. Balasubramanian, A. Bernamonti, J. de Boer, N. Copland, B. Craps, E. Keski-Vakkuri, B. Muller, A. Schafer, M. Shigemori, and W. Staessens, “Thermalization of Strongly Coupled Field Theories,” *Phys. Rev. Lett.*, vol. 106, p. 191601, 2011.

[112] V. Balasubramanian, A. Bernamonti, J. de Boer, N. Copland, B. Craps, E. Keski-Vakkuri, B. Muller, A. Schafer, M. Shigemori, and W. Staessens, “Holographic Thermalization,” *Phys. Rev.*, vol. D84, p. 026010, 2011.

[113] V. Balasubramanian, A. Bernamonti, N. Copland, B. Craps, and F. Galli, “Thermalization of mutual and tripartite information in strongly coupled two dimensional conformal field theories,” *Phys. Rev.*, vol. D84, p. 105017, 2011.

[114] A. Allais and E. Tonni, “Holographic evolution of the mutual information,” *JHEP*, vol. 01, p. 102, 2012.

[115] H. Liu and S. J. Suh, “Entanglement Tsunami: Universal Scaling in Holographic Thermalization,” *Phys. Rev. Lett.*, vol. 112, p. 011601, 2014.

[116] H. Liu and S. J. Suh, “Entanglement growth during thermalization in holographic systems,” *Phys. Rev.*, vol. D89, no. 6, p. 066012, 2014.

[117] V. Keranen, H. Nishimura, S. Stricker, O. Taanila, and A. Vuorinen, “Dynamics of gravitational collapse and holographic entropy production,” *Phys. Rev.*, vol. D90, no. 6, p. 064033, 2014.

[118] V. Keranen, H. Nishimura, S. Stricker, O. Taanila, and A. Vuorinen, “Gravitational collapse of thin shells: Time evolution of the holographic entanglement entropy,” *JHEP*, vol. 06, p. 126, 2015.

[119] S. Leichenauer and M. Moosa, “Entanglement Tsunami in (1+1)-Dimensions,” *Phys. Rev.*, vol. D92, p. 126004, 2015.

[120] H. Casini, H. Liu, and M. Mezei, “Spread of entanglement and causality,” *JHEP*, vol. 07, p. 077, 2016.

[121] T. Hartman and N. Afkhami-Jeddi, “Speed Limits for Entanglement,” 2015.

[122] X. Bai, B.-H. Lee, L. Li, J.-R. Sun, and H.-Q. Zhang, “Time Evolution of Entanglement Entropy in Quenched Holographic Superconductors,” *JHEP*, vol. 04, p. 066, 2015.

[123] C. Ecker, D. Grumiller, and S. A. Stricker, “Evolution of holographic entanglement entropy in an anisotropic system,” *JHEP*, vol. 07, p. 146, 2015.

[124] P. M. Chesler and L. G. Yaffe, “Numerical solution of gravitational dynamics in asymptotically anti-de Sitter spacetimes,” *JHEP*, vol. 07, p. 086, 2014.

[125] V. E. Hubeny and M. Rangamani, “Unstable horizons,” *JHEP*, vol. 05, p. 027, 2002.

[126] A. Buchel and L. Lehner, “Small black holes in $AdS_5 \times S^5$,” *Class. Quant. Grav.*, vol. 32, no. 14, p. 145003, 2015.

[127] R. Gregory and R. Laflamme, “Black strings and p-branes are unstable,” *Phys. Rev. Lett.*, vol. 70, pp. 2837–2840, 1993.

[128] D. Christodoulou and S. Klainerman, “The global nonlinear stability of the minkowski space,” *Séminaire Équations aux dérivées partielles (Polytechnique)*, pp. 1–29, 1993.

[129] H. Friedrich, “On the existence ofn-geodesically complete or future complete solutions of einstein’s field equations with smooth asymptotic structure,” *Communications in Mathematical Physics*, vol. 107, no. 4, pp. 587–609, 1986.

[130] P. Bizon and A. Rostworowski, “On weakly turbulent instability of anti-de Sitter space,” *Phys. Rev. Lett.*, vol. 107, p. 031102, 2011.

[131] M. Maliborski and A. Rostworowski, “Lecture Notes on Turbulent Instability of Anti-de Sitter Spacetime,” *Int. J. Mod. Phys.*, vol. A28, p. 1340020, 2013.

[132] I. Yang, “Ads instability and holographic thermalization,” 2014. Talk presented at the workshop *CERN-CKC TH Institute on Numerical Holography* at CERN.

[133] M. Maliborski, “Instability of Flat Space Enclosed in a Cavity,” *Phys. Rev. Lett.*, vol. 109, p. 221101, 2012.

[134] M. Maliborski and A. Rostworowski, “What drives AdS spacetime unstable?,” *Phys. Rev.*, vol. D89, no. 12, p. 124006, 2014.

[135] A. Buchel, S. L. Liebling, and L. Lehner, “Boson stars in AdS spacetime,” *Phys. Rev.*, vol. D87, no. 12, p. 123006, 2013.

[136] O. J. C. Dias, G. T. Horowitz, D. Marolf, and J. E. Santos, “On the Nonlinear Stability of Asymptotically Anti-de Sitter Solutions,” *Class. Quant. Grav.*, vol. 29, p. 235019, 2012.

[137] P. Bizon, “Trying to understand the instability of ads through toy models,” 2014. Talk presented at the workshop *New frontiers in dynamical gravity* at Cambridge U.

[138] P. Basu, C. Krishnan, and A. Saurabh, “A stochasticity threshold in holography and the instability of AdS,” *Int. J. Mod. Phys.*, vol. A30, no. 21, p. 1550128, 2015.

[139] F. V. Dimitrakopoulos, B. Freivogel, M. Lippert, and I.-S. Yang, “Position space analysis of the AdS (in)stability problem,” *JHEP*, vol. 08, p. 077, 2015.

[140] M. Maliborski and A. Rostworowski, “Time-Periodic Solutions in an Einstein AdS-Massless-Scalar-Field System,” *Phys. Rev. Lett.*, vol. 111, p. 051102, 2013.

[141] M. Maliborski and A. Rostworowski, “A comment on ”Boson stars in AdS”,” 2013.

[142] A. Buchel, L. Lehner, and S. L. Liebling, “Scalar Collapse in AdS,” *Phys. Rev.*, vol. D86, p. 123011, 2012.

[143] F. Dimitrakopoulos and I.-S. Yang, “Conditionally extended validity of perturbation theory: Persistence of AdS stability islands,” *Phys. Rev.*, vol. D92, no. 8, p. 083013, 2015.

[144] V. Balasubramanian, A. Buchel, S. R. Green, L. Lehner, and S. L. Liebling, “Holographic Thermalization, Stability of Anti-de Sitter Space, and the Fermi-Pasta-Ulam Paradox,” *Phys. Rev. Lett.*, vol. 113, no. 7, p. 071601, 2014.

[145] B. Craps, O. Evnin, and J. Vanhoof, “Renormalization group, secular term resummation and AdS (in)stability,” *JHEP*, vol. 10, p. 048, 2014.

[146] B. Craps, O. Evnin, and J. Vanhoof, “Renormalization, averaging, conservation laws and AdS (in)stability,” *JHEP*, vol. 01, p. 108, 2015.

[147] P. Bizon, M. Maliborski, and A. Rostworowski, “Resonant Dynamics and the Instability of Anti-de Sitter Spacetime,” *Phys. Rev. Lett.*, vol. 115, no. 8, p. 081103, 2015.

[148] A. Buchel, S. R. Green, L. Lehner, and S. L. Liebling, “Conserved quantities and dual turbulent cascades in anti-de Sitter spacetime,” *Phys. Rev.*, vol. D91, no. 6, p. 064026, 2015.

[149] O. Evnin and C. Krishnan, “A Hidden Symmetry of AdS Resonances,” *Phys. Rev.*, vol. D91, no. 12, p. 126010, 2015.

[150] O. Evnin and R. Nivesvivat, “AdS perturbations, isometries, selection rules and the Higgs oscillator,” *JHEP*, vol. 01, p. 151, 2016.

[151] S. R. Green, A. Maillard, L. Lehner, and S. L. Liebling, “Islands of stability and recurrence times in AdS,” *Phys. Rev.*, vol. D92, no. 8, p. 084001, 2015.

[152] F. V. Dimitrakopoulos, B. Freivogel, J. F. Pedraza, and I.-S. Yang, “Gauge dependence of the AdS instability problem,” *Phys. Rev.*, vol. D94, no. 12, p. 124008, 2016.

[153] F. V. Dimitrakopoulos, B. Freivogel, and J. F. Pedraza, “Fast and Slow Coherent Cascades in Anti-de Sitter Spacetime,” 2016.

[154] B. Freivogel and I.-S. Yang, “Coherent Cascade Conjecture for Collapsing Solutions in Global AdS,” *Phys. Rev.*, vol. D93, no. 10, p. 103007, 2016.

[155] P. Basu, C. Krishnan, and P. N. Bala Subramanian, “AdS (In)stability: Lessons From The Scalar Field,” *Phys. Lett.*, vol. B746, pp. 261–265, 2015.

[156] M. Banados, C. Teitelboim, and J. Zanelli, “The Black hole in three-dimensional spacetime,” *Phys. Rev. Lett.*, vol. 69, pp. 1849–1851, 1992.

[157] M. Banados, M. Henneaux, C. Teitelboim, and J. Zanelli, “Geometry of the (2+1) black hole,” *Phys. Rev.*, vol. D48, pp. 1506–1525, 1993. [Erratum: Phys. Rev.D88,069902(2013)].

[158] M. W. Choptuik, “Universality and scaling in gravitational collapse of a massless scalar field,” *Phys. Rev. Lett.*, vol. 70, pp. 9–12, 1993.

[159] P. Bizon and J. Jalmuzna, “Globally regular instability of AdS_3,” *Phys. Rev. Lett.*, vol. 111, no. 4, p. 041102, 2013.

[160] F. Pretorius and M. W. Choptuik, "Gravitational collapse in (2+1)-dimensional AdS space-time," *Phys. Rev.*, vol. D62, p. 124012, 2000.

[161] B. Craps, E. J. Lindgren, A. Taliotis, J. Vanhoof, and H.-b. Zhang, "Holographic gravitational infall in the hard wall model," *Phys. Rev.*, vol. D90, no. 8, p. 086004, 2014.

[162] B. Craps, E. J. Lindgren, and A. Taliotis, "Holographic thermalization in a top-down confining model," *JHEP*, vol. 12, p. 116, 2015.

[163] P. Bizon, "Gravitational turbulent instability of ads$_5$," 2014. Talk presented at the *Strings 2014* at Princeton U. and IAS.

[164] O. J. C. Dias, G. T. Horowitz, and J. E. Santos, "Gravitational Turbulent Instability of Anti-de Sitter Space," *Class. Quant. Grav.*, vol. 29, p. 194002, 2012.

[165] O. Dias and J. E. Santos, "AdS nonlinear instability: moving beyond spherical symmetry," *Class. Quant. Grav.*, vol. 33, no. 23, p. 23LT01, 2016.

[166] A. Rostworowski, "Comment on "AdS nonlinear instability: moving beyond spherical symmetry" [Class. Quantum Grav. 33 23LT01 (2016)]," 2016.

[167] G. T. Horowitz and J. E. Santos, "Geons and the Instability of Anti-de Sitter Spacetime," *Surveys Diff. Geom.*, vol. 20, pp. 321–335, 2015.

[168] A. Polkovnikov, K. Sengupta, A. Silva, and M. Vengalattore, "Nonequilibrium dynamics of closed interacting quantum systems," *Rev. Mod. Phys.*, vol. 83, p. 863, 2011.

[169] E. Fermi, J. Pasta, and S. Ulam, "Studies of nonlinear problems," *Los Alamos Report LA-1940*, vol. 978, 1955.

[170] T. Kinoshita, T. Wenger, and D. S. Weiss, "A quantum newton's cradle," *Nature*, vol. 440, no. 7086, pp. 900–903, 2006.

[171] M. Gring, M. Kuhnert, T. Langen, T. Kitagawa, B. Rauer, M. Schreitl, I. Mazets, D. A. Smith, E. Demler, and J. Schmiedmayer, "Relaxation and prethermalization in an isolated quantum system," *Science*, vol. 337, no. 6100, pp. 1318–1322, 2012.

[172] S. Trotzky, Y.-A. Chen, A. Flesch, I. P. McCulloch, U. Schollwöck, J. Eisert, and I. Bloch, "Probing the relaxation towards equilibrium in an isolated strongly correlated one-dimensional bose gas," *Nature Physics*, vol. 8, no. 4, pp. 325–330, 2012.

[173] E. T. Jaynes, "Information theory and statistical mechanics," *Physical review*, vol. 106, no. 4, p. 620, 1957.

[174] M. Rigol, V. Dunjko, V. Yurovsky, and M. Olshanii, "Relaxation in a completely integrable many-body quantum system: an ab initio study of the dynamics of the highly excited states of 1d lattice hard-core bosons," *Physical review letters*, vol. 98, no. 5, p. 050405, 2007.

[175] M. Kollar, F. A. Wolf, and M. Eckstein, "Generalized gibbs ensemble prediction of prethermalization plateaus and their relation to nonthermal steady states in integrable systems," *Physical Review B*, vol. 84, no. 5, p. 054304, 2011.

[176] D. A. Smith, M. Gring, T. Langen, M. Kuhnert, B. Rauer, R. Geiger, T. Kitagawa, I. Mazets, E. Demler, and J. Schmiedmayer, "Prethermalization revealed by the relaxation dynamics of full distribution functions," *New Journal of Physics*, vol. 15, no. 7, p. 075011, 2013.

[177] G. Mussardo, "Infinite-time average of local fields in an integrable quantum field theory after a quantum quench," *Physical review letters*, vol. 111, no. 10, p. 100401, 2013.

[178] T. Takayanagi and T. Ugajin, "Measuring Black Hole Formations by Entanglement Entropy via Coarse-Graining," *JHEP*, vol. 11, p. 054, 2010.

[179] O. J. C. Dias, G. T. Horowitz, and J. E. Santos, "Black holes with only one Killing field," *JHEP*, vol. 07, p. 115, 2011.

[180] H. Okawa, J. C. Lopes, and V. Cardoso, "Collapse of massive fields in anti-de Sitter spacetime," 2015.

[181] T. Albash and C. V. Johnson, "Evolution of Holographic Entanglement Entropy after Thermal and Electromagnetic Quenches," *New J. Phys.*, vol. 13, p. 045017, 2011.

[182] M. Nozaki, T. Numasawa, and T. Takayanagi, "Holographic Local Quenches and Entanglement Density," *JHEP*, vol. 05, p. 080, 2013.

[183] M. A. Cazalilla, "Effect of Suddenly Turning on Interactions in the Luttinger Model," *Phys. Rev. Lett.*, vol. 97, no. 15, p. 156403, 2006.

[184] M. Greiner, O. Mandel, T. W. Hänsch, and I. Bloch, "Collapse and revival of the matter wave field of a bose-einstein condensate," *Nature*, vol. 419, no. 6902, pp. 51–54, 2002.

[185] F. Iglói and H. Rieger, "Quantum relaxation after a quench in systems with boundaries," *Physical review letters*, vol. 106, no. 3, p. 035701, 2011.

[186] J. Häppölä, G. B. Halász, and A. Hamma, "Revivals of a closed quantum system and lieb-robinson speed," *Phys. Rev. A*, vol. 85, p. 032114, 2012.

[187] J. Cardy, "Thermalization and Revivals after a Quantum Quench in Conformal Field Theory," *Phys. Rev. Lett.*, vol. 112, p. 220401, 2014.

[188] C. V. Johnson, "Large N Phase Transitions, Finite Volume, and Entanglement Entropy," *JHEP*, vol. 03, p. 047, 2014.

[189] C. Ecker, D. Grumiller, P. Stanzer, S. A. Stricker, and W. van der Schee, "Exploring nonlocal observables in shock wave collisions," *JHEP*, vol. 11, p. 054, 2016.

[190] E. T. Jaynes and F. W. Cummings, "Comparison of quantum and semiclassical radiation theories with application to the beam maser," *IEEE Proc.*, vol. 51, pp. 89–109, 1963.

[191] E. M. Wright, D. Walls, and J. Garrison, "Collapses and revivals of bose-einstein condensates formed in small atomic samples," *Physical review letters*, vol. 77, no. 11, p. 2158, 1996.

[192] R. W. Robinett, "Quantum wave packet revivals," *Physics Reports*, vol. 392, no. 1, pp. 1–119, 2004.

[193] D. Santos-Oliván and C. F. Sopuerta, "Moving closer to the collapse of a massless scalar field in spherically symmetric anti–de Sitter spacetimes," *Phys. Rev.*, vol. D93, no. 10, p. 104002, 2016.

[194] N. Deppe, A. Kolly, A. R. Frey, and G. Kunstatter, "Black Hole Formation in AdS Einstein-Gauss-Bonnet Gravity," *JHEP*, vol. 10, p. 087, 2016.

[195] N. Kim, "Time-periodic solutions of massive scalar fields in dynamical AdS background: Perturbative constructions," *Phys. Lett.*, vol. B742, pp. 274–278, 2015.

[196] M. Maliborski, *Dynamics of Nonlinear Waves on Bounded Domains.* PhD thesis, Jagiellonian U., 2014.

[197] E. Poisson, *A relativist's toolkit : the mathematics of black-hole mechanics.* Cambridge, UK New York: Cambridge University Press, 2004.

[198] J. Jalmuzna, "Three-dimensional Gravity and Instability of AdS_3," *Acta Phys. Polon.*, vol. B44, no. 12, pp. 2603–2620, 2013.

[199] V. Keranen, H. Nishimura, S. Stricker, O. Taanila, and A. Vuorinen.

[200] V. E. Hubeny and M. Rangamani, "Causal Holographic Information," *JHEP*, vol. 06, p. 114, 2012.

[201] R. Brito, V. Cardoso, and J. V. Rocha, "Interacting shells in AdS spacetime and chaos," *Phys. Rev.*, vol. D94, no. 2, p. 024003, 2016.

[202] P. Basu, J. Bhattacharya, S. Bhattacharyya, R. Loganayagam, S. Minwalla, and V. Umesh, "Small Hairy Black Holes in Global AdS Spacetime," *JHEP*, vol. 10, p. 045, 2010.

[203] O. J. C. Dias, P. Figueras, S. Minwalla, P. Mitra, R. Monteiro, and J. E. Santos, "Hairy black holes and solitons in global AdS_5," *JHEP*, vol. 08, p. 117, 2012.

[204] S. A. Gentle, M. Rangamani, and B. Withers, "A Soliton Menagerie in AdS," *JHEP*, vol. 05, p. 106, 2012.

[205] G. T. Horowitz and M. M. Roberts, "Zero Temperature Limit of Holographic Superconductors," *JHEP*, vol. 11, p. 015, 2009.

[206] P. Basu, C. Krishnan, and P. N. B. Subramanian, "Phases of Global AdS Black Holes," *JHEP*, vol. 06, p. 139, 2016.

[207] R.-G. Cai, L. Li, and L.-F. Li, "A Holographic P-wave Superconductor Model," *JHEP*, vol. 01, p. 032, 2014.

[208] F. Aprile, D. Roest, and J. G. Russo, "Holographic Superconductors from Gauged Supergravity," *JHEP*, vol. 06, p. 040, 2011.

[209] U. Gursoy, A. Jansen, and W. van der Schee, "New dynamical instability in asymptotically anti-de Sitter spacetime," *Phys. Rev.*, vol. D94, no. 6, p. 061901, 2016.

[210] D. Astefanesei and E. Radu, "Boson stars with negative cosmological constant," *Nucl. Phys.*, vol. B665, pp. 594–622, 2003.

[211] S. Bhattacharyya, S. Minwalla, and K. Papadodimas, "Small Hairy Black Holes in AdS_5xS^5," *JHEP*, vol. 11, p. 035, 2011.

[212] T. Ishii, E. Kiritsis, and C. Rosen, "Thermalization in a Holographic Confining Gauge Theory," *JHEP*, vol. 08, p. 008, 2015.

[213] T. Ishii, E. Kiritsis, and C. Rosen, "Thermalization and confinement in strongly coupled gauge theories," *PoS*, vol. EPS-HEP2015, p. 365, 2015.

[214] U. Gursoy and E. Kiritsis, "Exploring improved holographic theories for QCD: Part I," *JHEP*, vol. 02, p. 032, 2008.

[215] U. Gursoy, E. Kiritsis, and F. Nitti, "Exploring improved holographic theories for QCD: Part II," *JHEP*, vol. 02, p. 019, 2008.

[216] E. Caceres, A. Kundu, J. F. Pedraza, and W. Tangarife, "Strong Subadditivity, Null Energy Condition and Charged Black Holes," *JHEP*, vol. 01, p. 084, 2014.

[217] S. R. Das, "Old and New Scaling Laws in Quantum Quench," in *Nambu Memorial Symposium Chicago, IL, USA, March 11-13, 2016*, vol. 2016, p. 12C107, 2016.

[218] A. O'Bannon, J. Probst, R. Rodgers, and C. F. Uhlemann, "A First Law of Entanglement Rates from Holography," 2016.

[219] G. T. Horowitz and R. C. Myers, "AdS/CFT correspondence and a new positive energy conjecture for general relativity," *Physical Review D*, vol. 59, no. 2, p. 026005, 1998.

[220] J.-P. Berrut and L. N. Trefethen, "Barycentric lagrange interpolation," *SIAM Review*, vol. 46, pp. 501–517, jan 2004.

[221] A. Buchel, R. C. Myers, and A. van Niekerk, "Universality of Abrupt Holographic Quenches," *Phys. Rev. Lett.*, vol. 111, p. 201602, 2013.

[222] G. Clement, "Classical solutions in three-dimensional Einstein-Maxwell cosmological gravity," *Class. Quant. Grav.*, vol. 10, pp. L49–L54, 1993.

[223] E. W. Hirschmann and D. L. Welch, “Magnetic solutions to 2+ 1 gravity,” *Physical Review D*, vol. 53, no. 10, p. 5579, 1996.

[224] M. Cataldo and P. Salgado, “Static Einstein-Maxwell solutions in (2+1)-dimensions,” *Submitted to: Phys. Rev. D*, 1996.

[225] O. J. Dias and J. P. Lemos, “Rotating magnetic solution in three dimensional einstein gravity,” *Journal of High Energy Physics*, vol. 2002, no. 01, p. 006, 2002.

[226] R. Olea, “Charged rotating black hole formation from thin shell collapse in three dimensions,” *Modern Physics Letters A*, vol. 20, no. 34, pp. 2649–2665, 2005.

[227] M. Cataldo, J. Crisóstomo, S. del Campo, and P. Salgado, “On magnetic solution to 2+ 1 einstein–maxwell gravity,” *Physics Letters B*, vol. 584, no. 1, pp. 123–126, 2004.

[228] T. Andrade and B. Withers, “A simple holographic model of momentum relaxation,” *JHEP*, vol. 05, p. 101, 2014.

[229] N. Deppe, A. Kolly, A. Frey, and G. Kunstatter, “Stability of AdS in Einstein Gauss Bonnet Gravity,” *Phys. Rev. Lett.*, vol. 114, p. 071102, 2015.

[230] V. Cardoso and J. V. Rocha, “Collapsing shells, critical phenomena and black hole formation,” *Phys. Rev.*, vol. D93, no. 8, p. 084034, 2016.

[231] J. Crisostomo, R. Troncoso, and J. Zanelli, “Black hole scan,” *Phys. Rev.*, vol. D62, p. 084013, 2000.

[232] V. Cardoso and G. Khanna, “Black holes in anti–de Sitter spacetime: Quasinormal modes, tails, and flat spacetime,” *Phys. Rev.*, vol. D91, no. 2, p. 024031, 2015.

[233] P. Bosch, S. R. Green, and L. Lehner, “Nonlinear Evolution and Final Fate of Charged Anti–de Sitter Black Hole Superradiant Instability,” *Phys. Rev. Lett.*, vol. 116, no. 14, p. 141102, 2016.

[234] M. Ammon, S. Grieninger, A. Jimenez-Alba, R. P. Macedo, and L. Melgar, “Holographic quenches and anomalous transport,” *JHEP*, vol. 09, p. 131, 2016.

[235] S. Banerjee, T. Ishii, L. K. Joshi, A. Mukhopadhyay, and P. Ramadevi, “Time-dependence of the holographic spectral function: Diverse routes to thermalisation,” *JHEP*, vol. 08, p. 048, 2016.